Modelling of perovskite-based materials for intermediate temperature solid oxide fuel cell cathodes

Ailbhe Gavin

A thesis submitted in partial fulfillment of the requirements
for the degree of Doctor of Philosophy
at the University of Dublin, Trinity College

2018

Declaration of Authorship

I declare that this thesis has not been submitted as an exercise for a degree at this or any other university and it is entirely my own work, except where otherwise cited.

I agree to deposit this thesis in the University's open access institutional repository or allow the Library to do so on my behalf, subject to Irish Copyright Legislation and Trinity College Library conditions of use and acknowledgement.

Ailbhe Gavin

2018
University of Dublin, Trinity College

Summary

In recent years it has become clear that a move to cleaner, more efficient energy generation is required. Solid oxide fuel cells (SOFCs) are a promising technology for electricity generation as they can overcome combustion efficiency limitations, and can utilise a range of fuels, including hydrogen, methanol and ethanol. However, there are a number of challenges currently associated with them. High temperatures are required for operation of current generation fuel cells, leading to high costs and accelerated performance degradation. Recently, the development of more efficient SOFCs which operate at intermediate temperature, in the region of 600–1000 K, has been investigated. Both optimisation of the materials currently used for components for SOFCs, and development of alternative materials have been considered as methods of improving their efficiency. The cathode, at which the oxygen reduction reaction takes place, currently requires a high operating temperature due to poor catalytic activity for the reaction at lower temperature, thus development of improved materials for intermediate temperature SOFCs is of great importance.

In this thesis, we first investigate $LaMnO_3$, which has been widely used in high temperature SOFCs, examining the performance of density functional theory (DFT) and post-DFT methods in modelling its structural and electronic properties. Our results show that DFT fails to model the structural and electronic properties of $LaMnO_3$ correctly and although hybrid DFT can give an improved description of the structure, it does not correctly model features in the electronic density of states. The PBEsol + U functional is used to model the low index surfaces, and oxygen vacancy formation in the bulk and at these surfaces are examined. Nudged elastic band calculations are used to determine the activation energy for oxygen migration in bulk $LaMnO_3$. The introduction of alkaline earth defects to bulk $LaMnO_3$ in investigated, considering both the site selectivity and the charge compensation mechanism. Larger dopant cations (Ca, Sr, Ba) are found to have lower formation energies on the La site, while the smaller Mg cation shows preference for the Mn site. For all defects, charge compensation by hole formation is preferred over oxygen vacancy formation.

Secondly, the layered Ruddlesden-Popper oxide La_2NiO_4 is examined, which has attracted attention due to its good ionic and electronic conductivity in the intermediate temperature range, and stability under SOFC operating conditions. As the Ruddlesden-Popper structure can accommodate both oxygen vacancies and interstitials, both are modelled in bulk La_2NiO_4 and at its low index surfaces, to establish

the dominant oxygen defects. As interstitial defects are found to be dominant, nudged elastic band calculations are used to determine the mechanism and activation energy for oxygen interstitial migration, with the lowest activation energy found to be significantly lower than was predicted in $LaMnO_3$. Sr and Fe defects are introduced to both the La and Ni site, to determine their site selectivity and charge compensation mechanism, with Sr defects having lower formation energies on the La site, and Fe defects on the Ni site. Under SOFC operating conditions, doping with Sr is compensated by the formation of delocalised, unbound holes, which will improve the electronic conductivity of the material. Doping with Fe is compensated by the formation of oxygen interstitials, which can improve the ionic conductivity, but strong binding of the defect will limit the improvement.

Finally, $LaCrO_3$ is investigated as a potential mixed ionic and electronic conductor. The origin of the charge carriers in $LaCrO_3$ and Sr-doped $LaCrO_3$ is established, considering intrinsic and extrinsic defect formation. The thermodynamic transition levels are calculated, allowing identification of defects with low formation energies and shallow transition levels. The activation energy for oxygen migration in bulk $LaCrO_3$ is found to be significantly higher than in either La_2NiO_4 and $LaMnO_3$, therefore La_2NiO_4 and $LaMnO_3$ are likely to be more suitable for SOFC applications.

Acknowledgements

First and foremost, I would like to thank my supervisor, Prof. Graeme Watson, for his expertise and advice on the project. Thanks to the Watson group members, past and present, for being a mine of information for various aspects of the project, and for making the group an enjoyable place to work: Dr Jeremy Allen, Dr Mario Burbano, Dr John Carey, Dr Umadevi Deivasigamani, Dr Patrick Keating, Dr Aoife Kehoe, Aoife Lucid, Aoife Plunkett, Julia Savioli, Swetanshu Tandon, and Douglas Temple.

I would like to thank SFI for funding, without which this research would not have been possible. I would also like to acknowledge the computing resources on which the calculations in this thesis have been performed: Research IT for maintaining the Kelvin, Lonsdale and Pople clusters, and ICHEC for computing time on Fionn.

I wish to express my gratitude to all my friends, equestrian and elsewhere, for providing me with welcome distractions throughout the past few years. A huge thank you also to Shaun, for his endless patience and support during my postgraduate studies. Finally, thank you to my family for supporting my education over the years.

Publications

1. A. L. Gavin and G. W. Watson, Modelling the electronic structure of orthorhombic $LaMnO_3$, *Solid State Ionics*, 2017, **299**, 13–17

2. A. L. Gavin and G. W. Watson, Modelling oxygen defects in orthorhombic $LaMnO_3$ and its low index surfaces, *Phys. Chem. Chem. Phys.*, 2017, **36**, 24636–24646

3. A. L. Gavin and G. W. Watson, Defects in orthorhombic $LaMnO_3$ – ionic *versus* electronic compensation, *Phys. Chem. Chem. Phys.*, 2018, **20**, 19257–19267

Conference Talks

1. Irish Atomic Simulators Meeting 2016, University College Dublin, *Modelling of $LaMnO_3$ for intermediate temperature solid-oxide fuel-cell cathodes*

2. E-MRS Spring Meeting 2016, Lille, France, *Modelling of defects in $LaMnO_3$ for intermediate temperature solid oxide fuel cell cathodes*

3. Dublin Chemistry Postgraduate Conference 2016, Trinity College Dublin, *Defect modelling in $LaMnO_3$ for cathodes in intermediate temperature solid oxide fuel cells*

4. MRS Fall Meeting 2016, Boston, USA, *Defect Engineering in $LaCrO_3$ to develop a p-type semiconducting oxide*

5. ACS Spring Meeting 2017, San Francisco, USA, *Assessing the potential of $LaCrO_3$ as a p-type semiconducting oxide*

6. ACS Spring Meeting 2017, San Francisco, USA, *Modelling La_2NiO_4 for solid oxide fuel cell cathode applications*

Contents

List of Figures

List of Tables

List of Abbreviations

B3LYP	**B**ecke, **3** parameter, **L**ee-**Y**ang-**P**arr functional
CBM	**C**onduction **B**and **M**inimum
CPLAP	**C**hemical **P**otential **L**imits **A**nalysis **P**rogram
DFT	**D**ensity **F**unctional **T**heory
EDOS	**E**lectronic **D**ensity **o**f **S**tates
GGA	**G**eneralised **G**radient **A**pproximation
HF	**H**artree-**F**ock
HSE	**H**eyd, **S**cuseria and **E**rnzerhof functional
IT	**I**ntermediate **T**emperature
LDA	**L**ocal **D**ensity **A**pproximation
LEIS	**L**ow **E**nergy **I**on **S**cattering
LSDA	**L**ocal **S**pin **D**ensity **A**pproximation
MD	**M**olecular **D**ynamics
NEB	**N**udged **E**lastic **B**and
ORR	**O**xygen **R**eduction **R**eaction
PAW	**P**rojector **A**ugmented **W**ave
PBE	**P**erdew-**B**urke-**E**rnzerhof functional
PBEsol	**P**erdew-**B**urke-**E**rnzerhof functional revised for **sol**ids
PEDOS	**P**artial **E**lectronic **D**ensity **o**f **S**tates
PW91	**P**erdew-**W**ang **91** functional
SIE	**S**elf-**I**nteraction **E**rror
SOFC	**S**olid **O**xide **F**uel **C**ell
TEC	**T**hermal **E**xpansion **C**oefficient
TPB	**T**hree-**P**hase **B**oundary
VASP	**V**ienna ***ab*** *initio* **S**imulation **P**ackage
VBM	**V**alence **B**and **M**aximum
XAS	**X**-ray **A**bsorption **S**pectroscopy
XPS	**X**-ray **P**hotoelectron **S**pectroscopy
YSZ	**Y**ttria-**S**tabilised **Z**irconia

Chapter 1

Introduction

In recent years, there has been a drive to develop technologies for more environmentally friendly, sustainable, and efficient energy generation. In the period from 2015–2040, world energy consumption is projected to rise by 28% [1], with much of the increase in energy demand in non-Organisation for Economic Co-operation and Development countries due to strong economic growth, fast-growing populations and increased access to marketed energy. Currently, oil, coal and natural gas account for over 80% of the world primary energy supply [2]. The dependence on fossil fuels is not viable long-term, due to geopolitical instabilities in regions of supply, environmental consequences associated with burning fossil fuels, and limited supply, with the reserves of crude oil and natural gas projected to be exhausted by 2070 at the current reserves-to-production ratio [3]. Biofuels and nuclear account for $\sim$15% of the world energy supply, but there are safety concerns associated with the use of nuclear power, and biofuels have significant land and process water requirement, as well as producing greenhouse gases. Therefore, the development of other methods of energy generation is required.

More environmentally friendly energy sources, such as wind, hydro, solar, tidal and geothermal currently account for only 4% of the global energy supply [2]. Though these technologies offer advantages such as sustainability and production of little or no harmful waste products, one of the major drawbacks of wind or solar electricity generation is their intermittent nature. Due to fluctuations in energy demand, these technologies can often provide either an energy surplus or deficit. Fuel cells are an alternative method of energy generation, offering a cleaner method of producing electricity than combustion of fossil fuels, and are suitable for large-scale electricity generation [4].

They can be used as stand-alone energy generators or can be incorporated into smart grids. The issue of fluctuation in energy production from tidal or solar sources can be addressed by use of a combination of electrolysis and fuel cells. When the supply of electricity exceeds the demand, the excess can be used for water electrolysis, storing energy in the form of hydrogen. This hydrogen can then be supplied to the fuel cell to generate electricity when demand increases.

1.1 Fuel Cells

Fuel cells are electrochemical devices which convert the chemical energy of a fuel into electrical power by reaction of the fuel with oxygen, with greater theoretical efficiency than conventional heat engines, as the process is reversible and they are not limited by the Carnot cycle [5]. In addition, in a combined heat and power (CHP) system, excess heat can be used for heating or cooling. A number of types of fuel cell exist, with a range of applications. Depending on fuel cell type, fuels such as hydrogen, methanol, or light hydrocarbons may be used.

Polymer electrolyte fuel cells (also known as proton exchange membrane fuel cells, PEMFCs) use a solid polymer membrane electrolyte which exhibits high proton conductivity, such as perfluorosulfonic acid [6]. They operate at relatively low temperatures, (below 100°C for low-temperature, and up to 300°C for high-temperature), so have fast start-up and experience less wear on components, but require noble metal catalysts due to their stability in the acidic conditions inside the cell, which increases their cost. These fuel cells, which use hydrogen as fuel, have attracted recent attention due to their use in fuel cell vehicles, such as the Toyota Mirai [7]. Direct methanol fuel cells (DMFCs) are a type of PEMFC, which use methanol mixed with water as fuel [8]. Methanol, as a liquid, is easier to transport as a fuel than hydrogen gas and has a higher energy density. However, DMFCs exhibit sluggish methanol oxidation and low efficiency of 20–30%, limiting their applications. They are suitable for use for backup power or portable devices as the energy density is more important for these devices than the conversion efficiency.

Alkaline fuel cells (AFCs) use an alkaline electrolyte and can exhibit very high performance, with efficiencies of over 50% reported for a 6 kW stack [9, 10]. However, AFCs are highly susceptible to CO_2 poisoning, which can have a significant negative impact on the cell durability, performance and lifetime due to the formation of carbonate. Alkaline membrane fuel cells offer an advantage over AFCs as they are less susceptible to this poisoning and corrosion, but have poor membrane conductivity and power density.

Phosphoric acid fuel cells (PAFCs) use liquid phosphoric acid as electrolyte and Pt for the cathode and anode [11, 12]. They operate at temperatures of 150–190°C under conditions of ambient pressure up to 5 atm. They can achieve efficiencies of up to 85% in CHP systems, but electricity generation alone is $\sim$37%. PAFCs are typically less powerful than other fuel cell types for the same weight and volume and due to the size requirements and use of Pt electrodes, there are high costs associated with PAFCs.

Molten carbonate fuel cells (MCFCs) are high-temperature fuel cells, operating at 600–700°C, for electrical utility, military, or industrial applications [13]. Advantages of MCFCs are their high efficiency and fuel flexibility, and their operating temperatures mean they are suitable for use in CHP systems. Sub-megawatt MCFC power plants have been reported to have electrical efficiencies of up to 50%, and very high efficiency can be achieved in CHP systems, with total efficiencies of up to 80%. However, due to the high operating temperatures, they experience accelerated breakdown of components, and they have long start-up times. In addition, they use corrosive liquid electrolytes, such as Li_2CO_3, leading to difficulties with handling.

SOFCs have attracted significant attention for electricity generation as they offer a number of advantages over other fuel cell types [4]. They use a ceramic electrolyte, which means there are no issues with handling. They are highly efficient, with electrical efficiency of over 60% [5], and in CHP systems can achieve efficiencies of greater than 85%. They can reform hydrocarbons internally, allowing the use of a variety of fuels such as hydrogen, methanol, ethanol or natural gas [14–16], and are suitable for use in distributed generation [17]. Components which do not contain noble metals may be used, with greater availability of materials and reduced cost. SOFCs have low emissions compared to combustion-based electricity generation, with by-products of

CO_2 and H_2O, or H_2O alone when hydrogen fuel is used. Solid oxide cells may be used as reversible cells, which can be operated in fuel cell mode, or in electrolysis mode. When operated in fuel cell mode they generate electricity, and in electrolysis mode, they use electricity for water electrolysis. As many renewable sources of energy (wind, solar) are intermittent, and electricity demand fluctuates, operation in electrolysis mode allows storage of excess energy in the form of hydrogen. This hydrogen can be used as fuel in the fuel cell to generate electricity if demand requires it.

1.2 Solid oxide fuel cells

Current technologies operate at high temperatures ($T > 1000\,K$), due to poor electrolyte conductivity and poor activity of cathode materials for oxygen reduction at low temperature. However, operation at high temperature requires the use of expensive materials for the interconnects, and leads to accelerated performance degradation rates and issues with the mismatch of thermal expansion coefficients (TECs), which can cause cracking of components during operation. As a result, work is now being carried out to reduce the operating temperature of SOFCs to the intermediate temperature (IT) range (600–1000 K). Development of alternative materials, capable of operating at lower temperatures is one option for this, while optimisation of current materials for operation at IT is another.

1.2.1 Solid oxide fuel cell operation

A SOFC consists of a cathode, separated from an anode by a solid electrolyte, and the electrodes are connected to an external circuit, as shown in figure 1.1 [18]. The cathode is often a mixed ionic and electronic conducting ceramic, which must have good electronic conductivity and a high oxygen diffusion coefficient; the electrolyte is a dense oxygen ion conducting ceramic with high ionic conductivity; and the anode is often a metal-ceramic composite with suitable electronic conductivity and catalytic reactivity for promotion of anodic reactions. In addition, the components must have

good chemical compatibility with other components, good TEC match to avoid cracking, stability under the SOFC operating conditions, high strength and, to make them viable for widespread application, should have low cost [4].

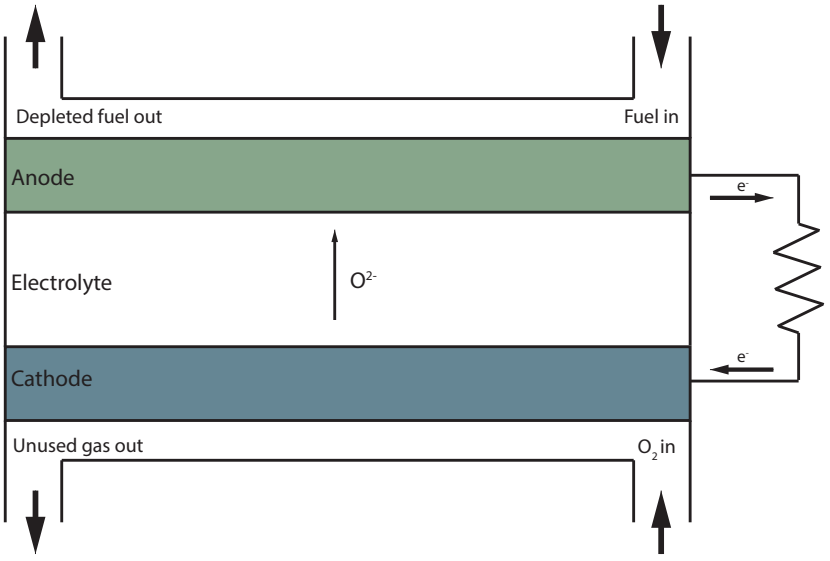

FIGURE 1.1: Schematic of a solid oxide fuel cell

Oxide-based ceramics are used for the electrolyte, and include yttria stabilised zirconia (YSZ), gadolium doped ceria (GDC), samarium doped ceria (SDC), and the perovskite $La_{1-x}Sr_xGa_{1-y}Mg_yO_{3-0.5(x+y)}$ (x,y = 0.1–0.2) (LSGM). The anode is usually a porous ceramic-metallic composite, often of the electrolyte material and NiO (*e.g.* NiO/YSZ, NiO/GDC, NiO/SDC), which gives a TEC close to that of the other cell components. At high temperatures, noble metals or electronically conducting oxides can be used for the cathode, with insufficient long-term stability and high costs associated with noble metals making them unsuitable for commercial applications. Electronically conducting perovskite-based materials, such as Sr- or Ca-doped $LaMnO_3$ provide good performance at high temperature, and excellent TEC match with electrolyte materials. At lower operating temperatures, mixed ionic and electronic conducting perovskites are required, with A- and B-site co-doped $LaFeO_3$, $LaCoO_3$ or $LaMnO_3$, or layered perovskite-based materials, such as Ruddlesden-Popper materials considered as potential cathode materials. The interconnects have high electronic conductivity, using doped $LaCrO_3$ or

metal alloys such as ferritic stainless steel, as they are stable under both oxidising and reducing conditions.

At the cathode, oxygen from the air is reduced, generating oxide ions in the electrolyte, according to the oxygen reduction reaction (ORR)

$$\frac{1}{2}\mathrm{O_2(g)} + 2e^- \rightarrow \mathrm{O^{2-}} \tag{1.1}$$

The generated oxide ions are transported through the electrolyte to the anode, where they react with the fuel, generating water (and CO_2 where hydrocarbon fuels are used), and releasing electrons to the external circuit, generating electrical power [5]. At the anode, the (hydrogen) fuel reacts with the oxide ions according to

$$\mathrm{H_2(g)} + \mathrm{O^{2-}} \rightarrow \mathrm{H_2O} + 2e^- \tag{1.2}$$

The ORR is often limited by poor ionic conductivity of the cathode to taking place at three-phase boundaries (TPB), a narrow region, where air, electrode and electrolyte meet (figure 1.2 (a)). In order to ensure the reaction is not restricted to the TPB, mixed ionic and electronic conductors are ideally used as cathode materials, allowing oxygen incorporation on the whole surface of the cathode [19] (figure 1.2 (b)). This increases the region in which the ORR can take place, improving the performance of the fuel cell. Options for improving the performance of SOFCs include optimising the

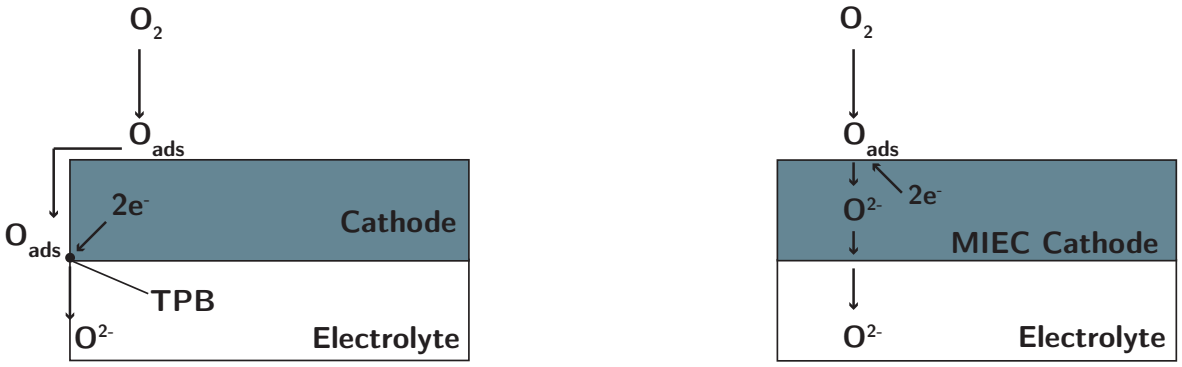

FIGURE 1.2: Schematic of a three-phase boundary in a solid oxide fuel cell showing (a) oxygen reduction at the three-phase boundary and (b) oxygen reduction at a mixed ionic and electronic conducting (MIEC) cathode surface

currently used materials for use at IT, or developing potential new materials for the SOFC components.

1.3 Perovskite Oxides

Perovskite oxides are a family of compounds with crystal structure related to that of $CaTiO_3$ [20]. The ideal perovskite structure, ABX_3 (where A and B are cations, with a combined charge of +6 (*e.g.* A^{1+} and B^{5+}, A^{2+} and B^{4+} or A^{3+} and B^{3+}) and X is often oxygen), has cubic symmetry, with space group $Pm\bar{3}m$, and consists of 12-coordinate A ions and corner-sharing BX_6 octahedra, as shown in figure 1.3.

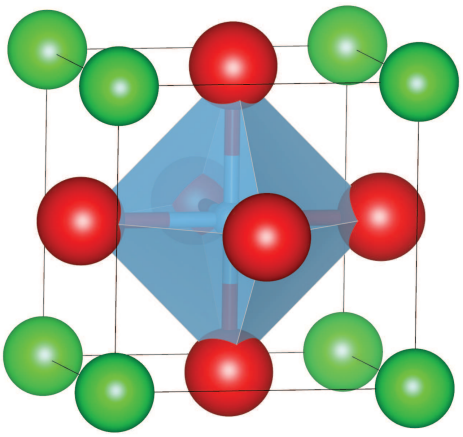

FIGURE 1.3: Ideal cubic perovskite structure. A ions are shown in green, B ions are shown in blue and X ions in red

Perovskite oxides can exhibit superconductivity, colossal magnetoresistance, ferroelectricity, piezoelectricity, and optical transparency, depending on their composition [21–26]. Materials with similar pseudocubic structures and matching lattice constants can be synthesised, and they can exhibit both *p*- and *n*-type conductivity, and thus could be used to fabricate all-perovskite-oxide transparent electronics. They can accommodate ionic substitution on both the A- and B-sites, carrier doping and oxygen non-stoichiometry. Sb- and Nb-doped $SrSnO_3$ thin films have shown high optical transmittance, above 90%, and good *n*-type conductivity, as well as good compatibility with other perovskite oxide thin films [27]. Recently, the transparent perovskite $BaSnO_3$ has been shown to exhibit high electron mobility when doped at the Ba site with La

(200–300 $cm^2V^{-1}s^{-1}$), and conductivity (10^4 Scm^{-1}), which is comparable with current n-type TCOs such as In-doped SnO_2 [26].

1.3.1 Goldschmidt tolerance factor

The cubic perovskite structure is uncommon, and the main factors responsible for its distortion are strain effects (ionic radii), deviation from the ideal composition, and Jahn-Teller effects, with a combination of these effects often observed [28]. In the cubic cell, shown in figure 1.4, the lattice parameter, a, can be written in terms of the ionic radii, r_A, r_B and r_X, in the A-X and B-X planes.

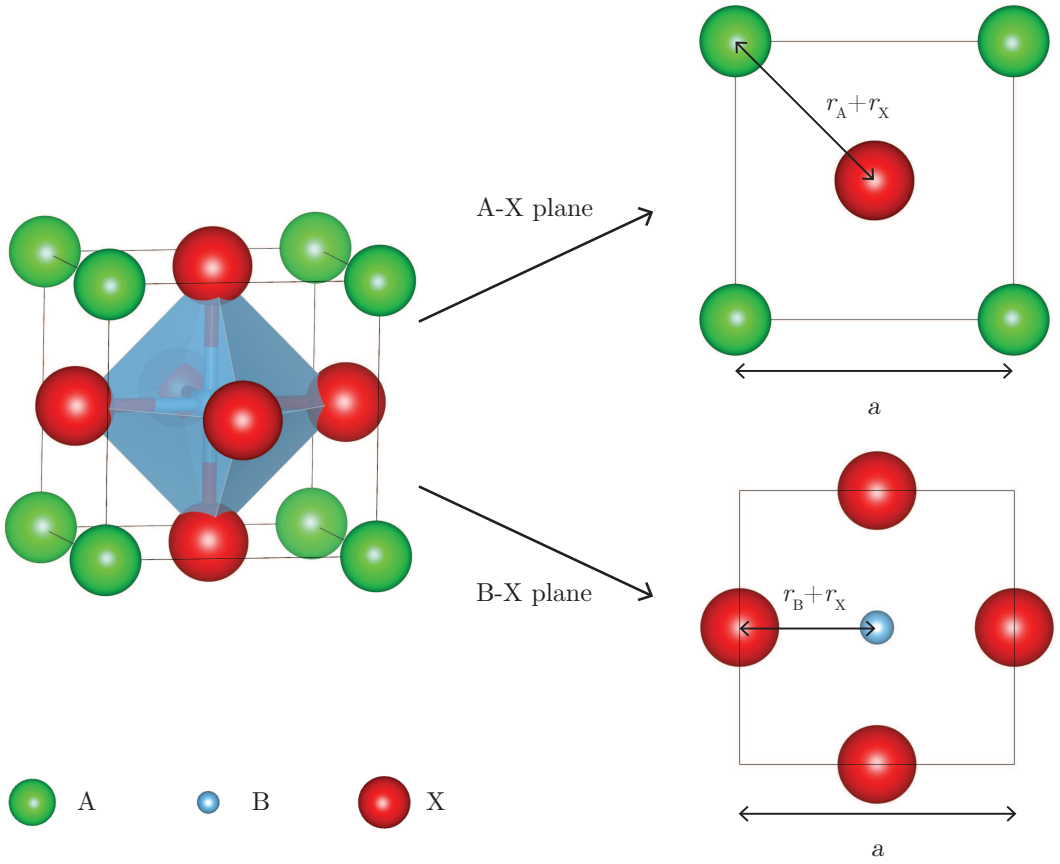

FIGURE 1.4: Goldschmidt tolerance factor in the cubic perovskite unit cell. The lattice parameter a is given in terms of the ionic radii in the A-X and B-X planes

Thus, the lattice parameter of the unit cell is given by

$$a = \sqrt{2}(r_A + r_X) = 2(r_B + r_X) \tag{1.3}$$

The ratio of these expressions for a is known as the Goldschmidt tolerance factor, t [29], which allows estimation of the size mismatch and hence the degree of distortion expected.

$$t = \frac{(r_A + r_X)}{\sqrt{2}(r_B + r_X)} \tag{1.4}$$

In the ideal case, $t = 1$, and values of t between 0.9 and ~ 1 give a cubic or pseudocubic structure *e.g.* $SrTiO_3$ ($t = 1.00$). When t is greater than 1, due to either large A or small B cation, the A cations do not fit into their interstices, and hexagonal or tetragonal structures become more stable, *e.g.* $BaNiO_3$-type structures ($t = 1.13$). If $t < 0.9$, the BX_6 octahedra tilt to fill space ($GdFeO_3$-type distortion), giving orthorhombic (figure 1.5 (a)) *e.g.* $GdFeO_3$ ($t = 0.89$) [30], or rhombohedral (figure 1.5 (b)) structures. It should be noted that the Goldschmidt tolerance factor is simply a tool which allows rough estimation of the structure, and the crystal structure may differ from what is predicted by this factor *e.g.* $BaTiO_3$ (cubic, with $t = 1.06$), $LaMnO_3$ (orthorhombic, with $t = 0.95$) and $LaAlO_3$ (rhombohedral, with $t = 1.01$).

In perovskite materials, distortion of the structure may also occur due to Jahn-Teller effects. The Jahn-Teller character of cations at the B site, such as Mn^{3+} in $LnMnO_3$ (Ln = La, Pr, Nb), or Mo^{5+} in the double perovskite Ba_2NdMoO_6, leads to elongation of the BO_6 octahedra (figure 1.5 (c)). Jahn-Teller distortions occur when there are degenerate d orbitals; the system undergoes distortion, lowering its symmetry and energy, and removing the degeneracy [31]. Variation of the oxygen content can also lead to deviation from the ideal structure. The presence of oxygen vacancies means that there are incomplete octahedra within the structure, causing it to distort from cubic, *e.g.* $SrFeO_x$ compounds, where $2.5 \leq x \leq 3$ (figure 1.5 (d)).

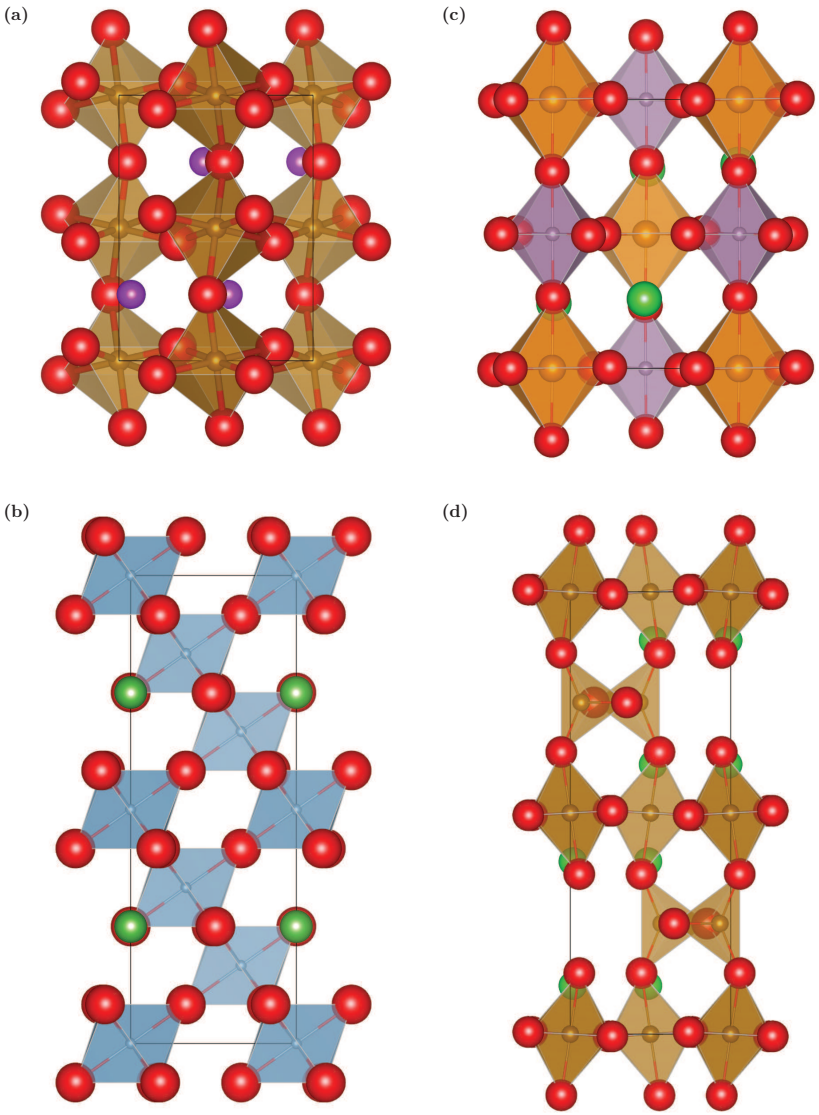

FIGURE 1.5: (a) Orthorhombic $GdFeO_3$ structure, showing octahedral rotations; (b) rhombohedral $LaAlO_3$; (c) tetragonal Ba_2NdMoO_6, showing elongated BO_6 octahedra; (d) orthorhombic $SrFeO_{2.5}$, showing oxygen vacancies and incomplete octahedra

1.4 Ruddlesden-Popper oxides

Ruddlesden-Popper phases, $A_{n+1}B_nO_{3n+1}$, where A is a rare-earth or alkaline earth and B is a transition metal, have shown promise as cathode materials for IT-SOFCs. These materials consists of n ABO_3 perovskite layers separated by AO rocksalt layers, shown in figure 1.6. They can accommodate either oxygen hypostoichiometry or hyperstoichiometry depending on their composition, allowing tuning of their electrochemical

and electrical properties for use as SOFC cathodes. Oxygen hyperstoichiometry can be achieved by incorporation of oxygen ions into interstitial sites in the rocksalt layers.

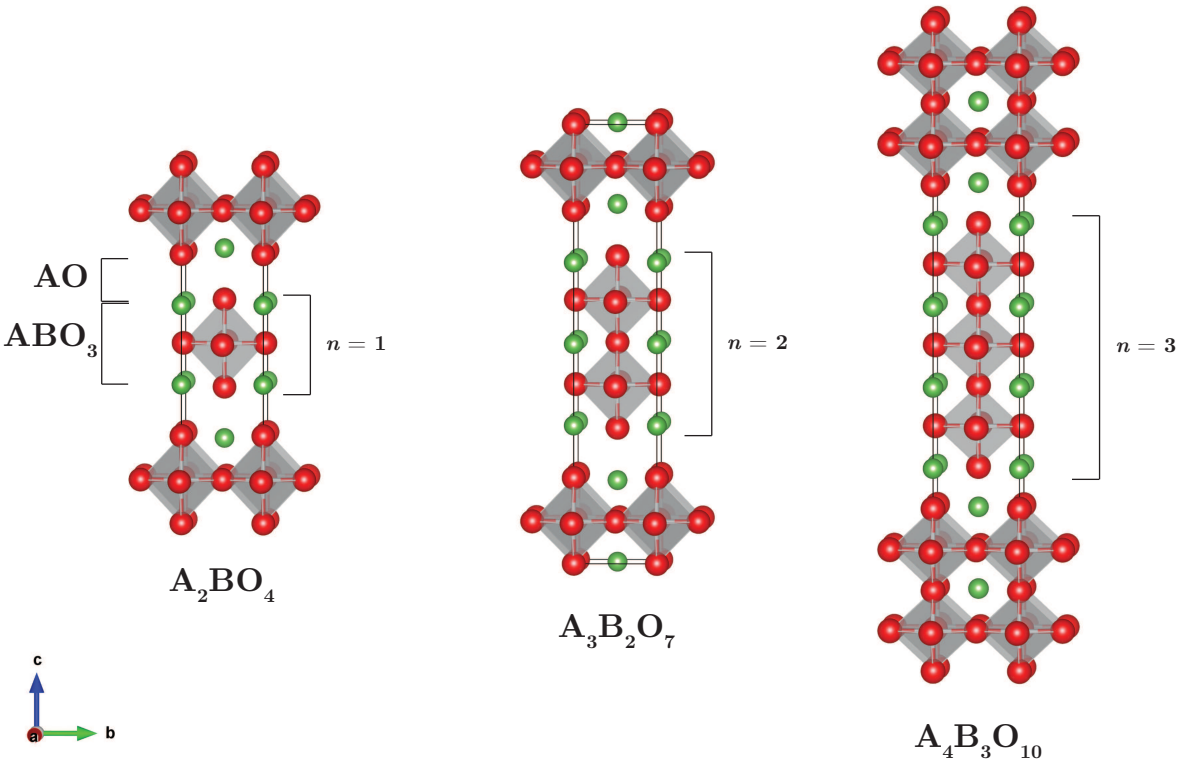

FIGURE 1.6: $A_{n+1}B_nO_{3n+1}$ Ruddlesden-Popper oxides, for n = 1–3, with A atoms shown in green, B atoms sit at the centre of the grey octahedra and O atoms are shown in red

1.5 Cathode Materials for SOFCs

The main family of materials which has been investigated for the cathode of SOFCs is the perovskite oxides, the structure of which is described in section 1.3. For high temperature operation, $La_{1-x}Sr_xMnO_{3-\delta}$ (LSM) is used due to good electrical conductivity, electrochemical activity for the ORR, high thermal stability, good TEC match with common electrolyte materials (table 1.1), and good compatibility with the commonly used electrolytes, such as YSZ, GDC and LSGM [18, 32–36]. In table 1.1, the conductivity listed is the reported experimental electrical conductivity in the temperature range 500–900°C unless specified as ionic (σ_i) or electronic (σ_{el}).

TABLE 1.1: Thermal expansion coefficients, and experimentally measured conductivity for perovskite based cathodes and commonly used electrolyte materials

Cathode	TEC ($\times 10^{-6}$ K^{-1})	σ (S cm¹)	Ref.
$LaMnO_3$	11.3–12.4	103	[37]
$La_{1-x}Sr_xMnO_{3-\delta}$	12.0-13.7	120–202	[33, 34, 37]
		$\sim 10^{-7}$–10^{-4} (σ_i)	[36, 38, 39]
$La_{0.6}Sr_{0.4}CoO_{3-\delta}$	21.3	1500–2500	[40]
$La_{0.6}Sr_{0.4}Co_{0.2}Fe_{0.8}O_{3-\delta}$	15.3	300–330 (σ_i);	[41]
		8×10^{-3} (σ_{el})	
$Ba_{0.5}Sr_{0.5}Co_{0.8}Fe_{0.2}O_{3-\delta}$	$\sim$24.0	30–35	[42]
$La_2NiO_{4+\delta}$	13.0	$\sim$50–60	[43]
$Pr_2NiO_{4+\delta}$	13.6	$\sim$100–120	[43]
$Nd_2NiO_{4+\delta}$	12.7	$\sim$30–40	[43]
$GdBaCo_2O_{5+\delta}$	16.4	400–900	[44]
$PrBaCo_2O_{5+\delta}$	24.6	~400–600	[45, 46]
$LaCrO_3$	$\sim$8.5	0.2–0.35	[47, 48]
Electrolyte			
GDC	13.5	$\sim 10^{-2}$ (σ_i)	[35, 49, 50]
YSZ	10.8	$\sim 10^{-3}$–10^{-1} (σ_i)	[35, 50]
LSGM	11.1	$\sim 10^{-2}$–10^{-1} (σ_i)	[35, 50]

Other perovskite oxides have been examined as potential cathode materials for IT operation, such as Sr-doped $LaCoO_3$, which has shown good mixed ionic and electronic conductivity, and good ORR activity [18, 35, 51]. In $La_{1-x}Sr_xCoO_{3-\delta}$, the introduction of Sr at low concentration ($x < 0.4$) is charge compensated by a change in Co valence, with a maximum in Co^{4+} concentration at $x = \approx 0.4$, while for higher concentration ($x > 0.4$), compensation is mainly by formation of oxygen vacancies. This results in improved catalytic activity and ionic conductivity of the cathode. However, Sr-doped $LaCoO_3$ reacts with YSZ at low temperature, forming insulating $SrZrO_3$ and $La_2Zr_2O_7$, and has a very high TEC. The use of GDC or SDC electrolytes which are stable with Sr-doped $LaCrO_3$, or a barrier interlayer between cathode and electrolyte can address the issue of reactivity with YSZ, reducing the formation of the Zr-containing insulating

phases. Composite cathode/electrolyte materials or doping at the Co site can reduce the TEC to values closer to those of the electrolyte materials. When doped with Fe at the Co site, ($La_{1-x}Sr_xCo_{1-y}Fe_yO_{3-\delta}$), it retains good catalytic activity, mixed ionic and electronic conductivity, and has improved TEC and improved thermomechanical stability compared to Sr-doped $LaCoO_3$, but lower electronic conductivity in the IT range (table 1.1) [40, 41, 52–55].

Perovskite oxides with alkaline-earth metals at the A-site have also been considered for SOFC cathodes, *e.g.* $Ba_{0.5}Sr_{0.5}Co_{0.8}Fe_{0.2}O_{3-\delta}$ (BSCF) [18]. BSCF has a very high bulk oxygen transport rate due to its high vacancy concentration ($\delta > 0.65$). However, it has low thermal stability, a high TEC, and lattice instability, with Ba-rich compositions lying at the border of the cubic perovskite stability [42, 56, 57]. Švarcová *et al.* report a phase transformation between the cubic phase and a mixture of the cubic and hexagonal phases results in decreased electrical conductivity and slower oxygen transport, which leads to performance degradation over time at low operating temperatures [57].

Layered double perovskites, $AA'B_2O_{5+\delta}$, where A is a rare earth, A' is an alkaline earth (usually Ba), and B is a transition metal, have recently attracted attention as potential SOFC cathode materials due to their good oxygen transport properties, high electronic conductivity above 600 K, and fast oxygen surface exchange kinetics [18, 46, 51, 58]. $GdBaCo_2O_{5+\delta}$ is one such material, which exhibits good chemical compatibility with GDC and LSGM electrolytes, but reacts with YSZ at temperatures greater than 700°C, forming $BaZrO_3$, and has a higher TEC than these electrolyte materials [44, 51, 59]. $PrBaCo_2O_{5+\delta}$ also shows very good oxygen transport properties and fast oxygen surface exchange. However, it has a high activation energy for oxygen diffusion and a very high TEC, so will mismatch with common electrolyte materials [45, 46].

Ruddlesden-Popper phases have also shown promise as cathode materials. The most widely studied Ruddlesden-Popper materials are those in the $n = 1$ series, with A = La, Nd and Pr and B = Ni. These materials show high diffusivity of oxygen interstitials in the LaO layers, promising electrocatalytic properties and TECs which show a good match to those of common electrolytes. They have lower electronic conductivity compared to perovskite-based materials, with higher conductivities observed in the $n = 2$, 3

series. They show improved ionic conductivity, good long-term stability, compatibility with LSGM, and good electrode performance.

While perovskite-based materials are the most widely studied for SOFC cathode applications, non-perovskite-based materials have also been examined, such as pyrochlores ($Bi_2Ru_2O_7$, $Pb_2Ru_2O_7$), which exhibit good ionic conductivity and high catalytic activity for the ORR. However, due to issues with long-term stability with GDC (degradation into Ru_2O) or YSZ (*e.g* partial transformation of $Bi_2Ru_2O_7$ into $Bi_3Ru_3O_{11}$) electrolytes and the high cost of Ru-based pyrochlores, they are unlikely to be suitable for large-scale development [60, 61]. Bismuth oxides based on $Bi_4V_2O_{11}$ Aurivillius phases (BIMEVOX materials, BI = bismuth, ME = metal dopant, V = vanadium, OX = oxygen) show good oxide ion conduction at reduced SOFC operating temperatures [55, 62]. They have poor electronic conductivity so have been investigated in composites with electronically conducting metals. These materials also have poor thermal stability so may not exhibit the long-term stability required for commercial use.

1.5.1 Previous studies on $LaMnO_3$-based SOFC cathodes

Very little experimental work has been carried out on $LaMnO_3$-based materials for use in IT-SOFCs, with the main focus being on Sr-doped systems for high temperature applications [54]. Above 750 K, $LaMnO_3$ is pseudocubic, and below this, it is orthorhombic. The electronic conductivity of $LaMnO_3$ may be enhanced by substitution of La^{3+} by divalent cations such as Ca^{2+}, Sr^{2+} or Ba^{2+} [37, 63]. Sr is the most commonly used dopant for $LaMnO_3$-based cathodes, as Sr-doped $LaMnO_3$ is stable and has high electronic conductivity under the oxidising conditions at the cathode. The structure of $La_{1-x}Sr_xMnO_{3-\delta}$ varies with the Sr content, with different works reporting different crystal structures. The early work of Hammouche *et al.* found $La_{1-x}Sr_xMnO_{3-\delta}$ to have a hexagonal-rhombohedral structure for $x = 0.1$–0.5 [64], while later works report an orthorhombic structure for $x \leq 0.2$, a monoclinic or hexagonal structure for $0 \leq x \leq 0.2$, and a rhombohedral or tetragonal structure for $x \geq 0.5$ [65–67].

The enhancement of the electronic conductivity is due to the formation of charge compensating holes when La is substituted by a divalent cation [68]. In $La_{1-x}Sr_xMnO_{3-\delta}$

($x \leq 0.5$), doping with Sr oxidises the Mn ion, effectively increasing the hole concentration and improving the electrical conductivity [69–72]. In Kröger-Vink notation, this is given by

$$\mathrm{Mn}_{\mathrm{Mn}}^{\mathrm{x}} + \mathrm{SrO} \xleftrightarrow{\mathrm{LaMnO_3}} \mathrm{Sr}_{\mathrm{La}}^{'} + \mathrm{Mn}_{\mathrm{Mn}}^{\bullet} + \mathrm{O}_{\mathrm{O}}^{\mathrm{x}} \tag{1.5}$$

where $\mathrm{Mn}_{\mathrm{Mn}}^{\mathrm{x}}$ is a Mn(III) ion $\mathrm{Sr}_{\mathrm{La}}^{'}$ is a Sr ion at a La site, $\mathrm{Mn}_{\mathrm{Mn}}^{\bullet}$ is a Mn(IV) ion and $\mathrm{O}_{\mathrm{O}}^{\mathrm{x}}$ is an oxygen ion in an oxygen site.

The TEC of $LaMnO_3$ is reported to be in the range 11.3–12.4 $\times$ $10^{-6}\,\mathrm{K}^{-1}$, which is higher than that of YSZ (10.8 $\times$ $10^{-6}\,\mathrm{K}^{-1}$) and lower than that of GDC (13.5 $\times$ $10^{-6}\,\mathrm{K}^{-1}$), but in good agreement with that of LSGM (11.1 $\times$ $10^{-6}\,\mathrm{K}^{-1}$) [35]. When doped with Sr, the TEC increases, with values of 12.0–13.7 $\times$ $10^{-6}\,\mathrm{K}^{-1}$ for increasing Sr content [33, 34, 37], giving improved compatibility with GDC. The electronic conductivity of $La_{1-x}Sr_xMnO_{3-\delta}$ (for $0 \leq x \leq 0.8$) as a function of oxygen pressure and temperature up to 1273 K has been investigated [72–74]. For lower Sr concentrations ($x \leq 0.2$), the conductivity was found to increase with temperature, while for higher Sr concentration ($x \geq 0.3$) a decrease in conductivity with temperature was observed. This change in behaviour was attributed to a metal-insulator transition in Sr-doped $LaMnO_3$. Under oxygen-excess conditions ($p_{O_2} > 10^{-5}$ bar), the conductivity was found to remain constant, but decreased sharply under oxygen-deficient conditions.

Oxygen surface exchange and diffusion are important for the ORR at the cathode, and by improving the ionic conductivity of the cathode, the active area for the ORR may be increased. The magnitude of the diffusion coefficient in $LaMnO_3$-based materials is low compared to other acceptor-doped $LaBO_3$ (B = transition metal) due to a low oxygen vacancy concentration, which limits the ionic conductivity in these materials. Secondary ion mass spectrometry (SIMS) has been used to determine the oxygen diffusion coefficient of $La_{1-x}Sr_xMnO_{3-\delta}$, which was found to increase with increasing Sr content for x = 0.35–0.5 at 1173 K ($\sim 10^{-14}$–10^{-12} $\mathrm{cm^2 s^{-1}}$) [75], or with increasing temperature from 973–1273 K in $La_{0.8}Sr_{0.2}MnO_3$ ($\sim 10^{-16}$–10^{-12} $\mathrm{cm^2 s^{-1}}$) [76, 77]. Substitution by Co on the Mn site was found to further increase the oxygen diffusion

coefficient ($\sim 10^{-14}$–10^{-8} cm^2s^{-1}), but caused a decrease in the electronic conductivity [75]. Short circuit diffusion was observed by De Souza *et al.* in $La_{0.8}Sr_{0.2}MnO_3$, which was speculated to be fast oxygen diffusion along grain boundaries [76]. An ^{18}O exchange study, followed by SIMS, and numerical analysis of ^{18}O depth profiles, by Navickas *et al.* found the oxygen diffusion coefficient for grain boundaries to be three orders of magnitude higher than for grains [78]. This indicates that grain boundary transport of oxygen could enhance the performance of $La_{1-x}Sr_xMnO_{3-\delta}$ cathodes for SOFCs. A range of ionic conductivities have been reported for Sr-doped $LaMnO_3$ in the temperature range 1073–1273 K, with values of $\sim 10^{-7}$–10^{-4} S cm^{-1} with increasing Sr content [36, 38, 39]. The variation in reported ionic conductivity may be due to differences in preparation methods and measurement of the samples. The low ionic conductivity of Sr-doped $LaMnO_3$ indicates that further doping or modification is required for it to be suitable for use in IT operation. As the oxygen vacancy concentration is not increased, at IT the ionic conductivity of $La_{1-x}Sr_xMnO_{3-\delta}$ is low and the reduction of oxygen is limited to the TPB regions. Doping $La_{1-x}Sr_xMnO_{3-\delta}$ at the B site with Mg or a transition metal cation such as Co, Fe or Ni can cause an increase in the oxygen vacancy content which can improve the ionic conductivity and the performance of $LaMnO_3$-based materials for IT operation [79].

Composite cathode materials may offer improved ionic conductivity and a larger TPB, and can provide reaction sites for the ORR across the surface of the cathode. Composites of $La_{0.8}Sr_{0.2}MnO_3$/YSZ, with 30–40 wt.% LSM have been investigated [80, 81] to determine their thermal stability and oxygen diffusion properties. At high temperature, the oxygen diffusion coefficient of $La_{0.8}Sr_{0.2}MnO_3$/YSZ composites is higher than that of $La_{0.8}Sr_{0.2}MnO_3$ but lower than that of YSZ, and ionic conductivities of 3–5 $\times$ 10^{-3} S cm^{-1} at 1173 K are reported. However, the thermal stabilities of the composites are an issue at higher temperatures, with the reaction of $La_{0.8}Sr_{0.2}MnO_3$ and YSZ forming $La_2Zr_2O_7$ and MnO, which can impede cathode performance [82].

One of the disadvantages of the use of $LaMnO_3$-based materials as SOFC cathodes is that they can readily react with other components of the fuel cell, such as the YSZ electrolyte and the Cr-containing interconnects, at high temperature. The reactivity

between $La_{1-x}Sr_xMnO_3$ and YSZ electrolyte has been extensively studied [83–86]. The reactivity of the cathode can be affected by the ratio of A- and B-site cations present, which can either enhance or degrade the cathode performance [66]. When A/B ≤ 1, Mn_3O_4 is formed, which can improve performance. However, in A-site deficient material, the Mn^{3+} reactivity is enhanced, which leads to greater Mn dissolution in YSZ. When A/B > 1, La_2O_3 is formed, which has a negative impact on performance due to low conductivity and poor stability of its hydrated phase $La(OH)_3$. In addition, La_2O_3 reacts with YSZ, forming the highly resistive $La_2Zr_2O_7$ phase at the boundary of cathode and electrolyte. In $La_{1-x}Sr_xMnO_{3-\delta}$, a high Sr content can lead to Sr depletion from the lattice and formation of the insulating phase $SrZrO_3$, again degrading cathode performance. In contrast to YSZ, no reactivity is reported between GDC and $La_{1-x}Sr_xMnO_{3-\delta}$ [87], and studies on the compatibility of LSGM found that there is minimal diffusion of Mg and Ga into $La_{1-x}Sr_xMnO_{3-\delta}$, even at high temperature [88, 89]. $La_{1-x}Sr_xMnO_{3-\delta}$ may also react with the interconnects, which are often Cr-containing materials, such as stainless steel or $LaCrO_3$-based materials. At high temperature under oxidising conditions, volatile Cr-containing species are generated. These species can interact with $LaMnO_3$-based cathode materials, poisoning them and reducing their performance [90–92].

Extensive theoretical studies have been carried out on both cubic and orthorhombic bulk $LaMnO_3$, further discussed in section 4.1. Density functional theory (DFT) and DFT + U (discussed in sections 2.2.5 and 2.2.6) studies have been carried out to investigate the performance of the local density approximation (LDA) and generalised gradient approximation (GGA) in the simulation of structure, electronic and magnetic properties [93–96]. In these studies, both LDA and GGA (using Perdew-Wang-91 (PW91) and Perdew, Burke, and Ernzerhof (PBE) approximations) can reproduce the volume to within 1% of the experimental values, but underestimate the Jahn-Teller and $GdFeO_3$ distortions, and the band gap of orthorhombic $LaMnO_3$. Use of DFT + U, which corrects for the self-interaction error by penalising delocalisation of electrons (discussed in section 2.2.6) improves the description of the electronic and magnetic structures and the structural parameters [96]. Previous DFT + U studies have only applied

a $+U$ correction to the Mn $3d$ states, the effect the application of a $+U$ correction to the O $2p$ states as well as the Mn $3d$ states has not previously been examined. Hybrid DFT (discussed in section 2.2.7), using the Heyd, Scuseria and Ernzerhof (HSE06), Becke, 3-parameter, Lee-Yang-Parr (B3LYP) and PBE0 functionals also provide an improved description of electronic and magnetic structure of $LaMnO_3$ compared to standard DFT [97–100]. Previous theoretical studies of $LaMnO_3$ surfaces, using DFT and hybrid calculations, have focused mainly on the high-temperature phase [101–104], and work on the orthorhombic phase has only focused on some of the low index surfaces [105]. Further investigation is required to determine the stability of all the low index surfaces of $LaMnO_3$ and formation of defects at these surfaces.

In this thesis, the structural and electronic properties of $LaMnO_3$ are examined, testing the performance of PBE, PBE + U, PBEsol, PBEsol + U, and HSE06 functionals to describe these properties. The low index surfaces of $LaMnO_3$ are modelled using the functional which best describes the bulk properties. In bulk $LaMnO_3$ and at its low index surfaces, the formation of oxygen vacancies is investigated, and in bulk $LaMnO_3$ the energy barriers to oxygen migration are calculated. In addition, doping $LaMnO_3$ with akaline earth metals is examined, to determine site selectivity and the charge compensation mechanism for the dopants.

1.5.2 Previous $La_2NiO_{4+\delta}$ studies for SOFC cathodes

$La_2NiO_{4+\delta}$ (Ruddlesden-Popper phase with $n = 1$, as shown in figure 1.6) has attracted attention as a cathode material for SOFCs as it can accommodate oxygen interstitial ions in the LaO layers, centred in a tetrahedron of nearby La ions [106], providing a path for oxygen diffusion [107]. Hybrid DFT calculations using B3LYP in CRYSTAL09 [108] show rotation of the NiO_6 octahedra away from the oxygen interstitial in orthorhombic $La_2NiO_{4+\delta}$ ($\delta = 0.125$), with the apical oxygen ions nearest the interstitial displaced towards their Ni centres. For $\delta = 0$, La_2NiO_4 is reported to undergo two structural phase transitions, with a low temperature tetragonal phase (space group $P4_2/ncm$) present up to $\sim 80\,K$, an orthorhombic phase present up to $\sim 770\,K$ (space group $Bmab$) and a high temperature tetragonal phase above this (space group $I4/mmm$) [106, 109, 110].

$La_2NiO_{4+\delta}$ based materials exhibit good electronic conductivity in the temperature range 600–1100 K (10-110 S cm^{-1}), higher ionic conductivity than perovskite-based materials ($\sim 10^{-2}$ S cm^{-1}), good TEC match with electrolyte materials, and stability at SOFC operating conditions [55, 62].

Oxygen diffusion in La_2NiO_4 has been examined by a number of groups, using SIMS to examine oxygen tracer diffusion. Studies on $La_2NiO_{4+\delta}$ single crystal [43, 111], polycrystalline $La_2Ni_{1-x}Co_xO_{4+\delta}$ [112], and epitaxial films [113] find the oxygen diffusion coefficient to be one to two orders of magnitude higher in the *ab* plane (LaO layers) compared to along the perpendicular direction (*c* axis). Although there is limited mobility in the perpendicular direction due to this anisotropy, the conductivity in the *ab* plane is high enough to give ionic conductivity suitable for mixed ionic and electronic conducting cathodes.

The effect of introducing dopants to the La and Ni sites has also been investigated, with alkaline-earth or rare-earth dopants introduced at the La site, and transition metals such as Cu, Co or Fe at the Ni site. Substitution of Sr for La can increase the electronic conductivity (up to $\sim$270 S cm^{-1}) of La_2NiO_4 and improve its stability, though the TEC increases with Sr content to values greater than those of the electrolyte (up to 17 $\times 10^{-6}$ K for high Sr content), and causes a decrease in the oxygen diffusion coefficient [43, 114].

The introduction of Co was found to have little effect on the oxygen diffusion coefficient in $La_2Ni_{1-x}Co_xO_{4+\delta}$ for $x \leq 0.3$, and higher diffusion coefficients were observed when the Co content was high ($x \geq 0.5$) [112]. The behaviour of crystal lattice deformation in La_2NiO_4-based materials due to interstitial oxygen has been investigated for 10% Fe-, Co- and Cu-doped systems, in the temperature range 873–1173 K (high temperature tetragonal structure), for oxygen partial pressure $p_{O_2} = 10^{-24}$–1 bar [115]. Both Fe- and Co-doped only exhibit oxygen-excess stoichiometry, while Cu-doped can exhibit oxygen deficiency under low p_{O_2}, which is also seen in Sr-doped La_2NiO_4 and La_2CuO_4. Previous studies on La_2NiO_4 and Nd_2NiO_4 showed that oxygen vacancies and oxygen interstitials are unlikely to coexist in these materials, therefore the value of δ can be assumed to be the oxygen interstitial concentration [116, 117]. The interstitial

concentration is found to be dependent on dopant species, with Fe-doped showing the highest hyperstoichiometry. Fe doped in La_2NiO_4 is trivalent according to Mössbauer spectroscopy measurements, with a magnetic sextet observed at 4 K [118], with Fe doping charge compensated according to

$$Fe_2O_3 + V_i^{"} \rightarrow 2Fe_{Ni}^{\bullet} + O_i^{"} + 2O_O^X \tag{1.6}$$

Oxygen transport in Sr- and Fe-doped La_2NiO_4 ($La_{2-x}Sr_xNi_{1-y}Fe_yO_{4+\delta}$, $x = 0.5$, $y =$ 0.1–0.4 and $x = 0.8$, $y = 0.1$,0.2 and 0.4) has been examined for the high-temperature tetragonal phase [119]. It was found that effect of Sr substitution on the oxygen permeation flux was dependent on the Fe content, with an increase in the oxygen flux for low Fe content ($y = 0.1$), which was attributed to an increase in oxygen vacancy concentration. For higher Fe content ($y = 0.2$–0.4), the oxygen overstoichiometry is significantly higher than for $y = 0.1$, and doping with Sr led to a decrease in the oxygen flux due to a decrease in the interstitial oxygen concentration. The highest oxygen permeation flux was obtained for $La_{1.5}Sr_{0.5}Ni_{0.6}Fe_{0.4}O_{4+\delta}$, which although it showed lower ionic conductivity than undoped La_2NiO_4, the oxygen surface exchange, which has a significant role in cathode performance, was improved, giving an overall improvement in its properties for SOFC application.

Recent experimental work on the {110} and {001} surfaces of Sr-doped La_2NiO_4 using low energy ion scattering (LEIS) have determined that Ni is not present at the outermost surface layer, and using angle-resolved photoelectron spectroscopy near-surface region of these terminations saw that the amount of Ni decreases as the surface is approached [120, 121]. This was supported by their study of the thermodynamic stability of La_2NiO_4 [122]. A Ni-enriched layer was found a few nanometres below the surface. This Ni-rich region is reported to be due to segregation of the La cations to the surface, and partial decomposition at the surface of La_2NiO_4 into La_2O_3 Ni-rich $n > 1$ Ruddlesden-Popper phases.

The compatibility of La_2NiO_4 with GDC, YSZ and LSGM electrolytes has been investigated for temperatures up to 1273 K. La_2NiO_4 was found to react with both GDC

and YSZ at 973 and 1173 K, decomposing into higher order Ruddlesden-Popper phases and insulating Zr-containing phases (YSZ electrolyte) which limits its suitability as cathode material for SOFCs [123, 124]. However, it has been found to be stable with LSGM electrolyte, with no evidence of formation of secondary phases after a period of 72 h at temperatures up to 1273 K.

Previous computational studies on La_2NiO_4 have been carried out on the orthorhombic and tetragonal phases using DFT, DFT + U, hybrid-DFT and molecular dynamics (MD), further discussed in section 6.1. The incorporation of oxide ions into the lattice, oxide ion mobility, interaction of molecular oxygen and oxygen surface exchange have been investigated using DFT and DFT + U calculations [108, 125–127]. MD has also been used to investigate the oxygen transport in La_2NiO_4, to determine the diffusion mechanism and determine the effect of oxygen content on the activation energy [128]. In their work, the low index surfaces have been examined using METADISE, with the crystal morphology predicted, as well as the effect of doping with Fe or Cu at the Ni site on the surface stability, and the compensation mechanism for doping with Sr on the La site [129].

Orthorhombic La_2NiO_4 is investigated in this thesis, with the formation energy of oxygen defects in the bulk and at its low index surfaces examined. The oxygen diffusion mechanism for interstitial oxygen as investigated, considering paths within the rocksalt layers and across the perovskite layers. In addition, the site selectivity and the charge compensation mechanism for Sr and Fe doping is examined.

1.5.3 Previous studies on $LaCrO_3$ for use in SOFCs

$LaCrO_3$-based materials may be suitable as SOFC cathodes as they have good electronic conductivity and good chemical stability under SOFC operating conditions [130]. $LaCrO_3$ has mainly been investigated as interconnects for high temperature SOFCs. The TEC of $LaCrO_3$ when undoped is 8.5×10^{-6} K, which is significantly lower than other components, but doping with Sr or Ca increases it to $\sim$10–11 $\times 10^{-6}$ K, which is closer to that of YSZ [131–134]. Co-doping with Sr at the La site and Co or Mn at the Cr site was also found to increase the TEC, which is attributed to an increase in

the average ionic radius of the B-site cation, while doping with other transition metals (Fe, Ni) did not have an observable effect [134].

$LaCrO_3$-based materials have attracted attention as oxygen transport membranes for applications in energy conversion, gas separation and syngas production (*e.g.* by partial oxidation of coal, oil or natural gas) [48]. Doped $LaCrO_3$ materials have excellent thermochemical stability across a range of temperatures up to 1273 K, and oxygen partial pressure from 10^{-20}–0.21 atm. They exhibit predominantly electronic conductivity, and undoped $LaCrO_3$ has low ionic conductivity. The introduction of dopants at the La and Cr sites of $LaCrO_3$ may be used to obtain the desired thermal and electrical properties. Sr and Ca are used as La site dopants, and are expected to improve the electronic conductivity [135, 136]. The use of transition metal dopants on the Cr site is to maintain the thermal and structural stability and to increase the oxygen vacancy concentration. In the oxidising conditions of SOFC cathodes, substitution of La with Ca or Sr will be charge compensated by hole formation. There is little experimental work on Cr site doping, with Fe, Ni or Co doping reported to cause an increase in the oxygen vacancy concentration of doped $LaCrO_3$ [137].

Undoped $LaCrO_3$ has a lower orthorhombic to rhombohedral phase transition temperature ($\sim$550 K) than other perovskite oxides used for SOFC cathodes, but the introduction of dopants can stabilise the structure at higher temperatures, depending on dopants concentration and type. $La_{0.75}Sr_{0.25}Cr_{0.5}Mn_{0.5}O_{3-\delta}$ when fired at 900°C for 120h [138], and $LaCr_{0.8}Fe_{0.2}O_3$ and $LaCr_{0.6}Co_{0.2}Fe_{0.2}O_3$ calcined at 1123 K are stable in the orthorhombic structure [139]. Both $La_{1-x}Sr_xCrO_3$ ($x < 0.2$), sintered at temperatures from 1173–1873 K [133, 140, 141], and $La_{0.8}Sr_{0.2}Cr_{0.8}Mg_{0.2}O_3$ at 1673 K [142] were also found to have orthorhombic structure.

In this thesis, the ionic and electronic conductivity of $LaCrO_3$ is investigated for application in SOFC cathodes. The formation of intrinsic and Sr defects in $LaCrO_3$ is investigated, to determine the origin of charge carriers in $LaCrO_3$. The formation energies and barriers to migration of oxygen vacancies in bulk $LaCrO_3$ were calculated to examine its potential as an ionic conductor.

1.6 Oxygen diffusion in perovskite-based materials

Oxygen vacancies are the dominant oxygen defect in ABO_3 perovskite-based materials, with diffusion occurring via migration of the vacancies. In this mechanism, the atoms move from a lattice site into a neighbouring vacancy, which allows migration of oxygen through the crystal, as shown in figure 1.7 (a) [143]. In materials which can accommodate interstitial oxygen, such as Ruddlesen-Popper phases in their rocksalt layers, there are two possible diffusion mechanisms for the interstitial oxygen. The simplest mechanism of diffusion of interstitials is that where an interstitial migrates directly from one interstitial site to the next, shown in figure 1.7 (b). This mechanism is known as interstitial diffusion. The second mechanism is one where interstitial atoms migrate via a neighbouring lattice site, known as interstitialcy diffusion. The interstitial displaces an atom from a lattice site to the next interstitial site. This mechanism can occur via collinear interstitialcy diffusion, where the path is straight, shown in figure 1.7 (c), or via non-collinear diffusion, shown in figure 1.7 (d).

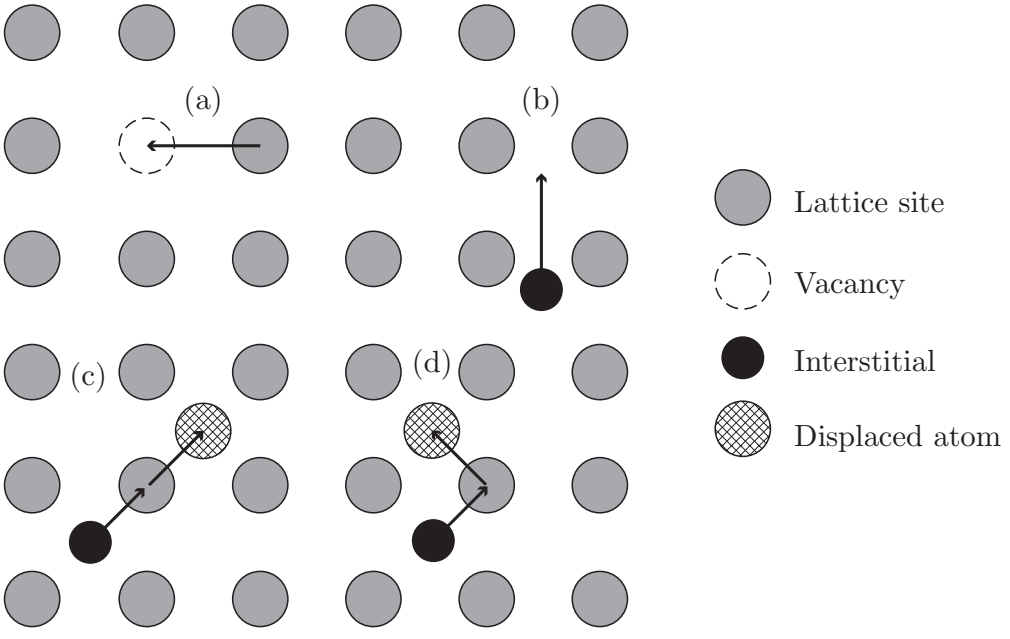

FIGURE 1.7: Diffusion mechanisms for oxygen ions in perovskites and perovskite-based materials. (a) vacancy diffusion, (b) interstitial diffusion, (c) interstitialcy diffusion (collinear), (d) interstitialcy diffusion (non-collinear)

1.7 Thesis outline

The flexibility of SOFCs and their potential for high efficiency fuel conversion has made them an attractive technology for electricity generation. However, the high costs and performance degradation associated with operation at high temperatures ($> 1000\,\mathrm{K}$) has driven research to investigate materials suitable for lower temperature operation. The work presented in this thesis has been motivated by the need to develop suitable cathodes for lower temperature operation of SOFCs. Chapter 1 has introduced fuel cells, with a focus on SOFCs and the materials used for the cathode. The materials which are of interest in this thesis are introduced, with background on their application in SOFCs.

Chapter 2 covers the computational theory behind the methods used in thesis, outlining the theory of electronic structure methods. Chapter 3 focuses on the implementation of these methods within the Vienna *ab initio* simulation package (VASP). This includes an overview of the methods used to gain insight into the geometric and electronic properties of the materials under investigation.

In Chapter 4, the structural and electronic properties of $LaMnO_3$ are examined. Analysis of the performance of PBE, PBE + U, PBEsol, PBEsol + U, and HSE06 functionals to describe these properties is carried out. From this investigation, a suitable functional is chosen to simulate the low index surfaces of $LaMnO_3$. Chapter 5 examines defect formation in $LaMnO_3$. The formation of oxygen vacancies in bulk $LaMnO_3$ and at its low index surfaces is investigated, and the energy barriers to oxygen migration in bulk $LaMnO_3$ are determined. In addition, the site selectivity and charge compensation mechanisms for alkaline earth defect formation in $LaMnO_3$ are examined.

The Ruddlesden-Popper oxide La_2NiO_4 is investigated in Chapter 6, with determination of the formation energy of oxygen defects in the bulk and at its low index surfaces. As La_2NiO_4 can accommodate oxygen vacancies in the perovskite layers and oxygen interstitials in the rocksalt layers, both are simulated in the bulk and at the surfaces in order to determine the dominant oxygen defect. The oxygen diffusion mechanism

for interstitial oxygen as investigated, considering paths within the rocksalt layers and across the perovskite layers.

In Chapter 7, $LaCrO_3$ is investigated as a potential mixed ionic and electronic conductor for SOFC cathode applications. The origin of charge carriers in $LaCrO_3$ is investigated, considering intrinsic defects and Sr defects, and calculating the thermodynamic transition levels. In addition, the formation and migration of oxygen vacancies in the bulk material was investigated.

Finally, in Chapter 8, the findings presented in this thesis are summarised. This is followed by an outline of possible future work in the investigation of these materials for SOFC applications.

Chapter 2

Computational Theory

Computational chemistry methods allow us to examine the properties of a wide range of materials, to rationalise experimental observations, gain information about properties which cannot be measured experimentally, and predict structural and electronic properties of materials which have not yet been synthesised. A range of theoretical methods are available, and it is important to employ a suitable approach for the system size, properties being calculated, and level of accuracy required. Classical methods, which use force fields to model interactions between atoms, can calculate large systems in a relatively short period of time but do not explicitly consider electrons. Quantum mechanical methods can be used to determine the electronic structure of materials, but are more computationally expensive.

In this chapter, quantum chemistry is discussed, along with some widely used quantum chemistry methods. These methods include Hartree-Fock (HF), density functional theory (DFT), and hybrid-DFT, and their advantages and disadvantages are addressed. The application of the DFT-based methods used in this work is then outlined.

2.1 Quantum chemistry

2.1.1 The Schrödinger Equation

The aim of quantum chemical calculations is the approximate solution of the Schrödinger equation, which in its time-independent form is

$$\hat{H}\Psi = E\Psi \tag{2.1}$$

where $\hat{H}$ is the Hamiltonian operator, E is the energy and Ψ is the wavefunction. The Hamiltonian operator is defined as the sum of the kinetic and potential energy operators

$$-\frac{\hbar^2}{2}\sum_i \frac{1}{m_i}\nabla_i^2 + V(r) \tag{2.2}$$

where $\hbar = \frac{h}{2\pi}$, i is the index over all particles in the system, m_i is the mass of particle i, the Laplacian, $\nabla_i^2 = (\frac{\partial^2}{\partial x_i^2} + \frac{\partial^2}{\partial y_i^2} + \frac{\partial^2}{\partial z_i^2})$, is the kinetic energy operator, and *V(r)* is the potential energy of the system as a function of its coordinates, r. The Hamiltonian can be split into its nuclear and electronic components, with contributions to the kinetic energy from the nuclei ($\hat{T_N}$) and the electrons ($\hat{T_e}$), and to the potential energy from nuclei-nuclei ($\hat{V_{NN}}$), nuclei electron ($\hat{V_{Ne}}$) and electron-electron ($\hat{V_{ee}}$) interactions, as shown in equation 2.3

$$\hat{H} = \hat{T}_N + \hat{T}_e + \hat{V}_{NN} + \hat{V}_{Ne} + \hat{V}_{ee} \tag{2.3}$$

The solution of the Schrödinger equation would allow calculation of the ground state energy and the wavefunction of the system being studied. However, the electron-electron interaction in equation 2.3 cannot be determined analytically, therefore an exact solution can only be obtained for systems with one electron (*e.g.* H, He^+, Li^{2+}, etc.). In order to solve the equation numerically for systems with greater than one electron, various approximations are necessary.

2.1.2 The Born-Oppenheimer approximation

The wavefunction may be separated into its nuclear and electronic contributions to aid in solving the Schrödinger equation. As the nuclear mass is so large compared to that of the electrons they move significantly more slowly than the electrons, and can be treated as static relative to the electrons. This is known as the Born-Oppenheimer approximation. The Born-Oppenheimer approximation is applied in the majority of cases, only failing when dealing with very light atoms, or when the motion of nuclei and electrons is strongly correlated. The kinetic energy of the nuclei is approximated

as zero, meaning that the $\hat{T}_N$ term in equation 2.3 can be neglected. As the nuclear positions are treated as fixed, the potential energy of the nuclei-nuclei interactions only needs to be calculated once for each atomic configuration, and is defined as

$$\hat{V}_{NN} = \sum_{A<B} = \frac{Z_A Z_B}{r_{AB}} \tag{2.4}$$

where e is the electron charge, Z_A and Z_B are the nuclear charges of atoms A and B, and r_{AB} is the distance between them.

When the nuclear-nuclear terms are excluded, the electronic Hamiltonian contains three terms to be calculated:

$$\hat{H}_e = \hat{T}_e + \hat{V}_{Ne} + \hat{V}_{ee} \tag{2.5}$$

For a system with N electrons, $\hat{T}_e$ is defined as

$$\hat{T}_e = -\sum_{i}^{N} \frac{1}{2} \nabla_i^2 \tag{2.6}$$

The nuclei-electron potential energy is calculated using

$$\hat{V}_{Ne} = -\sum_{A}^{M} \sum_{i}^{N} \frac{Z_A}{r_{iA}} \tag{2.7}$$

where r_{iA} is the distance between nucleus A and electron i in a system with M nuclei and N electrons.

However, the electron-electron term, $\hat{V}_{ee}$ is not simple to solve, and requires further approximation.

2.2 Quantum chemistry methods

2.2.1 The Hartree model

The Hartree model divides the many-electron wavefunction into the product of one-electron wavefunctions involving a one-electron Hamiltonian, *h(i)*, and ignores electron-electron interactions, as shown in equation 2.8a, with *h(i)* defined in equation 2.8b.

$$H = \sum_{i}^{N} h(i) \tag{2.8a}$$

$$h(i) = -\frac{1}{2}\nabla_i^2 - \sum_{A}^{M} \frac{Z_A}{r_{iA}} \tag{2.8b}$$

This gives a set of spin orbitals, χ_i, occupied by electron i, and with energy ε_i, which satisfy

$$h(i)\chi_i(x_i) = \varepsilon_i \chi_i(x_i) \tag{2.9}$$

The resulting wavefunction, which is known as the Hartree product, is the product of the individual one-electron wavefunctions (equation 2.10a), and the total system energy is given by the sum of the spin orbital eigenvalues (equation 2.10b)

$$\Psi^{HP} = \chi_i(x_1)\chi_j(x_2)\chi_k(x_3)\ldots\chi_n(x_N) \tag{2.10a}$$

$$E = \langle\Psi|H|\Psi\rangle = \varepsilon_1 + \varepsilon_2 + \varepsilon_3 + \ldots + \varepsilon_N \tag{2.10b}$$

2.2.2 The Hartree self-consistent field model and variational principle

The first issue with this approach is that the electron-electron interactions are neglected, ignoring the fact that electrons repel each other. In the Hartree self-consistent

field (SCF) model, this is treated by assuming that electrons move in the average potential field of all nuclei and electrons in the system. However, this potential field is determined by the form of the wavefunction, which is unknown.

The variation principle states that the expectation value, E_T of a Hamiltonian, $\hat{H}$, calculated using a trial wavefunction, Ψ_T, can never be lower than the true ground state energy E_0, as shown in equation 2.11

$$\langle \Psi_T | \hat{H} | \Psi_T \rangle = E_T \geq E_0 = \langle \Psi_0 | \hat{H} | \Psi_0 \rangle \tag{2.11}$$

This means that the energies calculated from a set of trial wavefunctions can never be lower than those of the true wavefunctions, therefore the lowest energy trial wavefunction will be closest in energy to the ground state. In the SCF model, a set of trial wavefunctions is chosen for each electron, which are used to generate the potential field, which in turn generates a new set of wavefunctions. This process is iterated until there is no change in the wavefunctions, or until the given convergence criteria are reached. From this, calculations can be improved by varying the wavefunction until the lowest energy solution is obtained. However, there is no way of determining how close the trial solution is to the true ground state.

2.2.3 Slater Determinant

The second issue with the Hartree wavefunction, is that it does not satisfy the Pauli exclusion principle, *i.e.* the sign of the wavefunction must be inverted under the operation of interchange of two electrons, as shown in equation 2.12

$$\Psi(\ldots x_i \ldots x_j \ldots) = -\Psi(\ldots x_j \ldots x_i \ldots) \tag{2.12}$$

An antisymmetric wavefunction can be constructed for a system with N electrons and N spin orbitals, by expressing it as the determinant of the $N \times N$ matrix of orbitals

$$\Psi = \frac{1}{\sqrt{N!}} \begin{vmatrix} \chi_1(x_1) & \chi_2(x_1) & \dots & \dots & \chi_N(x_1) \\ \chi_1(x_2) & \chi_2(x_2) & \dots & \dots & \chi_N(x_2) \\ \dots & \dots & \dots & \dots & \dots \\ \dots & \dots & \dots & \dots & \dots \\ \chi_1(x_N) & \chi_2(x_N) & \dots & \dots & \chi_N(x_N) \end{vmatrix} \tag{2.13}$$

This is known as the Slater determinant, which for a two electron system is given by equation 2.14, and produces a wavefunction that is antisymmetric with respect to the interchange of the electrons.

$$\Psi = \frac{1}{\sqrt{2}}[\chi_1(x_1)\chi_2(x_2) - \chi_1(x_2)\chi_2(x_1)];\ \ \frac{1}{\sqrt{2}}[\chi_1(x_2)\chi_2(x_1) - \chi_1(x_1)\chi_2(x_2)] = -\Psi \tag{2.14}$$

2.2.4 The Hartree-Fock method

There are three contributions to the total energy of the system, a one-electron term, a Coulomb term and an exchange term. The one-electron term is given by the one-electron operator $H_1 = \sum_i h(i)$, which includes the kinetic energy and the nucleus-electron interaction and is the energy (denoted as H_{ii}^{core}) associated with the contribution from molecular orbital χ_i, given by

$$H_{ii}^{core} = \int \chi_i(1)h(i)\chi_i(1)\partial\tau_1 \tag{2.15}$$

The 1 in equation 2.15 represents the electron in an integral involving the coordinates of a single electron. For N electrons in N orbitals, the contribution to the total energy is negative and is given by

$$E_{total}^{core} = \sum_{i=1}^{N} \int \chi_i(1)h(i)\chi_i(1)\partial\tau_1 \tag{2.16}$$

The second contribution to the total energy is the Coulomb integral, J_{ij}, which represents the electrostatic repulsion between orbitals.

$$J_{ij} = \iint \chi_i(x_1)\chi_j(x_2)\frac{1}{r_{12}}\chi_i(x_1)\chi_j(x_2)\partial\tau_1\partial\tau_2 \tag{2.17}$$

The Coulomb energy, which is repulsive and increases the energy of a system, is given by a double sum over orbitals i and j.

$$E_{Coulomb} = \sum_{i=1}^{N}\sum_{j=i+1}^{2}\iint \chi_i(x_1)\chi_j(x_2)\frac{1}{r_{12}}\chi_i(x_1)\chi_j(x_2)\partial\tau_1\partial\tau_2 \tag{2.18}$$

The third term is the exchange integral, K_{ij}, which has no classical analogue and results from the condition of antisymmetry of the wavefunction.

$$K_{ij} = \iint \chi_i(x_1)\chi_j(x_2)\frac{1}{r_{12}}\chi_i(x_2)\chi_j(x_1)\partial\tau_1\partial\tau_2 \tag{2.19}$$

Electrons with the same spin cannot occupy the same point in space and tend to avoid each other, and so experience a lower Coulomb repulsion. The K_{ij} term is only non-zero for electrons of the same spin and reduces the Coulombic repulsion between these electrons, with the total energy given by a double sum over the orbitals

$$E_{exchange} = \sum_{i=1}^{N}\sum_{j^*=i+1}\iint \chi_i(x_1)\chi_j(x_2)\frac{1}{r_{12}}\chi_i(x_2)\chi_j(x_1)\partial\tau_1\partial\tau_2 \tag{2.20}$$

where the j^* represents electrons with the same spin as i.

The HF approach, although a useful method for the description of many systems, suffers from a number of limitations. In HF, the electron-electron potential is described as an average effect and does not treat the correlated motion of electrons. The correlated motion means that electrons try to avoid each other and are less likely to be found close together than the HF approach suggests. Correlation may be divided into (i) dynamical and (ii) non-dynamical correlation. Dynamical correlation is due to the movement of electrons; for two electrons, the probability of finding one electron at a certain position

at any instant depends on the instantaneous position of the second electron. Non-dynamical correlation is due to degenerate or near-degenerate states around the highest occupied molecular orbital. The correlation is usually 0.1% or less of the total energy, but the energy differences are around the same order of magnitude, so large errors can occur in the calculation of properties where electrons are redistributed.

Post-HF methods, such as Configuration Interaction, Møller-Plesset perturbation theory, and Coupled Cluster, have been developed to attempt to achieve greater accuracy. However, these methods are very computationally expensive and thus only suitable for the simulation of relatively small systems. Large periodic supercells are required for defect calculations in semiconductors, and DFT is widely used for these calculations.

2.2.5 Density Functional Theory

Modern DFT originates from the work of Hohenberg and Kohn [144]. They put forward two theorems: (a) the ground state energy of a system is uniquely defined by the electron density (E is a unique functional of $\rho(r)$), and (b) the ground state electron density gives the exact total energy of a system, and a variational principle applies. The information contained in the ground state electron density can be used to determine the ground state properties of the system. The ground state electron density depends only on three variables, compared to $3N$ variables for the wavefunction of a system containing N atoms. In principle, this offers an advantage over HF, as there is a large reduction in the number of variables, although in practice, the electron density is obtained from the wavefunction.

The total energy can be written a function of the electron density, which itself is a function of the position vector, r

$$E[\rho(r)] = T[\rho(r)] + E_{ee}[\rho(r)] + E_{Ne}[\rho(r)] \tag{2.21}$$

where $T[\rho(r)]$ is the kinetic energy, $E_{ee}[\rho(r)]$ is due to the electron-electron interactions and $E_{Ne}[\rho(r)]$ is due to the nuclei-electron interactions. The energy can be rewritten

as

$$E[\rho(r)] = \int \rho(r)V(r)dr + F[\rho(r)] \tag{2.22}$$

where the $\int \rho(r)V(r)dr$ term represents the interaction of an external potential in which the electrons move, $V(r)$, with the electron density, $\rho(r)$, and $F[\rho(r)]$ is the Hohenberg and Kohn universal functional, valid for any number of particles and any external potential. The universal functional contains the kinetic energy and electron-electron interaction terms, so is dependent only on the electron density. If the nature of the functional was known, it would allow computation of the exact ground state energy. However, the exact form of the universal functional is unknown.

Kohn and Sham proposed a scheme to address the kinetic energy, in which a theoretical system of non-interacting electrons with the same exact ground state density as a fully interacting system is considered [145]. The allows splitting of the kinetic energy into the energy associated with the non-interacting electrons (T_S) and a correction due to electron-electron interactions (T_C). The E_{ee} term is split into the Coulombic interaction, $J[\rho(r)]$, and the non-classical part of the electron electron interaction, E_{NC}. The Hohenberg and Kohn universal functional becomes

$$F[\rho(r)] = T_S + J[\rho(r)] + E_{XC}[\rho(r)] \tag{2.23}$$

$\mathrm{E}_{XC}[\rho(r)]$ is the exchange-correlation energy, which contains T_C, and E_{NC}, which describes the non-classical part of the electron-electron interaction. T_s can be calculated using a similar approach to HF. The density is expressed as the sum of the square of a set of one-electron orbitals, with the Kohn-Sham equations a function of the exact ground state density

$$\rho_s(r) = \sum_i |\chi_i(r)^2| \tag{2.24}$$

T_s can then be expressed in terms of these one-electron orbitals

$$T_s = -\frac{1}{2}\sum_i \langle \chi_i | \nabla^2 | \chi_i \rangle \tag{2.25}$$

The Coulombic term can be written in terms of the density

$$J[\rho(r)] = \frac{1}{2}\iint \rho(r_1)\frac{1}{r_{12}}\rho(r_2)dr_1 dr_2 \tag{2.26}$$

The total energy is then given by

$$E[\rho(r)] = \underbrace{T_s + J[\rho(r)] + E_{XC}[\rho(r)]}_{\mathrm{F}[\rho(r)]} + E_{Ne}[\rho(r)] \tag{2.27}$$

E_{Ne}, the energy of the nuclei-electron interactions is given by

$$E_{Ne}[\rho(r)] = -\sum_A^M \sum_i^N \int \frac{Z_A}{r_{iA}}\rho(r)dr \tag{2.28}$$

The one-electron Kohn-Sham equations may then be solved for the wavefunction and energy using a SCF approach. The variation principle is applied to the equation to obtain the set of orthonormal molecular orbitals which minimise the energy.

In principle, this approach is exact, but only if the exact form of the exchange-correlation functional is known. However, it is unknown and must be approximated. Unlike HF, which captures the exact exchange but zero correlation, DFT includes approximate exchange and correlation. In order to solve the Kohn-Sham equations for the total energy, an expression for the exchange-correlation energy is required. One of the advantages of DFT is that even relatively simple approximations of $E_{XC}[\rho(r)]$ can provide a reasonable description of structural and electronic properties.

Many exchange-correlation functionals are based on the uniform electron gas model, in which the electron density is constant throughout space, which is similar to the behaviour of valence electrons in a metal. One such functional, introduced by Kohn and Sham is the local density approximation (LDA) or local spin density approximation (LSDA), for closed and open shell systems respectively. In this approximation, the

energy depends only on the local density, and it is assumed that at each point the energy is the same as for a uniform electron gas of the same density. The exchange energy is then given as a function of the electron density by Dirac's equation [146]. The correlation energy has been determined using Monte Carlo methods [147], with the exchange energy subtracted from the total energy. A fit to this data was performed by Vosko *et al.* [148] to give an expression for the correlation energy. LDA performs reasonably well for predicting structural properties, but tends to overestimate binding energies and underestimate bond lengths.

Work was later carried out to improve on LDA, to calculate the energy not only in terms of the local density, but also the gradient (the variation of the density close to r) [149, 150]. The generalised gradient approximation (GGA) introduces terms involving the gradient, often in the form of a correction to LDA. GGA functionals can be derived by fitting to experimental data, such as that of Becke which is a correction to the LSDA exchange [151], or the Lee-Yang-Parr correlation functional, which is a functional form for the correlation energy [152]. However, these functionals are usually fitted to data for small molecules and the first few rows of the periodic table, and are less suited to heavier elements. Other GGA functionals which do not depend on empirical parameters exist, such as that of Perdew and Wang (PW91) [150], Perdew, Burke, and Ernzerhof (PBE) [153], and PBEsol, a revision of PBE [154]. PBEsol is designed to improve equilibrium properties of solids and their surfaces, such as their lattice parameters and bond lengths.

As well as the exact form of the exchange-correlation functional being unknown, DFT suffers from some other significant disadvantages. Unlike post-HF methods such as coupled cluster or configuration interaction, where the addition of higher order terms can improve the system and eventually obtain the exact energy, there is no systematic way to improve DFT functionals, and improvements can only be recognised by the results they produce. Another significant disadvantage arises due to the approximate nature of the exchange-correlation functional. The total HF energy includes the Coulomb integral which contains the self-interaction, and the exchange integral, and these terms cancel. In DFT the Coulomb and exchange integrals do not necessarily

cancel, leading to the self-interaction error (SIE), which is an issue in systems containing localised electrons. This can result in delocalisation of states which should be localised, or prediction of a metallic system in some materials known to have a band gap. SIE can be corrected by inclusion of an empirical correction parameter on specific orbitals, or by using hybrid functionals, which mix a percentage of exact HF exchange with DFT exchange-correlation functionals.

2.2.6 DFT + *U*

One method used to reduce the effect of SIE is the introduction of a Hubbard term, U, to valence states to describe the interaction between the ions, along with an exchange term, J. Combining these terms gives the effective U_{eff}, where $U_{eff} = U–J$ of Dudarev *et al.* [155]. The correction to the energy is given by

$$\mathrm{E}_{\mathrm{DFT}+U} = E_{DFT} + \frac{U_{eff}}{2} \sum_{I\sigma} \sum_{i} \lambda_i^{I\sigma}(1 - \lambda_i^{I\sigma}) \tag{2.29}$$

and encourages integer occupation of specific orbitals (σ) on specific atoms (I) with occupations $\lambda_i^{I\sigma}$, to which U_{eff} is applied, by penalising partial occupation of orbitals. Integer occupation of orbitals is encouraged using a quadratic correction by increasing the energy of the delocalised system. The correction is zero when the orbital has integer occupation ($n = 0$ or 1) and is at a maximum halfway between integer occupations, as shown in figure 2.1 [156]. An advantage of the DFT + U approach is that it does not increase the computational cost compared to standard DFT functionals. However, the $+U$ parameter is system dependent, and a value which produces the correct localisation of defect states may not necessarily be the optimum value for other properties of the system as they are not due to the SIE.

The selection of a U value may be done by *ab initio* derivation, *e.g.* using a linear response method [156], using a Koopmans-like approach [157–159], or by empirical fitting to experimental parameters. The band gap is often used to fit values of U, but fitting to experimental data rather than employing a U value to correctly localise a polaronic defect state can result in defect states which do not agree with experimental

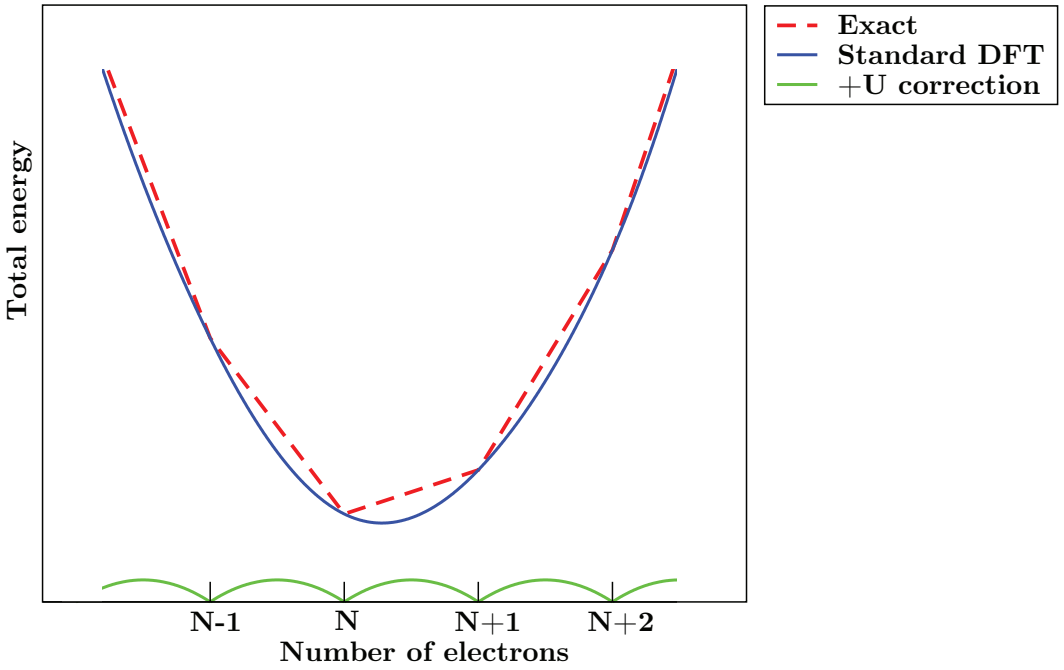

FIGURE 2.1: Sketch of the total energy as a function of the number of electrons. The bottom curve is the difference between the DFT energy and the exact result

spectra. The comparison of features in the band structure or the relative position of a defect state in the band gap to experimental data, such as x-ray photoelectron spectroscopy or ultraviolet photoelectron spectroscopy, is a more suitable means of fitting a U value.

2.2.7 Hybrid DFT

Hybrid functionals are another approach used to improve upon DFT results, in which the exchange-correlation energy is expressed as a linear combination of exact HF exchange with approximated DFT exchange and correlation. Hybrid functionals have been developed, which include parameters fit to experimental data. One such functional is B3LYP [160], which combines Becke's exchange functional, LDA exchange and correlation, HF exchange, and the LYP correlation expression. The exchange-correlation energy is given by

$$E_{XC}^{B3LYP} = (1 - \mathrm{a})E_X^{LDA} + aE_X^{HF} + b\Delta E_X^{B88} + (1 - c)E_C^{LDA} + cE_C^{LYP} \tag{2.30}$$

with $a = 20\%$, and b and c both fitted to atomisation energies, ionisation potentials and proton affinities of compounds of a small number of light elements. This makes the functional less accurate for heavier elements or compounds containing them, such as metals and metal oxides. The PBE0 functional [161], which has a combination of 25% HF with 75% PBE exchange and 100% PBE correlation, has been reported to work well for metals and metal oxides.

The HSE06 functional used in this thesis combines a screened short-range (SR) HF exchange with short- and long-range components of the PBE exchange [162, 163]. The functional applies a screened Coulomb potential to the exchange interaction, with the extent of the screening controlled by a screening parameter, ω. At long range, the exchange functional has PBE behaviour only, while at short range it consists of a percentage of HF exchange, with the remainder given by PBE exchange. The HSE06 exchange-correlation energy is given by

$$\mathrm{E_{xc}^{HSE}} = \alpha \mathrm{E_x^{HF,SR}}(\omega) + (1-\alpha)\mathrm{E_x^{PBE,SR}}(\omega) + \mathrm{E_x^{PBE,LR}}(\omega) + \mathrm{E_c^{PBE}} \tag{2.31}$$

For HSE06, α, the mixing parameter (percentage of HF exchange), is 0.25. The term ω is a screening parameter which controls the extent of the SR interactions. At $\omega = 0$, the functional gives the PBE0 functional, at $\omega = \infty$ it approaches PBE behaviour, and in HSE06, a value of $\omega = 0.207\ a_0^{-1}$ is used.

Hybrid functionals may be used to help correct for SIE, although this can depend on the percentage of HF exchange used. A disadvantage of hybrid DFT is that it is not possible to get the exact energy, as it combines non-local HF exchange with local DFT exchange and correlation. As well as this, it is much more computationally intensive than DFT methods due to the HF exchange when using a plane wave basis. HSE06 has, however, been shown to give improved results for structure and electronic properties for many materials [164–168].

2.2.8 Density Functional Perturbation Theory

Many physical properties of a solid, such as polarisability, phonons, and dielectric, are dependent on the system's response to some form of perturbation. Density functional perturbation theory (DFPT) allows calculation of these properties within the framework of DFT. Two main formalisms of DFPT have been developed, by Baroni [169, 170] and Gonze [171, 172]. Baroni's method uses Green's function methods to self-consistently solve a series of equations; Gonze's method is based on a perturbative expansion of the Kohn-Sham energy functional, giving a variational problem for even orders of expansion.

2.3 Solid state simulation

2.3.1 Periodic boundary conditions

Owing to the large number of electrons in a macroscopic crystal, it is unrealistic to attempt to perform calculations for the entire system. Due to the fact that these crystals are a highly ordered arrangement of atoms repeating in three dimensions, periodic boundary conditions may be employed. This means that instead of attempting to perform calculations for the entire system, a finite repeat unit is used, with special boundary conditions. The size (a, b and c lattice vectors) and shape (α, β and γ cell angles), along with the atomic coordinates define the crystal structure. This is repeated periodically in three dimensions, as shown in figure 2.2. For pure systems, calculations are carried out on this unit cell, while for defective systems, it is necessary to use a supercell expansion of the unit cell in order to minimise interactions between the defects and their periodic images.

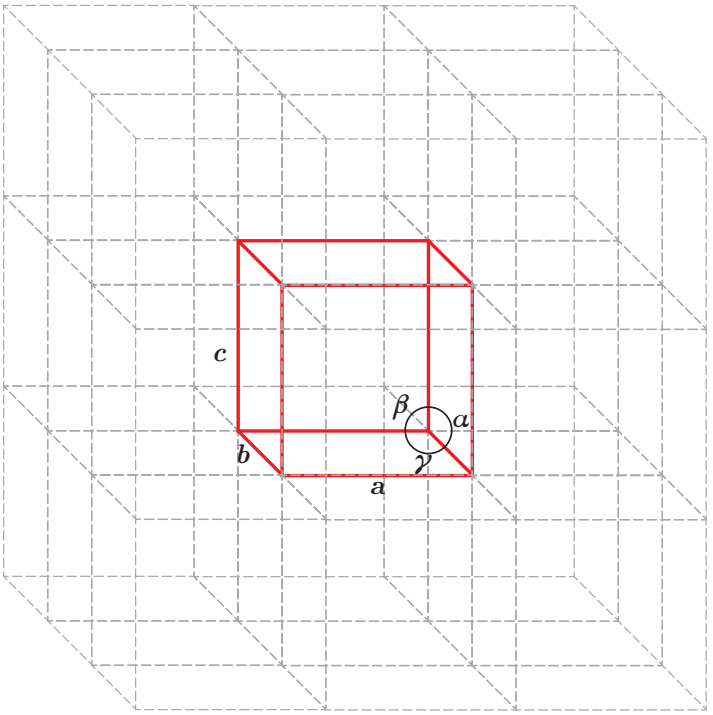

FIGURE 2.2: A 3 × 3 × 3 expansion of a unit cell, with the unit cell shown in solid red lines

2.3.2 Brillouin zone and *k*-points

Bloch's theorem [173] states that the electronic wavefunction of a periodic system can be written in the form

$$\Psi(r) = e^{ikr}u(r) \tag{2.32}$$

where e^{ikr} is the phase factor which describes the interactions between repeating unit cells, r is a spatial direction, and k is the wavevector. $u(r)$ is the periodic Bloch function representing the cell periodic part of the wavefunction, which can be expanded into a finite number of plane waves summed over the range of reciprocal space vectors. The use of plane wave basis sets is described in section 2.3.3.

The wavevector in equation 2.32 represents the phase relationship of the wavefunction between unit cells, with in-phase and out-of-phase interactions between orbitals in different unit cells varying as a function of k. Figure 2.3 is a schematic band structure

of a hypothetical one-dimensional system, each unit cell of length a containing an s orbital. At k=0, the cells are in-phase with each other, and at $\pm\frac{\pi}{a}$ they are out of phase with each other. k only has unique values within a $\frac{2\pi}{a}$ range (equation 2.33), but an infinite number of points exists between these two points. This region in which all k values are unique is known as the Brillouin zone.

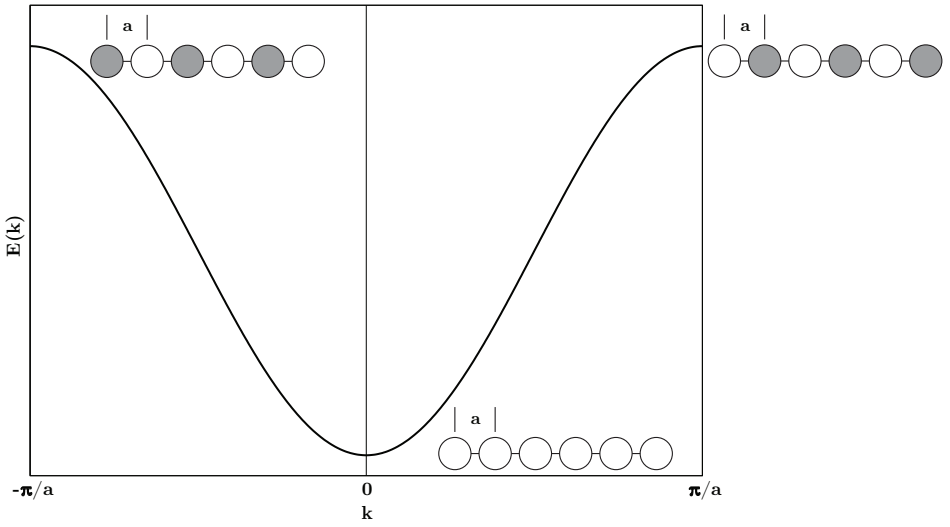

FIGURE 2.3: Schematic band structure showing the in-phase and out-of-phase interactions in the first Brillouin zone

$$\begin{aligned} k' &= k + \frac{2n\pi}{a} \\ e^{ik'a} &= e^{i(k+\frac{2n\pi}{a})a} \\ &= e^{ika}e^{2in\pi} \\ &= e^{ika} \end{aligned} \tag{2.33}$$

In DFT calculations, the electron density is calculated at each iterative step of the electronic optimisation (section 2.3.4), and is obtained by integrating the square of the Kohn-Sham wavefunction over the Brillouin zone. This integral can be approximated by summing over a set of k-points, which minimises the computational cost. The density of k-points required is dependent on the system, with metallic systems requiring a denser mesh of k-points than non-metallic systems, in order to accurately describe the Fermi level. The Monkhorst-Pack method is used here to generate k-point meshes,

which contain k-points evenly spaced, either from the origin, giving an even mesh, or offset from a given k-point, giving an odd mesh, as in Γ-centred meshes [174].

2.3.3 Basis sets and pseudopotentials

In quantum chemical approaches, the representation of orbitals as mathematical functions is required. These representations are usually a linear combination of functions, known as basis functions. Molecular orbitals may be approximated as localised atomic-like functionals, derived from Gaussian functions. Plane waves (of the form e^{iGr}, where G is a reciprocal lattice vector) are widely used as the basis set for solid state calculations, due to their periodic nature, and can offer high accuracy.

The standing wavefunction can be expressed as a linear combination of plane waves, differing by reciprocal lattice vectors.

$$u(r) = \sum_{G} c_j^G e^{iGr} \tag{2.34}$$

where c_j^G are the plane wave coefficients, and j is the band index used to identify the bands determined at each wavevector k in the first Brillouin zone. Although the Fourier series needed to fully describe a system is in principle infinite, the basis set can be reduced to a finite size by introduction of a plane wave cutoff. The plane wave cutoff produces the minimum number of plane waves required to accurately model the system. The basis set is dependent only on the size of the cell, and not the number of atoms, so basis set superposition error and the Pulay force do not arise compared to localised basis sets. However, there is the issue of Pulay stresses which arises in plane-wave calculations due to the incompleteness of the basis set with respect to changes in volume. A high cutoff is required to represent a wavefunction with rapid changes in electron density (*i.e.* electrons close to the core of an atom), but must not be so high as to make the calculation intractable. An advantage of using a plane wave basis set over a localised basis set is that it can be optimised through the variation of this single energy cutoff.

In order to describe core electrons in an all-electron calculation, an unreasonably high cutoff would be required, as the wavefunction changes so rapidly. The pseudopotential approximation is used to overcome this, and can be made as the core electrons are relatively unaffected by the chemical environment of an atom. The strong potential of the ionic nucleus and core electrons is replaced by a weaker pseudopotential [175]. The pseudopotential has the same shape as the valence electrons outside the core region, within the core region it has fewer nodes, and reduces the size of the plane wave basis required. The cutoff in systems with multiple elements must offer adequate convergence for all species in the system. In oxide materials, such as the ones examined in this thesis, the cutoff energy is limited by the electrons of oxygen, not the heavier cations.

Blöchl introduced the projector augmented wave (PAW) method, for high-quality, efficient calculation of the electronic structure of materials [176]. In the PAW method, core states are represented by localised basis sets, the effect of which is projected onto valence electrons, which are represented by plane waves. This approach retains the physics of all-electron calculations and produces the correct nodal behaviour of valence electron wavefunctions, while offering the numerical advantages of the pseudopotential methods.

2.3.4 Electronic and geometric optimisation

In order to optimise a periodic system, the lattice vectors and atomic positions, which are often obtained from experimental results, are required. An iterative process is carried out for the electronic and geometric optimisation, as outlined by the schematic in figure 2.4. A trial wavefunction and charge density are generated, either from a previous iteration, or randomly generated if there is no previous iteration, and these are used to generate the Hamiltonian. Diagonalisation of the Kohn-Sham Hamiltonian to obtain the eigenvalues is carried out. The computational cost of traditional diagonalisation methods is high for plane wave methods, scaling as N^3, where N is the size of the basis set. Iterative diagonalisation schemes use only a subset of the eigenvalues, and are more efficient than traditional methods. When the Kohn-Sham equations are solved, a new charge density and wavefunction are obtained, allowing generation

of a new Hamiltonian. This procedure is iterated until the energy of two electronic iterations (ΔE) is within a given threshold (E_{diff}).

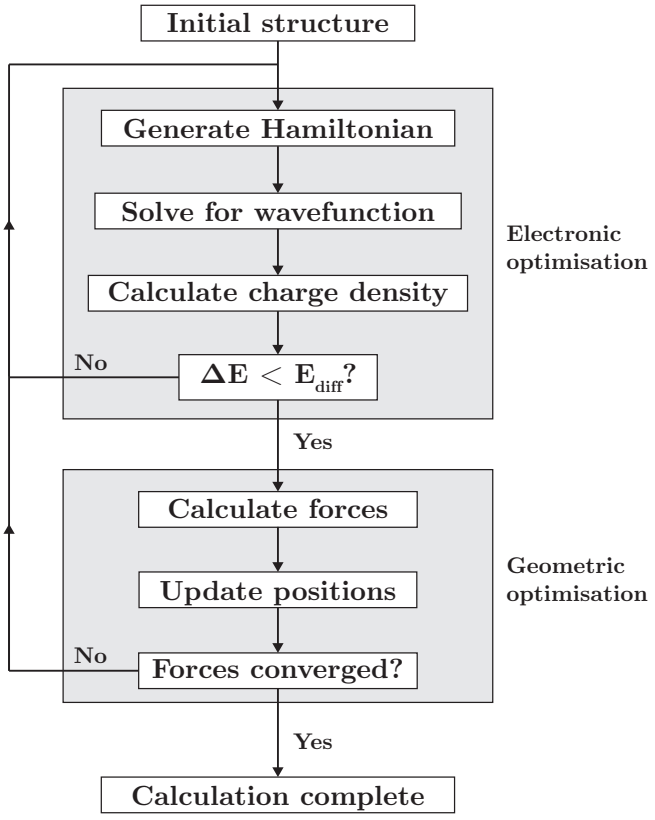

FIGURE 2.4: Schematic showing the iterative process for electronic and geometric optimisation

Once the convergence criteria are met, the new wavefunction is then used to calculate the forces and update the ionic positions. Force is the derivative of the energy with respect to position; therefore, forces can be determined by moving each atom in all directions and calculating their energy. However, this will require $6N$ calculations of the energy for a system with N atoms. The Hellmann-Feynman theorem [177] states that the force on any fixed nucleus in a system of electrons and nuclei is simply the classical electrostatic interaction exerted on the nucleus, therefore once the wavefunction has been determined, the forces can be estimated directly from it. At each step, the forces on each ion are calculated and the positions are updated, and if the force convergence criterion is not met, a new SCF step starts. The system has reached a minimum energy ionic configuration when there are zero net forces on each ion (or as close to zero as specified by the force convergence criterion).

Chapter 3

Computational Methods

All calculations were performed using VASP [178–180]. VASP is a widely used quantum mechanical code due to its flexibility, with DFT, DFT + U, HF and hybrid-DFT methods implemented within it, and contains its own set of PAW pseudopotentials, optimised for each element. VASP simulates solid state systems through the use of periodic boundary conditions, modelling a given unit cell as an infinite lattice. When a fully optimised geometric and electronic structure has been obtained, further calculations can be carried out to determine properties such as density of states and band structure. In this chapter, the methods used in structural optimisation, calculation of the electronic structure, defects and surface simulation are outlined.

3.1 Structural optimisation

For all materials described within this thesis, the first step in their simulation is to optimise the unit cell geometry. This is done by using an experimental crystal structure as the starting point for the simulations. The unit cell is optimised over a range of volumes, with atomic positions, lattice vectors and cell shape allowed to relax while holding the cell volume fixed. This is repeated until the optimisation completes in one step, so there is no change in basis set. An energy-volume curve is fitted to the Murnaghan equation of state [181], with the minimum of this curve used to determine the equilibrium cell volume (figure 3.1). This minimises the problem of Pulay stresses and changes in basis set which arise in plane-wave calculations due to the incompleteness of the basis set with respect to changes in volume [182].

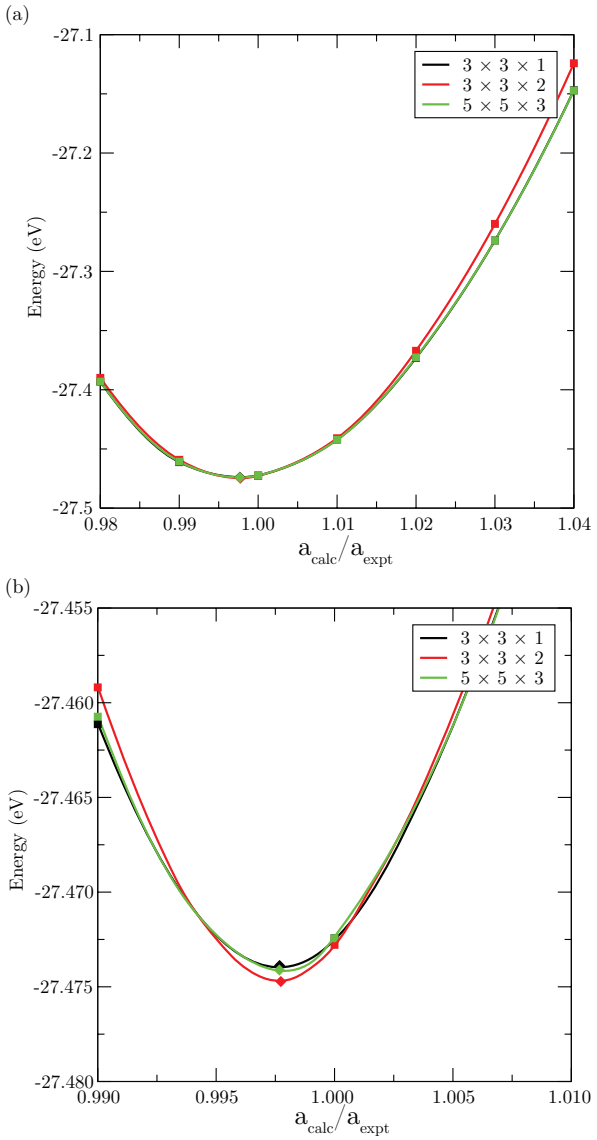

FIGURE 3.1: (a) Murnaghan equation of state fite (lines) to energy-volume data (points) for $LaMnO_3$ for three different k-point meshes. The $3 \times 3 \times 1$, $3 \times 3 \times 2$ and $5 \times 5 \times 3$ curves are shown in black, red and green respectively. (b) Close-up of the region around the minimum, showing the energy convergence of the k-point meshes

The plane wave cutoff is required to be sufficiently high to describe rapid changes in the electron density, but also low enough that the calculation does not become prohibitively expensive (section 2.3.3). Usually, a lower cutoff (200–300 eV) is sufficient for heavier elements, but as the systems examined in this thesis contain lighter elements such as oxygen, higher cutoffs are often required (400–500 eV) to describe the rapid changes in electron density. The PAW pseudopotentials in VASP provide a minimum cutoff required to accurately describe each element and its electronic configuration. The

cutoff used in this work is the highest minimum cutoff (400 eV), which is that of oxygen, as it has been previously shown to be sufficient for semiconducting oxides such as the ones examined here [183–185].

The optimum values for various calculation parameters must be determined to ensure that they are appropriate to model the desired properties of the system. To test for convergence, a series of energy-volume curves were plotted using different k-point densities. A suitable estimate for the k-point grid for semiconducting oxides results in a sampling density of approximately 0.04 Å^{-1}. The k-point grid is determined by dividing the inverse of each lattice vector by the sampling density and rounding up. k-points grids either side of this initial estimate are also tested, to ensure that convergence to within 0.005 eV per formula unit is obtained. The convergence of k-point meshes of $3 \times 3 \times 1$, $3 \times 3 \times 2$ and $5 \times 5 \times 3$ are tested for $LaMnO_3$, with little variation in the energy-volume curves for the $3 \times 3 \times 2$ and $5 \times 5 \times 3$ meshes. Figure 3.1 shows the PBEsol + U energy-volume curve, fitted to the Murnaghan equation of state for $LaMnO_3$, for these k-point meshes. The structure was optimised for a range of volumes with lattice constants of 98% to 104% of the experimental values. A $3 \times 3 \times 2$ Monkhorst-Pack grid (sampling density of 0.06 Å^{-1}) is used in further calculation of perovskite-structured materials.

For geometric and electronic optimisation of unit cells, the quasi-Newton residual minimization scheme, direct inversion in the iterative subspace (RMM-DIIS) algorithm [186], is employed. Quasi-Newton methods are based on Newton's method, which requires the Hessian matrix (a second derivative matrix) to be calculated, a computationally expensive process. Instead of calculating the Hessian, the quasi-Newton method gradually builds an approximation of the inverse of the Hessian using the gradient of previous iterations. The matrix can be built such that is positive definite, and avoid convergence to local maxima.

In nudged elastic band (NEB) calculations, the limited-memory Broyden-Fletcher-Goldbard-Shanno (L-BFGS) method is used. This is a quasi-Newton method which allows the images in the NEB to be optimised collectively, improving the efficiency of the calculations [187].

3.2 Electronic analysis

3.2.1 Band structure

The band structure of a material can be obtained by plotting the Kohn-Sham eigenvalues as a function of k. In order to calculate the band structure using DFT in VASP, first, a self-consistent calculation is carried out to obtain the charge density and wave function. Then a non-self-consistent calculation is performed, using the charge density of the self-consistent calculation, to obtain the eigenvalues along the high-symmetry directions of the Brillouin zone. The eigenvalues of the high symmetry points, and a specified number of points between them are plotted. The high symmetry points used to plot band structures in this thesis are taken from the handbook of Bradley and Cracknell [188].

The band structure can provide information such as the band gap of the material, the k-points at which the valence band maximum (VBM) and conduction band minimum (CBM) occur, and hence the nature of the band gap. Dispersion of the bands can give an indication of the strength of the interactions between atomic orbitals of the system, with disperse bands representing stronger interactions, and flat, non-disperse bands resulting from weak interactions, typically from highly localised orbitals with little or no mixing.

3.2.1.1 Effective mass

The effective mass of the band edges can be used as an indicator of the conductivity of a material. The conductivity, σ, is related to the carrier concentration, n, and carrier mobility, μ, by

$$\sigma = ne\mu \tag{3.1}$$

The carrier mobility is inversely proportional to the effective mass. A material which exhibits good p-type conductivity will have a low hole effective mass at the VBM, while a good n-type semiconductor has a low electron effective mass at the CBM. The

effective mass is dependent on the curvature at the band edges. A system with low effective mass will have highly disperse, curved bands around the VBM or CBM. A high level of dispersion means that the holes or electrons are delocalised, which results in high mobility and high conductivity. When the effective mass is high, and carrier mobility is low, the bands will be non-disperse and flat, and the electron or hole is localised.

In this work, the transport effective mass (m_T^*), which can be compared to experimental values, is calculated using [189]

$$\frac{1}{m_T^*(E_k)} = \frac{1}{\hbar^2 k}\frac{dE}{dk} \tag{3.2}$$

The first derivative of the band energy, E_k, with respect to k is assumed to be equal to that of a parabolic band at that k-point. However, in most materials, the curvature of the band edge is not parabolic. As a result, the effective masses reported here provide an estimate of whether a material will exhibit good conductivity, but the quantitative accuracy will be dependent on the system.

3.2.2 Electronic density of states

The electronic density of states (EDOS) plots the density of eigenvalues as a function of energy. The total density of states is essentially an integrated band structure with respect to energy. An energy range in the band structure with a large number of bands close together within it will result in a large peak in the EDOS. The EDOS can provide information on the electronic structure of the valence and conduction bands of a material, as well as any states resulting from the introduction of defects.

The partial electronic density of states (PEDOS), in which the states are decomposed by element, orbital eigenvalue, or both, can provide extra information about the electronic structure, allowing identification of the orbital or element contributing to the peaks, and can be compared to experimental spectra. Spheres of a given radius are defined around each ion, with all electron density within that sphere attributed to the ion. The wavefunctions are projected onto spherical harmonics within these spheres to determine

the orbital in which the density is located. The projection radius can be determined by examining the charge density around each ion, from which the ratio of the different atomic radii can be determined. The radii are then varied while keeping this ratio fixed, until the correct number of electrons is reached.

3.3 Defect calculations

The presence of a defect in a material can greatly affect its properties. The introduction of aliovalent defects to a system generates charge compensating defects, which can modify its electronic or ionic conductivity. Defects are usually randomly distributed within a crystalline material, and are usually in low concentrations, which is not possible to simulate in the unit cells used for structural optimisation. Introducing a defect to the unit cell can lead to defect-defect interactions and defect concentrations much higher than those observed experimentally. Instead, a supercell expansion of the unit cell is generated, which is treated with periodic boundary conditions. The use of a supercell minimises the interaction of defects with their periodic images and allows properties of individual isolated defects to be obtained. It is preferable to use a large supercell, though the supercell size is often limited by the method used and the computational resources available.

3.3.1 Neutral defect formation

The formation energy $\Delta H_f(D, q)$ of a charge neutral defect, D, is given by

$$\Delta H_f(D) = (E^D - E^P) + \sum_i n_i(E_i + \Delta\mu_i) \tag{3.3}$$

where Δ H$_f(D)$ is the formation energy of defect D, E^D is the energy of the defective system, where the shape and volume of the defective cell are constrained to that of the pure supercell, E^P is the energy of the pure supercell, n is the number of atoms of type i taken from or added to an external reservoir, and $E_i + \Delta\mu_i$ are the chemical potentials which represent the equilibrium growth conditions.

Taking the example of an oxygen vacancy, $n_{\mathrm{O}} = +1$, the formation energy is given by

$$\Delta H_f(\mathrm{O}_{vac}) = E^{\mathrm{O}_{vac}} - E^P + \frac{1}{2}E_{\mathrm{O}_2} + \Delta\mu_{\mathrm{O}}(T,p) \tag{3.4}$$

where E_{O_2} is the energy of an oxygen molecule. The calculation of chemical potentials is outlined in section section 3.3.3.

3.3.2 Charged defect formation

When an aliovalent defect is introduced into a system, the defect can be present in multiple charge states. Equation 3.3 can be modified to include additional terms required for the calculation of the formation energy of a defect with charge q, as in equation 3.5.

$$\Delta H_f(D,q) = (E^{D,q} - E^P) + \sum_i n_i(E_i + \Delta\mu_i) + q(E_{Fermi} + \varepsilon^P_{VBM} + E_{align}) \tag{3.5}$$

where $E^{D,q}$ is the energy of the charged cell, E_{Fermi} is the electron chemical potential, varying from the VBM (E_{Fermi} = 0 eV) to the CBM (E_{Fermi} = the value of the material's band gap), ε^P_{VBM} is the VBM eigenvalue of the pure system. E_{align} is a correction term used to align the electrostatic potential between the bulk and defective systems and reduce the uncertainties in defect formation energies calculated for finite size supercells [190]. This term requires the dielectric constant of the host material, which is calculated using DFPT in VASP, or can be taken from experiment.

3.3.3 Chemical potentials and oxygen partial pressure

The effect of varying the oxygen partial pressure experimentally can be modelled by varying the chemical potential $\Delta\mu_i$, which set the conditions under which the material is formed. In a ternary oxide, such as the ABO_3 perovskites examined in this thesis, the growth conditions can be oxygen-rich/cation-poor oxygen-poor/cation-rich, or in between. Taking $LaMnO_3$ as an example (energies quoted are taken from Chapter 4), the formation energy is equal to the sum of the chemical potentials.

$$\Delta\mu_{\mathrm{La}} + \Delta\mu_{\mathrm{Mn}} + 3\Delta\mu_{\mathrm{O}} = \Delta H_f^{LaMnO_3} = -12.82 \text{ eV} \tag{3.6}$$

The limiting conditions on the chemical potentials are determined by the formation of competing phases, La_2O_3, MnO, MnO_2, Mn_2O_3 and Mn_3O_4. The sum of the chemical potentials is set as equal to the formation energy, allowing a set of linear equations to be generated, which can be solved to determine intersection points of a region of stability.

Within the constraint that the calculated formation energy of $LaMnO_3$ is equal to the sum of the chemical potentials ($\Delta\mu_{\mathrm{La}} + \Delta\mu_{\mathrm{Mn}} + 3\Delta\mu_{\mathrm{O}} = \Delta \mathrm{H}_f^{\mathrm{LaMnO_3}}$), the optimum conditions for defect formation can be determined. In order to avoid precipitation into solid elemental La, Mn and O_2 gas, chemical potentials of $\Delta\mu_{\mathrm{La}} \leq 0$, $\Delta\mu_{\mathrm{Mn}} \leq 0$, $\Delta\mu_{\mathrm{O}} \leq 0$ are required. The chemical potentials are also constrained by the formation of binary compounds, La_2O_3, MnO, MnO_2, Mn_2O_3, and Mn_3O_4, setting the limits $2\Delta\mu_{\mathrm{La}} + 3\Delta\mu_{\mathrm{Mn}} \leq \Delta \mathrm{H}_f^{\mathrm{La_2O_3}}$, $\Delta\mu_{\mathrm{Mn}} + \Delta\mu_{\mathrm{O}} \leq \Delta \mathrm{H}_f^{\mathrm{MnO}}$, $\Delta\mu_{\mathrm{Mn}} + 2\Delta\mu_{\mathrm{O}} \leq \Delta \mathrm{H}_f^{\mathrm{MnO_2}}$, $2\Delta\mu_{\mathrm{Mn}} + 3\Delta\mu_{\mathrm{O}} \leq \Delta \mathrm{H}_f^{\mathrm{Mn_2O_3}}$ and $3\Delta\mu_{\mathrm{Mn}} + 4\Delta\mu_{\mathrm{O}} \leq \Delta \mathrm{H}_f^{\mathrm{Mn_3O_4}}$. The chemical potential of alkaline earth (AE) dopants is determined from the formation energy of their binary oxides $\Delta\mu_{AE} + \Delta\mu_{\mathrm{O}} \leq \Delta \mathrm{H}_f^{AE\mathrm{O}}$. The chemical potential limits for determining the defect formation energies were calculated using CPLAP [191].

The temperature and partial pressure dependence of the oxygen chemical potential, $\Delta\mu_{\mathrm{O}}(T, p)$, is calculated by the method of Reuter and Scheffler [192]

$$\Delta\mu_{\mathrm{O}}(T, p) = \Delta\mu_{\mathrm{O}}(T, p^\circ) + \frac{1}{2} kT \ln\left(\frac{p}{p^\circ}\right) \tag{3.7}$$

where p is the oxygen partial pressure, and p° is 1 atm. The zero reference state of the oxygen chemical potential is given by the total energy of an isolated oxygen molecule

$$\Delta\mu_{\mathrm{O}}(0\,\mathrm{K}, p^\circ) \equiv 0 \tag{3.8}$$

With respect to this zero reference state, $\Delta\mu_{\mathrm{O}}(T, p^{\circ})$ is given by

$$\begin{aligned}\Delta\mu_{\mathrm{O}}(T, p^{\circ}) &= \Delta\mu_{\mathrm{O}}(0\,\mathrm{K}, p^{\circ}) + \frac{1}{2}\Delta G(\Delta T, p^{\circ}, \mathrm{O}_2) \\ &= \frac{1}{2}[H(T, p^{\circ}, \mathrm{O}_2) - H(0\,\mathrm{K}, p^{\circ}, \mathrm{O}_2)] \\ &- \frac{1}{2}T[S(T, p^{\circ}, \mathrm{O}_2) - S(0\,\mathrm{K}, p^{\circ}, \mathrm{O}_2)]\end{aligned} \tag{3.9}$$

The temperature dependent values of H and S can be obtained from thermochemical tables [193], allowing the oxygen chemical potential under realistic conditions to be determined. Vibrational and entropic contributions are neglected, as they are reported to be typically less than DFT error. [194]. Reuter and Scheffler report the vibrational contribution to be of the same order as the numerical uncertainty in the calculations, and that the uncertainty does not affect the physical conclusions in their study [192].

3.3.4 Thermodynamic transition levels

When defects are introduced into a system they can generate states in the band gap. Although these defect levels may be detected experimentally, using techniques such as deep level transient spectroscopy, which involve the final charge state relaxing to its equilibrium configuration after the charge-state transition, it can be difficult. Therefore, computation identification of the defect levels is becoming a more commonly used procedure. Thermodynamic transition levels, where a defect switches from one charge state to another as a function of Fermi energy, are of particular interest. The thermodynamic transition level is defined as the Fermi energy at which the energies of q and q' are equal (equation 3.10).

$$\varepsilon_E(q/q') = \frac{\Delta H_f(D, q) - H_f(D, q')}{q' - q} \tag{3.10}$$

Transition level diagrams, which plot the defect formation energy of the various charge states as a function of Fermi energy, allow identification of transitions between the charge states of defects in a system and the Fermi level at which they occur. The lowest energy charge state of a defect at any given Fermi energy over the range of the

band gap is plotted. In some cases, where the transition levels lie within the valence band or conduction band, the region plotted extends beyond the band gap. These plots allow identification of the charge states of a defect and the Fermi energy at which they occur. Each defect usually has a number of different charge states (dashed lines in figure 3.2), normally only the most stable charge state at each Fermi energy is plotted (solid lines in figure 3.2).

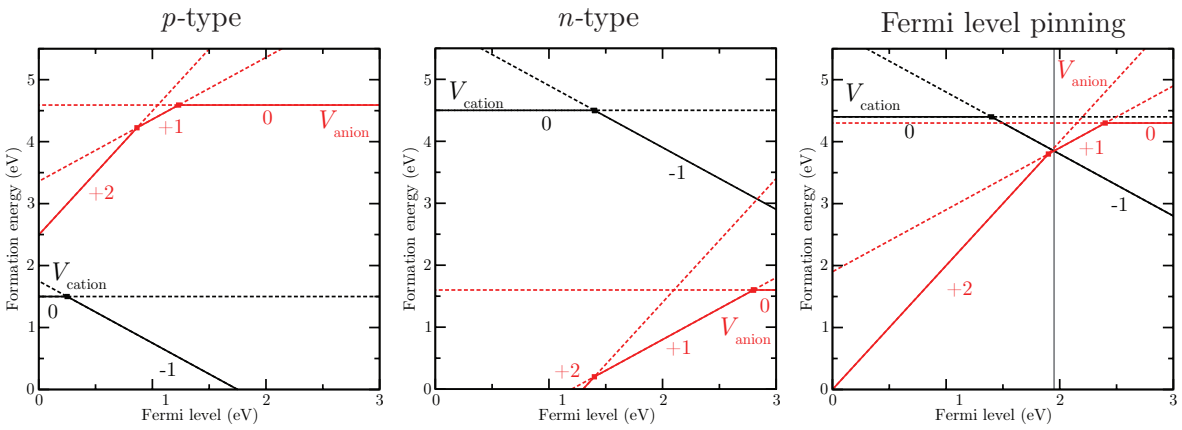

FIGURE 3.2: Thermodynamic transition level diagrams for a notional binary oxide, containing a metal vacancy (black) and an oxygen vacancy (red). (a) shows a p-type system, (b) shows an n-type system, and (c) shows pinning of the Fermi level at the point of intersection of the defect charge states.

In a transition level diagram, the slope of the line is equal to the charge state of the defect. Neutral defects (denoted by an x superscript in Kröger-Vink notation) have zero slope, n-type defects (positive charge states, which are denoted by a $\bullet$ superscript in Kröger-Vink notation) have a positive slope, and p-type defects (negative charge states, which are denoted by a $'$ superscript in Kröger-Vink notation) have a negative slope. The transition levels are marked by solid points on the plot and indicate where two charge states are in equilibrium with one another.

A transition level diagram can show a number of properties of interest. The inclusion of the chemical potential allows simulation of experimental growth conditions. The formation energy of the defect will indicate how likely it is that the defect will form under the given conditions. When assessing the conductivity of a material, ideally the first transition level should be close to or within the valence band for p-type conductivity, or the conduction band for n-type conductivity. This allows holes to readily

move from acceptor levels to the valence band, or electrons from donor levels to the conduction band, improving the conductivity. If a defect intersects with one of opposite polarity, charge compensation occurs and causes pinning of the Fermi level at this point, preventing the material from being either p- or n-type.

Figure 3.2 shows three scenarios for a notional binary oxide, containing a p-type metal vacancy and an n-type oxygen vacancy. The charge states of the defects are plotted as dashed lines in the figure. Generally, only the lowest energy charge state is plotted; this is shown by the solid lines. Figure 3.2 (a) represents a system in which the p-type defect is more likely to form under the given conditions. The metal vacancy has a lower formation energy than the oxygen vacancy, and has a relatively shallow (0/-1) transition level, shifting the Fermi level to the VB which allows easy promotion of an electron formation of a hole in the VB. The oxygen vacancy is high in energy and has a deep transition level, so n-type behaviour in this material is very unlikely, and anion vacancies will not compensate for cation vacancies. Figure 3.2 (b) represents conditions where the n-type defect is more likely to form. The first transition level of the oxygen vacancy is shallow relative to the conduction band minimum, shifting the Fermi level to the CB and has a much lower formation energy than the metal vacancy. Figure 3.2 (c) is a system in which the charge state of the donor and acceptor overlap, pinning the Fermi level at that point, shown by the grey line.

3.3.5 Nudged elastic bands

NEB calculations are a method of finding a minimum energy path (MEP) between two stable states [187, 195]. These two states are the initial and final state, and are local minima on the potential energy surface. On a MEP, any point on the path is at an energy minimum in all directions perpendicular to the path, and the path passes through at least one first-order saddle point. A NEB is a chain-of-states method, in which a string of configurations of the system, connected by spring forces, is used to describe a reaction pathway. When the NEB is converged, the string of images describes the reaction pathway.

NEB calculations are started from an initial pathway connecting the initial and final states, and in most cases, a linear pathway is suitable for the initial path [187]. The images along the NEB are allowed to relax to the MEP through a force projection scheme in which the potential forces act perpendicular to the band and the spring forces act along the band. The tangent along the path is defined as the unit vector to the higher energy neighbouring image, in order to make the projections. To ensure that the direction of the tangent does not change abruptly, a linear interpolation between the vectors to the neighbouring images is used. This improves the stability of the NEB and prevents the development of artificial kinks in high force regions along it.

The use of a climbing-image NEB (CI-NEB) allows determination of the system configuration at the transition state. In a CI-NEB, the highest energy image does not feel any spring forces and is allowed to climb to the saddle point via a reflection in the force along the tangent, giving a maximum in energy along the band and a minimum in all other directions.

3.4 Surface simulation

3.4.1 Tasker surfaces

Surface terminations were classified by Tasker [196], depending on the atomic composition of the layers. A Type I surface is composed of stoichiometric layers, giving a charge neutral surface with equal numbers of anions and cations in each layer, and has no net dipole perpendicular to the surface, as shown in figure 3.3 (a). The individual layers in a Type II surface are charged, but there is no net dipole perpendicular to the surface due to symmetric stacking of the layers, as shown in figure 3.3 (b). In a Type III surface, shown in figure 3.3 (c), there is a net dipole moment due to the alternating charged layers.

As they have no net dipole, Type I and Type II surfaces are generally stable, but Type III surfaces are unstable due to the dipole perpendicular to the surface, and have large surface energies, which increase with crystal thickness. These surfaces can be stabilised by modifying them to remove the dipole. One method used is surface reconstruction

by transferring half the atoms from the top layer to the bottom of the surface slab, as shown in figure 3.3 (d). When modelling a surface, different terminations may arise from the same Miller index by cleaving the lattice along different planes of atoms, as illustrated schematically for the {010} surface of $LaMnO_3$ in figure 3.4.

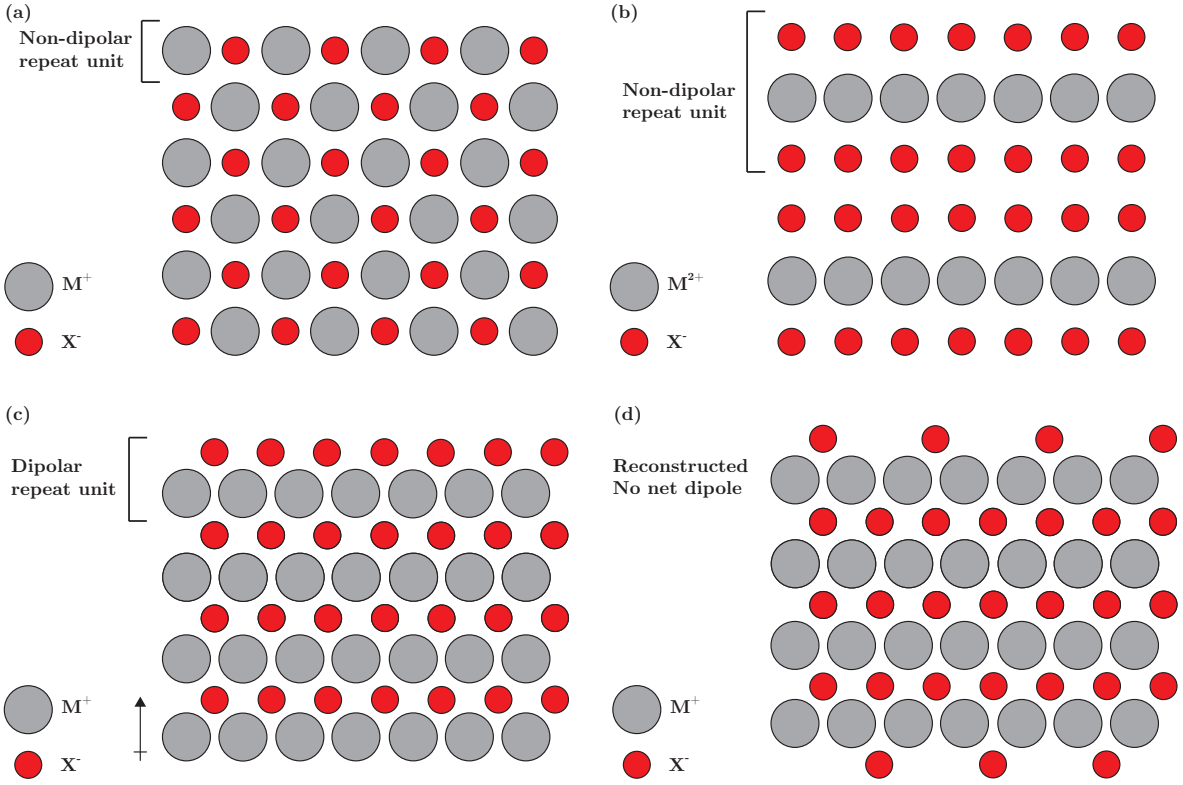

FIGURE 3.3: Tasker classification of surfaces. (a) Type I for a sample system with M^+ cations and X^- anions, (b) Type II for a sample system with M^{2+} cations and X^- anions, (c) Type III for a sample system with M^+ cations and X^- anions, (d) reconstruction of Type III

3.4.2 Slab model

The slab model is used for calculations on surfaces, in which a slab of finite thickness is repeated in 3 dimensions, with a vacuum gap in the direction perpendicular to the surface. The surface slab should be thick enough to ensure that there is minimal interaction between the top and bottom of the slab, and the vacuum gap must be sufficiently large that the interaction perpendicular to the surface between periodic slabs is minimised. The top and bottom layers of the slab are both exposed, generating two surfaces per slab. Non-dipolar surface slabs were generated for each surface from

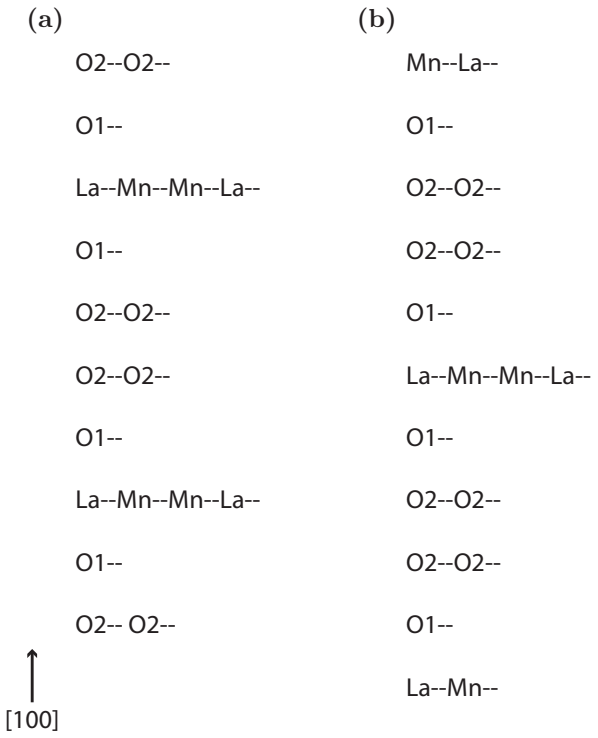

FIGURE 3.4: Different terminations of the {100} surface, depending on the plane cleaved (a) O2 plane cleaved, (b) La-Mn plane cleaved

the optimised bulk structure using the METADISE code [197]. The METADISE code cleaves the optimised bulk crystal according to a specified Miller index. The surface energy is calculated using

$$\gamma_s = \frac{E_{slab} - nE_{bulk}}{2A} \tag{3.11}$$

where γ is the surface energy per unit area, E_{slab} is the energy of the optimised surface slab, n is the number of bulk units, E_{bulk} is the energy of the optimised bulk and A is the area of the surface slab.

When considering defective surfaces, such as those containing vacancies or interstitial ions, the two-dimensional expansion of the surface must be large enough to avoid interaction between defects and their periodic images. In this work, surface expansions are chosen such that there is a minimum of 15 Å between defects. Charged defects are not considered in surface slabs as the energy of a charged defect is divergent with vacuum thickness. In defect simulations, to ensure that there is no net dipole across

the surface slab, defects are introduced on both sides of the slab. The expression for the defect formation energy is modified to account for this, as shown in equation 3.12.

$$\Delta H_f(D) = \frac{1}{2}[(E^D - E^P) + \sum_i n_i(E_i + \Delta\mu_i)] \tag{3.12}$$

In this thesis, the formation energy and structure for the most stable termination of each of the low index surfaces examined are discussed. Oxygen defects are then considered at these surfaces, to investigate their potential for improving the ionic conductivity of the material for use as a SOFC cathode.

3.4.3 Wulff construction

The equilibrium crystal structure can be determined based on the calculated surface energies using the Wulff construction [198]. Wulff stated that for an equilibrium crystal there exists a point in its interior such that the perpendicular distance, h_i, from the i^{th} face is proportional to the surface energy γ_i.

$$\frac{\gamma_1}{h_1} = \frac{\gamma_2}{h_2} = \cdots = \frac{\gamma_n}{h_n} = \text{constant} \tag{3.13}$$

where γ_i is the specific surface free energy of the i th crystal plane and h_i is the central distance of the i th crystal plane. This allows a gamma plot, which is a polar plot of surface energy as a function of the orientation, to be generated. The equilibrium crystal shape is that which minimises the Gibbs free energy

$$\Delta G_i = \sum_j \gamma_j A_j \tag{3.14}$$

where A_j is the area of the i th plane. The Wulff construction uses the Wulff plot to determine which crystal faces will be present. This is done by drawing lines from the origin to every point on the Wulff plot. A plane perpendicular to each line is drawn at each point of intersection of the gamma plot. The region enveloped by these planes gives the equilibrium crystal shape, as shown in figure 3.5.

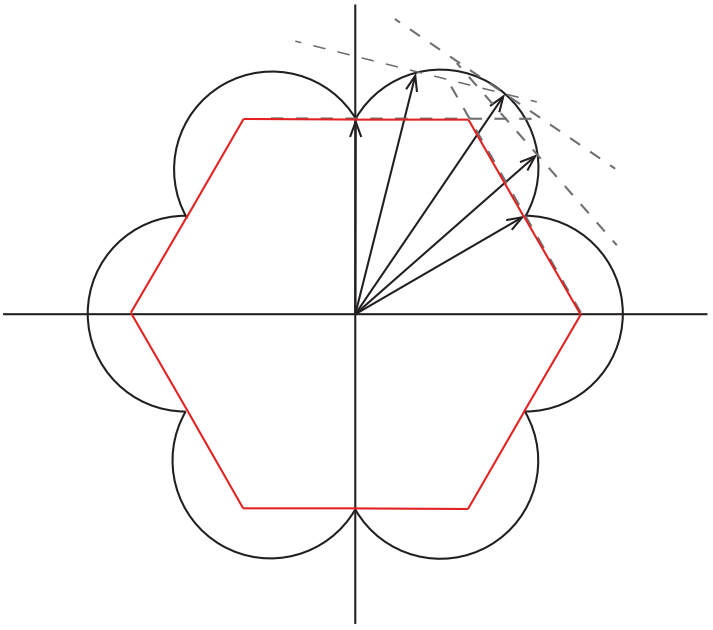

FIGURE 3.5: The Wulff construction of a two-dimensional crystal structure. The solid black outline represents the gamma plot, lines of length h_i are shown by black arrows, dashed grey lines represent the planes perpendicular to h_i, and the region enclosed by red lines is the equilibrium crystal shape

Chapter 4
Structural and electronic properties of $LaMnO_3$

4.1 Introduction

$LaMnO_3$ has been widely investigated for a range of applications, due to its excellent catalytic properties, low cost and ease of preparation compared to noble metal catalysts, magnetic properties and good thermal stability at high temperatures. $LaMnO_3$-based materials have been examined as cataylst for removal of pollutants [199–202], methane combustion [203], and for the ORR in metal-air batteries and SOFCs [55, 204]. It has also been shown to exhibit promising behaviour for use as an electrode material for supercapacitor applications when undoped or doped with Sr [205–207]. At low temperature, $LaMnO_3$ exhibits colossal magnetoresistance [208], giving applications in magnetic sensors and magnetic memory [209, 210].

$LaMnO_3$-based perovskites are one of the most widely investigated cathode materials for high-temperature SOFCs due to their good electrical conductivity, good stability, reasonable catalytic activity for the oxygen reduction reaction (ORR) and relatively low cost [211]. They can also exhibit mixed ionic and electronic conductivity, which increases the active area for the ORR at the cathode [55]. Above 750 K, $LaMnO_3$ is pseudocubic, and below this, it is orthorhombic. There has been extensive computational work done on the high-temperature system [102, 103, 212–215], however, the calculations can be difficult due to defects lowering the symmetry of the system, and

allowing the distortion of the cubic cell towards the more stable phase. The orthorhombic phase, in the *Pbnm* space group, has experimentally determined lattice parameters $a = 5.552$ Å, $b = 5.727$ Å and $c = 7.737$ Å [216, 217]. In the bulk crystal, La ions are coordinated to 12 O ions, and Mn ions are coordinated to 6 O ions. The orthorhombic cell is distorted relative to the cubic perovskite structure due to a combination of Jahn-Teller distortion of the MnO_6 octahedra, and a $GdFeO_3$-type distortion, characterised by alternating rotation and tilts of the octahedra (tilt system $a^-b^+a^-$ in Glazer notation [218, 219]), resulting in two different Mn-O-Mn angles, θ_1 (Mn-O1-Mn) and θ_2 (Mn-O2-Mn) [220]. In the MnO_6 octahedra, the Mn is surrounded by two apical (O1) and four planar (O2) oxygen atoms, as shown in figure 4.1, with short and long Mn-O2 in-plane distances (Mn-$O2_s$ and Mn-$O2_l$ respectively) and a Mn-O1 (Mn-$O1_m$) distance which has a length in between that of Mn-$O2_s$ and Mn-$O2_l$ [100].

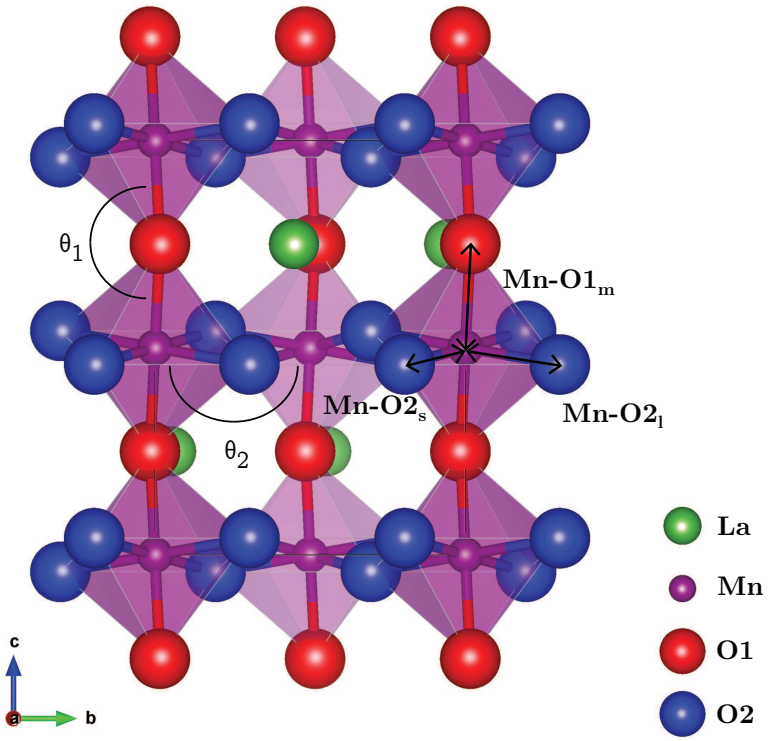

FIGURE 4.1: Unit cell of $LaMnO_3$ used in these calculations, with Mn-O-Mn angles and Mn-O bond lengths labelled

Orthorhombic $LaMnO_3$ displays A-type antiferromagnetic ordering (A-AFM), with ferromagnetic coupling of Mn spin in the basal plane, and antiferromagnetic coupling

between planes [221], with reported Mn magnetic moment ranging between 3.42 and 3.87 μ_B/Mn [221–223]. A-AFM $LaMnO_3$ is a semiconductor, with an O $2p$ dominated valence band, with Mn t_{2g} states at the bottom of the main O $2p$ region, and an unoccupied peak with Mn e_g character is seen between the top of the valence band and the bottom of the main unoccupied states [224].

The most common methods of calculating the structural and electronic properties of perovskite oxides have been DFT and hybrid-DFT. LDA and GGA (PW91, PBE) are reported to reproduce the experimental lattice parameters to within 1% and magnetic structure of the $LaMnO_3$ unit cell [215, 225], but underestimate the Jahn-Teller and $GdFeO_3$-type distortions [94, 96, 98]. LDA and GGA calculations also underestimate the band gap of orthorhombic $LaMnO_3$ [96, 215] or predict a metallic system [94], and do not give the correct splitting of the Mn $3d$ states. The description of the magnetic and electronic structures, and the structural parameters can be improved by using DFT + U or hybrid DFT. DFT + U, (PBE + U, LDA + U) with U values of 2–5 eV applied to Mn $3d$ states [96, 226, 227], or hybrid DFT, results in an improved description of the electronic structure and opens the band gap [96–100]. However, both DFT + U and hybrid DFT may overestimate the cell volume, leading to errors in the structural distortion, with poor description of the tilting of the MnO_6 octahedra.

Previous theoretical studies of $LaMnO_3$ surfaces have focused mainly on the high-temperature cubic phase, investigating the stability of the {001}, {110} and {111} surfaces, and oxygen adsorption at these surfaces, using PW91 [102] and B3LYP functionals [102, 104, 105]. The MnO_2 terminated surfaces of the cubic phase were found to be the most stable ones, and dissociative adsorption of O on Mn ions was observed [103].

Studies of the low index surfaces of the orthorhombic phase have focused on surface energetics and the relaxation of a subset of the surfaces [101, 102]. A recent study by Ahmad *et al.* [105], using hybrid DFT with the B3LYP functional, investigated a subset of the low index surfaces of orthorhombic $LaMnO_3$ [105], focusing on the O-terminated Tasker type 2 surfaces [196]; the {010}, {100}, {011} and {110}. They report the longest Mn-O bond distance in the bulk to be 2.31 Å, which significantly overestimates

the experimental value of 2.18 Å [216]. Of the surfaces studied, the {010} was found to be the most stable, followed by the {110}, {100} and {011}. The equilibrium crystal morphology was predicted, the Mn sites at each surface were identified and used to determine the percentage of 4- and 5-coordinate Mn sites at which the ORR can take place. Few experimental studies have been carried out on the surfaces of orthorhombic $LaMnO_3$. A recent study by Symianakis *et al.* [228] characterised the surfaces of orthorhombic $LaMnO_3$ using x-ray photoelectron spectroscopy (XPS) and LEIS. XPS was used to determine the atomic concentrations of La, Mn and O, and LEIS was used to determine the La/Mn surface atomic ratio, which was found to be 1.7 ± 0.3.

In this chapter, the PBE, PBE + U, PBEsol, PBEsol+ U, and HSE06 functionals were examined for modelling of bulk orthorhombic $LaMnO_3$, in order to determine a suitable functional for calculation of its defect properties. A suitable functional was then used to investigate the structure and stability of the low index surfaces of $LaMnO_3$. The equilibrium crystal structure was calculated based on the formation energies of the low index surfaces, allowing determination of the surface terminations.

4.2 Methodology

Different approaches towards treating the exchange and correlation were employed in this work to investigate their suitability in describing the structural and electronic properties of $LaMnO_3$. GGA was used to treat the exchange and correlation using the PBE functional [153], and the PBEsol functional [154]. Mn(III) ions have a partially filled d shell which leads to SIE, due to the localised nature of the $3d$ states. There is also a significant contribution of Mn $3d$ and O $2p$ states to the valence band of $LaMnO_3$, so upon the generation of holes, standard DFT incorrectly predicts their delocalisation over all of the Mn and O atoms. A set of calculations was carried out with a + U correction applied to Mn $3d$ states, which can improve the description of the electronic properties of $LaMnO_3$, giving the correct splitting of the occupied Mn $3d$ states [96, 227, 229, 230]. A U value of 4.5 eV is applied to Mn $3d$ states in this work (referred to as U_1 in the results). A second set with both a U value of 4.5 eV applied

to Mn $3d$ states and a U value of 5.5 eV applied to O $2p$ states (referred to as U_2 in the results), which reduces SIE associated with O $2p$ states [159, 231, 232], and also reduces the overbinding of the O_2 molecule seen in LDA and GGA calculations [233–235]. The HSE06 [162, 163] functional was employed in a further set of calculations. The structure was relaxed using the quasi-Newton RMM-DIIS algorithm [186], with electronic and ionic convergence criteria of 10^{-6} eV and 0.005 eV/Å respectively.

Surface slabs were generated from the optimised bulk, with a 15 Å vacuum gap between surfaces. Convergence of surface energy with slab thickness was tested for the {010} surface and used to determine the required slab thickness for other surfaces. Surface energies were calculated using equation 3.11.

4.3 Structural properties of $LaMnO_3$

From convergence tests of the bulk structure, the $3 \times 3 \times 2$ k-point mesh was chosen for optimisation of bulk $LaMnO_3$, as it was found to give convergence of the energy to within 0.005 eV.

The data from the calculation of the structure of bulk $LaMnO_3$ is presented in table 4.1, along with data from experiment [216] and selected previous computational studies, using HSE and B3LYP [97, 100, 105]. Calculations carried out using PBE give good agreement with the structural properties of $LaMnO_3$, with the experimental volume reproduced within 2%, the Mn-O distances within 2.4% and the Mn-O-Mn bond angles within $\sim$1%. Two sets of PBE + U calculations were carried out, one with U applied to Mn $3d$ states only, one with U applied to both Mn $3d$ and O $2p$ states. For both sets of calculations, the volume is overestimated, by 4.4–4.8%. All 3 lattice vectors are overestimated, with the most significant overestimation in the b vector (2.5% for calculations with $U_{\mathrm{Mn}} = 4.5$ eV and 2.2% for calculations with $U_{\mathrm{Mn}} = 4.5$ eV and $U_{\mathrm{O}} = 5.5$ eV). A greater overestimation of the lattice vectors is observed in the calculations carried out with U applied only to the Mn $3d$ states. In both sets of data, the Mn-O distances are overestimated, with the calculations with U on Mn $3d$ states again showing a larger overestimation. The Mn-O2$_l$ distance shows the largest

overestimation, (2.6–2.8% for the calculations with U on Mn $3d$ states, and 2.2–2.5% for the calculations with U on Mn $3d$ and O $2p$ states.

Calculations carried out using PBEsol show a significant underestimation of the volume, the b lattice parameter, and Mn-O2$_l$, and overestimation of the short Mn-O2$_s$ distance, giving a value greater than that for the Mn-O1$_m$ distance. Calculations carried out using PBEsol + U, with U on Mn $3d$ states only, and with U on both Mn $3d$ and O$2p$ states give excellent agreement with the experimental structure. HSE06 calculations give very good agreement with the experimental volume, Mn-O1$_m$ and Mn-O2$_s$ distances and the Mn-O-Mn bond angles. However, as with the PBE + U calculations, the b vector and Mn-O2$_l$ distance show the greatest deviation from the experimental values.

From the analysis of the data fitted to the Murnaghan equation, it was evident that the Mn-O-Mn angles are sensitive to the volume of the cell. For each functional, an increase in the cell volume resulted in a decrease in the calculated angles, showing the importance of correctly modelling the volume. At the experimental volume, calculation of the distortion of the structure, as indicated by the octahedral rotation, gives good agreement with experimental values, with a deviation of 0.2–1% from the experimental value for θ_1 and deviation of 0.2–1.4% for θ_2. However, for the PBE and PBE + U calculations the calculated equilibrium volume is 1.7–4.8% greater than the experimentally determined volume, resulting in deviations of up to 2.1% from the Mn-O-Mn angles. The PBEsol calculation underestimates the volume by 3.7%, and although it gives good agreement with the θ_1 angle, with an overestimation of 0.9%, the θ_2 angle is overestimated by 3.6%. The PBEsol + U and HSE06 calculations give better agreement with the experimental volume, giving values within 1% of the experimental value for θ_1 and θ_2.

Previous theoretical work (presented in table 4.1) shows good agreement with the experimentally determined structural properties of $LaMnO_3$. The HSE-15 (HSE calculations with screening parameter = 0.15) calculations of He and Franchini [100] reproduce the lattice vectors, Mn-O distances and Mn-O-Mn angles to within 2% of the experimental

TABLE 4.1: Structural data for $LaMnO_3$, $3 \times 3 \times 2$ k-point mesh, experimental data from Ref. [216]. θ_1 is the Mn-O1-Mn angle and θ_2 is the Mn-O2-Mn angle. PBEsol is abbreviated to PS. Volumes are presented in $Å^3$, lattice vectors and bond lengths in Å, and angles in degrees. Previous computational studies from refs. [100][a] and [97, 105][b]. % differences between the experimental and calculated values of the structural parameters are given in parentheses

	Expt.	HSE[a]	B3LYP[b]	PBE	PBE+U_1	PBE+U_2	PS	PS+U_1	PS+U_2	HSE06
V	244.80	247.36	243.37	249.21	256.55	254.57	235.69	244.97	243.13	248.98
		(1.05)	(-0.59)	(1.80)	(4.80)	(3.99)	(-3.72)	(0.07)	(-0.68)	(1.71)
a	5.537	5.553	5.536	5.578	5.601	5.585	5.533	5.533	5.516	5.557
		(0.29)	(-0.02)	(0.74)	(1.16)	(0.87)	(-0.07)	(-0.07)	(-0.38)	(0.36)
b	5.747	5.820	5.730	5.774	5.890	5.874	5.580	5.755	5.745	5.857
		(1.27)	(-0.30)	(0.47)	(2.49)	(2.21)	(-2.91)	(0.14)	(-0.03)	(1.91)
c	7.693	7.653	7.672	7.737	7.777	7.760	7.635	7.693	7.673	7.650
		(-0.52)	(-0.27)	(0.57)	(1.09)	(0.87)	(-0.75)	(0.00)	(-0.26)	(-0.56)
Mn-O2$_l$	2.178	2.213	2.31	2.151	2.235	2.226	2.004	2.162	2.158	2.236
		(1.61)	(6.06)	(-1.24)	(2.62)	(2.20)	(-7.99)	(-0.73)	(-0.92)	(2.66)
Mn-O1$_m$	1.968	1.962	1.99	1.980	2.002	1.998	1.949	1.963	1.969	1.962
		(-0.30)	(1.12)	(0.61)	(1.73)	(1.52)	(-0.97)	(-0.25)	(0.05)	(-0.30)
Mn-O2$_s$	1.907	1.914	1.92	1.953	1.947	1.946	1.982	1.928	1.926	1.908
		(0.37)	(0.68)	(2.41)	(2.10)	(2.05)	(3.93)	(1.10)	(1.00)	(0.05)
θ_1	155.48	154.36	–	155.24	152.50	152.23	156.82	154.23	153.95	154.20
		(-0.72)		(-0.15)	(-1.92)	(-2.09)	(0.86)	(-0.80)	(-0.98)	(-0.82)
θ_2	155.11	154.17	–	155.93	152.68	152.44	160.64	154.74	154.34	153.79
		(-0.61)		(0.53)	(-1.57)	(-1.72)	(3.57)	(-0.24)	(-0.50)	(-0.85)

values, however the calculated electronic structure does not show the splitting of the Mn e_g peak from the conduction band. The B3LYP calculations of Ahmad *et al.* [97, 105] show very good agreement with experiment, with the exception of the Mn-O2$_l$ distance, which is overestimated by 6%, and the data for the Mn-O-Mn angles is not presented. Their study does not examine the electronic structure of $LaMnO_3$.

From the structural study of $LaMnO_3$, PBE, PBEsol + U_1, PBEsol + U_2 and HSE06 give good agreement with the experimental structure. In addition to calculating the structural properties of $LaMnO_3$, the electronic structure was examined to identify a suitable functional for use in this thesis.

4.4 Electronic and magnetic structure of $LaMnO_3$

The calculated EDOS for each of the functionals tested is shown in figure 4.2, and calculated band gaps are presented in table 4.2. $LaMnO_3$ has an O $2p$ dominated valence band, with Mn t_{2g} states at the bottom of the main O $2p$ region, and an unoccupied peak with Mn e_g character is seen between the top of the valence band and the bottom of the main unoccupied states [224]. PBE and PBEsol calculations are found to significantly underestimate the band gap of $LaMnO_3$, and fail to predict the separation of the Mn e_g peak from the main conduction band (figure 4.2 (a), (b)). Both PBE and PBEsol give incorrect splitting of the Mn d orbital, with the occupied t_{2g} peak above the main O $2p$ states in the valence band, as seen in figure 4.2 (a) and (b). Both sets of PBE + U calculations correctly predict $LaMnO_3$ to be semiconducting, and the expected features of the EDOS are well modelled (figure 4.2 (c)–(f)), showing the O $2p$ dominated valence band, with Mn $3d$ contribution, and the correct splitting of the Mn d orbital. The calculated direct band gaps lie within the experimentally reported range of 1.1–2.0 eV, given in table 4.2. The EDOS calculated using PBEsol + U calculations are also in good agreement with experiment. The calculated band gaps are lower than those predicted by PBE + U but are still in good agreement with the values given by experimental values. HSE calculations also produce the expected electronic structure of the valence band, though the empty Mn e_g peak below the main conduction band is shifted to higher energy, while the main CB is not shifted, resulting in an overestimation of the band gap, as shown in figure 4.2 (h). All calculations give good agreement with the reported experimental values of the Mn magnetic moment (3.4–3.9 μ_B/Mn) [221–223], with inclusion of U causing an increase in the magnetic moment, as shown in table 4.2.

Table 4.2: Calculated magnetic moment and band gaps for $LaMnO_3$. Experimental Mn magnetic moment from refs. [221–223], optical band gap from refs. [224, 236–238]. Previous HSE results[a] from ref. [100]

	Expt.	HSE[a]	PBE	PBE+U_1	PBE+U_2	PS	PS+U_1	PS+U_2	HSE06
m (μ_B/Mn)	3.42–3.87	3.67	3.5	3.9	3.9	3.4	3.9	3.9	3.8
Direct gap (eV)	1.1–1.9	1.63	0.51	1.437	1.43	0	1.36	1.37	1.91
Indirect gap (eV)			0.06	1.10	1.09	0	0.99	0.99	1.48

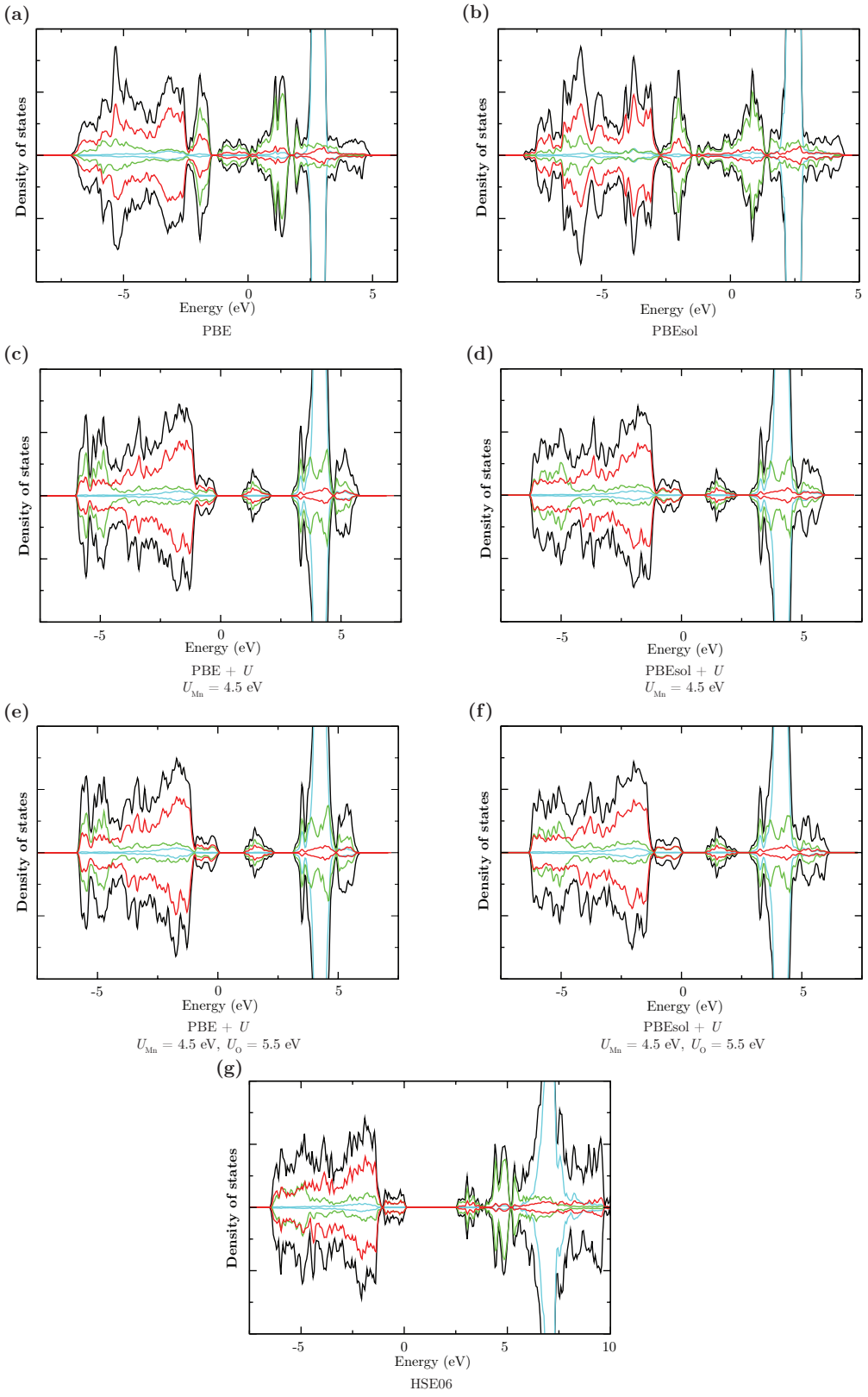

FIGURE 4.2: EDOS for $LaMnO_3$: (a) PBE, (b) PBEsol (c) PBE + U ($U_{\mathrm{Mn}} = 4.5$ eV), (d) PBEsol + U ($U_{\mathrm{Mn}} = 4.5$ eV), (e) PBE + U ($U_{\mathrm{Mn}} = 4.5$ eV, $U_{\mathrm{O}} = 5.5$ eV), (f) PBEsol + U ($U_{\mathrm{Mn}} = 4.5$ eV, $U_{\mathrm{O}} = 5.5$ eV) (g) HSE06. The top of the highest occupied band is aligned to 0 eV. Total DOS is shown in black, O p states in red, Mn d states in green and La f states in cyan

Calculations carried out using PBEsol + U with U on both Mn $3d$ and O $2p$ states give good agreement with both the structural and electronic properties, and the inclusion of + U corrections on Mn $3d$ and O $2p$ states gives the correct splitting of the d orbitals and band gaps in good agreement with experiment (figure 4.2(f)). Hence, the $LaMnO_3$ structure optimised using this functional is the most suitable for use in surface and defect studies. Recently, PBEsol + U (U = 4 eV) has been shown to give a good description of the structural properties of distorted $LaCoO_3$ [239].

4.4.1 PBEsol + U electronic structure

The calculated electronic EDOS is in good agreement with experiment and other recent computational studies on orthorhombic $LaMnO_3$ [98, 226]. O $2p$ states make up the valence band, with Mn $3d$ contribution at -5 eV and Mn $3d$ and O $2p$ at 0 eV, and an unoccupied Mn peak below the main unoccupied states. Mn d states are observed in the peak at approx. 1.5 eV, in agreement with photoemission studies, which also report the character of the band gap to be of p to d charge transfer type [237].

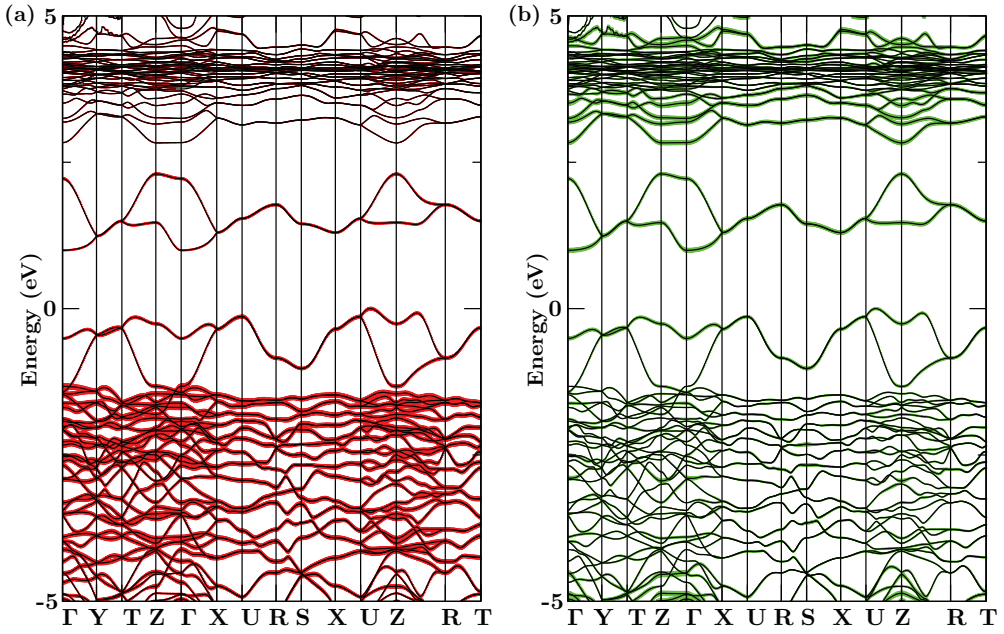

FIGURE 4.3: $LaMnO_3$ band structure (black) calculated using PBEsol + U (U_{Mn} = 4.5 eV, U_O = 5.5 eV). (a) shows the O $2p$ contribution (in red) to the bands and (b) shows the Mn $3d$ contribution (in green). The top of the highest occupied band is aligned to 0 eV

The calculated direct band gap of 1.37 eV is within the range of 1.2–2.0 eV reported by experiment [224, 236, 237, 240, 241] and the indirect gap was calculated to be 0.99 eV, with the VBM between U and Z, and the CBM at Γ. Weighting of the bands was carried out for Mn d contributions and O p contributions, which shows the predominantly O $2p$ character of the valence band, with Mn $3d$ contributions, and the Mn $3d$ character of the bands between the VBM and the main conduction band, as shown in figure 4.3.

4.5 Low index surfaces of $LaMnO_3$

The surface slabs generated for convergence testing using METADISE were a minimum of 10 Å thick to minimise interactions between the slab surfaces, and a vacuum gap of 15 Å was introduced to reduce interactions between the surface and its periodic image. A 3 × 2 × 1 k-point mesh was employed for the {010} surface, and slabs containing two, three and four unit cells (40, 60 and 80 atoms), and thickness 11.6, 17.4 and 23.2 Å were tested. The surface energy of the slab containing 2 unit cells was found to be converged to within 0.01 J/m^2. Based on this, slabs with a minimum thickness of 11 Å were constructed for the other surfaces. The {010}, {001} and {100} slabs contain 40 atoms with depths of 11.5, 15.4 and 11.0 Å, the {110}, {011}, and {101} slabs contain 60 atoms with depths of 11.9, 13.8 and 13.5 Å and the {111} slab contains 70 atoms, with a depth of 14.1 Å.

TABLE 4.3: Unrelaxed (γ_{un}) and relaxed (γ_s) surface energies, relaxation energy (ΔE), surface coordination and Mn-O bonds cleaved in the low index surfaces of $LaMnO_3$

	γ_{un}	γ_s	ΔE	Surface coordination				
Miller indices	(J/m^2)	(J/m^2)	(J/m^2)	La	Mn	O (La)	O (Mn)	Bond cleaved
{010}	1.48	0.97	0.51	9	5	1, 2	1, 2	Mn-O2$_l$
{100}	2.07	1.07	1.00	9	5	1, 2	1, 2	Mn-O2$_s$
{111}	2.09	1.27	0.82	6	4, 5	1, 2	1, 2	Mn-O1$_m$, Mn-O2$_s$, Mn-O2$_l$
{110}	2.14	1.31	0.83	6	5, 6	2	1, 2	Mn-O2$_l$
{101}	2.22	1.67	0.55	9	3	1, 2	1, 2	Mn-O1$_m$, Mn-O2$_s$, Mn-O2$_l$
{001}	2.54	1.72	0.82	5	5, 6	1	1, 2	Mn-O1$_m$
{011}	2.41	1.80	0.61	5	4, 5	1, 2	1	Mn-O1$_m$, Mn-O2$_l$, Mn-O2$_l$

Different k-point meshes were used for the surfaces, based on the surface lattice vectors, with a $3 \times 3 \times 1$ k-point mesh for the {001} surface, $3 \times 2 \times 1$ k-point mesh for the {100}, {011} and {101} surfaces, and a $2 \times 2 \times 1$ k-point mesh for the {110} surface. All possible terminations of the low index surfaces were investigated, and the most stable terminations are reported here. The unrelaxed and relaxed surface energies, relaxation energies, surface coordination and Mn-O bonds cleaved at the surface for each of the low index surfaces are given in table 4.3, in order of decreasing stability. The surface La-O and Mn-O coordination is similar at all surfaces. The relaxed surface structures are shown in figures 4.4–4.10, with the sites from which oxygen atoms may be removed to form oxygen vacancies identified and labelled in the figure with $O1/O2_{a/b}$.

4.5.1 The {010} surface

The {010} surface (figure 4.4), which has the lowest relaxation and surface energies, is terminated by 9-coordinate La ions, 5-coordinate Mn ions, and O1 and O2 ions (1- and 2-coordinate to both La and Mn ions). Surface relaxation results in relatively small deviation of the Mn-$O1_m$ bonds by -2.2 to 0.7% from the bulk, and -2.2 to 1.0% in Mn-O2 distances at the surface, due to movement of Mn ions by 0.11 Å towards the surface and O ions by 0.35 Å. Alternating increases of 0.1% and decreases of 0.03% in the Mn-O1-Mn angles along the surface indicate small rotations of the octahedra at the surface, giving rise to a low relaxation energy.

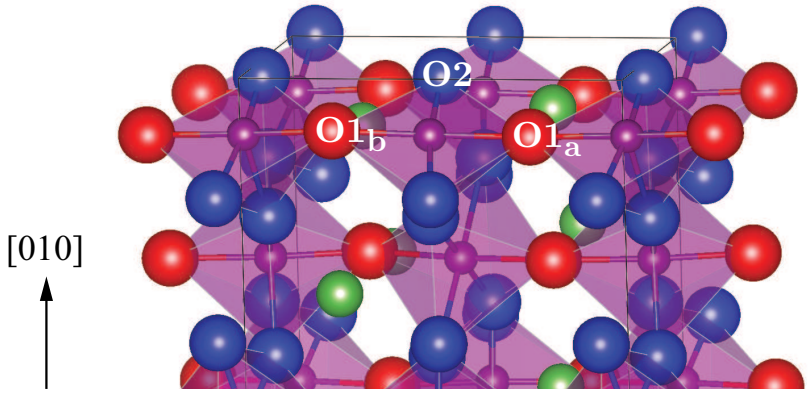

FIGURE 4.4: Relaxed surface slab {010} surface of $LaMnO_3$. O1 atoms are shown in red and O2 atoms are shown in blue. Oxygen vacancy sites are labelled with a, b

In the subsurface layer, variation in Mn-O1 and Mn-O2 distances is less than 1%, with movement of the Mn ions by 0.03 Å and O ions by 0.07 to 0.10 Å, and Mn-O-Mn bond angles vary by 0.1 to 2%.

4.5.2 The {100} surface

The {100} surface (figure 4.5) is also terminated by 9-coordinate La ions, 5-coordinate Mn ions and O1 and O2 ions (1- and 2-coordinate to both La and Mn ions), and has a similar surface energy to the {010} surface, 0.1 J/m^2 higher in energy. The {010} and {100} surfaces are identical in the cubic perovskite structure, but differ in the orthorhombic phase due to the Jahn-Teller and $GdFeO_3$-type distortions (figure 4.4 and 4.5). When generating the {100} surface, a Mn-$O2_s$ bond is cleaved, which requires more energy than cleaving a Mn-$O2_l$ bond for the {010} surface, resulting in a higher unrelaxed energy and greater potential for relaxation. Movement of the Mn ions by 0.11 Å away from the surface and of the O ions by 0.25 to 0.40 Å causes shortening of the Mn-$O1_m$ bonds by 1–3%, while Mn-O2 bonds relax significantly, deviating from the bulk, with decreases of up to 11% in the Mn-$O2_l$ bonds and increases of up to 11% in the Mn-$O2_s$ bonds. Significant changes in the octahedral rotation are also observed, with increases of 4 to 9% in θ_1.

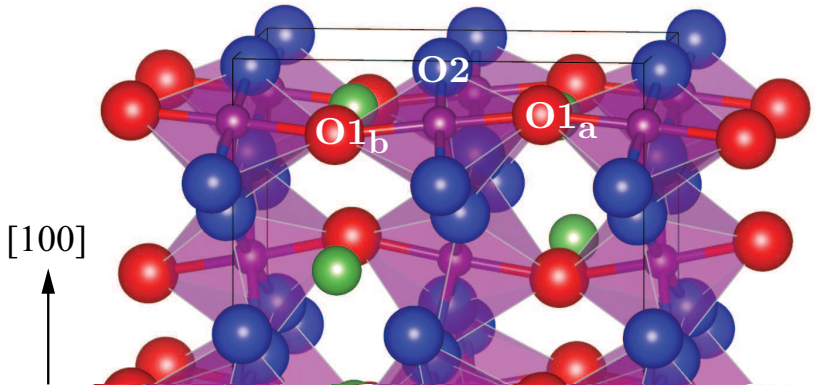

FIGURE 4.5: Relaxed surface slab {100} surface of $LaMnO_3$. O1 atoms are shown in red and O2 atoms are shown in blue. Oxygen vacancy sites are labelled with a, b

In the first subsurface layer, changes in octahedral rotation are much smaller, with decreases of 0.2–2% in θ_1 and 0.8% in θ_2 compared to the bulk, and decreases of 0.1–0.4% in the Mn-$O1_m$ distances are observed. As in the surface layer, there are significant

decreases in the Mn-$O2_l$ and increases in the Mn-$O2_s$ distances, due to movement of the O ions by 0.16 to 0.21 Å, giving deviations of up to 11% from the bulk. The difference in the bond cleaved, and the distortions and rotations give rise to its large unrelaxed surface energy and large relaxation energy, resulting in similar surface energies for the {010} and {100} surfaces.

4.5.3 The {111} surface

The {111} surface (figure 4.6) is terminated by 6-coordinate La ions, 4- 5- and 6-coordinate Mn ions, and O1 and O2 ions (1- and 2-coordinate to both La and Mn ions). Significant distortions are observed on relaxation of the slab, both at the surface and in the first subsurface layer, leading to a large relaxation energy. Around the 4-coordinate Mn, where a Mn-$O1_m$ and Mn-$O2_s$ bond have been cleaved, the remaining Mn-O1 distance increases by 2%, Mn-$O2_l$ distances decrease by up to 6% and Mn-$O2_s$ distances increase by up to 5% on relaxation due to significant movement of the O ions of 0.67 to 0.86 Å, and movement of the Mn ions by 0.29 Å away from the surface. Around the 5-coordinate Mn, where a Mn-$O2_l$ bond has been cleaved, the Mn-$O1_m$ distances decrease by 2–5%, Mn-$O2_l$ distances decrease by up to -4% and Mn-$O2_s$ increase by up to 5%, due to movement of O ions by 0.34 to 0.67 Å, and movement of the Mn ions by 0.29 Å away from the surface.

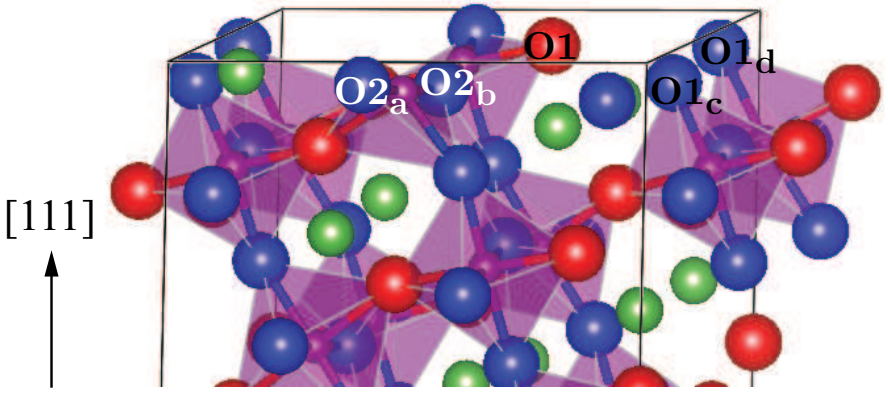

FIGURE 4.6: Relaxed surface slab {111} surface of $LaMnO_3$. O1 atoms are shown in red and O2 atoms are shown in blue. Oxygen vacancy sites are labelled with a, b, c, d

In the complete Mn-O_6 octahedra, alternating increases of 4% and decreases of 3% are observed in the Mn-$O1_m$ distances within a layer. The Mn-$O2_l$ distances are found to decrease by 1 to 4%. The θ_2 angles do not show a significant change, varying by up to 1%, but the θ_1 angles show an increase of 4 to 9% at the surface and the first subsurface layer. In this subsurface layer, the Mn-$O1_m$ distances show deviations from the bulk of -7 to 4%, the Mn-$O2_l$ distances show decreases of approximately 8%, and the Mn-$O2_s$ distances show increases of 5 to 8% compared to the bulk system.

4.5.4 The {110} surface

The {110} surface (figure 4.7) is terminated by 6-coordinate La ions, 5-coordinate Mn ions, where a Mn-$O2_l$ bond has been cleaved, and 6-coordinate Mn ions, O1 and O2 ions (2-coordinate to La ions and 1- and 2-coordinate to Mn ions). Relaxation of the surface causes a significant change to the Mn-O distances in the terminating layer, due to movement of O ions by 0.24 to 0.5 Å. Movement of the Mn ions by 0.22 Å away from the surface is observed in the 5-coordinate Mn-polyhedra, with increases of 2% to 5% in the Mn-$O1_m$ distances, along with an increase of approximately 1% in the Mn-$O2_s$ distances (to the 1-coordinate O atoms), and a 5% decrease in the Mn-$O2_l$ distance, resulting in a large relaxation energy. In the complete Mn-O_6 octahedra, movement of the Mn ions by 0.17 Å away from the surface, increases of 1% and decreases of 5% in the Mn-$O1_m$ distances within a layer are observed, along with decreases of up to 4% in Mn-$O2_l$ distances and increases of up to 2% in the Mn-$O2_s$ distances. A significant rotation of the polyhedra at the surface is observed, with increase and decrease of 5% and 18% respectively in the θ_1 angles, and a 12% increase in θ_2.

In the subsurface layer, increases and decreases of up to 1% are observed in all Mn-O distances. Changes in Mn-O-Mn angles are smaller than at the surface, with a 4% decrease in θ_1 and a 1% increase in θ_2. As with the {111} surface, the as-cleaved slab is unstable, resulting in significant relaxation of the Mn-O distances and Mn-O-Mn bond angles at the surface and in the subsurface layer, and leading to a large relaxation energy for the surface.

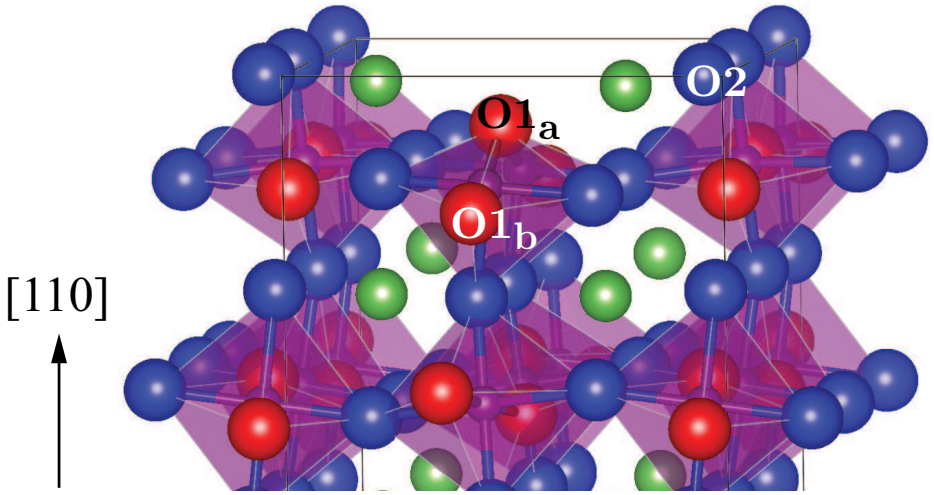

FIGURE 4.7: Relaxed surface slab {110} surface of $LaMnO_3$. O1 atoms are shown in red and O2 atoms are shown in blue. Oxygen vacancy sites are labelled with a, b

4.5.5 The {101} surface

The {101} surface (figure 4.8) is terminated by 9-coordinate La ions, 3-coordinate Mn ions, O1 and O2 ions (1- and 2-coordinate to both La and Mn ions). Surface relaxation results in a 2% decrease in the Mn-O1 distance in the truncated octahedra, which consist of a Mn ion coordinated to three O ions, by Mn-$O1_m$, Mn-$O2_l$ and Mn-$O2_s$ bonds, a 1% increase in the Mn-$O2_s$ distance and a significant decrease of approximately 11% of the Mn-$O2_l$ distance. The significant changes in the Mn-$O2_l$ are likely to be due to the low Mn coordination at the surface, and movement of surface Mn ions by 0.36 Å, and O ions by 0.16 to 0.39 Å. A decrease of 8% compared to the bulk is observed in the θ_1 angle at the surface, along with increases and decreases of 4% and 6% respectively in θ_2. In the subsurface layer, the Mn-$O1_m$ distances are found to change from that of the bulk by -2–4%, and the Mn-O2 distances both change by -4–4% due to movement of O ions by approximately 0.12 Å, θ_1 angles by -1–2% and θ_2 angles by -1–1%. Despite the significant distortions on optimisation the {101} surface has the second lowest relaxation energy, in contrast to other surfaces which had significant distortions and higher relaxation energies. The low Mn coordination at the surface leads to a less stable surface termination.

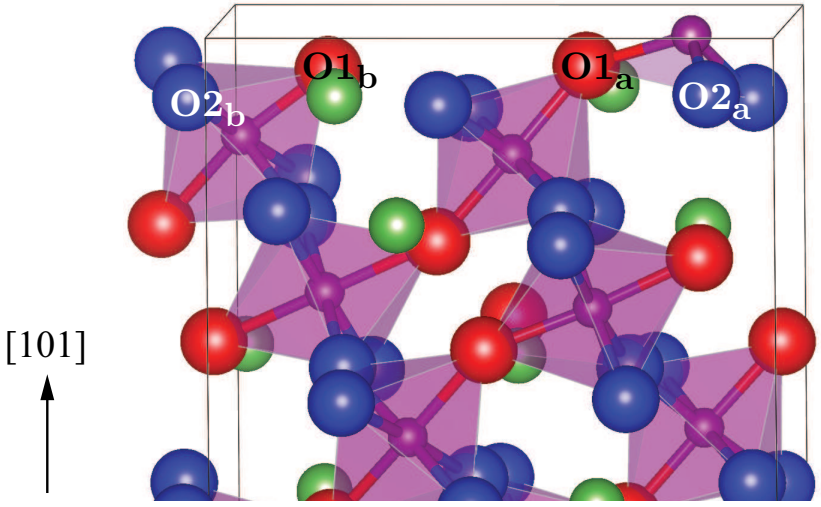

FIGURE 4.8: Relaxed surface slab {101} surface of $LaMnO_3$. O1 atoms are shown in red and O2 atoms are shown in blue. Oxygen vacancy sites are labelled with a, b

4.5.6 The {001} surface

The {001} surface (figure 4.9) is terminated by 5-coordinate La, 5- and 6-coordinate Mn ions, and O1 and O2 ions (2-coordinate to La ions and 1- and 2-coordinate to Mn ions). At the surface, the Mn-O1 distances are found to decrease by 6%, and increases of up to 9% are observed in the Mn-O2 distances, due to movement of 0.2 to 0.4 Å of the O ions and 0.1 Å of the Mn ions around both the 5- and 6-coordinate Mn-O polyhedra. Changes of ±2% in the θ_1 angle are observed at the surface, and θ_2 angles increase by 3–5%. In the subsurface layer, changes in Mn-O-Mn angles are considerably less than at the surface for both the θ_1 ($< 1\%$) and in θ_2 ($< \pm 2\%$). Mn-O1 distances show a 1–3% increase in the subsurface layer, and Mn-O2 distances show deviations of -1–1% compared to bulk values. The relaxation energy is the same as that for the {111} surface, which exhibits similar percentage changes in the Mn-O distances and Mn-O-Mn bond angles at the surface. The {001} surface has a similar termination to the {110} surface, differing in the bonds cleaved, with a Mn-$O2_l$ bond cleaved at the {110} surface, and a Mn-$O1_m$ bond cleaved at the {001} surface. The {001} surface has a shorter Mn-$O1_m$ bond cleaved, and lower La coordination, resulting in a higher surface energy, similar to that seen for the {010} and {100} surfaces. The surfaces have similar relaxation energies, with similar movement of O ions on relaxation, despite the difference in Mn-O bond broken at the surface.

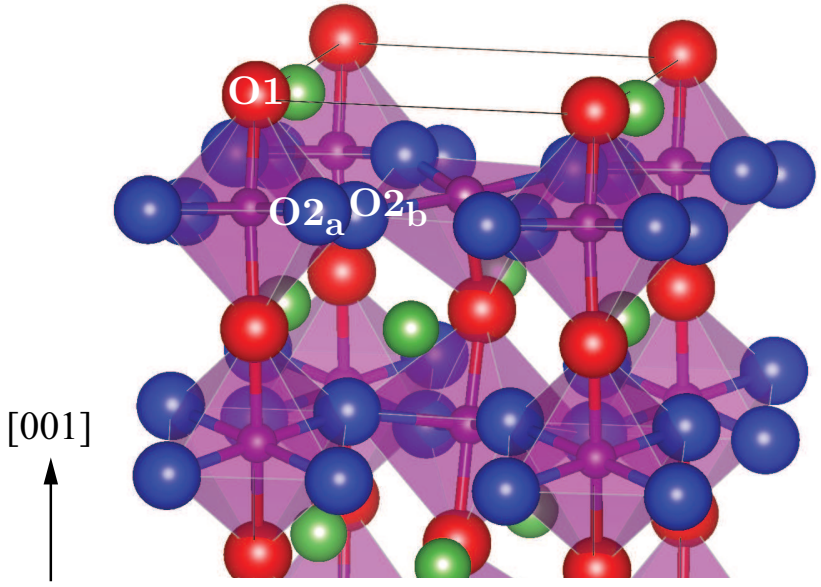

FIGURE 4.9: Relaxed surface slab {001} surface of $LaMnO_3$. O1 atoms are shown in red and O2 atoms are shown in blue. Oxygen vacancy sites are labelled with a, b

4.5.7 The {011} surface

The {011} surface (figure 4.10) is terminated by 5-coordinate La ions, 4- and 5- coordinate Mn ions and O1 and O2 ions (1- and 2-coordinate to La ions and 1-coordinate to Mn ions). Around the 4-coordinate Mn ions, where a Mn-O1 and Mn-$O2_l$ bond have been cleaved, the Mn-O1 distances are observed to increase by 1.6%, while the Mn-O2 distances decrease by approximately 1–2% on relaxation of the surface, as a result of movement of O ions by 0.2 Å and Mn ions by 0.18 Å. Around the 5-coordinate Mn ions, where a Mn-$O2_l$ bond has been cleaved, O ions are observed to move by 0.26 to 0.56 Å and Mn ions by 0.24 Å, the Mn-O1 distances show decreases of 2–3%, while the Mn-O2 distances are seen to decrease by 0.4–2.7%. Significant changes are observed in the Mn-O-Mn angles, with a 7% decrease in θ_1 and increase and decrease of 4% in the θ_2 angles within a layer.

In the subsurface layer, Mn-O-Mn angles deviate from the bulk by less than 1%, Mn-O1 distances show increases and decreases of up to 1%, Mn-$O2_s$ distances show decreases of up to 0.8% and increases up to 0.3%, and Mn-$O2_l$ distances show increases of 1–3% compared to the bulk values. The {011} surface has the same Mn coordination as the {111} surface, with 4- and 5-coordinate Mn. Similar to the {111} surface, a Mn-$O2_l$

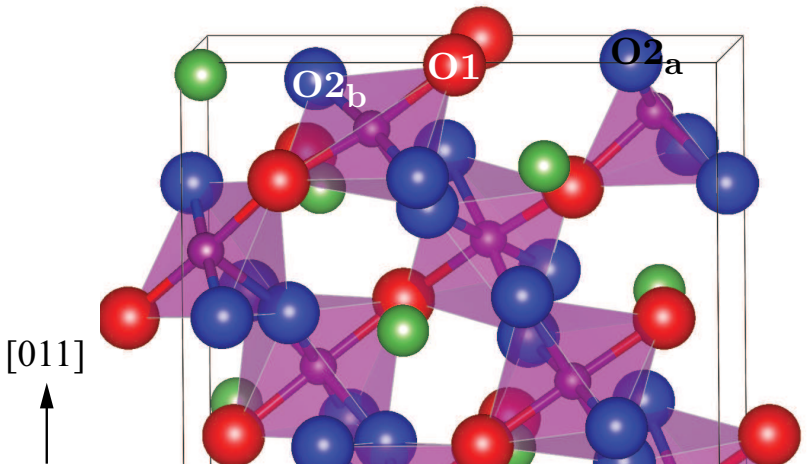

FIGURE 4.10: Relaxed surface slab {011} surface of $LaMnO_3$. O1 atoms are shown in red and O2 atoms are shown in blue. Oxygen vacancy sites are labelled with a, b

bond is cleaved around the 5-coordinate Mn. However, around the 4-coordinate Mn, a Mn-$O2_l$ and Mn-$O1_m$ bonds are cleaved, unlike the {111} surface, where Mn-$O2_s$ and Mn-$O1_m$ bonds are cleaved. The {011} surface shows less significant changes in the Mn-O distances and Mn-O-Mn angles than the {111} surface, accounting for the smaller change in energy on relaxation of the surface. It also has lower La coordination, with 5-coordinate La at the {011} surface and 6-coordinate La at the {111} surface. The lower La coordination results in the higher surface energy of the {011} surface compared to the {111} surface, as was seen for the {110} and {001} surfaces.

4.5.8 Summary

The order of surface energy is found to be $\{010\} < \{100\} < \{111\} \approx \{110\} < \{101\} \approx \{001\} < \{011\}$, with the Mn coordination, La coordination, and breaking of different Mn-O2 bonds affecting the surface stability. Surface stability is often linked to coordination, with low coordination representing less stable and reactive surfaces. Surfaces with higher La and Mn coordination were more stable, with high La coordination having a greater effect on the stability than high Mn coordination. This is seen in the {101} surface, which has the lowest Mn coordination, but has higher La coordination and is more stable than the {001} and {011} surfaces. Lower relaxation energies were observed when a Mn-$O2_l$ bond was broken compared to a Mn-$O2_s$ bond, as in the {010} and {100} surfaces. Breaking a Mn-$O2_l$ bond compared to a Mn-$O1_m$ bond, as

in the {110} and {001} surfaces, did not result in a large difference in the relaxation energy.

Ahmad *et al.* report the order of surface energy from B3LYP calculations to be {010} < {110} < {100} < {011} [105]. In agreement with our work, the {010} exhibits the lowest surface energy and relaxation energy, and the {011} exhibited the highest surface energy. In contrast to the results obtained here, they report the {100} to have a higher energy than the {110} surface. The long Mn-O bond in their bulk structure was reported to be significantly longer than was found in the current study and that found by experiment, indicating an excessive degree of Jahn-Teller distortion. This affects the structure of the system and the Mn-$O2_s$ bond length, and may have affected their order of surface energies.

A Wulff plot of the equilibrium crystal morphology was constructed using VESTA [242], based on the surface energies of the low index surfaces. In the Wulff construction, shown in figure 4.11, the {111} termination is dominant due to its orientation, contributing 49% of the surface area, with the {010} and {100} surfaces also contributing to a large percentage of the surface area, 23% and 18% respectively, the {001} surface contributes 9%, and the {110} contributes 1%. While the equilibrium morphology shows the surfaces that will be present in thermodynamic equilibrium, other surfaces may be able to be expressed by controlling crystal growth conditions. Hence we have examined all surfaces with respect to vacancy formation.

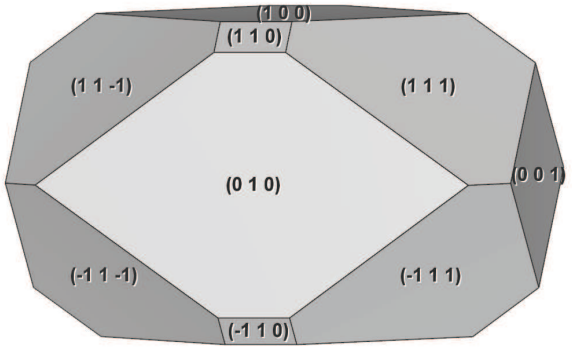

FIGURE 4.11: Wulff plot of the equilibrium crystal morphology based on surface energies of the low index surfaces of $LaMnO_3$

4.6 Conclusions

The structural and electronic properties of orthorhombic $LaMnO_3$ have been calculated using a range of functionals. The lattice parameters and distortions within the unit cell were found to be dependent on the cell volume, with both sets of PBEsol + U and HSE06 giving the closest agreement with experiment. Correction for the SIE was found to be necessary to correctly predict the electronic structure of $LaMnO_3$, with both PBE and PBEsol failing to give the correct splitting of the Mn $3d$ states, while PBE + U and PBEsol + U predict this splitting. HSE06 provides a good description of the valence band features, but fails to predict the separation of the unoccupied Mn e_g between the top of the valence band and the main unoccupied states. As it provides a good description of the distorted structure and electronic properties, with the correct splitting of the Mn e_g and t_{2g} states, PBEsol + U_2, with $U_{\mathrm{Mn_{3d}}} = 4.5$ eV, and $U_{\mathrm{O_{2p}}} = 5.5$ eV was found to be the most appropriate for calculation of the defect properties of orthorhombic $LaMnO_3$.

PBEsol + U ($U_{\mathrm{Mn}} = 4.5$ eV, $U_{\mathrm{O}} = 5.5$ eV) calculations give a good description of both the structural and electronic properties of bulk $LaMnO_3$, the optimised structure of which was used to generate slabs for surface studies. The surface energies, in increasing order, for the low index surfaces of $LaMnO_3$ were found to be $\{010\} < \{100\} < \{111\} \approx \{110\} < \{101\} \approx \{001\} < \{011\}$, with the most stable surfaces having both high La and Mn surface coordination. The equilibrium crystal morphology showed that the $\{111\}$ surface has the largest contribution to the overall surface area (49%), followed by the $\{010\}$ (23%) and $\{100\}$ (18%) surfaces. The $\{110\}$ and $\{001\}$ surfaces contribute less than 6% of the total surface area, and the $\{101\}$ and $\{011\}$ surfaces were not present in the equilibrium morphology.

Chapter 5

Defect properties of $LaMnO_3$

5.1 Introduction

$LaMnO_3$-based materials have attracted interest as they can undergo ionic substitution on both the La and Mn sites, accommodate oxygen non-stoichiometry, and exhibit both ionic and electronic conductivity when doped with alkaline earth metals. These materials can be used as catalysts for the removal of volatile organic compounds (VOCs), methane combustion and NO_x storage and reduction, and as the cathode in SOFCs [55, 79, 199–203, 211]. VOCs are a major contributor to air pollution and can cause human health issues. Noble metal catalysts show excellent performance for VOC oxidation but are limited in their industrial application due to the associated high costs and low poisoning resistance. A-site doped perovskite catalysts, such as Sr- or Ce-doped $LaMnO_3$ have shown good performance for the catalytic oxidation of VOCs [199, 202], and doping $LaMnO_3$ at the B-site with Mg^{2+} can improve the catalytic activity for methane combustion, for $x \leq 0.2$ [203].

The catalytic properties of La-based perovskites such as $LaMnO_3$, $LaCoO_3$ and $LaFeO_3$ can be tuned by substituting a fraction of the A-site cations with other cations, such as Ba, Ce or Sr [201]. This work reports that when doped with Sr, the Mn- and Co-based perovskite catalysts can exhibit NO oxidation activity similar to or higher than those of Pt-based catalysts. Sr-doped $LaMnO_3$ has been used for NO_x storage and reduction, where NO is oxidised to NO_2, then, during a fuel-rich period, hydrocarbons reduce it to N_2 [200]. In perovskites such as doped $LaMnO_3$, NO_x adsorption occurs at the A-site (La or Sr), and the B-site (Mn) exhibits high activity for NO oxidation to NO_2.

$LaMnO_3$-based perovskites are one of the most widely investigated cathode materials for high-temperature SOFCs due to their good electrical conductivity, good stability, reasonable catalytic activity for the oxygen reduction reaction (ORR) and relatively low cost [211]. Doped $LaMnO_3$ has also been suggested as a potential material for IT-SOFCs as it can exhibit mixed ionic and electronic conductivity, which increases the active area for the ORR at the cathode. The electrical conductivity of $LaMnO_3$ can be improved by doping with alkaline earth metals at the La site. The introduction of Sr causes oxidation of manganese ions, which can enhance the electrical conductivity and increase the catalytic activity of the Mn cations [200, 243]. Sr is a widely used dopant, due to a small mismatch between ionic radii of La and Sr in the 12-coordinate sites (r_{Sr} = 1.44 Å, r_{La} = 1.36 Å) [244]. A smaller size mismatch between lattice and dopant cations has been found to reduce cation segregation at the surface of perovskite oxides [245]. However, due to low oxygen ion conductivity in the intermediate temperature (IT) range, Sr-doped $LaMnO_3$ is limited in its application as a cathode under IT operating conditions [79].

Previous computational work has investigated the ORR using GGA-PW91 calculations, for high-temperature SOFC operating conditions, and a pathway for oxygen incorporation at the $LaMnO_3$ {001} surface was identified [246]. The reaction pathway was divided into several parts, with different combinations of the parts used to achieve the overall reaction. The chemisorption of oxygen on the defect-free $LaMnO_3$ surface, dissociation of O_2 into two O^- ions with and without interaction with a surface oxygen vacancy, and incorporation of the dissociated O into the oxygen vacancy were investigated as possible reaction steps. Direct chemisorption of O_2 into a surface oxygen vacancy followed by dissociation and incorporation into the $LaMnO_3$ lattice was also examined as an alternative mechanism. The most likely reaction pathway was found to be one involving chemisorption of O_2 on the $LaMnO_3$ surface, dissociation into two O^- ions, and encounter of O^- with an oxygen vacancy. A mechanism for oxygen adsorption and reduction on the {001} surface of ferromagnetic cubic $LaMnO_3$ was examined using NEB calculations to determine the minimum energy pathway and *ab initio* MD to simulate SOFC operating temperature [103].

The ionic conductivity of A-site doped $LaMnO_3$ may be improved by introducing dopants at the B-site, which may result in oxygen deficiency. Recent experimental work has shown that $La_{0.7}Sr_{0.3}Mn_{1-x}Mg_xO_3$ ($x = 0.1$, 0.2) exhibits increased oxygen vacancy concentration compared to $La_{0.7}Sr_{0.3}MnO_3$, which is also closely related to the oxygen reduction reactivity, thus improving the cathode performance [79]. Oxide ion conduction in $LaMnO_3$ occurs by diffusion of oxygen vacancies, with their concentration directly affecting the ionic conductivity. Oxygen migration in orthorhombic $LaMnO_3$ [247] and Sr-doped $LaMnO_3$ has previously been modelled using interatomic potentials, considering paths from O1–$O2_s$, O1–$O2_l$ and O2–O2, as illustrated in figure 5.1. In orthorhombic $LaMnO_3$ barriers of 0.30 eV for O1–$O2_s$, 0.51 eV for O1–$O2_l$ and 0.67 eV for O2–O2 are calculated, and a preferred migration pathway from O1–$O2_s$–O1–$O2_s$ [247]. In Sr-doped $LaMnO_3$ barriers of 0.70 eV and 0.67 eV were reported for $La_{0.8}Sr_{0.2}MnO_3$ and $La_{0.5}Sr_{0.5}MnO_3$ respectively, with good agreement with the experimentally determined value of 0.73 eV for $La_{0.8}Sr_{0.2}MnO_3$ [248, 249].

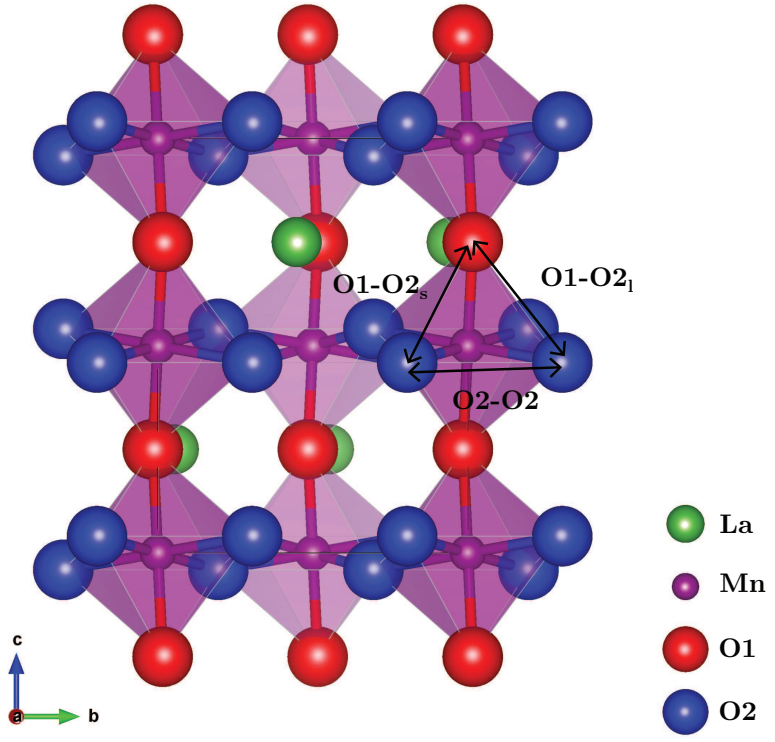

FIGURE 5.1: O1–$O2_s$, O1–$O2_l$ and O2–O2 oxygen migration paths in $LaMnO_3$

Previous computational studies on doped $LaMnO_3$ for SOFC cathodes have focused on

Sr doping of the cubic phase, with high dopant concentrations of 25-50%. Pavone *et al.* [250] investigated oxygen vacancy formation in cubic $La_{1-x}Sr_xMnO_{3-\delta}$ (x = 0, 0.25, 0.5) using PBE + U and HSE06 calculations in a 40-atom cell, and found that the Sr content strongly influences oxygen vacancy formation, with lower vacancy formation energies with higher Sr content. The stability of cubic $LaMnO_3$ and $La_{1-x}Sr_xMnO_3$ surfaces has been investigated, for $x = 0.125$ [104]. When undoped, the MnO_2-termination of the {001} surface of $LaMnO_3$ is the most stable. Doping with Sr makes the (La,Sr)O termination stable at room temperature, and the preferred termination at SOFC operating conditions. The segregation of O vacancies and Sr to the surface was predicted to occur, with segregation energies of $\sim$0.5 eV per defect. To our knowledge, a computational study of the site selectivity and charge compensation for defects at the La and Mn sites of orthorhombic $LaMnO_3$ has not been carried out previously.

In this chapter, the formation of oxygen vacancies in bulk $LaMnO_3$ and at its low index surfaces was investigated, as well as the temperature dependence of vacancy formation, within the operating temperature range of IT-SOFCs. The migration of oxygen vacancies in bulk between O1 and O2, and O2 and O2 sites in $LaMnO_3$ was examined using CI-NEB calculations. The site selectivity and charge compensation mechanisms for alkaline earth defects on the La and Mn sites in orthorhombic $LaMnO_3$ was determined. The individual defects were placed in the bulk at both sites and the charge compensation mechanism was investigated by considering both Mn hole and oxygen vacancy formation.

5.2 Methodology

Oxygen vacancy formation was investigated for the bulk and surfaces, by introducing an oxygen vacancy to a supercell of the previously optimised bulk and surface structures. For the bulk, a 3 × 3 × 2 supercell was generated from the optimised bulk to limit vacancy-vacancy interactions, generating a 360 atom system. The expansion was chosen to ensure a minimum of 15 Å between oxygen vacancies. For the surfaces, supercells were generated using the optimised surface structures, with the sizes of the supercells chosen to limit vacancy-vacancy interactions. The systems were generated using a 3 × 2

expansion of the slab for the {010}, {100}, {011} and {101} surfaces, a 3 × 3 expansion for the {001} surface, and 2 × 2 expansion for the {110} and {111} surfaces, to give a minium vacancy-vacancy separation of 15 Å. This results in systems containing 240 atoms for the {010}, {100}, and {110} surfaces, 280 atoms for the {111} surface, and systems containing 360 atoms for the {001}, {011} and {101} surfaces. For supercell calculations, a 1 × 1 × 1 Monkhorst-Pack k-point mesh was used. Oxygen vacancies were introduced on both sides of the surface slab to ensure no net dipole across the slab. The structure was relaxed using the quasi-Newton RMM-DIIS algorithm [186], with electronic and ionic convergence criteria of 10^{-6} eV and 0.005 eV/Å respectively.

The effect of varying the oxygen partial pressure experimentally can be modelled by varying the chemical potentials $\Delta\mu_i$. Elemental chemical potentials were calculated relative to the competing phases, La_2O_3, MnO, MnO_2, Mn_2O_3 and Mn_3O_4, using CPLAP [191], as outlined in section 3.3.3. The chemical potentials of the alkaline earth dopants are determined from the formation energies of their binary oxides.

One set of defect calculations was carried out by placing a single charged defect in the supercell, with a uniform background charge assumed to maintain overall charge neutrality. The formation energies of the charged defects were combined to form charge neutral defect energies (referred to in results as combined isolated defects). In addition, neutral defect clusters were considered by combining the alkaline earth dopant and charge compensating defects in the same supercell. The binding energies of the defects were obtained from the difference in energy between the clusters and isolated defects. The formation energies of the defects were calculated using

$$E_f(D) = E_{tot}(D) - E_{tot}(\mathrm{LaMnO_3}) + \sum_i n_i(E_i + \Delta\mu_i) \tag{5.1}$$

where $E_{tot}(D)$ is the energy of the defective supercell, $E_{tot}(\mathrm{LaMnO_3})$ is the energy of the pure supercell, n is the number of atoms of type i added to ($+n$) or removed from ($-n$) an external reservoir, and $E_i + \Delta\mu_i$ is the chemical potential of species i.

The site selectivity of the alkaline earth dopants was investigated by calculating the defect formation energy of placing a Mg, Ca, Sr or Ba ion on both the La and Mn

site respectively. The charge compensation mechanism for these defects is investigated by considering both ionic (formation of an oxygen vacancy for every 2 alkaline earth defects) and electronic compensation (formation of a hole on a Mn ion for each alkaline earth defect).

The creation of an oxygen vacancy can be represented in Kröger-Vink notation as

$$\mathrm{O_O^x} \rightarrow V_\mathrm{O}^{\bullet\bullet} + 2\mathrm{e}' + \frac{1}{2}\mathrm{O_2} \tag{5.2}$$

For an oxygen vacancy, $n_\mathrm{O} = +1$, and n_La and $n_\mathrm{Mn} = 0$, so equation 5.1 becomes

$$E_f(D) = E_{tot}(D) - E_{tot}(\mathrm{LaMnO_3}) + \frac{1}{2}E_{\mathrm{O_2}} + \Delta\mu_\mathrm{O} \tag{5.3}$$

The expression for oxygen vacancy formation is modified for the surfaces, to take account for the slabs having oxygen vacancies introduced on both sides.

$$E_f(\mathrm{O}_{vac}) = \frac{1}{2}[E_{tot}(D) - E_{tot}(\mathrm{LaMnO_3}(surf)) + E_{\mathrm{O_2}} + 2\Delta\mu_\mathrm{O}] \tag{5.4}$$

where $\mathrm{E}_{tot}(D)$ is the energy of the optimised surface slab and $E_{tot}(\mathrm{LaMnO_3}(surf))$ is the energy of the reduced slab.

The defect reaction for doping an alkaline earth metal (denoted as M_E^X, where E denotes an external cation) on either the La or Mn site (denoted as L), compensated by oxygen vacancy formation is given by

$$2L_L^\mathrm{X} + 2\mathrm{M}_E^\mathrm{X} + \mathrm{O_O^X} \xrightarrow{\mathrm{LaMnO_3}} 2L_E^\mathrm{X} + 2\mathrm{M}_L' + V_\mathrm{O}^{\bullet\bullet} + \frac{1}{2}\mathrm{O_2} \tag{5.5}$$

For ionic compensation, two L ions are removed from the system and replaced with alkaline earth defects ($n_L = +2$, n_M = -2), and an oxygen ion is removed to create a

vacancy ($n_{\mathrm{O}} = +1$), so equation 5.1 becomes

$$E_f(D) = E_{tot}(D) - E_{tot}(\mathrm{LaMnO_3}) + 2(E_L + \Delta\mu_L) - 2(E_M + \Delta\mu_M) + \frac{1}{2}E_{\mathrm{O_2}} + \Delta\mu_{\mathrm{O}} \tag{5.6}$$

Oxidation of a Mn ion is given in Kröger-Vink notation by

$$\mathrm{Mn}^{\mathrm{x}}_{\mathrm{Mn}} + \mathrm{h}^{\bullet} \rightarrow \mathrm{Mn}^{\bullet}_{\mathrm{Mn}} \tag{5.7}$$

In this case, no ions have been added to or removed from the system, so n_{La}, n_{Mn} and $n_{\mathrm{O}} = 0$, hence equation 5.1 becomes

$$E_f(D) = E_{tot}(D) - E_{tot}(\mathrm{LaMnO_3}) \tag{5.8}$$

For electronic compensation, the defect reaction is

$$L^{\mathrm{X}}_L + \mathrm{M}^{\mathrm{X}}_E + \mathrm{Mn}^{\mathrm{X}}_{\mathrm{Mn}} \xrightarrow{\mathrm{LaMnO_3}} L^{\mathrm{X}}_E + \mathrm{M}'_L + \mathrm{Mn}^{\bullet}_{\mathrm{Mn}} \tag{5.9}$$

with one L ion removed from the system ($n_L = +1$), and one akaline earth defect added (n_M = -1), equation 5.1 becomes

$$E_f(D) = E_{tot}(D) - E_{tot}(\mathrm{LaMnO_3}) + (E_L + \Delta\mu_L) - (E_M + \Delta\mu_M) \tag{5.10}$$

Oxygen vacancy migration in $LaMnO_3$ was investigated using CI-NEB calculations, considering O1-O2 and O2-O2 paths. The structures were relaxed using the L-BFGS method, with ionic and electronic convergence criteria of 0.05 eV/Å and 10^{-6} respectively.

5.3 Oxygen vacancy formation

5.3.1 Oxygen chemical potential and partial pressure

The chemical potential limits for determining the oxygen vacancy formation energies were calculated using CPLAP [191], using the formation energies of the competing phases to determine the chemical potential limits presented in table 5.1, in addition to the magnetic ordering of Mn-containing phases (where AFM is antiferromagnetic, FM is ferromagnetic and FiM is ferrimagnetic). The shaded area of figure 5.2 shows the region of stability for $LaMnO_3$ spanned by the La chemical potential ($\Delta\mu_{La}$) and Mn chemical potential ($\Delta\mu_{Mn}$), and the lines show the limits set by $LaMnO_3$ and its competing phases. The La, Mn and O chemical potentials at the limits A–E, determined from the foramtion energies at 0 K, and the relevant competing phases at each point are given in table 5.2. Oxygen vacancy formation was examined at the oxygen-rich ($\Delta\mu_O$ = 0 eV) and oxygen-poor ($\Delta\mu_O$ = -2.13 eV) limits.

TABLE 5.1: Formation energies and magnetic ordering of $LaMnO_3$ and its competing phases

Phase	Formation energy (eV)	Magnetic ordering
$LaMnO_3$	-12.82	A-AFM
La_2O_3	-16.08	
MnO	-3.71	AFM
MnO_2	-4.05	AFM
Mn_2O_3	-8.50	FM
Mn_3O_4	-12.49	FiM

In addition to studying the chemical potential limits, we are also interested in the properties under standard SOFC operating conditions. The oxygen chemical potentials relevant to the operation of intermediate temperature SOFCs have been calculated, in order to determine the oxygen vacancy formation energies under these conditions. Under standard SOFC operating conditions, the oxygen partial pressure at the cathode

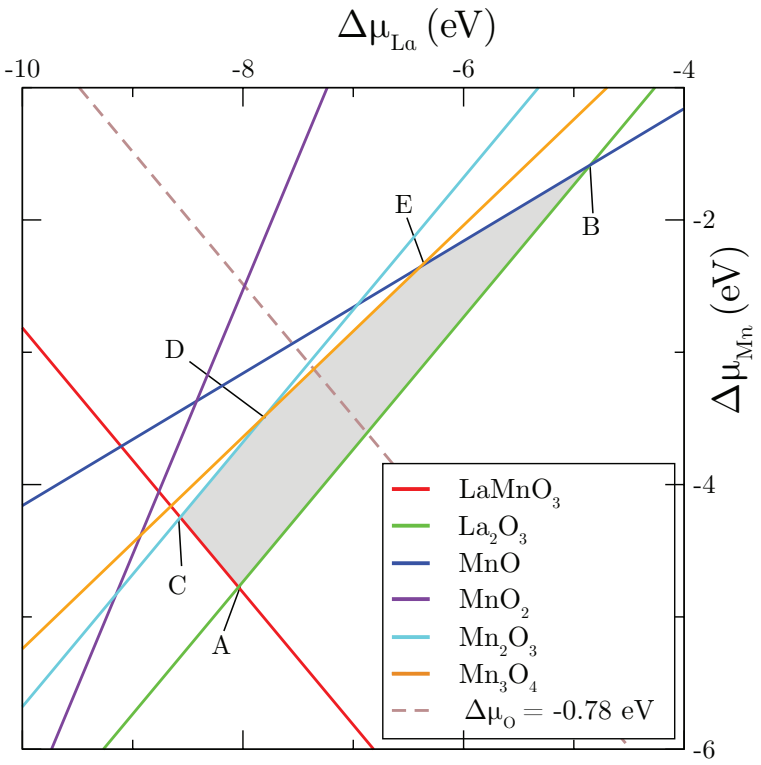

FIGURE 5.2: Plot showing region of stability (grey) for $LaMnO_3$ spanned by $\Delta\mu_{La}$ and $\Delta\mu_{Mn}$, showing oxygen-poor ($\Delta\mu_O$ = -2.13 eV) and oxygen-rich ($\Delta\mu_O$ = 0.00 eV) limits. The solid coloured lines show the limits determined by $LaMnO_3$ and its competing phases, limits A–E show the intersection points of the region of stability determined by these limits. The dashed brown line shows the oxygen chemical potential for p_{O_2} = 0.21 atm, T = 700 K

TABLE 5.2: Chemical potential limits, in eV, for $LaMnO_3$, with the phases present at each limit

	$\Delta\mu_{La}$	$\Delta\mu_{Mn}$	$\Delta\mu_O$	Phases
Limit A	-8.57	-4.25	0.00	Mn_2O_3, $LaMnO_3$
Limit B	-4.85	-1.58	-2.13	La_2O_3, MnO
Limit C	-8.04	-4.78	0.00	La_2O_3, $LaMnO_3$
Limit D	-7.81	-3.49	-0.51	Mn_2O_3, Mn_3O_4
Limit E	-6.39	-2.36	-1.36	MnO, Mn_3O_4

is normally 0.21 atm, and the oxygen chemical potential is determined for the temperature range 600–1000K (800–1000 K is outside the orthorhombic stability field) (table 5.3). The calculated chemical potentials are used to calculate the oxygen vacancy formation energy in the bulk and at the surfaces, with 700 K chosen for surface studies as

it is at the low end of the IT range and within the orthorhombic stability field.

TABLE 5.3: Oxygen chemical potential and temperature relationship for $p_{O_2} = 0.21$ atm, $p^\circ = 1$ atm

T (K)	600	700	800	900	1000
$\Delta\mu_O$ (eV)	-0.66	-0.78	-0.90	-1.03	-1.12

5.3.2 Bulk $LaMnO_3$

Oxygen vacancy formation energies at chemical potentials corresponding to the range of operating temperatures are presented in table 5.4. Oxygen vacancy formation at the O1 site (O1 sites shown in red in figure 5.1) in bulk $LaMnO_3$ has an energy of 3.61 eV at the oxygen-rich limit, and 1.48 eV at the oxygen-poor limit. In the temperature range from 600–800 K oxygen vacancy formation energy decreases from 2.96 eV to 2.71 eV with increasing temperature (table 5.4). On introduction of a vacancy at the O1 site in bulk $LaMnO_3$, the La and Mn ions around the vacancy are displaced away from the vacancy, while surrounding O ions are displaced towards the vacancy. This causes an increase of 0.1 to 3% in the Mn-$O1_m$ distances surrounding the vacancy, a decrease of 3 to 4% in the Mn-$O2_l$ distances, and a 1–2% increase in the Mn-$O2_s$ distances neighbouring the vacancy due to tilting of the octahedra. Alternating increases of 0.6–1% and decreases of 0.5 to 2%, in θ_1 surrounding the vacancy are observed, as well as increases of 1 to 3% and decreases of 0.8 to 3% in θ_2 angles surrounding the oxygen vacancy.

At the O2 site (O2 sites shown in blue in figure 5.1), oxygen vacancy formation is 0.28 eV higher than at the O1 site, with an energy of 3.89 eV at the oxygen-rich limit and 1.76 eV at the oxygen-poor limit. In the temperature range 600–800 K, the O2 vacancy energy is high (table 5.4). As with the O1 vacancy, the introduction of an oxygen vacancy causes La and Mn ions surrounding the vacancy to be displaced outwards from the vacancy, while neighbouring O ions move towards the vacancy. Alternating increases of 1–2%, and decreases of 2 to 4%, in the Mn-$O1_m$ distances surrounding the oxygen vacancy are observed, along with increase of 0.5% and decrease of 1 to 2% in the Mn-$O2_l$ distances, and increases of 1 to 2% and decreases of less than 0.5% in the

Mn-$O2_s$ distances neighbouring the vacancy. Surrounding the vacancy, at increasing distance from the vacancy site, alternating increases of 1 to 2%, and decreases of 3 to 8% in θ_1, and increases of 3%, and decreases of 1 to 2% in θ_2 are observed. The higher vacancy formation energy than at the O1 site is likely to be due to the greater degree of distortion around the vacancy. For both O1 and O2 vacancies in bulk $LaMnO_3$ the excess electrons are localised on Mn ions of opposite spin neighbouring the O vacancy.

The oxygen vacancy formation energies calculated here are significantly lower than that reported previously for bulk orthorhombic $LaMnO_3$. Kotomin *et al.* report vacancy formation of 7.64 eV for an oxygen vacancy in bulk $LaMnO_3$, but do not report different formation energies for the inequivalent oxygen sites [101]. The supercell size, and thus oxygen vacancy concentration, is not reported and so it is difficult to compare to our study in which a large supercell is used here to minimise interactions between defects and their periodic images.

TABLE 5.4: Oxygen vacancy formation energies for bulk $LaMnO_3$ under the IT-SOFC operating temperature range, 600–800 K, $p_{O_2} = 0.21$ atm, $p^\circ = 1$ atm

		O1	O2
T (K)	$\Delta\mu_O$ (eV)	E_{Ovac} (eV)	E_{Ovac} (eV)
600	-0.65	2.96	3.23
700	-0.78	2.83	3.11
800	-0.90	2.71	2.98

5.3.3 Low index surfaces of $LaMnO_3$

The vacancy formation energies at the low index surfaces of $LaMnO_3$, across the calculated oxygen chemical potential range, are presented in table 5.5, and figures 4.4–4.10 shows the labelling of the oxygen vacancy sites. Of the surfaces seen in the equilibrium crystal structure, vacancies at the O1 site at the {111} surface, and the $O1_a$ site (shown in figures 4.6 4.5) at the {100} surface exhibit the lowest formation energies (1.82 eV and 1.95 eV respectively). With the exception of the {100} $O1_a$ vacancy, at the {010} and {100} surfaces, oxygen vacancy formation energies are greater than 2 eV. The {110} surface, which contributes less than 2% to the overall crystal surface

TABLE 5.5: Oxygen vacancy formation energies for the low index surfaces of $LaMnO_3$, at the chemical potential limits for $LaMnO_3$ ($\Delta\mu_O$ = 0.00, -2.13 eV), and under the IT-SOFC operating temperature range at 700 K ($\Delta\mu_O$ = -0.78 eV)

		E_{Ovac} at $\Delta\mu_O = x$ (eV)		
Surface	Site	$x =$ 0.00	-0.78	-2.13
{010}	$O1_a$	3.30	2.52	1.17
	$O1_b$	3.32	2.54	1.19
	O2	2.91	2.13	0.78
{100}	$O1_a$	2.73	1.95	0.60
	$O1_b$	3.62	2.84	1.49
	O2	2.99	2.22	0.86
{111}	O1	2.60	1.82	0.47
	$O2_a$	2.98	2.20	0.85
	$O2_b$	3.42	2.65	1.30
	$O2_c$	3.04	2.27	0.91
	$O2_d$	3.12	2.34	0.99
{110}	$O1_a$	3.76	2.98	1.63
	$O1_b$	3.79	3.01	1.66
	O2	3.39	2.61	1.26
{101}	$O1_a$	2.74	1.96	0.61
	$O1_b$	0.65	-0.13	-1.48
	$O2_a$	3.65	2.88	1.53
	$O2_b$	0.65	-0.14	-1.49
{001}	O1	0.90	0.13	-1.22
	$O2_a$	2.52	1.74	0.39
	$O2_b$	2.45	1.68	0.33
{011}	O1	0.90	0.12	-1.23
	$O2_a$	3.22	2.44	1.09
	$O2_b$	2.22	1.44	0.09

area, exhibits some of the highest vacancy formation energies, along with the {100} $O1_b$ site, and {111} $O2_b$ site. At the least stable surfaces, (the {101}, {001} and {011} surfaces), the {101} $O1_b$, $O2_b$, {011} O1 and {001} O1 vacancies exhibit formation energies of less than 1 eV, with negative formation energies at higher temperatures or at

the oxygen-poor limit. At 700 K, an oxygen chemical potential of -2.13 eV corresponds to an extremely low oxygen partial pressure of 7.3×10^{-21} atm. However the {101} and {011} surfaces are not seen in the equilibrium crystal morphology, and the {001} surface only contributes to a small percentage of the total surface area. Experimentally, morphology control could be used to obtain these surfaces and improve surface vacancy formation. At the {010}, {100} and {110} surfaces, the excess electrons are localised on Mn ions of opposite spin neighbouring the O vacancy, and at the {011} surface the electrons are delocalised over the Mn ions neighbouring the vacancy. At the {111}, {101} and {001} surfaces, the electrons are delocalised over Mn ions with the same spin neighbouring the vacancy.

Although there are sites at these surfaces for which the oxygen vacancy formation is low, large variations in the formation energy are seen, with differences of 3.02 eV, 2.32 eV and 1.62 eV between the highest and lowest vacancy formation energies at the {101}, {011} and {001} surfaces respectively. This variation may lead to segregation to the surface by the vacancies, which will have a negative impact on the oxygen diffusion. In order for $LaMnO_3$ to be a potential cathode material for SOFC operation at intermediate temperature, doping will be required to attempt to lower the oxygen vacancy formation energies in bulk $LaMnO_3$ and at other surfaces found in the equilibrium crystal morphology.

Previous computational studies on the {001} surface reported a range of oxygen vacancy formation energies. As in this work, Kotomin *et al.* find the oxygen vacancy formation energy at the {001} surface to be significantly lower than in the bulk, though as with the bulk defect formation, the formation energy at the surface is significantly higher than that found here [101]. In contrast to what is found here, Mastrikov *et al.* report formation energies the O1 vacancy to have a higher formation than the O2 vacancy at the {001} surface (5.5 and 3.3 eV respectively) [246]. The surface slab used in their work is reported to be a $2\sqrt{2} \times 2\sqrt{2}$ expansion of a 16 Å^2 surface unit cell (total surface area 128 Å^2), which is significantly smaller than the 3×3 expansion of a 32 Å^2 (total surface area approx. 288 Å^2) surface unit cell used in this work. The surface supercell

used in these previous calculations is smaller than that used in our calculations, which is likely to have an impact on the vacancy formation energies.

5.4 Oxygen vacancy migration in bulk $LaMnO_3$

In $LaMnO_3$, oxygen diffusion occurs via oxygen vacancies along the edge of the MnO_6 octahedra. Due to the distortion of the MnO_6 octahedra and resultant inequivalent oxygen sites and O1–O2 distances, three oxygen migration pathways are investigated. Two paths are considered between an O1 to an O2 site, one to an O2 coordinated to the central Mn ion by a long Mn-$O2_l$ bond (O1-$O2_l$), and the second to an O2 coordinated to the central Mn ion by a short Mn-$O2_s$ bond (O1-$O2_s$). The third path considered is between two O2 sites. The energy barriers to the migration of an oxygen vacancy in $LaMnO_3$ were calculated using NEB calculations. The paths along which the oxygen ions migrate are shown in figure 5.3, and the energy profiles are shown in 5.4. The O1-O2 paths are similar (figures 5.3 and 5.4 (a)), differing Mn-O2 distance and O2 site at the endpoint, and in barrier energy. The O2-O2 path is shown in figure 5.3 (b), with the energy profile in figure 5.4 (b).

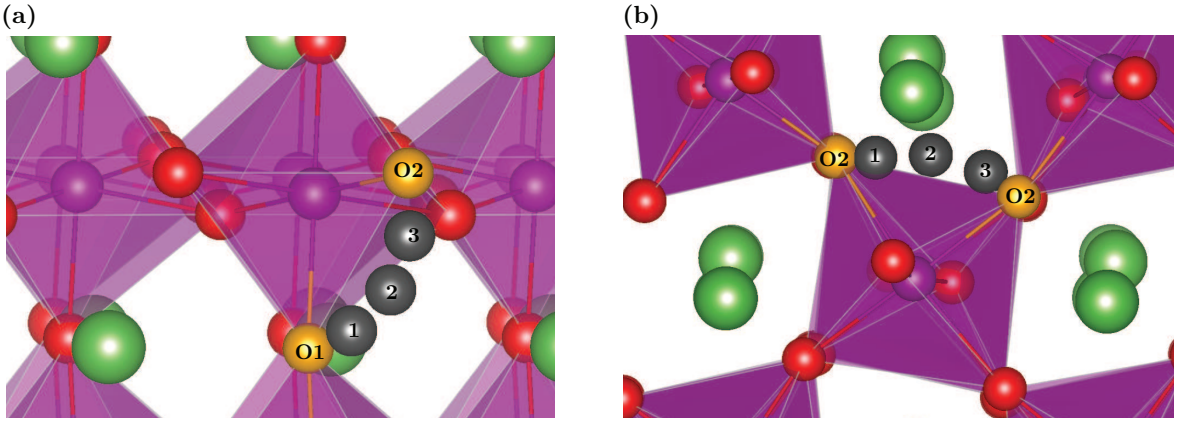

FIGURE 5.3: Oyxgen vacancy migration pathways in orthorhombic $LaMnO_3$ for (a) an O1 site to an O2 site and (b) for an O2 site to an O2 site

The barrier energy for migration from an O1 site to an $O2_s$ site is 0.98 eV and the barrier for the reverse is 0.71 eV. The barrier energy for migration from an O1 site to an $O2_l$ site is lower, with a barrier of 0.82 eV and the barrier for the reverse is 0.56 eV.

For the migration between O2 sites, the energy barrier is 0.21 eV higher than for an $O2_l$ site to an O1 site, at 0.77 eV. The results of the elastic band calculations indicate that the preferred oxygen migration pathway will be O1–$O2_l$–O1–$O2_l$ in $LaMnO_3$.

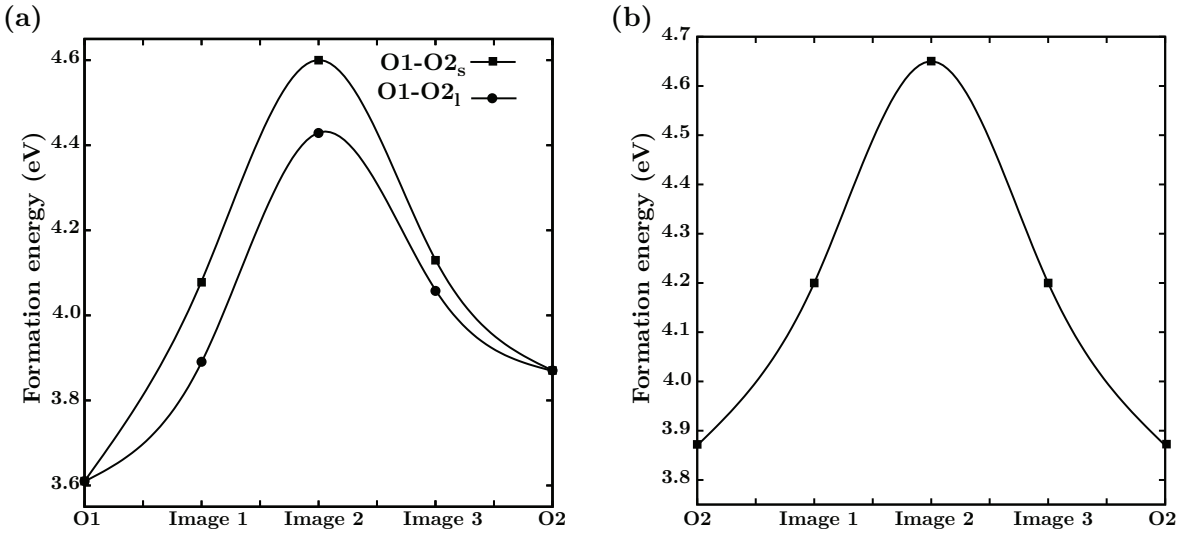

FIGURE 5.4: Energy profiles for oxygen migration in $LaMnO_3$ (a) O1-$O2_s$ (squares) and O1-$O2_l$ (circles) paths and (b) O2-O2 path

5.5 Alkaline earth defect formation in $LaMnO_3$

A range of alkaline earth defects in $LaMnO_3$ has been considered, examining the effect of placing the defect on both the La and Mn site. The charge compensation mechanism for the defects was investigated by considering both ionic (formation of an oxygen vacancy for two alkaline earth defects) and electronic (formation of a hole on a Mn ion) compensation. We have introduced a number of isolated defects into the supercell, in formal charge states -1 for alkaline earth defects, +1 for a Mn hole, and +2 for oxygen defects. Charged defects were combined to form charge-neutral defects, with their formation energies calculated from those of the individual charged defects. In addition, neutral defect clusters were considered by combining alkaline earth dopant and charge compensating defect in the same supercell, so that the binding energy could be obtained from the difference in energy. The chemical potentials at the oxygen-rich, oxygen-poor and for SOFC operating conditions are presented in table 5.6. For alkaline earth defect formation, SOFC operating conditions of 700 K, with $p_{O_2} = 0.21$ atm are

chosen, with an oxygen chemical potential of -0.78 eV, which gives La_2O_3 and Mn_3O_4 limits. The chemical potentials at these limits are presented in table 5.6.

TABLE 5.6: Chemical potential of La, Mn, O, and the alkaline earth dopants for the given oxygen chemical potentials, in eV

	$\Delta\mu_{La}$	$\Delta\mu_{Mn}$	$\Delta\mu_{O}$	$\Delta\mu_{Mg}$	$\Delta\mu_{Ca}$	$\Delta\mu_{Sr}$	$\Delta\mu_{Ba}$
Limit A (O-rich)	-8.57	-4.25	0.00	-5.70	-6.12	-5.62	-5.04
Limit B (O-poor)	-4.85	-1.58	-2.13	-3.57	-3.99	-3.49	-2.92
700 K (La_2O_3 limit)	-6.88	-3.61	-0.78	-4.93	-5.34	-4.84	-4.27
700 K (Mn_3O_4 limt)	-7.36	-3.13	-0.78	-4.93	-5.34	-4.84	-4.27

5.5.1 La site doping

5.5.1.1 Combined isolated defects

The defect formation energies for the combinations of isolated defects on the La site of $LaMnO_3$ are listed in table 5.7, with the defect combinations listed using Kröger-Vink notation. When the dopants and charge compensating O vacancy are isolated from each other, the vacancy is more likely to form at the O1 site than the O2 site, and defects are more stable at the Mn_3O_4 limit of the SOFC operating conditions. The formation energy of the combined $2M'_{La} + V_{O1}^{\bullet\bullet}$ defects is 0.23 eV lower than $2M'_{La} + V_{O2}^{\bullet\bullet}$, with formation energies of 5.74 (2.64, 1.62, 1.62) eV for $2Mg'_{La} + V_{O1}^{\bullet\bullet}$ (Ca, Sr, Ba) defects at the Mn_3O_4 limit at 700 K. Hole formation, however, is the more stable charge compensating mechanism under all conditions of chemical potential considered in this work. Across the chemical potential range, the $Mg'_{La} + Mn_{Mn}^{\bullet}$ defect is significantly higher in energy than all other defects, 1.5513 eV higher than $Ca'_{La} + Mn_{Mn}^{\bullet}$, the next highest energy defect. Under the SOFC operating conditions considered, hole-compensated Ca, Sr and Ba defects have low formation energies (-0.11–0.89 eV), with their formation energies 0.48 eV lower at the Mn_3O_4 limit (0.41, -0.10 and -0.11 eV for Ca, Sr and Ba respectively). The most stable combinations of isolated defects are Sr or Ba on the La site, compensated by hole formation on a Mn ion. Under the O-poor limit of the chemical potential, and the La_2O_3 limit at 700 K, there is little variation

TABLE 5.7: Formation energies of the combined isolated defects, in eV, of alkaline earth defects on the La site of $LaMnO_3$, with two alkaline earth defects compensated by an oxygen vacancy, or one defect compensated by hole formation on a Mn ion

Limit A (O-rich)	$2M'_{La} + V_{O1}^{\bullet\bullet}$	$2M'_{La} + V_{O2}^{\bullet\bullet}$	$M'_{La} + Mn_{Mn}^{\bullet}$
Mg	5.65	5.88	1.52
Ca	2.55	2.78	-0.03
Sr	1.53	1.76	-0.54
Ba	1.53	1.75	-0.54
Limit B (O-poor)			
Mg	6.71	6.93	3.12
Ca	3.60	3.83	1.56
Sr	2.59	2.81	1.05
Ba	2.58	2.81	1.05
700 K–La_2O_3			
Mg	6.71	6.93	2.44
Ca	3.60	3.83	0.89
Sr	2.59	2.81	0.38
Ba	2.58	2.81	0.38
700 K–Mn_3O_4			
Mg	5.74	5.97	1.96
Ca	2.64	2.87	0.41
Sr	1.62	1.85	-0.10
Ba	1.62	1.84	-0.11

in the formation energies of the oxygen-containing defects. This is due to the change in the La and O chemical potentials being balanced by the change in the chemical potential of the alkaline earth dopant (the sum of chemical potentials at the O-poor limit is ≈-4.85 eV, and at the La_2O_3 limit at 700 K it is ≈-4.86 eV).

5.5.1.2 Defect clusters

The defect formation energies for clustered defects, with an alkaline earth dopant on the La site, are listed in table 5.8. In undoped $LaMnO_3$, an O1 ion lies in the same plane as the 4 nearest La ions, which are at distances 2.41 Å, 2.53 Å, 3.16 Å and 3.30

Å, as shown in figure 5.5 (a). The nearest La ions to an O2 ion are 2.44 Å, 2.62 Å, 2.70 Å and 3.42 Å away, as shown in figure 5.5 (b). When the dopants are placed on the La site and compensated by a vacancy on an O1 or O2 site, the structure is distorted locally, with neighbouring O ions displaced towards the vacancy and the dopant ions are displaced outwards. The lowest formation energy is found for the system in which one of the dopants is 2.41 Å from the vacancy and the second dopant ion is 2.53 Å from the vacancy, for all defects, with the dopant ions shown in grey in figure 5.5. The structural distortion around the oxygen vacancy is greatest in the Mg-doped systems, where the alkaline earth defects are 5.3 Å and 4.50 Å apart, for O1 and O2 compensation respectively. The distance between the alkaline earth defects decrease for the larger

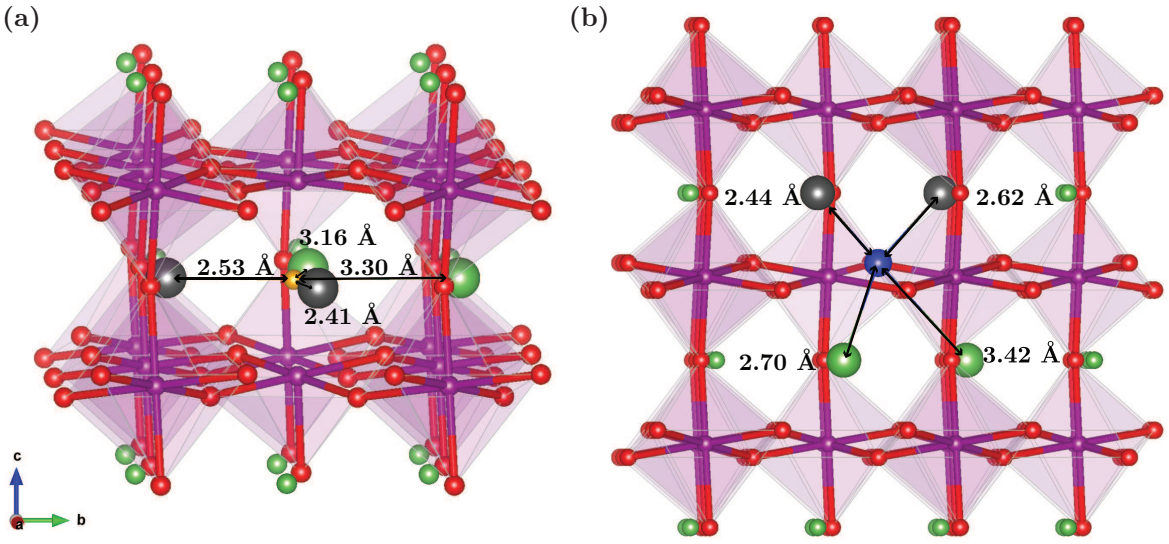

FIGURE 5.5: La ions neighbouring (a) an O1 vacancy and (b) an O2 vacancy in $LaMnO_3$. For clarity, Mn-O bonds and polyhedra are omitted surrounding the central O ion. La ions are shown in green, Mn ions in purple, O ions in red, the O1 vacancy in orange and the O2 vacancy in blue. The positions of alkaline earth defects in the lowest energy configuration are shown in grey

cations, which are displaced from the lattice sites, are 4.50 Å ($2Ca'_{La} + V^{\bullet\bullet}_{O1}$) and 4.17 Å ($2Ca'_{La} + V^{\bullet\bullet}_{O2}$), 4.28 Å ($2Sr'_{La} + V^{\bullet\bullet}_{O1}$) and 4.09 Å ($2Sr'_{La} + V^{\bullet\bullet}_{O2}$), and 4.09 Å ($2Ba'_{La} + V^{\bullet\bullet}_{O1}$) and 4.01 Å ($2Ba'_{La} + V^{\bullet\bullet}_{O2}$).

Defect clusters where the dopants are compensated by the formation of an oxygen vacancy on the O1 site are lower in energy than those compensated by an oxygen vacancy on an O2 site, as was seen in the combined charged defects, with very similar energies for Mg-doped, differing by 0.03 eV. The formation energies are $\sim$0.2–0.3 eV

lower for O1 vacancy compensation for Ca, Sr and Ba, although these are significantly higher than those compensated by the formation of a hole on Mn, (which have formation energies of 0.37 (-0.13, -0.14) eV), which are $\sim$1.66 (1.21, 1.06) eV lower than the O1 vacancy compensated Ca (Sr, Ba) defects. This limits the formation of oxygen vacancies in $LaMnO_3$, therefore doping with an alkaline earth metal on the La site is unlikely to significantly improve its ionic conductivity. The formation of holes as the charge compensating defect can contribute to the electronic conductivity of $LaMnO_3$.

TABLE 5.8: Formation energies of the defect clusters, in eV, of alkaline earth defects on the La site of $LaMnO_3$, with two alkaline earth defects compensated by an oxygen vacancy, or one defect compensated by hole formation on a Mn ion

Limit A (O-rich)	$2M'_{La} + V_{O1}^{\bullet\bullet}$	$2M'_{La} + V_{O2}^{\bullet\bullet}$	$M'_{La} + Mn_{Mn}^{\bullet}$
Mg	4.51	4.53	1.47
Ca	1.94	2.15	-0.07
Sr	0.99	1.24	-0.57
Ba	0.83	1.06	-0.58
Limit B (O-poor)			
Mg	5.56	5.59	3.06
Ca	2.99	3.21	1.53
Sr	2.05	2.30	1.03
Ba	1.89	2.12	1.01
700 K–La_2O_3			
Mg	5.56	5.59	2.39
Ca	2.99	3.21	0.85
Sr	2.05	2.30	0.35
Ba	1.89	2.12	0.34
700 K–Mn_3O_4			
Mg	4.60	4.62	1.90
Ca	2.03	2.24	0.37
Sr	1.08	1.33	-0.13
Ba	0.92	1.15	-0.14

For all combinations, clustering the defects lowers the energy, shown in table 5.9, where a negative energy indicated greater stability of the cluster and a positive energy

indicates greater stability of the isolated defects. This suggests increased stability when the defects are in close proximity to one another compared to when they are isolated, in particular for the oxygen vacancy clusters, which have binding energies of $\sim$0.51–1.35 eV. In all cases, electronic compensation for the dopant is still lower in energy than ionic compensation. As was seen for the combined isolated defects, the most stable defect clusters are Sr or Ba on the La site, compensated by hole formation on a Mn ion. The energies of the defect-hole clusters are lower than those of the combined isolated defects by $\sim$0.03–0.04 eV, with formation energies of -0.13 eV (Sr) and -0.14 eV (Ba) at the Mn_3O_4 limit of SOFC operating conditions. The very small binding energies, which are independent of temperature, indicate there is little difference in the stability when the defects occur in close proximity compared to when they are isolated. This suggests that the holes are not bound, and hopping of the holes will not be hindered and will contribute to increased electronic conductivity.

TABLE 5.9: The binding energy of defect clusters on the La site of $LaMnO_3$. The binding energy is the difference in formation energy of the cluster and the combined isolated defects

	Mg	Ca	Sr	Ba
$2M'_{\mathrm{La}} + V^{\bullet\bullet}_{\mathrm{O1}}$	-1.14	-0.61	-0.54	-0.69
$2M'_{\mathrm{La}} + V^{\bullet\bullet}_{\mathrm{O2}}$	-1.35	-0.63	-0.51	-0.69
$M_{\mathrm{La}} + \mathrm{Mn}^{\bullet}_{\mathrm{Mn}}$	-0.05	-0.04	-0.03	-0.04

The EDOS for the doped systems are very similar to each other, with the $\mathrm{Sr}'_{\mathrm{La}} + \mathrm{Mn}^{\bullet}_{\mathrm{Mn}}$ EDOS shown in figure 5.6, and show an unoccupied defect state at 0.3 eV above the VBM (circled in figure 5.6), which is a mixture of Mn 3*d* and O 2*p* character. A partial charge density plot of this defect state is shown in figure 5.7, and shows the charge density in the Ca-doped system for this state to be delocalised over the nearest Mn ions in the Mn-O layer above the defect, with the greatest amount on the nearest-neighbour Mn, some density on Mn ions in that layer far from the defect, and some density on the O2 ions. (The charge density in the Sr- and Ba-doped systems is very similar, so these are omitted.) These delocalised hole states are not bound in the defect clusters,

shown by the very low binding energies ($\leq$-0.05 eV), so will improve the electronic conductivity of $LaMnO_3$.

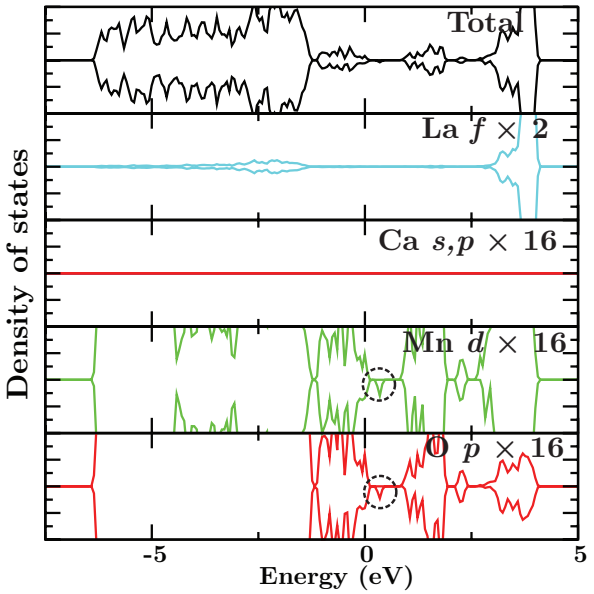

FIGURE 5.6: PEDOS for the Ca dopant on the La site, compensated by hole formation

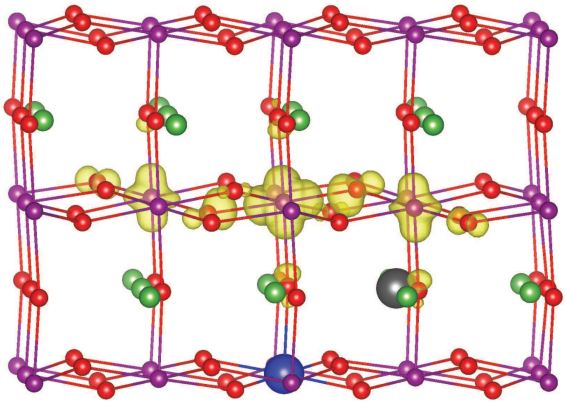

FIGURE 5.7: Partial charge density plot of the defect state split from the VBM, at isosurface level of 0.03 eV/Å^3. The location of the Ca dopant on the La site is represented by a grey atom

5.5.2 Mn site doping

5.5.2.1 Combined isolated defects

The defect formation energies for the combinations of isolated defects on the Mn site of $LaMnO_3$ are listed in table 5.10. Similar to those on the La site, when the dopants and charge compensating O vacancy are isolated from each other, the vacancy is more likely to form at the O1 site than the O2 site. Over the range of chemical potentials investigated, the lowest energy defect combinations are those where the dopant is compensated by hole formation. Under SOFC operating conditions at 700 K, defect formation energies are lower at the La_2O_3 limit, however, for comparison to La site doping, the energies at the Mn_3O_4 limit are discussed.

As was seen for doping on the La site, when the alkaline earth dopants are compensated by and oxygen vacancy, the vacancy is more likely to form on the O1 site than on the O2 site, with formation energies of 3.94 (5.59, 8.03, 11.98) eV for $2Mg'_{Mn} + V_{O1}^{\bullet\bullet}$ (Ca, Sr, Ba) compared to 4.17 (5.82, 8.27, 12.21) eV for $2Mg'_{Mn} + V_{O2}^{\bullet\bullet}$ (Ca, Sr, Ba) at the Mn_3O_4 limit. For all dopants, the defect formation energies are high, so charge compensation by oxygen vacancies is unlikely to occur.

The $Mg'_{Mn} + Mn_{Mn}^{\bullet}$ defect is significantly lower in energy than all other defects across the chemical potential range, with a formation energy of 1.06 eV at the Mn_3O_4 limit under the Mn_3O_4 limit of SOFC operating conditions. In addition, its formation energy is lower than when placed on the La site (1.96 eV), indicating that the Mg defect is more likely to form on the Mn site than on the La site. The Ca, Sr, and Ba defect combinations have significantly higher formation energies at the Mn site than the La site, with higher formation energies for the larger cations (1.88, 3.10 and 5.08 eV for Ca, Sr and Ba respectively at the 700 K Mn_3O_4 limit, compared to 0.41, -0.10 and -0.11 eV at the La site) therefore are more likely to form at the La site.

5.5.2.2 Defect clusters

In undoped $LaMnO_3$, there are two Mn ions at a distance of 1.97 Å from an O1 ion, two Mn ions are 4.10 Å from the O1 ion, and two are 4.23 Å from it, shown in figure

TABLE 5.10: Formation energies of the combined isolated defects, in eV, of alkaline earth defects on the Mn site of $LaMnO_3$, with two alkaline earth defects compensated by an oxygen vacancy, or one defect compensated by hole formation on a Mn ion

Limit A (O-rich)	$2M'_{Mn} + V_{O1}^{\bullet\bullet}$	$2M'_{Mn} + V_{O2}^{\bullet\bullet}$	$M'_{Mn} + Mn_{Mn}^{\bullet}$
Mg	4.03	4.26	0.71
Ca	5.68	5.91	1.54
Sr	8.12	8.35	2.76
Ba	12.07	12.30	4.73
Limit B (O-poor)			
Mg	2.97	3.20	1.25
Ca	4.63	4.86	2.08
Sr	7.07	7.30	3.30
Ba	11.01	11.24	5.27
700 K–La_2O_3			
Mg	2.97	3.20	0.57
Ca	4.63	4.86	1.40
Sr	7.07	7.30	2.62
Ba	11.01	11.24	4.59
700 K–Mn_3O_4			
Mg	3.94	4.17	1.06
Ca	5.59	5.82	1.88
Sr	8.03	8.26	3.10
Ba	11.98	12.21	5.08

5.8. The most stable structures for the alkaline earth-oxygen vacancy clusters are different from each other, unlike La-site doping (figures 5.8 and 5.9). When the system is doped with Mg, and compensated by formation of a vacancy on the O1 site, the system has the lowest formation energy when the Mg dopants are 1.97 Å and 4.10 Å from the oxygen vacancy (figure 5.8 (a)). For Mg-doped $LaMnO_3$ compensated by an O2 vacancy, the lowest energy configuration is that where one Mg ion is 1.97 Å from the vacancy, and the other Mg ion is 4.88 Å from the vacancy (figure 5.9 (a)). In the case of Ca-doped $LaMnO_3$, when compensated by an O1 vacancy, the lowest energy structure is one where one Ca ion is 5.43 Å from the vacancy and the other is 6.25 Å

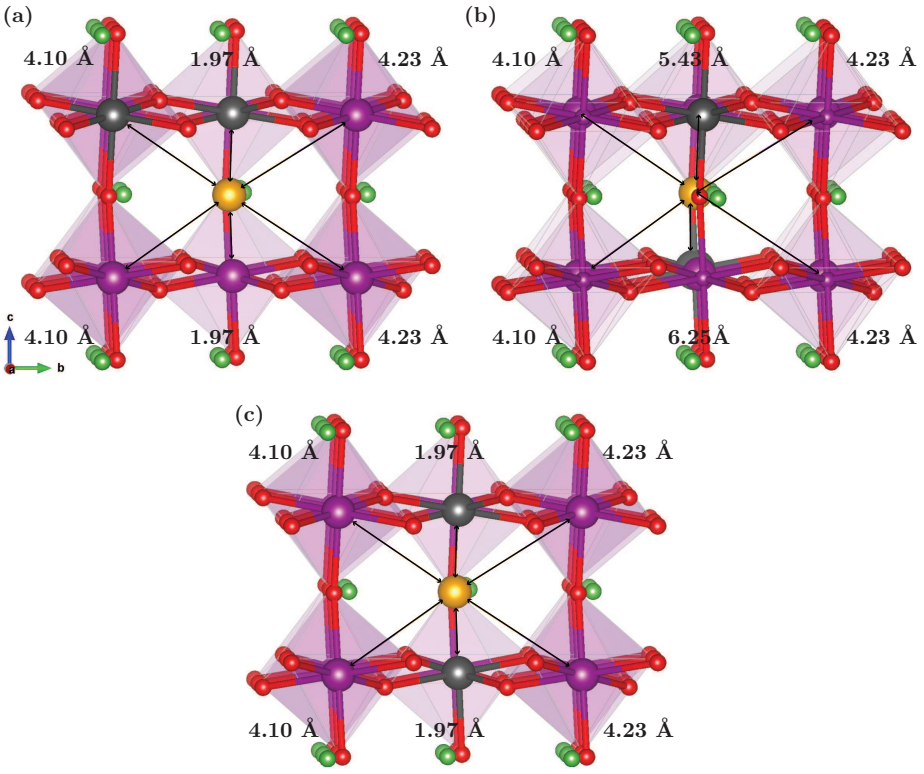

FIGURE 5.8: Mn ions neighbouring an O1 vacancy in $LaMnO_3$. (a) shows the most stable structure for Mg-doped, (b) Ca-doped and (c) Sr- and Ba-doped $LaMnO_3$. For clarity, Mn-O bonds and polyhedra are omitted surrounding the central O ion. La ions are shown in green, Mn ions in purple, O ions in red and the O1 vacancy in orange. The positions of alkaline earth defects are shown in grey

from it (figure 5.8 (b)). When compensated by an O2 vacancy, the Ca ions are 4.64 Å and 4.88 Å from the vacancy (figure 5.9 (b)).

When the Sr or Ba dopants are introduced, and the charge compensating defect is an O1 vacancy, the dopant ions are both 1.97 Å from the vacancy (figure 5.8 (c)). When the charge compensating defect is an O2 vacancy, the Sr dopants are in the same configuration as Mg compensated by an O2 vacancy (figure 5.9 (a)). For Ba dopants compensated by an O2 vacancy, the Ba ions are 1.97 Å and 2.16 Å from the vacancy (figure 5.9 (c)). The defect formation energies for clustered defects, with an alkaline earth dopant on the Mn site, at chemical potential limits A and B, and SOFC operating conditions at 700 K are listed in table 5.11. Under SOFC operating conditions, defects on the Mn site have lower formation energies at the La_2O_3 limit. As was seen for doping on the La site, charge compensation by the formation of a hole on Mn is predicted to be more stable than charge compensation by an oxygen vacancy on the O1 or O2 site.

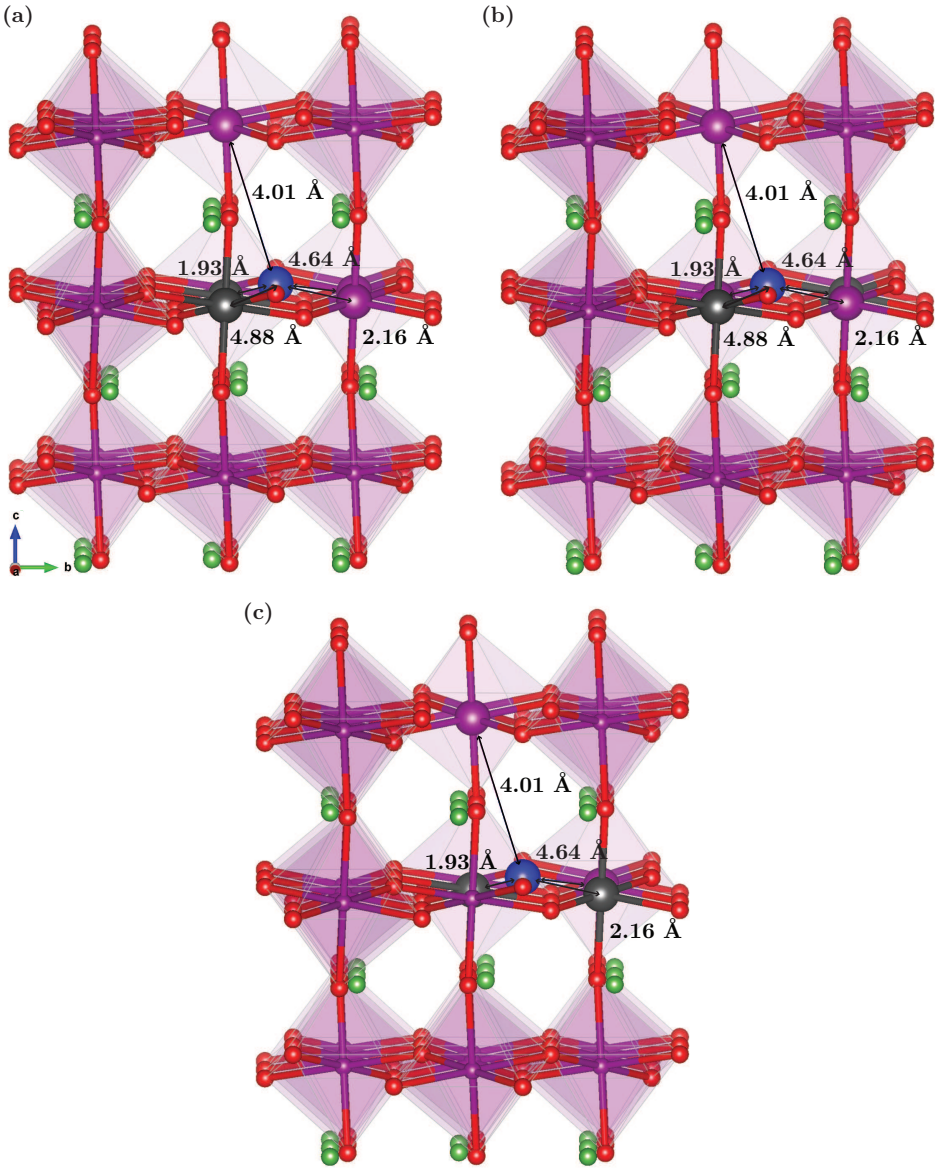

FIGURE 5.9: Mn ions neighbouring an O2 vacancy in $LaMnO_3$. (a) shows the most stable structure for Mg- and Sr-doped (b) for Ca-doped and (c) for Ba-doped $LaMnO_3$. For clarity, Mn-O bonds and polyhedra are omitted surrounding the central O ion. La ions are shown in green, Mn ions in purple, O ions in red and the O2 vacancy in blue. The positions of alkaline earth defects in the lowest energy configuration are shown in grey

Formation energies of 0.63 (1.40, 2.36, 4.26) eV are calculated for $Mg'_{Mn} + Mn^{\bullet}_{Mn}$ (Ca, Sr, Ba) at the La_2O_3 limit, compared to 2.88 (4.65, 6.50, 8.10) eV for $2Mg'_{Mn} + V^{\bullet\bullet}_{O1}$ (Ca, Sr, Ba) or 2.84 (4.29, 5.94, 8.00) eV for $2Mg'_{Mn} + V^{\bullet\bullet}_{O2}$ (Ca, Sr, Ba). This suggests again that the formation of oxygen vacancies in alkaline earth-doped $LaMnO_3$ will be limited.

TABLE 5.11: Formation energies of the defect clusters, in eV, of alkaline earth defects on the Mn site of $LaMnO_3$, with two alkaline earth defects compensated by an oxygen vacancy, or one defect compensated by hole formation on a Mn ion

Limit A (O-rich)	$2M'_{Mn} + V_{O1}^{\bullet\bullet}$	$2M'_{Mn} + V_{O2}^{\bullet\bullet}$	$M'_{Mn} + Mn_{Mn}^{\bullet}$
Mg	3.94	3.90	0.77
Ca	5.71	5.34	1.54
Sr	7.55	7.00	2.50
Ba	9.15	9.06	4.40
Limit B (O-poor)			
Mg	2.88	2.84	1.31
Ca	4.65	4.29	2.07
Sr	6.50	5.94	3.04
Ba	8.09	8.00	4.93
700 K–La_2O_3			
Mg	2.88	2.84	0.63
Ca	4.65	4.29	1.40
Sr	6.50	5.94	2.36
Ba	8.09	8.00	4.26
700 K–Mn_3O_4			
Mg	3.85	3.81	1.12
Ca	5.62	5.25	1.88
Sr	7.46	6.91	2.84
Ba	9.06	8.97	4.74

Unlike the La site, clustering of the defects does not lower the energy in all cases, shown in table 5.12. Small, positive energies are observed for Mg compensated by hole formation and Ca compensated by O1 vacancy formation, suggesting a slight decrease in stability when the defects are close, compared to when they are isolated. Increasing the dopant cation radius appears to favour defect clustering, with the exception of $2Ca'_{Mn} + V_{O1}^{\bullet\bullet}$, with values of 0.02 (-0.57, -2.92) eV for $2Ca'_{Mn} + V_{O1}^{\bullet\bullet}$ (Sr, Ba), -0.57 (-1.35, -3.24) eV for $2Ca'_{Mn} + V_{O2}^{\bullet\bullet}$ (Sr, Ba), and 0.00 (-0.26, -0.33) eV for $Ca'_{Mn} + Mn_{Mn}^{\bullet}$ (Sr, Ba). This suggests a stabilisation when defects occur in close proximity, however, the formation energies of these defects are higher than on the La site.

TABLE 5.12: The binding energy of defect clusters on the Mn site of $LaMnO_3$. The binding energy is the difference in formation energy of the defect cluster and the combined isolated defect

	Mg	Ca	Sr	Ba
$2M'_{Mn} + V_{O1}^{\bullet\bullet}$	-0.09	0.02	-0.57	-2.92
$2M'_{Mn} + V_{O2}^{\bullet\bullet}$	-0.36	-0.57	-1.35	-3.24
$M'_{Mn} + Mn_{Mn}^{\bullet}$	0.06	0.00	-0.26	-0.33

From the formation energies of the defects, it can be seen that a Mg defect is more likely to form on the Mn site than on the La site, with formation energies for the clustered defects approximately 0.7–0.8 eV lower for oxygen vacancy compensation (3.85–3.81 eV at the Mn site compared to 4.60-4.62 eV at the La site), and 0.8 eV lower for hole compensation (1.12 eV compared to 1.90 eV) under SOFC operating conditions at the Mn_3O_4 limit. Ca (Sr, Ba) defects are more likely to form on the La site with formation energies up to 3.5914 (6.3798, 8.1382) eV lower for oxygen vacancy compensation of the dopants at the Mn_3O_4 limit. For hole compensation, defect formation energies for Ca (Sr, Ba) are 1.51 (2.97, 4.88) eV lower, at 0.37 (-0.13, -0.14) eV compared to 1.88 (2.84, 4.74) eV. Lower defect formation energies are seen under oxygen-rich conditions (limit A) than under oxygen-poor conditions (limit B) for all defects on the La site, as oxygen-rich conditions correspond to La-poor conditions. On the Mn site, defects compensated by an oxygen vacancy have lower formation energies under oxygen-poor conditions than at the other limits, while hole-compensated defects have lower formation energies under oxygen-rich conditions. For both La and Mn site doping under the limits of chemical potential investigated, defect compensation by hole formation has lower energy than by oxygen vacancy formation. Previously, Sr has been used as a dopant due to the small mismatch between its ionic radius and that of La [244]. Similarly, the ionic radius of Mg^{2+} (0.72 Å) has small mismatch with that of Mn^{3+} (0.65 Å), while Ca^{2+} (1.34 Å) and Ba^{2+} (1.61 Å) have ionic radii closer to that of La^{3+} (1.36 Å). From our results, it can be seen that the defects are more likely to form on the site with which they have a smaller mismatch.

The EDOS for Mn-site doped $LaMnO_3$ is shown in figure 5.10, with Mg-doped $LaMnO_3$

shown in 5.10 (a), and Ca-doped $LaMnO_3$ is presented in figure 5.10 (b) (Sr- and Ba-doped $LaMnO_3$ have very similar densities of states so are omitted). Introduction of the Mg dopant results in an unoccupied defect state at 0.3 eV (circled in figure 5.10 (a)), which is a mixture of Mn $3d$ and O $2p$ character, as was seen in La-site doped $LaMnO_3$. The partial charge density plot of this peak gives the same result as La-site doped $LaMnO_3$, with the charge compensating hole delocalised over Mn and O ions neighbouring the defect (figure 5.6). These delocalised hole states are not bound in the Mg-hole defect cluster, so will improve the electronic conductivity of $LaMnO_3$. The EDOS for Ca-, Sr- and Ba-doped $LaMnO_3$ show an unoccupied defect state at ≈ 0.8 eV circled in figure 5.10 (b)). As a hole state is not generated near the VBM, introduction of these defects on the Mn site would not lead to good p-type conductivity.

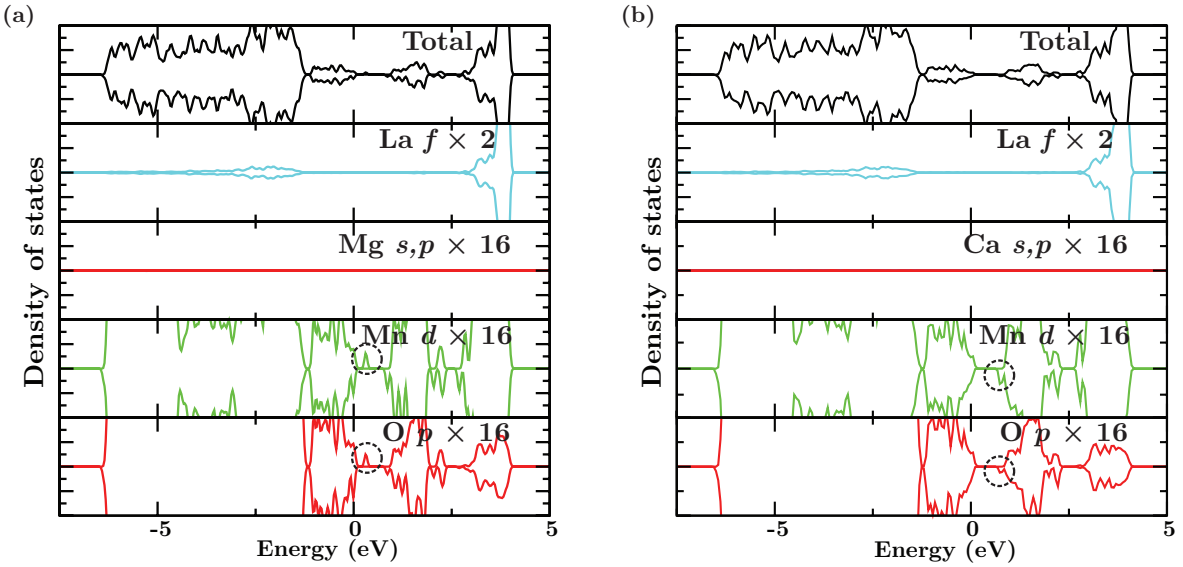

FIGURE 5.10: PEDOS for the alkaline earth defect on the Mn site, compensated by hole formation for (a) Mg-doped $LaMnO_3$ and (b) Ca-doped $LaMnO_3$

Our analysis has shown that under the limits of chemical potential investigated, dopants compensated by hole formation have lower formation energies than those compensated by oxygen vacancies, therefore charge compensation for doping with Mg, Ca, Sr or Ba is more likely to be electronic than ionic. For all dopants, the lowest defect formation energies for electronic compensation are observed under oxygen-rich conditions. This will limit the formation of oxygen vacancies, which means that alkaline earth doping is unlikely to have a large impact on the ionic conductivity of $LaMnO_3$. Analysis

of the electronic structure and partial charge density of the defect states shows the delocalisation of charge over Mn and O ions neighbouring the defect, which will improve the electronic conductivity of the material.

5.6 Conclusions

In bulk $LaMnO_3$ oxygen vacancy formation was found to be 0.28 eV more favourable at the O1 site than at the O2 site, with a greater degree of distortion observed around the O2 vacancy. At the surfaces, the lowest energy vacancy site was found to vary, with lower formation energies at higher energy surfaces, and Mn-O_6 octahedral distortion and displacement behaviour of atoms neighbouring the vacancy having an effect on vacancy formation energy. The large variation in their formation energies may lead to segregation of the vacancies to the surface, meaning that orthorhombic $LaMnO_3$ may not exhibit adequate oxygen diffusion for use as a mixed ionic and electronic conductor. Nudged elastic band calculations were used to examine oxygen vacancy migration in bulk $LaMnO_3$, with a migration pathway between $O2_l$–O1–$O2_l$–O1 predicted to have the lowest barrier energies.

The investigation into the site selectivity of the alkaline earth dopants showed that the smaller Mg^{2+} is more likely to be substituted on the Mn site, to which it has a smaller mismatch in ionic radius than the La site, while the larger Ca^{2+}, Sr^{2+}, and Ba^{2+} ions will substitute on the La site. The calculations predict that alkaline earth defects are preferentially charge compensated by hole formation on Mn ions over oxygen vacancy formation. This will limit the formation of oxygen vacancies in $LaMnO_3$, meaning that it is unlikely to exhibit good mixed ionic and electronic conductivity for low concentration of alkaline earth defects. The hole compensated defects have low formation energies under SOFC operating conditions, 1.1158 eV for $Mg'_{Mn} + Mn^{\bullet}_{Mn}$, and 0.37 (-0.13, -0.14) eV for $Ca'_{Mn} + Mn^{\bullet}_{La}$ (Sr, Ba) at the Mn_3O_4 limit. The binding energies of these hole compensated defects are small, 0.06 eV for Mg on the Mn site, -0.03 eV for Sr on the La site and -0.04 eV for Ca or Ba on the La site, indicating that there is little difference in the stability of defects which occur in close proximity compared to when they are far apart, and the holes are not bound. Analysis of the

EDOS shows two unoccupied defect peaks in the Mg-, Ca-, and Sr-doped systems, the first 0.3 eV above the VBM, and the second above the unoccupied Mn d states, 0.4 eV below the main unoccupied states. Partial charge density analysis of these peaks shows them to be due to hole delocalisation over Mn $3d$ and O $2p$ states, which will result in improved electronic conductivity of the material. Further work is required to determine whether the ionic conductivity of $LaMnO_3$ can be improved by doping it with lower valence cations.

Chapter 6

La_2NiO_4 for IT-SOFC cathodes

6.1 Introduction

Ruddlesden-Popper oxides with the structural formula $A_{n+1}B_nO_{3n+1}$, with n=1, are of interest as cathode materials for SOFCs due to their mixed ionic and electronic conductivity and very good surface reactivity with oxygen [126]. These materials, such as $La_2NiO_{4+\delta}$, can accommodate both oxygen vacancies and interstitials, with interstitials reported to be the majority oxygen defect under SOFC operating temperatures and partial pressure. For T $<$ 770 K [106, 251], $La_2NiO_{4+\delta}$ ($\delta = 0$) is orthorhombic, shown in figure 6.1 with experimentally determined lattice vectors a = 5.466 Å, b = 5.533 Å and c = 12.555 Å [106], and above this temperature it is tetragonal. The structure consists of n $LaNiO_3$ perovskite layers, separated by LaO rocksalt layers. Similar to the pervoskite structure, the Ni ions are 6-coordinate, but the La coordination is lower than that of the perovskite structure, with La coordinated to nine O ions. The O1 ions are coordinated to one Ni ion and three La ions, and the O2 ions are coordinated to two Ni ions and four La ions.

La_2NiO_4 is reported to have an O 2p dominated valence band, with Ni 3d contribution at the top of the band [252]. Chen *et al.* report a band gap of 2.6 ± 0.3 eV from combined scanning tunnelling microscopy and spectroscopy measurements [253]. Previous studies reported a wide range of band gaps, ranging from 70 meV (from resistivity measurements) [254] to 4 eV (from photoemisision spectra) [255].

In $La_2NiO_{4+\delta}$, oxygen interstitials are located in the LaO layers, tetrahedrally coordinated by La ions, and cause a distortion of the surrounding lattice. The most widely

reported mechanism for oxide ion transport in La_2NiO_4 is the interstitialcy mechanism, where the transport from an interstitial site occurs via displacement of a lattice oxygen into the next interstitial site [43, 111, 113, 128]. Some studies report an interstitial diffusion mechanism [125, 256], therefore both mechanisms will be investigated in this work.

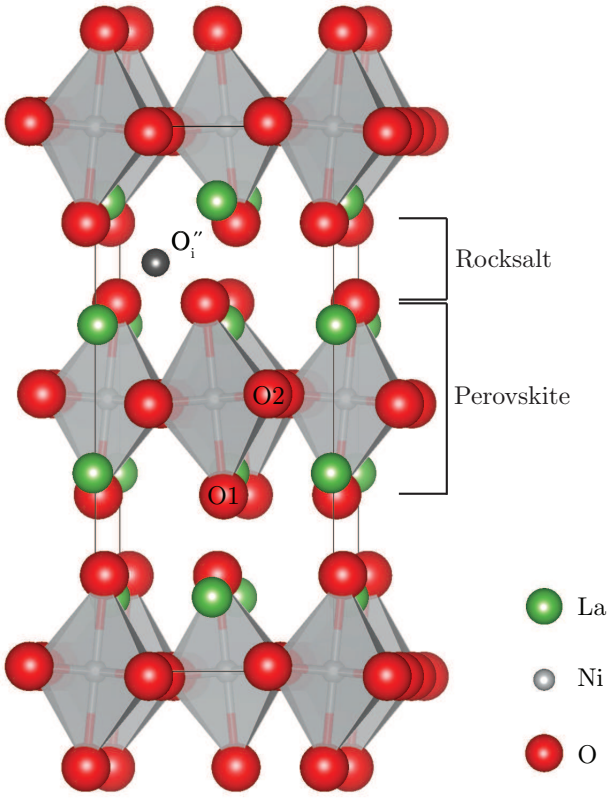

FIGURE 6.1: Unit cell of $LaMnO_3$ used in these calculations. La atoms are shown in green, Ni in silver and O atoms in red. An oxygen interstitial is shown in dark grey

The surfaces of tetragonal La_2NiO_4 have previously been simulated using a Born model in the METADISE code [129]. The order of stability was found to be {100} > {111} > {110} > {001} > {011}, with similar formation energies for the {001}, {110} and {011} surfaces. Significant relaxation of the surfaces was observed, with a change in the relative stability on relaxation. The crystal morphology was predicted from the Wulff construction, with the {111} surface found to be dominant, and the {100} and {001} surfaces also had a significant contribution to the structure. Partial substitution of Ni by Fe and Cu was found to give similar crystal morphologies to the undoped system. However, the {011} surface was expressed when doped with Fe, which was not seen

in either the pure or Cu-doped systems. The charge compensation mechanism for Sr doping at the low index surfaces was investigated, with the formation of Ni holes found to be more favourable than oxygen vacancy or oxygen hole formation. Defect energies at the surface were found to be lower than in the bulk, indicating that Sr segregation to the surface is likely to occur, which could affect the surface exchange and diffusion processes.

Oxygen point defects in distorted tetragonal $La_{1-x}Sr_xMO_{4+\delta}$ (x = 0–1, M = Co, Ni, Cu, δ = 0.0625–0.25) was investigated by Xie *et al.*, using PW-91 + U calculations in VASP, with U = 6.4 eV applied to Ni 3d states [126]. Three supercell sizes were examined, with 28, 56, and 112 atoms, and the structure used had the atoms in positions corresponding to the *Bmab* space group, to represent octahedral tilting when defects are introduced. The study investigated the stable sites for oxygen defects, their charge states and energetics as a function of the Sr content, transition metal on the B-site, and oxygen defect concentration, for oxygen chemical potential corresponding to T = 1000 K and p_{O_2} = 0.21 atm., with interstitials as the dominant defects in La-rich systems and vacancies as the dominant defects in Sr-rich systems. Their work shows that the dominant oxygen defect can change between interstitials and vacancies with increasing Sr content; with O interstitials preferred for $x = 0$. Similar stability of both interstitials and vacancies is observed when the Sr content is increased, *i.e.* for $x \sim 0.50$ for M = Cu, $x \sim 0.25$ for M = Ni, and $x \sim 0.10$ for M = Co when $\delta = 0.0625$. Above these values of x, oxygen vacancies become the most stable oxygen defects. An increase in the atomic number of M stabilises peroxide interstitials over oxide interstitials. It was found i their study that increasing the oxygen content (δ) destabilises the oxide interstitials and vacancies, but has no significant effect on the peroxide interstitials. Both apical and equatorial vacancies were considered, with equatorial vacancies found to be more stable than or equally as stable as the apical vacancies under all conditions examined, consistent with other studies on doped $n = 1$ Ruddlesden-Popper oxides. Unlike the vacancies, the relative stability of the interstitial states was found to be strongly dependent on the transition metal on the B-site and Sr content, and less on the oxygen content. When the Sr content is low ($x < 0.25$), for most systems

investigated, the oxide interstitial was more stable than or as stable as the peroxide interstitial, with the exception of the Cu-system with $\delta = 0.25$. At higher Sr content, the peroxide state is always more stable than the oxide. Therefore, the Sr content of $La_{1-x}Sr_xMO_{4+\delta}$ can be used to control the dominant oxygen defects in the material.

The interaction of molecular oxygen with the LaO-terminated {001} surface of La_2NiO_4 was investigated using GGA + U in VASP, using the PBE functional with $U = 6$ eV applied to Ni $3d$ states [110]. The oxygen reduction reaction at the surface of the SOFC cathode is a rate limiting factor for IT-SOFC operation, and the mechanism for the reaction has not been widely investigated. The LaO-terminated surface was examined as recent experimental studies found that the outermost layer of perovskite-based electrodes is dominated by the AO termination under SOFC operating conditions [120, 121, 257, 258], however, in this work the effect of chemical potential environment was not considered. As the surface chemistry has an impact on the kinetics of the oxygen reduction reaction, the effect of surface oxygen vacancies on energetics of the oxygen adsorption and dissociation reaction on the surface were examined in order [110]. The LaO-terminated surface was found to be energetically favourable for the O_2 adsorption and dissociation, with activation energies of approximately 1 eV for dissociation of chemisorbed oxygen on the defect-free surface and 0.28 eV on the defective surface, determined from NEB calculations. It was also observed that there is a binding interaction between surface La atoms and the adsorbed O_2, stabilising the dissociated oxygen atoms.

Ma *et al.* performed PBE + U ($U_{\mathrm{Ni}} = 6.4$ eV) calculations to examine oxygen exchange at the La- and Ni-oxide terminated {001} surfaces, and the {100} and {111} surfaces of tetragonal La_2NiO_4 [127]. The formation of oxygen vacancies via the migration of surface oxygen ions to interstitial sites, and the dissociative adsorption of oxygen on a vacant surface site, healing the vacancy and forming an oxygen adatom were investigated. On the La-oxide terminated {001} and the {100} surface, vacancy formation via migration of an oxygen ion to an interstitial site was found to be exothermic, with very high free energy barriers of 3.19 and 3.34 eV, while on the Ni-oxide terminated {001}) surface and the {111} surface the barriers were 0.48 and 0.71 eV respectively.

The dissociation of O_2 on the surface vacancy of the La-oxide terminated {001} surface was found to be almost barrierless, resulting in a very high barrier for the reverse step (6.75 eV), and on the {100} surface was 0.76 eV (6.61 eV for the reverse). On both the Ni-oxide terminated {001} surface and the {111} surface, the dissociation of O_2 is rate-limiting, with kinetic barriers of 1.73 eV and 2.08 eV respectively. On the La-oxide terminated {001} surface and the {100} surface, oxygen desorption is found to be the rate-limiting step. The Ni-oxide {001} surface has the lowest barrier at the rate-limiting step and was expected to exhibit the highest rates for surface oxygen exchange, which was confirmed by a microkinetic modelling analysis. They report that this surface offers the best compromise between the energetics associated with surface oxygen vacancy formation and oxygen adsorption and desorption, and predict that synthesis of La_2NiO_4 catalysts with a high concentration of this termination would offer improved oxygen exchange kinetics compared to other La_2NiO_4 catalysts.

The formation of intrinsic defects and oxygen migration in orthorhombic $La_2NiO_{4+\delta}$ has been investigated using a Buckingham potential with a shell model within the CASCADE code, by Minervini *et al.* [107]. Schottky ($2V'''_{La} + V''_{Ni} + 4V^{\bullet\bullet}_{O} + La_2NiO_4$), partial Schottky ($2V'''_{La} + 3V^{\bullet\bullet}_{O} + La_2O_3$ or $V''_{Ni} + V^{\bullet\bullet}_{O} + NiO$) and Frenkel defects ($V'''_{La} + La^{\bullet\bullet\bullet}_{i}$, $V''_{Ni} + Ni^{\bullet\bullet}_{i}$ or $V^{\bullet\bullet}_{O} + O''_{i}$) were considered, with anion Frenkel defects predicted to be the dominant type of lattice disorder. Calculations were carried out with the defects considered to be spatially isolated from each other, summing the energies of individual defects, and with defect clusters. The formation of an oxygen vacancy was found to be more energetically favourable at an equatorial (O2) site than an apical (O1) site. Excess oxygen is accommodated in interstitial sites in the lattice, and the compensation mechanism for excess oxygen in La_2NiO_4 was investigated, considering cation antisite defects, oxygen vacancies, O^- ions and Ni^{3+} ions. The most favourable charge compensation mechanisms were found to be those where the interstitial oxygen ion was compensated by oxidised nickel ions, or by a combination of an oxidised nickel ion and an oxidised lattice oxygen ion. Their results suggest that when defects are isolated (small values of δ), the charge compensating holes will be on nickel ions, while at larger values of δ, where defect clustering is more likely to occur, the holes will be

on lattice oxygen and nickel ions. Their investigation of the migration of oxygen interstitials in $La_2NiO_{4+\delta}$ showed migration via an interstitialcy mechanism. Migration of O^{2-} and O^- ions in the rocksalt layer and across the perovskite layer were considered, with charge transfer between the two charge states occurring readily (ΔE = 0.01 eV). The potential energy surface parallel and perpendicular to the diffusion path was examined and the saddle point energy was determined by placing a fixed defect at the saddle point of the migration pathway and the surrounding lattice was allowed to relax. The effect of the presence of Ni^{3+} near the migrating oxygen was also examined. Within the rocksalt layer, the activation energy for migration of an O^- ion was found to be 0.29 eV, while for an O^{2-} ion the activation energy was found to be 0.88 eV, and was unaffected by the presence of neighbouring Ni^{3+}. Across the perovskite layer, the activation energies are significantly higher, 2.90 eV (3.25 eV in the presence of neighbouring Ni^{3+}) and 3.15 eV (3.46 eV in the presence of neighbouring Ni^{3+}) for an O^- and an O^{2-} ion respectively. The anisotropy observed in the activation energies for oxygen migration within the rocksalt layers and across the perovskite layers is likely to affect oxygen transport properties from surface to bulk La_2NiO_4 cathodes.

Oxygen transport in tetragonal $La_2NiO_{4+\delta}$ has been investigated using MD simulations, in conjunction with Born model potentials [128]. In the temperature range 800–1100 K, an interstitialcy mechanism in the *a*-*b* plane was predicted for O^{2-} ions, with a lower activation energy than was seen in the orthorhombic structure (0.51 eV in tetragonal La_2NiO_4 compared to 1.2 eV in orthorhombic La_2NiO_4). An oxygen interstitial was found to displace an apical oxygen ion from a NiO_6 octahedron into an adjacent oxygen interstitial site. The effect of oxygen hyperstoichiometry was examined for $\delta = 0.055$ and 0.12 and was found not to have a significant effect on the activation energy.

The incorporation of oxygen ions into the high-temperature $La_2NiO_{4+\delta}$ ($\delta = 0.125$) lattice were investigated using the PW-91 functional in VASP [125], with no $+U$ correction on either Ni $3d$ states or O $2p$ states. An interstitial oxygen ion was introduced to one of the rocksalt layers (referred to in their work as La_2O_2 layers), leading to a structure with one $La_2O_{2.25}$ layer (the layer containing the oxygen interstitial) and one La_2O_2 layer. The nature of the interstitial oxygen, its diffusion within the $La_2O_{2.25}$

layer, and the formation of Frenkel defects were investigated. The incorporation of interstitial oxygen was reported to cause tilting of the NiO_6 octahedra surrounding the defect. The diffusion path considered in the study was one in which interstitial oxygen jumped between adjacent interstitial sites. It was determined that the interstitial oxygen is in the O^{2-} state at its equilibrium site, and also at the saddle point. The Frenkel pairs considered were an oxygen interstitial with (a) a vacancy on the equatorial oxygen site, (b) a vacancy on the apical site in the La_2O_2 layer, and (c) a vacancy on the apical site in the $La_2O_{2.25}$ layer. It was found that the lowest energy defect was the pair with the vacancy at the equatorial site, while the highest energy was that with the vacancy at an apical site in the oxygen excess layer. The authors suggest that the formation of Frenkel pairs in may be required for efficient oxygen transport in La_2NiO_4.

This chapter details the investigation into surface stability and defect formation in La_2NiO_4, to determine the dominant oxygen defects and examine the effect of doping with Sr and Fe, under different chemical potential environments. The structural and electronic properties were calculated using PBEsol + U, and the optimised bulk structure was used in surface and defect calculations. In this work $+U$ corrections are included on both Ni $3d$ states and O $2p$ states; previous studies have not included a $+U$ correction on the O $2p$ states. The order of stability of the low index surfaces of La_2NiO_4 was determined, and the formation of oxygen defects in the bulk and at the low index surfaces was investigated, considering oxygen chemical potentials corresponding to IT-SOFC operating conditions. The oxygen diffusion mechanism was investigated by examining oxygen migration paths through the rocksalt layers and across the perovskite layers, considering both interstitialcy and interstitial diffusion mechanisms. The site selectivity and charge compensation for defects at the A- and B-sites in orthorhombic La_2NiO_4 was examined for Sr and Fe defects. These defects were placed in the bulk at both the La- and Ni-sites to determine the site selectivity, and the charge compensation mechanism was determined by considering both ionic (formation of oxygen vacancies or interstitials) and electronic (localisation of electrons or holes at Ni ions) mechanisms.

6.2 Methodology

Calculations were carried out using PBEsol + U in VASP. There is a significant contribution of Ni $3d$ and O $2p$ states to the valence band of La_2NiO_4, and upon generation of holes, standard DFT predicts their delocalisation over all of the Ni and O atoms. A U value of 5.3 eV was applied to the Ni $3d$ states, which has been previously used on Ni $3d$ states in NiO [259–263], and of 5.5 eV to the O $2p$ states. PAW pseudopotentials were used to describe the interaction between core and valence electrons (La:[Kr], Cr:[Ar], O[He]). The structure of the orthorhombic bulk was relaxed using the quasi-Newton RMM-DIIS algorithm, with ionic and electronic convergence criteria of 0.005 eV/Å and 10^{-6} eV respectively.

Oxygen vacancy and interstitial formation were investigated for the orthorhombic bulk and low index surfaces. For the bulk, a 3 × 3 × 1 supercell was generated from the optimised bulk to limit defect-defect interactions, generating a 252 atom system. The expansion gives a minimum of 13 Å between defects. Surface supercells were generated using a 3 × 1 expansion of the surface vectors for the {010}, {100}, {101} and {011} surfaces, a 3 × 3 expansion for the {001} surface, and 2 × 2 expansion for the {110} and {111} surfaces. This results in systems containing 168 atoms for the {010}, {100}, {110} and {111} surfaces, and 252 atoms for the {001}, {011} and {101} surfaces. Oxygen defects were introduced on both sides of the surface slab to ensure no net dipole across the slab. The creation of an oxygen vacancy in bulk La_2NiO_4, given in Kröger-Vink notation, and the corresponding expression for the defect formation energy, are given by equations 6.1 and 6.2 respectively (equation 6.3 for surface oxygen vacancies).

$$O_O^x \rightarrow V_O^{\bullet\bullet} + 2e' + \frac{1}{2}O_2 \tag{6.1}$$

For an oxygen vacancy, $n_O = +1$, and n_{La} and $n_{Ni} = 0$, the defect formation energy is given by

$$E_f(D) = E_{tot}(D) - E_{tot}(La_2NiO_4) + \frac{1}{2}(E_{O_2} + \Delta\mu_{O_2}) \tag{6.2}$$

The expression for oxygen vacancy formation is modified for the surfaces, to take account for the slabs having oxygen vacancies introduced on both sides.

$$E_f(\mathrm{O}_{vac}) = \frac{1}{2}[E_{tot}(D) - E_{tot}(\mathrm{La_2NiO_4}(surf)) + E_{\mathrm{O_2}} + 2\Delta\mu_{\mathrm{O}}] \tag{6.3}$$

where $\mathrm{E}_{tot}(D)$ is the energy of the optimised surface slab and $E_{tot}(\mathrm{La_2NiO_4}(surf))$ is the energy of the defective surface slab. The creation of an oxygen interstitial can be represented in Kröger-Vink notation as

$$\frac{1}{2}\mathrm{O_2} \rightarrow \mathrm{O}_i'' + 2\mathrm{h}^{\bullet} \tag{6.4}$$

For an oxygen interstitial in bulk La_2NiO_4, n_{O} = -1, and n_{La} and $n_{\mathrm{Ni}} = 0$, so the defect formation energy is given by

$$E_f(D) = E_{tot}(D) - E_{tot}(\mathrm{La_2NiO_4}) - \frac{1}{2}(E_{\mathrm{O_2}} + \Delta\mu_{\mathrm{O_2}}) \tag{6.5}$$

The expression for oxygen interstitial formation is modified for the surfaces, to take account for the slabs having oxygen interstitials introduced on both sides.

$$E_{\mathrm{O_{vac}}} = \frac{1}{2}[E_{tot}(D) - E_{tot}(\mathrm{La_2NiO_4}(surf)) - (E_{\mathrm{O_2}} + 2\Delta\mu_{\mathrm{O}})] \tag{6.6}$$

The doping of La_2NiO_4 with Sr(II) and Fe(III) was examined, with the site selectivity of the dopants investigated by placing the defect on both the La and Ni sites. In defect calculations, a U value of 4.0 eV was applied to Fe $3d$ states which has previously been reported to provide a good description of the bulk properties of Fe_2O_3 [264–266]. The defect formation energy for substitution for La(III) or Ni(II), by Sr(II) or Fe(III), where L is the lattice atom and M is the dopant ($n_{\mathrm{L}} = +1$, n_{M} = -1), is given by

$$E_f D = E_{tot}(D) - E_{tot}(\mathrm{La_2NiO_4}) + (E_{\mathrm{L}} + \Delta\mu_{\mathrm{L}}) - (E_{\mathrm{M}} + \Delta\mu_{\mathrm{M}}) \tag{6.7}$$

The charge compensation mechanism for the aliovalent doping of La_2NiO_4 (Sr(II) on the La(III) site or Fe(III) on the Ni(II) site) was examined by considering both ionic

and electronic compensation mechanisms. When Sr(II) is placed on a La(III) site, the ionic charge compensation mechanism is the formation of an oxygen vacancy for every 2 dopant ions introduced.

$$2\mathrm{La}_{\mathrm{La}}^{\mathrm{X}} + 2\mathrm{Sr}_{E}^{\mathrm{X}} + \mathrm{O}_{\mathrm{O}}^{\mathrm{X}} \xrightarrow{\mathrm{La_2NiO_4}} 2\mathrm{La}_{E}^{\mathrm{X}} + 2\mathrm{Sr}_{\mathrm{La}}^{'} + V_{\mathrm{O}}^{\bullet\bullet} + \frac{1}{2}\mathrm{O}_2 \tag{6.8}$$

Here, two La ions have been replaced with two Sr ions, and an O ion has been removed to generate an oxygen vacancy ($n_{\mathrm{La}} = +2$, $n_{\mathrm{Sr}} = -2$, $n_{\mathrm{O}} = +1$), thus the defect formation energy is given by

$$E_f(D) = E_{tot}(D) - E_{tot}(\mathrm{La_2NiO_4}) + 2(E_{\mathrm{La}} + \Delta\mu_{\mathrm{La}}) - 2(E_{\mathrm{Sr}} + \Delta\mu_{\mathrm{Sr}}) + (\frac{1}{2}E_{\mathrm{O_2}} + \Delta\mu_{\mathrm{O}}) \tag{6.9}$$

The electronic compensation mechanism is the formation of a hole localised at a Ni site for each dopant ion introduced.

$$\mathrm{La}_{\mathrm{La}}^{\mathrm{X}} + \mathrm{Sr}_{E}^{\mathrm{X}} + \mathrm{Ni}_{\mathrm{Ni}}^{\mathrm{X}} \xrightarrow{\mathrm{La_2NiO_4}} \mathrm{La}_{E}^{\mathrm{X}} + \mathrm{Sr}_{\mathrm{La}}^{'} + \mathrm{Ni}_{\mathrm{Ni}}^{\bullet} \tag{6.10}$$

For charge compensation by formation of a hole at a Ni site ($n_{\mathrm{La}} = +1$, $n_{\mathrm{Sr}} = -1$), the defect formation energy is given by

$$E_f(D) = E_{tot}(D) - E_{tot}(\mathrm{La_2NiO_4}) + (E_{\mathrm{La}} + \Delta\mu_{\mathrm{La}}) - (E_{\mathrm{Sr}} + \Delta\mu_{\mathrm{Sr}}) \tag{6.11}$$

The introduction of Fe(III) on the Ni(II) site can be compensated by formation of an oxygen interstitial for every two dopant ions.

$$2\mathrm{Ni}_{\mathrm{Ni}}^{\mathrm{X}} + 2\mathrm{Fe}_{E}^{\mathrm{X}} + \frac{1}{2}\mathrm{O}_2 \xrightarrow{\mathrm{La_2NiO_4}} 2\mathrm{Ni}_{E}^{\mathrm{X}} + 2\mathrm{Fe}_{\mathrm{Ni}}^{\bullet} + \mathrm{O}_{i}^{''} \tag{6.12}$$

Here, two Ni ions have been replaced by two Fe ions, and an O^{2-} ion has been introduced to generate an oxygen interstitial ($n_{\mathrm{Ni}} = +2$, $n_{\mathrm{Fe}} = -2$, $n_{\mathrm{O}} = -1$), giving defect formation

energy

$$E_f(D) = E_{tot}(D) - E_{tot}(La_2NiO_4) + 2(E_{Ni} + \Delta\mu_{Ni}) - 2(E_{Fe} + \Delta\mu_{Fe}) - (\frac{1}{2}E_{O_2} + \Delta\mu_O) \tag{6.13}$$

The substitution of Fe for Ni may be compensated by an electron localised at a Ni site (equation 6.14).

$$Ni_{Ni}^{X} + Fe_{E}^{X} \xrightarrow{La_2NiO_4} Ni_{E}^{X} + Fe_{Ni}^{\bullet} + Ni_{Ni}^{'} \tag{6.14}$$

In this case, one Ni ion is replaced by an Fe ion ($n_{Ni} = +1$, $n_{Fe} = -1$), and the formation energy is given by

$$E_f(D) = E_{tot}(D) - E_{tot}(La_2NiO_4) + (E_{Ni} + \Delta\mu_{Ni}) - (E_{Fe} + \Delta\mu_{Fe}) \tag{6.15}$$

For Fe-containing defects, defect configurations replacing Ni ions of the same spin and of opposite spin were considered, and Fe ions in both high and low spin configurations, with the same spin and opposite spin were introduced to the Ni sites.

The chemical potentials are found with reference to the formation energy of the pure system:

$$2\Delta\mu_{La} + \Delta\mu_{Ni} + 4\Delta\mu_O = \Delta H_f[La_2NiO_4] = -22.32 \text{ eV} \tag{6.16}$$

The limiting conditions on the chemical potentials are determined by the formation of competing phases, La_2O_3, NiO, $La_3Ni_2O_7$, and $La_4Ni_3O_{10}$. Chemical potential limits were calculated using CPLAP [191].

Oxygen interstitial migration in La_2NiO_4 was investigated using CI-NEB calculations. The structures were relaxed using the L-BFGS method [187], with ionic and electronic convergence criteria of 0.05 eV/Å and 10^{-6} respectively.

6.3 Structural properties of La_2NiO_4

The calculated structural properties of La_2NiO_4 are presented in table 6.1. The lattice parameters of 5.396 Å, 5.482 Å and 12.448 Å are in good agreement with the experimental values, with deviation from them by $\sim$1%. The Ni-O bonds show slightly larger underestimation, and there is overestimation of the La-O1 distance across the LaO layers and of the Ni-O2-Ni angles.

TABLE 6.1: Structural properties of La_2NiO_4. Experimental values taken from ref [106]. % differences between the experimental and calculated values of the structural parameters are given in parentheses

	Expt.	Comp
V (Å^3)	379.65	368.18 (-3.02)
a (Å)	5.466	5.396 (-1.27)
b (Å)	5.533	5.482 (-0.92)
c (Å)	12.555	12.448 (-0.85)
Ni-O1 (Å)	2.232	2.202 (-1.39)
Ni-O2 (Å)	1.947	1.926 (-1.08)
Ni-O2-Ni (°)	173.569	173.232 (0.19)
La-O1 (across LaO layer) (Å)	2.324	2.353 (0.45)

6.4 Electronic and magnetic structure of La_2NiO_4

The electronic structure was investigated, and valence band features were compared to experiment. The calculated electronic structure is presented in figure 6.2 (a), with the top of the valence band aligned to 0 eV. The calculation predicts the valence band to have significant O $2p$ contribution, with Ni $3d$ mixing at the top of the valence band. This is in good agreement with the experimentally reported structure, of an O $2p$ dominated valence band, with Ni $3d$ contribution at the top of the band [252]. The calculated band structure is shown in figure 6.2 (b), predicting an indirect band gap of 1.92 eV from the VBM which lies along the S to R line, to the CBM at Γ, and a direct

gap of 2.57 eV at Γ. This is in agreement with the band gap of 2.6 ± 0.3 eV from combined scanning tunnelling microscopy and spectroscopy measurements reported by Chen *et al.* [253].

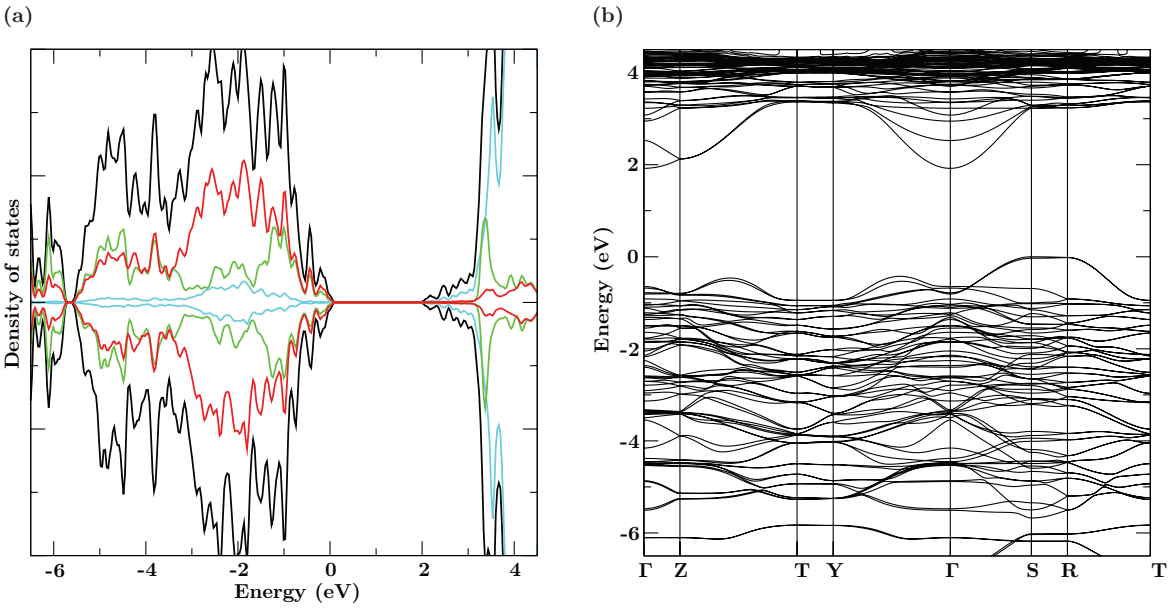

FIGURE 6.2: (a) EDOS calculated for La_2NiO_4 using PBEsol + U. Total EDOS is shown in black, p states are shown in red, d states in green and f states in cyan. (b) Calculated band structure for La_2NiO_4

6.5 Oxygen defects in bulk La_2NiO_4

6.5.1 Oxygen chemical potential and partial pressure

The chemical potential limits for determining the oxygen vacancy formation energies were calculated using CPLAP [191]. The formation energies of La_2NiO_4 and its competing phases used in the determination of the chemical potential limits are presented in table 6.2, in addition to the magnetic ordering of Ni-containing phases. The vertices of the upper triangle in figure 6.3 are determined by the formation of La_2NiO_4. The limits imposed by the formation of competing oxides give a narrow region of stability, marked by black circles (shown in the inset), with the chemical potentials at each of these points presented in table 6.3. Defect formation will be examined at the oxygen-rich ($\Delta\mu_O$ = -0.39 eV) and oxygen-poor ($\Delta\mu_O$ = -4.71 eV) limits.

TABLE 6.2: Formation energies and magnetic ordering of La_2NiO_4 and its competing phases

Phase	Formation energy (eV)	Magnetic ordering
La_2NiO_4	-20.79	AFM
La_2O_3	-16.08	
NiO	-4.66	AFM
$La_3Ni_2O_7$	-33.74	AFM
$La_4Ni_3O_{10}$	-46.35	AFM

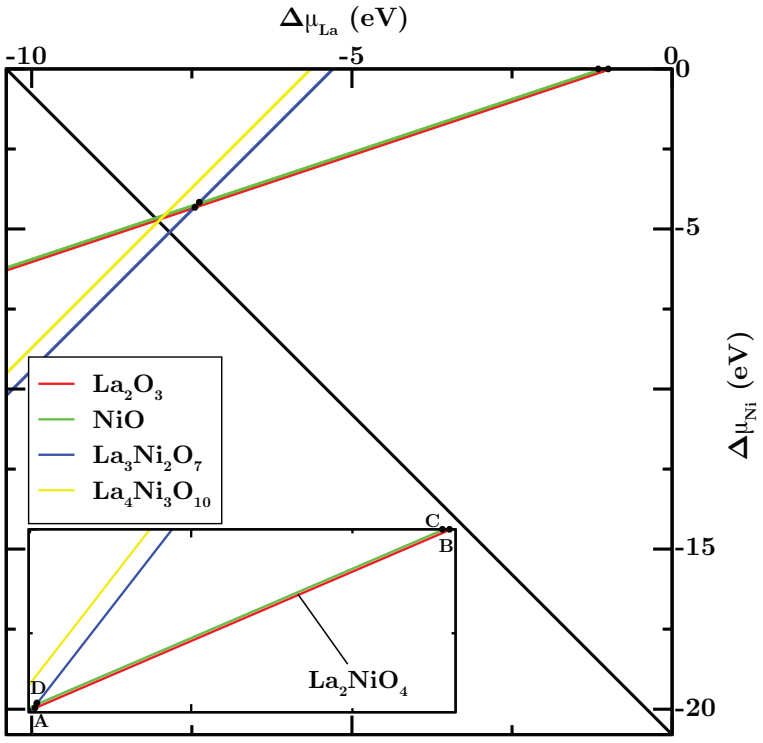

FIGURE 6.3: Plot showing region of stability (grey) for La_2NiO_4 spanned by $\Delta\mu_{La}$ and $\Delta\mu_{Ni}$, showing oxygen-rich (A: $\Delta\mu_O$ = -0.39 eV) and oxygen-poor (B: $\Delta\mu_O$ = -4.71 eV) limits. The vertices of the upper triangle are determined by the formation of La_2NiO_4 and the coloured lines show the limits determined by the competing phases. Points A–E show the intersection points of the region of stability determined by these limits

6.5.2 Oxygen vacancies

The formation energies for oxygen vacancies at the O1 and O2 sites in La_2NiO_4, corresponding to the O-rich, O-poor, and SOFC operating conditions considered in chapter 5 are presented in table 6.4. The O1 vacancy has a formation energy of 5.21 eV at

TABLE 6.3: Chemical potential limits, in eV, for La_2NiO_4, with the phases present at each limit

	$\Delta\mu_{La}$	$\Delta\mu_{Ni}$	$\Delta\mu_{O}$	Phases
A	-7.46	-4.32	-0.39	La_2O_3, $La_3Ni_2O_7$
B	-0.97	0.00	-4.71	La_2O_3
C	-1.08	0.00	-4.66	NiO
D	-7.40	-4.22	-0.44	NiO, $La_3Ni_2O_7$

the oxygen-rich limit and 0.88 eV at the oxygen-poor limit, which corresponds to an extremely low oxygen chemical potential. Under the SOFC operating conditions, the formation energy decreases from 4.95 eV to 4.69 eV with temperature. The introduction of an oxygen vacancy at the O1 site causes a structural distortion, with La ions neighbouring the vacancy displaced away from the vacancy, and the Ni ion nearest the vacancy and O1 and O2 ions displaced towards the vacancy. La ions are displaced away from vacancy by 0.03–0.10 Å, the nearest neighbour Ni ion is displaced towards the vacancy by 0.34 Å, the nearest O1 ions are towards the vacancy by 0.02–0.04 Å, and the O2 ions are displaced towards the vacancy by 0.03–0.08 Å.

TABLE 6.4: Oxygen vacancy formation energies for bulk La_2NiO_4 at the oxygen-rich and oxygen-poor limits, and under the IT-SOFC operating temperature range, 600–800 K, $p = 0.21$ atm, $p^\circ = 1$ atm

		O1	O2
	$\Delta\mu_O$ (eV)	E_{Ovac} (eV)	E_{Ovac} (eV)
O-rich	-0.39	5.21	4.11
O-poor	-4.71	0.88	-0.22
600 K	-0.65	4.95	3.85
700 K	-0.78	4.82	3.72
800 K	-0.90	4.69	3.59

At the O2 site, oxygen vacancy formation is lower than at the O1 site, in good agreement with previous works [107, 126], with a formation energy of 4.1080 eV at the oxygen-rich limit and -0.2166 eV at the extreme oxygen-poor limit. Under SOFC operating conditions, the formation energies decrease from 3.85 eV (600 K) to 3.59 eV

(800 K). Similar to the O1 vacancy, introduction of an O2 vacancy causes the La ions neighbouring the vacancy to be displaced away from the vacancy, and the nearest neighbour Ni ions are displaced towards the vacancy. Both the neighbouring O1 and O2 ions are displaced towards the vacancy. The cation displacements are smaller than observed for the O1 vacancy, with La ions moving outwards by 0.02–0.05 Å, Ni moving towards the vacancy by 0.18 Å, and the oxygen displacements are similar to the O1 vacancy, with O1 ions moving 0.03–0.10 Å closer to the vacancy, and O2 ions by 0.07–0.08 Å. The two remaining electrons are localiased on Ni atoms neighbouring the vacancy. As was observed for $LaMnO_3$, the lower formation energy of the O2 vacancy may be due to the smaller degree of distortion around the vacancy compared to the O1 site. This indicates that oxygen vacancies are more likely to form at the O2 site than in the O1 site in La_2NiO_4, but for both defects, the formation energy is high. For both O1 and O2 vacancies in bulk La_2NiO_4 the excess electrons are localised on Ni ions with the same spin neighbouring the O vacancy.

6.5.3 Oxygen interstitials

Oxygen interstitial formation (table 6.5) is found to be significantly lower in energy that oxygen vacancy formation. The formation energy of an oxygen interstitial in bulk La_2NiO_4 is 0.42 eV at the oxygen-rich limit and 4.84 eV at the oxygen-poor limit. The formation energy increases with temperature under the SOFC operating conditions considered, from 0.69 eV to 0.94 eV in the temperature range 600–800 K. When the interstitial is optimised it sits within a tetrahedron of La ions, shown in figure 6.4, 2.35–2.36 Å from three of the La ions, which are displaced outwards relative to their positions in the defect-free system and 2.6 Å from the fourth, which is displaced towards the interstitial. These distances are similar to the La-O bond lengths in La_2O_3 (2.36–2.71 Å, suggesting that this structure should be stable. The Ni ions nearest the interstitial are displaced towards it by 0.01–0.02 Å. The O1 ions nearest the interstitial show significant displacement away from the defect, by 0.33–0.46 Å, and the O2 ions are displaced towards it by 0.04–0.14 Å. On formation of an oxygen interstitial, holes are localised on Ni ions with the same spin neighbouring the interstitial. Due to the significant difference in the formation energy of the oxygen interstitial compared to

TABLE 6.5: Oxygen interstitial formation energies for bulk La_2NiO_4 at the oxygen-rich and oxygen-poor limits, and under the IT-SOFC operating temperature range, 600–800 K, textitp$_{O_2}$ = 0.21 atm, p° = 1 atm

	$\Delta\mu_O$ (eV)	E_{O_i} (eV)
O-rich	-0.39	0.42
O-poor	-4.71	4.84
600 K	-0.65	0.69
700 K	-0.78	0.82
800 K	-0.90	0.94

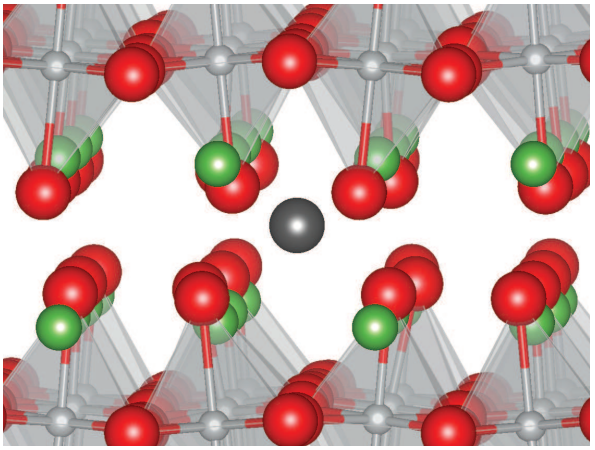

FIGURE 6.4: Structure of the oxygen interstitial in La_2NiO_4. La atoms are shown in green, Ni in silver and O atoms in red, and the oxygen interstitial is shown in dark grey

the oxygen vacancies, which has also been seen in previous works [107, 126], oxygen interstitials are likely to be the dominant oxygen defect in bulk La_2NiO_4 for O-rich and SOFC operating conditions. At very low oxygen chemical potential, however, oxygen vacancies are more stable than the interstitials.

6.5.4 Oxygen migration in bulk La_2NiO_4

Oxygen interstitial migration in La_2NiO_4 was investigated for the interstitialcy and interstitial mechanisms within the LaO layers and for an interstitialcy-type mechanism across the perovskite layers. The paths for migration of the oxygen interstitial are shown in figure 6.5, with (a) showing the interstitialcy mechanism, (b) showing the interstitial mechanism, and (c) showing the migration across the perovskite layer via

an O2 lattice site. The lowest barrier to migration is for the [010] direction, with an activation energy of 0.15 eV. In the [100] direction, the energy barrier is 0.53 eV, and in the [110] direction it is 0.40 eV. Three directions for migration via the interstitialcy are considered within the LaO plane, the [100], [010] and [110] directions. The activation energies for oxygen interstitial migration are presented in table 6.6.

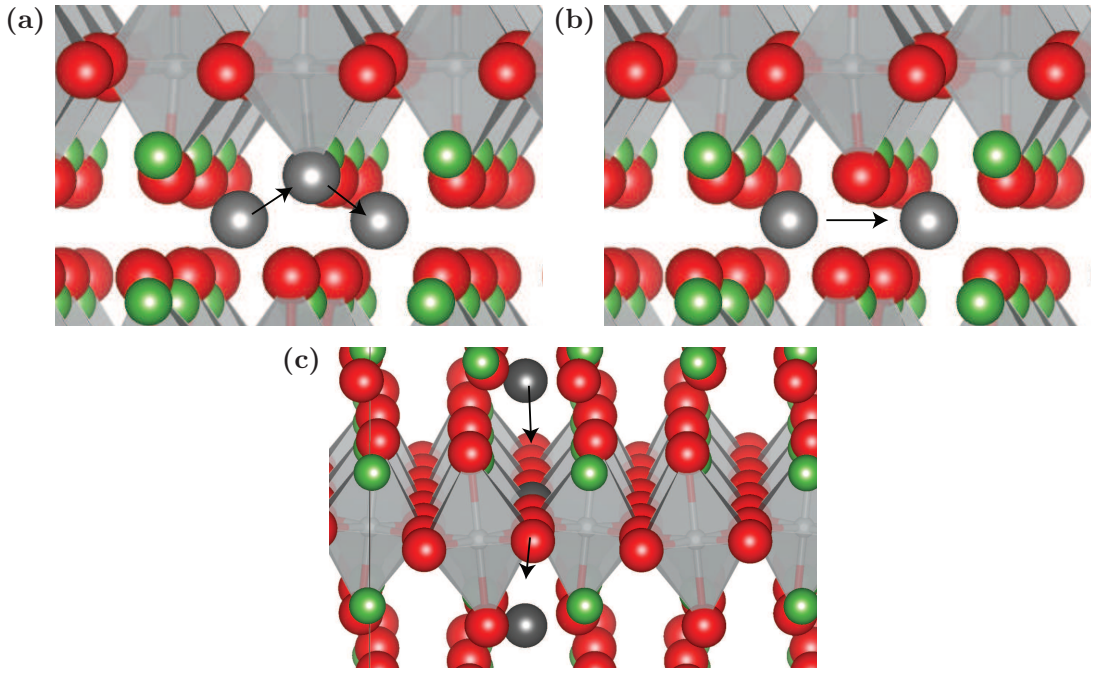

FIGURE 6.5: Oxygen migration paths in La_2NiO_4. (a) interstitialcy mechanism, (b) interstitial mechanism and (c) path across the perovskite layer via an O2 site

TABLE 6.6: Activation energies (E_a), in eV for oxygen interstitial migration in bulk La_2NiO_4, for interstiticialcy and interstitial mechanisms in the LaO plane, and for an interstitialcy-type mechanism across the perovkskite layers

Interstitialcy		Interstitial		Across perovskite layer
Direction	E_a	Direction	E_a	E_a
[010]	0.15			
[100]	0.53	[010]	0.87	1.57
[110]	0.40			

Migration via a direct path between two interstitial sites in the [100] direction leads to peroxide formation, with a formation energy of 0.83 eV under SOFC operating conditions of 700 K and $p_{O_2} = 0.21$ atm. (formation energy of an oxygen interstitial

under these conditions is 0.81 eV), giving a local minimum in the potential energy surface. Further work is required to determine the height of the barrier to this transition state. In addition, as the peroxide is very close in energy to the interstitial at the centre of the tetrahedron of La ions, it will need to be considered as a competing defect in future work. The energy barrier for the interstitial mechanism in the [010] direction is 0.87 eV, and at the transition state the interstitial is 2.14 Å from the nearest lattice oxygen, so does not form the peroxide. Oxygen diffusion across the perovskite layers via an O2 site has a significantly higher barrier energy than in the LaO plane, at 1.57 eV. From the difference in the activation energies, it can be seen that oxygen diffusion is much more likely to occur within the LaO layers than across the perovskite layers. The orientation of the LaO planes in the surface slabs will affect the diffusion of oxygen from the surface into bulk La_2NiO_4.

6.6 Low index surfaces of La_2NiO_4

The surface slabs generated using METADISE were a minimum of 10 Å thick to minimise interactions between slab surfaces. A vacuum gap of 15 Å was introduced between slabs to reduce interactions between a surface and its periodic image. The {001} slab contains 40 atoms, with a depth of 12.5 Å, the {010} and {100} surfaces each contain 56 atoms, with depths of 11.0 and 10.8 Å, and the {110}, {101}, {111} and {011} surfaces contain 84 atoms, with depths of 11.5, 14.9, 11.0 and 15.0 Å respectively. Different k-point meshes were used for the slabs, based on the lattice vectors, with a $3 \times 3 \times 1$ k-point mesh for the {001} surface, $3 \times 1 \times 1$ meshes for the {010}, {100}, {101} and {011} surfaces, $1 \times 2 \times 1$ for the {110} surface, and $2 \times 2 \times 1$ mesh for the {111} surface. Different terminations for each surface were investigated, with the most stable terminations reported here. The unrelaxed and relaxed surface energies, relaxation energies, La and Ni surface coordination and bonds cleaved at the surface are presented in table 6.7, in order of decreasing stability. The relaxed surface structures are shown in figures 6.6–6.12, with the oxygen vacancy sites labelled.

TABLE 6.7: Unrelaxed (γ_{un}) and relaxed (γ_s) surface energies, relaxation energy (ΔE), surface coordination and Ni-O bonds cleaved in the low index surfaces of La_2NiO_4. (*On relaxation of the {111} surface, one of the O2 atoms around the 6-coordinate Ni is displaced towards the LaO layer–section 6.6.6)

	γ_{un}	γ_s	ΔE	Surface coordination				
Miller indices	(J/m^2)	(J/m^2)	(J/m^2)	La	Ni	O (La)	O (Ni)	Bond cleaved
{010}	1.67	1.03	0.64	7	5	2	1	Ni-O2
{100}	1.63	1.03	0.60	7	5	2	1	Ni-O2
{001}	1.19	1.10	0.09	8	–	3	–	Between LaO layers
{110}	2.14	1.11	1.03	6	5, 6	2–4	1, 2	Ni-O2
{101}	1.8	1.24	0.57	6, 8	3	2, 3	1, 2	Ni-O1, 2 × Ni-O2
{111}	2.4	1.25	1.16	5	5, 6*	2	1, 2	Ni-O2
{011}	2.9	2.15	0.77	5, 6	4, 6	2	1, 2	2 × Ni-O2

6.6.1 The {010} surface

The {010} surface (figure 6.6) has the lowest surface energy and is terminated by 7-coordinate La ions, 5-coordinate Ni ions, with a Ni-O2 bond cleaved in the NiO_6 octahedra, and O1 and O2 ions (1- and 2-coordinate to Ni and La ions respectively). Surface relaxation results in distortion of the Ni-O octahedra at the surface, with a decrease of 2.9–3.9% in the Ni-O1 bonds, an increase of 3.4% in the Ni-O2 bond nearest the surface, an increase of 2.9% in one of the remaining Ni-O2 bonds, and a decrease of 1.2% in the final Ni-O2 bond. In bulk La_2NiO_4, the O1-Ni-O1 angle in the NiO_6 octahedra is 180°, which decreases by 8.1% in the relaxed surface, due to the O1 atoms moving away from the surface. The Ni-O2-Ni angles are found to decrease by 4–5% between the first and second layers of the slab, indicating significant rotation of the octahedra at the surface. In the bulk, the separation between the rocksalt layers, which are perpendicular to the surface, is 1.84 Å, this increases by 3.3% to 1.90 Å in the {010} surface, due to the decrease in the Ni-O1 bonds.

6.6.2 The {100} surface

The {100} surface (figure 6.7) is also terminated by 7-coordinate La ions, 5-coordinate Ni ions, with a Ni-O2 bond cleaved in the NiO_6 octahedra, and O1 and O2 ions (1 and 2-coordinate to Ni and La ions respectively). In a tetragonal Ruddlesden-Popper

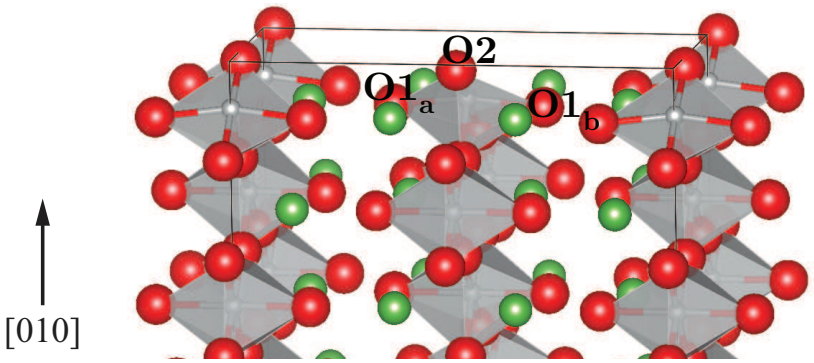

FIGURE 6.6: Relaxed surface slab of the {010} surface of La_2NiO_4. Oxygen vacancy sites are labelled with a, b

phase, the {010} and {100} surfaces are identical, but differ here due to the distortion of the NiO_6 octahedra, resulting in the *a* lattice parameter being shorter than the *b* lattice parameter in the bulk, and slight differences in the orthorhombic surfaces. This results in the {100} surface having a very similar surface energy to the {010} surface. On relaxation of the surface, one of the Ni-O1 bonds at in the surface NiO_6 octahedra decreases by 0.81%, and the second decreases by 4.5%. The Ni-O2 bond closest to the surface increases by 3.4%, one of the Ni-O2 bonds with the O2 ion in the second layer increases by 3.9%, and the other decreases by 1.0%. The O1-Ni-O1 angles at the surface are seen to decrease by up to 9% at the surface, due to the O1 ions moving away from the surface. The Ni-O2-Ni angles between octahedra decrease by 5.5–5.6%, again showing significant rotation of the octahedra on relaxation of the slab. As in the {010} surface, the rocksalt layers in the {100} surface are also perpendicular to the surface, with the separation between these layers increasing by 2.8% to 1.89 Å, due to the decrease in the Ni-O1 bonds.

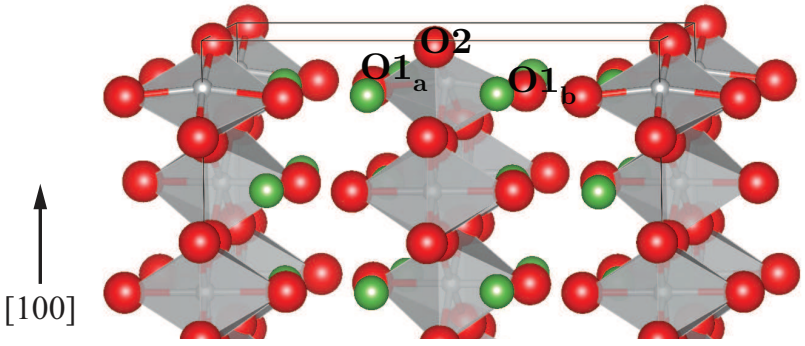

FIGURE 6.7: Relaxed surface slab of the {100} surface of La_2NiO_4. Oxygen vacancy sites are labelled with a, b

6.6.3 The {001} surface

The {001} surface (figure 6.8) is formed by cleaving between the LaO layers of La_2NiO_4, and is terminated by 3-coordinate O1 (to La ions) and 8-coordinate La atoms. This surface has a low unrelaxed surface energy and the smallest relaxation energy. The structural distortion of the surface on relaxation is less significant than seen in other surfaces. In the first layer of Ni-O_6 octahedra, the surface Ni-O1 bond decreases by 3.4% on relaxation, and the second Ni-O1 bond in the octahedron increases by 1.9%. In the bulk, the O1-Ni-O1 angle is 180°, which decreases by 1.7% to 176.9°on relaxation. Two of the Ni-O2 bonds in the octahedra increase by 0.40%, and the remaining two decrease by 0.2%. The Ni-O2-Ni angles show decreases of 1.8% and 0.4% between octahedra. The separation between the rocksalt layers in the {001} surface decreases by 0.7% to 1.83 Å, and the LaO layers are parallel to the surface.

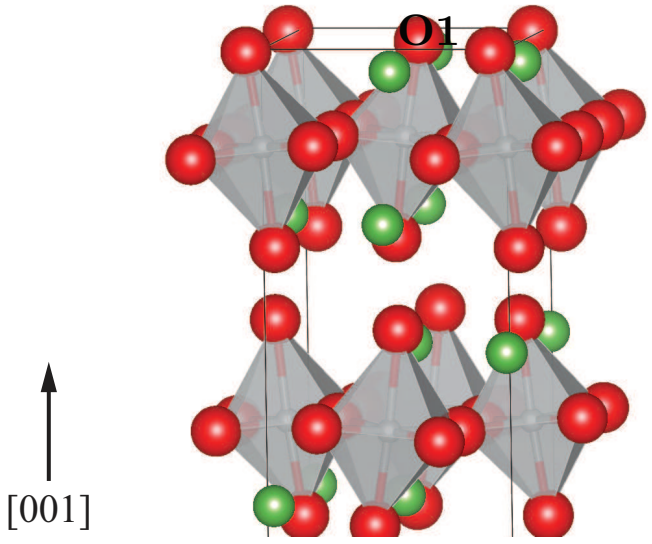

FIGURE 6.8: Relaxed surface slab of the {001} surface of La_2NiO_4. The oxygen vacancy site is labelled with O1

6.6.4 The {110} surface

The {110} surface (figure 6.9) is terminated by 6-coordinate La ions, 5- and 6 coordinate Ni ions, with Ni-O2 bonds cleaved at the 5-coordinate Ni. This surface has a high unrelaxed surface energy and shows significant distortion on relaxation of the surface. In the 5-coordinate octahedra, one of the Ni-O1 bonds decreases by 7.4%, while the

other Ni-O1 bond shows a significant increase of 24.9% due to displacement of the Ni and O ions. The surface Ni-O2 bonds in the 5-coordinate octahedra increase by 0.7%, and the Ni-O2 bond below the surface increases by 0.8%. The Ni-O2 bond to the Ni atom in the second layer increases by 15.2% on relaxation of the surface. At the surface, the Ni-O2-Ni angles increase by 2.4%, while the Ni-O2-Ni angle between the truncated NiO_5 octahedron and the Ni-O_6 octahedron below it decreases by 0.2%. Around the 5-coordinate Ni ion at the surface, the O ions are displaced significantly, with a decrease of 11.3% in the O1-Ni-O1 angle, and 8.4% in the O2-Ni-O2 angle. The separation between the rocksalt layers in the {110} surface, which are perpendicular to the surface termination, decreases to 1.33 Å due to the significant displacement of the O1 ions at the surface. These significant distortions of the surface on relaxation result in a large relaxation energy and a relatively low surface energy.

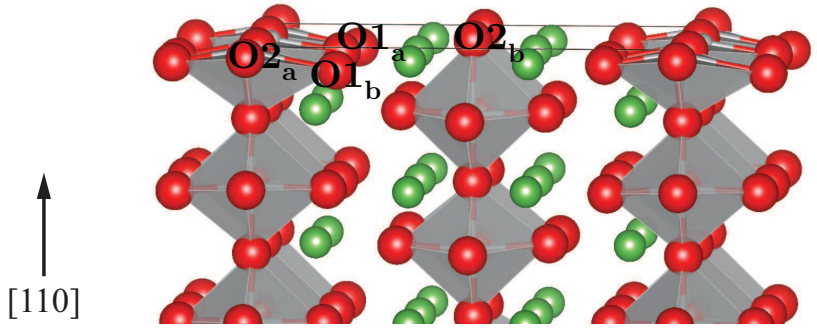

FIGURE 6.9: Relaxed surface slab of the {110} surface of La_2NiO_4. Oxygen vacancy sites are labelled with a, b

6.6.5 The {101} surface

The {101} surface is terminated by 6- and 8-coordinate La ions, 3-coordinate Ni ions, and O1 and O2 ions (1- and 2-coordinate and 2- and 3-coordinate for Ni and La ions respectively), with one Ni-O1 bond and two Ni-O2 bonds cleaved at the 3-coordinate Ni (figure 6.10). Around the 3-coordinate Ni ion at the surface, the Ni-O1 bond decreases by 16.7%, and the Ni-O2 bonds decrease by 6.4–6.8%. In the NiO_6 octahedra nearest the surface, one Ni-O1 bond increases by 7.2% and the second Ni-O1 bond decreases by 4.7%, and the Ni-O2 bonds show increases of 0.6–1.5%. There are two Ni-O2-Ni angles between the NiO_3 truncated octahedra at the surface and the NiO_6 octahedron

in the layer below, one decreases by 9.1% and the second increases by 0.5%, due to the displacement of the O2 ions on relaxation of the slab. On relaxation of the slab, the separation between the rocksalt layers in the {101} surface decreases by 1.1% compared to the bulk separation, to 1.82 Å.

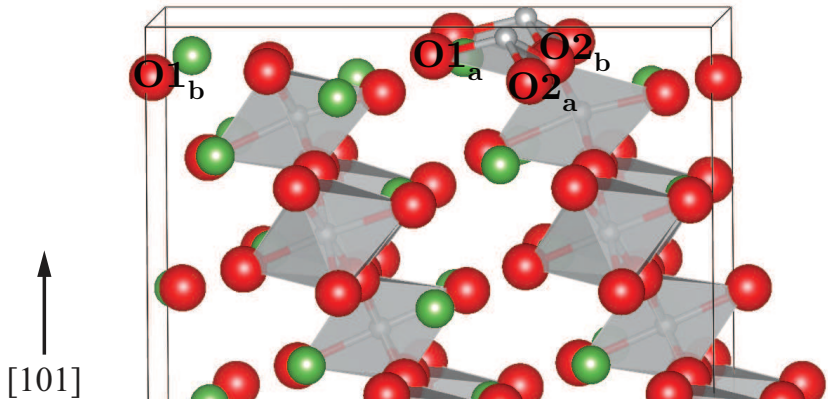

FIGURE 6.10: Relaxed surface slab of the {101} surface of La_2NiO_4. Oxygen vacancy sites are labelled with a, b

6.6.6 The {111} surface

The {111} surface is terminated by 5-coordinate La ions, 5- and 6-coordinate Ni ions, and O1 and O2 ions (1- and 2-coordinate and 2-coordinate for Ni and La ions respectively), with one Ni-O2 bond cleaved at the 5-coordinate Ni ions (figure 6.11). On relaxation of the surface slab, increases and decreases of up to 9% in the Ni-O1 bonds are observed at the surface. Below the surface, Ni-O1 bonds decrease by up to 0.3%. At the surface, the Ni-O2 bonds in the 5-coordinate octahedra increase by 0.7–0.8%, and three of the four Ni-O2 bonds in the 6-coordinate octahedra increase by 0.5–0.6%. The final Ni-O2 bond in the 6-coordinate octahedra shows a significant increase to 3.11Å, due to migration of the O2 ion towards the La-O plane. In the second layer, Ni-O2 bonds parallel to the surface decrease by 0.1–0.2%, and perpendicular to the surface, vary by -1.1–0.1%. The separation of the LaO planes increases by 8.2% compared to the bulk, to 1.99Å. The significant displacement of the O2 ions at the surface and the large increase in the LaO layer separation leads to a large relaxation energy for the {111} surface. The {111} surface has the same Ni coordination as the more stable {110} surface, and lower La coordination. It also has higher Ni coordination and lower

La coordination than the {101} surface, which is also more stable. This suggests that for Ni-terminated surfaces, the La coordination may have a greater influence on the surface stability than the Ni coordination.

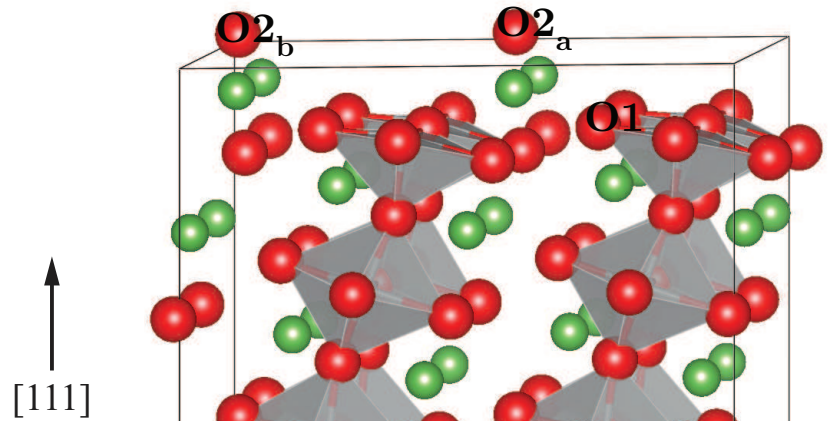

FIGURE 6.11: Relaxed surface slab of the {111} surface of La_2NiO_4. Oxygen vacancy sites are labelled with a, b

6.6.7 The {011} surface

The {011} surface is terminated by 5- and 6-coordinate La ions, 4- and 6-coordinate Ni ions and O1 and O2 ions (1- and 2-coordinate and 2-coordinate for Ni and La ions respectively), with two Ni-O2 bonds cleaved around the 4-coordinate Ni ions (figure 6.12). Significant distortion is seen in the Ni-O1 bonds on relaxation of the surface, with decreases of 8.2 and 11.5% in the Ni-O1 bonds at the 4-coordinate Ni and a decrease of 6.3% in the surface Ni-O1 bond at the 6-coordinate Ni. Below the 4-coordinate Ni, one of the Ni-O1 bonds increases by 4.7% and the second decreases by 1.7%. Below the 6-coordinate Ni one Ni-O1 bond increases by 0.3% and the second decreases by 2.5%. The changes in the Ni-O2 bonds are less significant, with those at the 4-coordinate Ni decreasing by 1.4% and two of the Ni-O2 bonds at the 6-coordinate Ni decreasing by 3.5%, with the remaining two increasing by 0.3%. In the first layer below the 4-coordinate Ni the Ni-O2 bonds increase by 0.3%, and below the 6-coordinate Ni they increase by 0.4%. Tilting of the octahedra is observed, with a decrease of 0.71% in the Ni-O2-Ni angles between the first and second layers of octahedra, and increases of 0.8–2.6% between the second and third layers. A large increase is observed in the LaO plane separation, by 5.4% to 1.94Å.

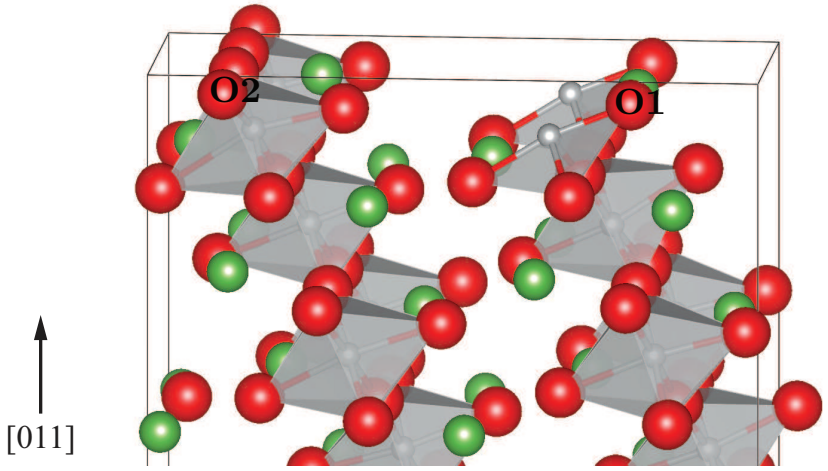

FIGURE 6.12: Relaxed surface slab of the {011} surface of La_2NiO_4. Oxygen vacancy sites are labelled with O1, O2

6.6.8 Discussion

The order of surface energy was found to be $\{010\} \approx \{100\} < \{001\} \approx \{110\} < \{101\} \approx \{111\} < \{011\}$. The coordination of the surface La and Ni affects the surface stability of the Ni-terminated surfaces. The {001} surface is the only surface that is not Ni-terminated at its most stable termination, and has the highest La coordination, but is higher in energy than the {010} and {100} surfaces. This suggests that Ni-termination can stabilise the surface. Of the Ni-terminated surfaces, those with both high La and Ni coordination were more stable, and where surfaces had the same Ni coordination, the surface with higher La coordination was more stable. The {101} surface, which has the lowest Ni coordination, but 6- and 8-coordinate La ions at the surface, was more stable than both the {111} and {011} surfaces, which have high surface Ni coordination but low La coordination. In the {001} slab, the LaO layers are parallel to the surface, so do not provide a path for oxygen diffusion through the surface via these layers, instead requiring diffusion across the perovskite layers. All other low index surfaces can provide a path for oxygen interstitial diffusion from surface to bulk through the LaO layers.

A Wulff plot of the equilibrium crystal morphology was constructed using VESTA [242], using the surface energies of the low index surfaces of La_2NiO_4. In the Wulff construction, shown in figure 6.13, the {001} surface is dominant, contributing 28% to

the total surface area. The {010}, {110}, {100} and {111} also contribute to a large percentage of the surface area, with 21%, 16%, 15% and 13% of the total surface area respectively. The {101} surface contributes the smallest percentage, at 7% and the {011} surface is not present in the calculated structure.

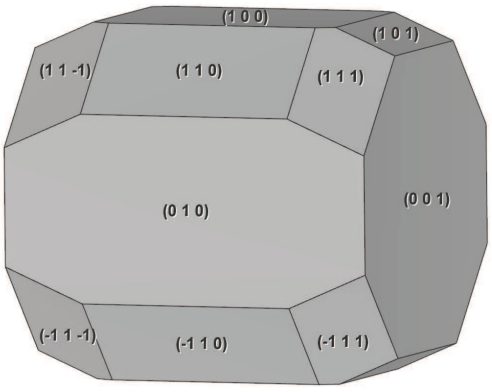

FIGURE 6.13: Wulff plot of the equilibrium crystal morphology based on surface energies of the low index surfaces of La_2NiO_4

6.6.9 La_2NiO_4 surface oxygen vacancies

The oxygen vacancy formation energies at the low index surface of La_2NiO_4, at the oxygen-rich and oxygen-poor chemical potential limits, along with the oxygen chemical potential corresponding to 700 K and $p_{O_2} = 0.21$ atm, are presented in table 6.8, and the oxygen vacancy sites are shown in figures 6.6–6.12. The calculated chemical potentials are used to calculate the oxygen vacancy formation energy at the surfaces, with 700 K chosen for surface studies as it is at the low end of the IT range and within the orthorhombic stability field. The {101} surface, which contributes the smallest percentage to the total surface area, exhibits the lowest formation energies. The $O1_b$ vacancy at the {101} surface has negative formation energy across the chemical potential range. Unlike all other surfaces, significant structural distortion is predicted on formation of the surface $O1_b$ vacancy. With the exception of those at the {011} surface, all other vacancy formation energies are high across the chemical potential range, and similar to that of the bulk system, with small local structural distortions around the oxygen vacancy. At the {010} (O1 vacancies), {001}, {110}, and {111}

TABLE 6.8: Oxygen vacancy formation energies, in eV, for the low index surfaces, at the chemical potential limits for La_2NiO_4 ($\Delta\mu_O$ = -0.39, -4.71), and under the IT-SOFC operating conditions of T = 700 K, p_{O_2} = 0.21 atm ($\Delta\mu_O$ = -0.78 eV)

		E_{Ovac} at $\Delta\mu_O = x$ (eV)		
Surface	Site	x = -0.39	-0.78	-4.71
{010}	$O1_a$	4.97	4.58	0.64
	$O1_b$	4.97	4.58	0.64
	O2	4.98	4.59	0.66
{100}	$O1_a$	4.94	4.55	0.61
	$O1_b$	5.05	4.66	0.72
	O2	4.25	3.86	-0.08
{001}	O1	4.10	3.71	-0.22
{110}	$O1_a$	5.85	5.45	1.52
	$O1_b$	5.20	4.81	0.87
	$O2_a$	3.94	3.55	-0.38
	$O2_b$	5.03	3.79	0.71
{101}	$O1_a$	3.90	3.51	-0.43
	$O1_b$	-0.95	-1.34	-5.28
	$O2_a$	3.21	2.82	-1.12
	$O2_b$	3.22	2.84	-1.00
{111}	O1	4.48	4.09	0.16
	$O2_a$	4.44	4.05	0.12
	$O2_b$	4.44	4.05	0.12
{011}	O1	0.41	0.02	-3.91
	O2	-1.06	-1.45	-5.38
Bulk	O1	5.21	4.82	0.88
	O2	4.11	3.72	-0.22

surfaces, the excess electrons are localised on Ni ions of opposite spin neighbouring the O vacancy. At the {010} (O2 vacancy), {100}, {101} and {011} surfaces, the electrons are delocalised over Ni ions with the same spin neighbouring the vacancy.

The high formation energies of oxygen vacancies in the bulk, and at the low index

surfaces, with the exception of the {101} $O1_b$ vacancy, which undergoes significant distortion on vacancy formation, indicate that oxygen vacancies are unlikely to contribute significantly to oxygen diffusion in undoped La_2NiO_4. Oxygen vacancy formation is also very low at the {011} surface, however, this surface is unstable, with a high surface energy of 2.15 eV, and is not present in the equilibrium crystal morphology. The formation of oxygen vacancies at these surfaces may improve the kinetics of the oxygen reduction and exchange reactions at the cathode surface. A study by Akbay *et al.* found that the dissociation of chemisorbed O_2 has a lower activation energy on the {001}) surface containing an oxygen vacancy than on the defect-free surface, and that oxygen vacancies act as active sites for O adsorption [110]. Further work is required to investigate the ORR at the defect-free low index surfaces and those containing oxygen vacancies of orthorhombic La_2NiO_4 to determine the active sites for the ORR.

6.6.10 La_2NiO_4 surface oxygen interstitials

At the low index surfaces, as was seen in the bulk, and under oxygen-rich conditions, interstitial formation is lower in energy than vacancy formation for all surfaces except the {101} surface. Interstitial formation was not considered for the {001} surface as oxygen migration into the surface cannot occur via the LaO layers, and the energy barrier for migration across the perovskite layers is significantly higher than through the LaO layers. Of the surfaces present in the equilibrium crystal structure, the formation energy is lowest at the {010} surface, which is significantly lower than in the bulk (0.07 eV at the surface compared to 0.42 eV in the bulk), which may lead to segregation of interstitials to this surface. There is a significant difference in the formation energy at the {010} and {100} surfaces despite the similarity of the undoped systems. On relaxation of the slab, the oxygen interstitial in the {010} surface moves away from the centre of the tetrahedron of La ions, towards a lattice oxygen, displacing the lattice oxygen towards the surface, whereas in the {100} surface the interstitial remains tetrahedrally coordinated to the La ions. This structural distortion of the {010} surface results in a lower formation energy. The interstitial formation energy increases, with decreasing oxygen chemical potential, as oxygen excess decreases. Under oxygen-poor conditions, the formation energy at the {110} surface is 0.05 eV lower than the $O2_a$

TABLE 6.9: Oxygen interstitial formation energies, in eV, for the low index surfaces, at the chemical potential limits for La_2NiO_4 ($\Delta\mu_O$ = -0.39, -4.71 eV), and under the IT-SOFC operating temperature of 700 K ($\Delta\mu_O$ = -0.78 eV)

	E_{Oi} at $\Delta\mu_O = x$ (eV)		
Surface	x = -0.39	-0.78	-4.71
{010}	0.07	0.46	4.40
{100}	0.96	1.35	5.28
{110}	1.40	1.78	5.72
{101}	1.74	2.13	6.06
{111}	0.56	0.95	4.89
{011}	-3.52	-3.13	0.80
Bulk	0.42	0.81	4.84

vacancy, and at the {101} surface, all vacancies have lower formation energies than the interstitial. At the {010}, {100} and {111} surfaces, interstitial formation is 0.80–2.41 eV lower than oxygen vacancy formation. Formation energies for both oxygen vacancies and interstitials are extremely low at the {011} surface, however, it is unstable, and not present in the equilibrium crystal morphology, so although interstitial formation energies are low, this surface termination is unlikely to be present. On formation of an oxygen interstitial, holes are delocalised over Ni ions of the same spin neighbouring the interstitial. Under the given SOFC operating conditions, interstitial formation energies are lower at all surfaces present in the equilibrium crystal morphology, with the exception of the {101} surface, which has a higher formation than the $O1_b$ vacancy. As the {101} surface contributes a smaller percentage of the surface area than the other low index surfaces, oxygen interstitials are still likely to be the dominant oxygen defect under these conditions.

6.7 La- and Ni-site doping in La_2NiO_4

The calculated chemical potentials are used to calculate the defect formation energies, and are presented in table 6.10. For alkaline earth defect formation, SOFC operating conditions of 700 K, with p_{O_2} = 0.21 atm are chosen as this is at the low end of the IT range and within the orthorhombic stability field. This corresponds to an oxygen

chemical potential of -0.78 eV, which gives La_2O_3 and NiO limits. The chemical potentials at these limits are presented in table 5.6. Isolated defects were introduced to the La_2NiO_4 supercell, in formal charge states -1 for Sr on a La site or an electron localised on Ni, +1 for Fe on a Ni site or a Ni hole, +2 for an oxygen vacancy and -2 for an oxygen interstitial. Charged defects were combined to form charge-neutral defects, representing systems where the dopants and charge compensating defects are far from each other, with their formation energies calculated from those of the individual defects. Neutral defect clusters were also considered by combining the dopant and charge compensating defect in the same supercell, considering different structural configurations, with the lowest energy systems presented here. The binding energy of the clusters was calculated from the difference between the neutral cluster and the combined isolated defects, allowing identification of defects which are stabilised when in proximity to one another compared to when they are far apart.

TABLE 6.10: Chemical potential of La, Ni, O, and the alkaline earth dopants for the given oxygen chemical potentials, in eV

	$\Delta\mu_{La}$	$\Delta\mu_{Ni}$	$\Delta\mu_{O}$	$\Delta\mu_{Sr}$	$\Delta\mu_{Fe}$
A (O-rich)	-7.46	-4.32	-0.39	-5.23	-5.86
B (O-poor)	-0.97	0.00	-4.71	-0.90	0.00
700 K (La_2O_3 limit)	-6.88	-3.94	-0.78	-4.84	-5.28
700 K (NiO limit)	-6.90	-3.88	-0.78	-4.84	-5.28

6.7.1 Combined isolated defects

The defect formation energies for combinations of isolated defects are listed in table 6.11, with the defect combinations listed using Kröger-Vink notation. When the Sr dopants and charge compensating O vacancies are far from each other, the vacancy is more likely to form on the O2 site than the O1 site. The formation energy for the combined $2Sr'_{La} + V_{O1}^{\bullet\bullet}$ is 0.58 eV higher than the $2Sr'_{La} + V_{O2}^{\bullet\bullet}$ combined defects. However, under O-rich and SOFC operating conditions, the oxygen vacancy-containing defects have significantly higher formation energies (1.96–2.01 eV for $2Sr'_{La} + V_{O1}^{\bullet\bullet}$ and 1.38–1.43 eV for $2Sr'_{La} + V_{O2}^{\bullet\bullet}$) than those of $Sr'_{La} + Ni_{Ni}^{\bullet}$. Under O-rich conditions, and

at elevated temperature under both La-richer and Ni-richer conditions, the formation energy of the $Sr'_{La} + Ni^{\bullet}_{Ni}$ defect is low (-0.02 eV, -0.00 eV and -0.03 eV respectively), indicating that when the dopant and charge compensating defect are far from each other, the defect will form easily. Under La-rich/O-poor conditions, the formation energy of the $Sr'_{La} + Ni^{\bullet}_{Ni}$ defect is 2.16 eV higher than at the O-rich/cation-poor limit (1.97 eV compared to -0.20 eV). Under SOFC operating conditions and in the O-rich environment (La-poor), the most energetically favourable combination of isolated defects is $Sr'_{La} + Ni^{\bullet}_{Ni}$, with formation energies ranging from -0.19–0.00 eV. Under SOFC operating conditions Sr-containing defects have lower formation energies at the NiO limit (-0.03–1.96 eV) than at the La_2O_3 limit (0.00–2.01 eV). Under these conditions, Fe-containing defects have lower formation energies at the La_2O_3 limit (2.33–2.59 eV) compared to at the NiO limit (2.44–2.64 eV). Charge compensation by an oxygen interstitial has lower formation energy at the O-rich limit (2.33 eV), and under SOFC operating conditions (2.33–2.44 eV), while compensation by an electron is more stable at the oxygen-poor limit (1.24 eV). Due to their high formation energies, Fe defects are unlikely to form when isolated from the charge compensating defects. The low energy of Sr doping compensated by hole formation suggests that this will contribute to increased electronic conductivity. Under SOFC operating conditions, Fe doping will be compensated by oxygen interstitials, which will improve the oxide ion conductivity, however, Fe doping will be more difficult than Sr doping.

TABLE 6.11: Formation energies of the combined isolated defects in La_2NiO_4, in eV

			700 K	
Defect	Limit A	Limit B	La_2O_3	NiO
$2Sr'_{La} + V^{\bullet\bullet}_{O1}$	2.01	2.02	2.02	1.96
$2Sr'_{La} + V^{\bullet\bullet}_{O2}$	1.43	1.43	1.43	1.38
$Sr'_{La} + Ni^{\bullet}_{Ni}$	-0.19	1.97	0.00	-0.03
$2Fe^{\bullet}_{Ni} + O''_i$	2.33	3.58	2.33	2.44
$Fe^{\bullet}_{Ni} + Ni'_{Ni}$	2.78	1.24	2.59	2.64
Fe^{X}_{La}	6.82	5.28	6.62	6.68
Sr^{X}_{Ni}	3.24	5.40	3.43	3.41

Under the chemical potential environments described by limits A (O-rich) and B (O-poor), and the La_2O_3 limit at 700 K, there is little variation in the formation energies of the oxygen-containing defects. For Sr on the La site, this is due to the change in the La and O chemical potentials being balanced by the change in the Sr chemical potential. Similarly, for Fe on the Ni site, the change in the Ni chemical potential is balanced by the change in the chemical potential of Fe and O.

The formation energies of the isovalent defects, Fe^{X}_{La} and Sr^{X}_{Ni}, are significantly higher than the aliovalent defects across the chemical potential range. This indicates that Sr defects are more likely to form on the La site than on the Ni site. Similarly, Fe defects are more likely to form on the Ni site than the La site.

6.7.2 Defect clusters

The defect formation energies for combinations of the defect clusters are listed in table 6.12. When the defects are clustered, the energy difference between the $2Sr'_{La} + V^{\bullet\bullet}_{O1}$ and $2Sr'_{La} + V^{\bullet\bullet}_{O2}$ clusters is smaller than the combined isolated systems, with the cluster containing an O2 vacancy 0.2466 eV lower than that containing an O1 vacancy. When the system is doped with Sr and compensated by formation of a vacancy on the O1 site, the system has the lowest energy when the dopants occupy La sites that are nearest neighbour and next nearest neighbour to the vacancy, and are 4.16 Å from each other, shown in figure 6.14 (a). When the charge compensating vacancy is at the O2 site, again the Sr dopants occupy La sites that are nearest neighbour and next nearest neighbour to the vacancy, but are 5.42 Å from each other, shown in figure 6.14 (b).

The binding energies of the systems are presented in table 6.12, where a negative energy indicated greater stability of the cluster and a positive energy indicates greater stability of the isolated defects. From the binding energies, it can be seen that clustering the defects lowers the energy of the $2Sr'_{La} + V^{\bullet\bullet}_{O1}$ and $2Fe^{\bullet}_{Ni} + O_i''$ clusters, showing a stabilisation when the defects occur in close proximity to one another compared to when they are isolated. Both $2Sr'_{La} + V^{\bullet\bullet}_{O2}$ and $Sr'_{La} + Ni^{\bullet}_{Ni}$ have small positive binding energies, suggesting that there is little difference in the stability of the system when the defects occur close to one another in comparison to when they are far apart. As

in the combined isolated systems, the $Sr'_{La} + Ni^{\bullet}_{Ni}$ cluster is lower in energy than the O vacancy compensated Sr defects. Under all values of chemical potential considered, $Sr'_{La} + Ni^{\bullet}_{Ni}$ is again the most stable La-site defect, with a slight negative formation energy at the O-rich/cation-poor limit.

TABLE 6.12: Formation and binding energies of the defect clusters in La_2NiO_4, in eV

			700 K		Binding energy
Defect	Limit A	Limit B	La_2O_3	NiO	
$2Sr'_{La} + V^{\bullet\bullet}_{O1}$	1.72	1.72	1.72	1.66	-0.30
$2Sr'_{La} + V^{\bullet\bullet}_{O2}$	1.47	1.47	1.47	1.42	0.04
$Sr'_{La} + Ni^{\bullet}_{Ni}$	-0.10	2.06	0.09	0.07	0.10
$2Fe^{\bullet}_{Ni} + O''_i$	0.81	2.06	0.81	0.91	-1.52
$Fe^{\bullet}_{Ni} + Ni'_{Ni}$	2.91	1.37	2.71	2.77	0.13

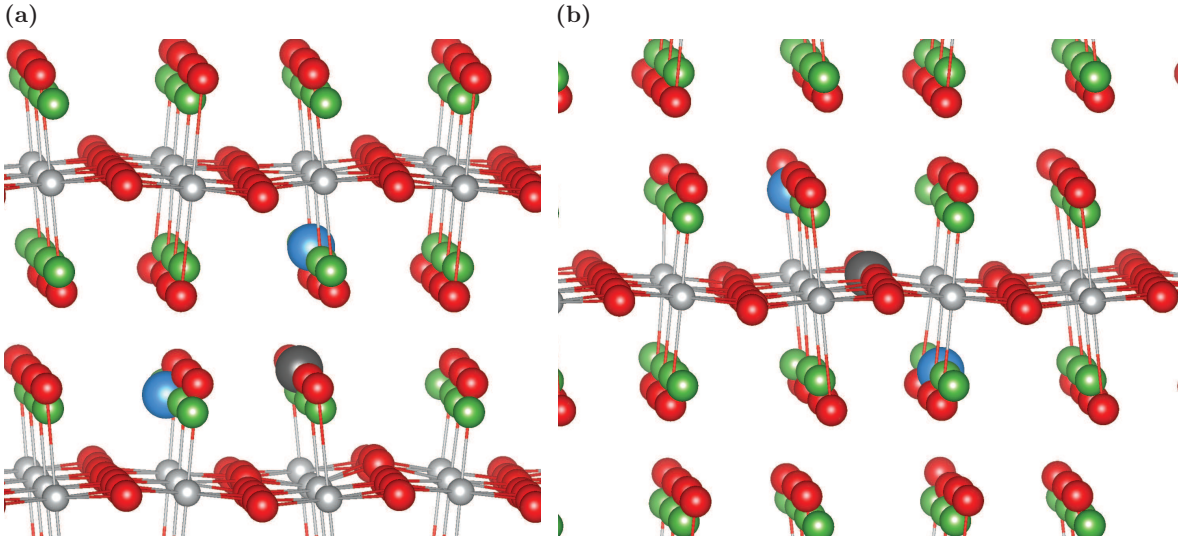

FIGURE 6.14: Structure of the defect clusters for Sr doping compensated by an O vacancy (a) shows the charge compensating O1 vacancy, (b) shows the charge compensating O2 vacancy. Sr ions are shown in blue, La ions are shown in green, Ni in grey, O in red and the vacancy site in grey

The partial EDOS of La_2NiO_4 is shown in figure 6.15 (a), the hole state in La_2NiO_4 is shown in figure 6.15 (b) and the partial EDOS of the $Sr'_{La} + Ni^{\bullet}_{Ni}$ cluster is shown in figure 6.15 (c), with the highest occupied state aligned to 0 eV. The partial EDOS

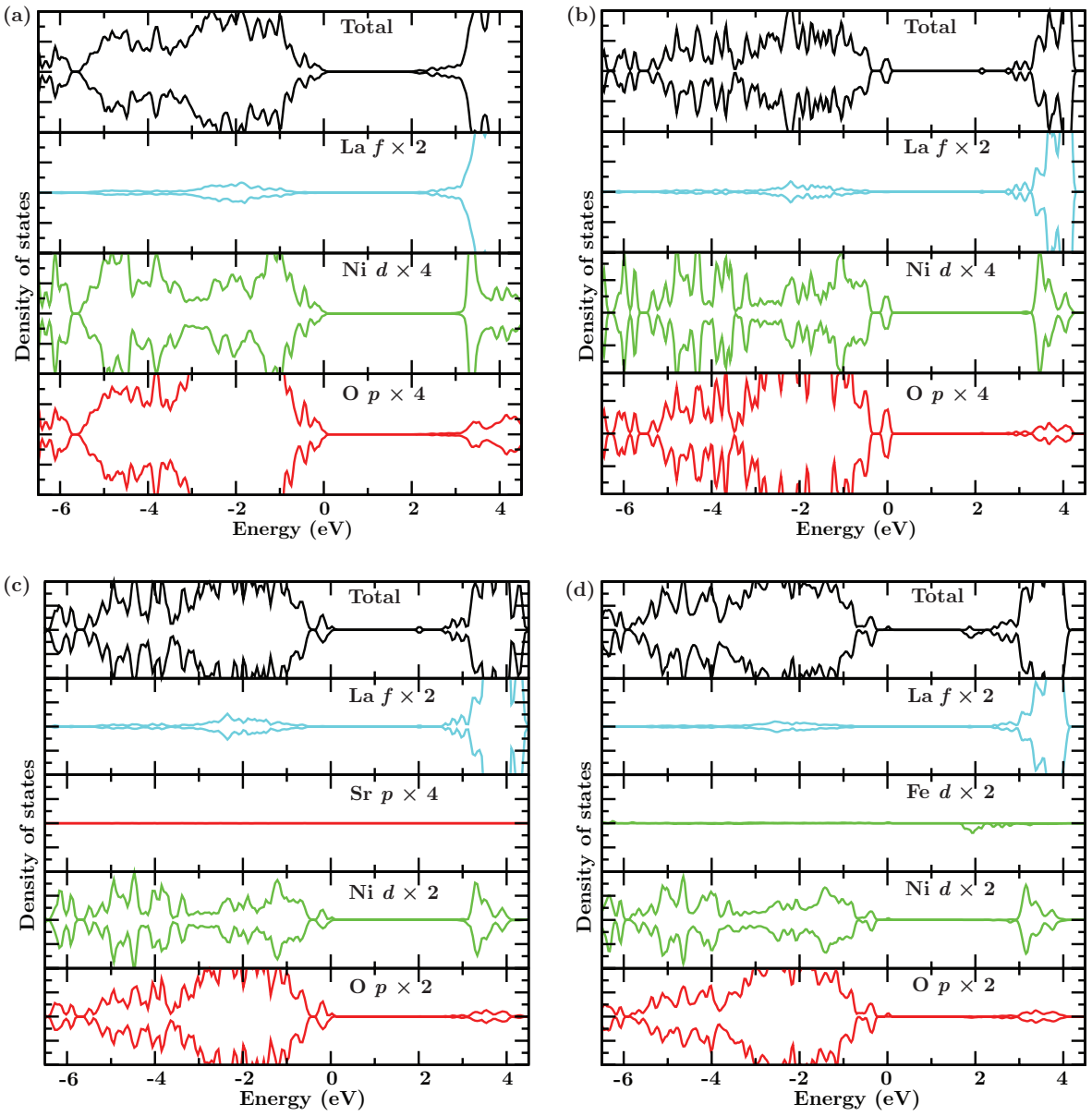

FIGURE 6.15: PEDOS of undoped and doped La_2NiO_4. (a) undoped La_2NiO_4, (b) hole state in La_2NiO_4 (c) Sr compensated by hole formation, (d) Fe compensated by an oxygen interstitial

is scaled for clarity, with the scaling shown on the plot. The partial charge density plot of the hole state in undoped La_2NiO_4 is shown in figure 6.16 (a), and shows delocalisation of the hole over the Ni and O2 atoms. A defect peak is seen at 0.07 eV in Sr-doped La_2NiO_4, which from partial charge density analysis (figure 6.16 (b)), shows delocalisation of charge over Ni ions in the layer below the defect, the nearest Ni ion in the layer above and O2 ions in the Ni-O2 layers above and below the defect, and is very similar to the hole state in undoped La_2NiO_4. These delocalised hole states

are not bound in the defect clusters, and will contribute to the electronic conductivity of La_2NiO_4.

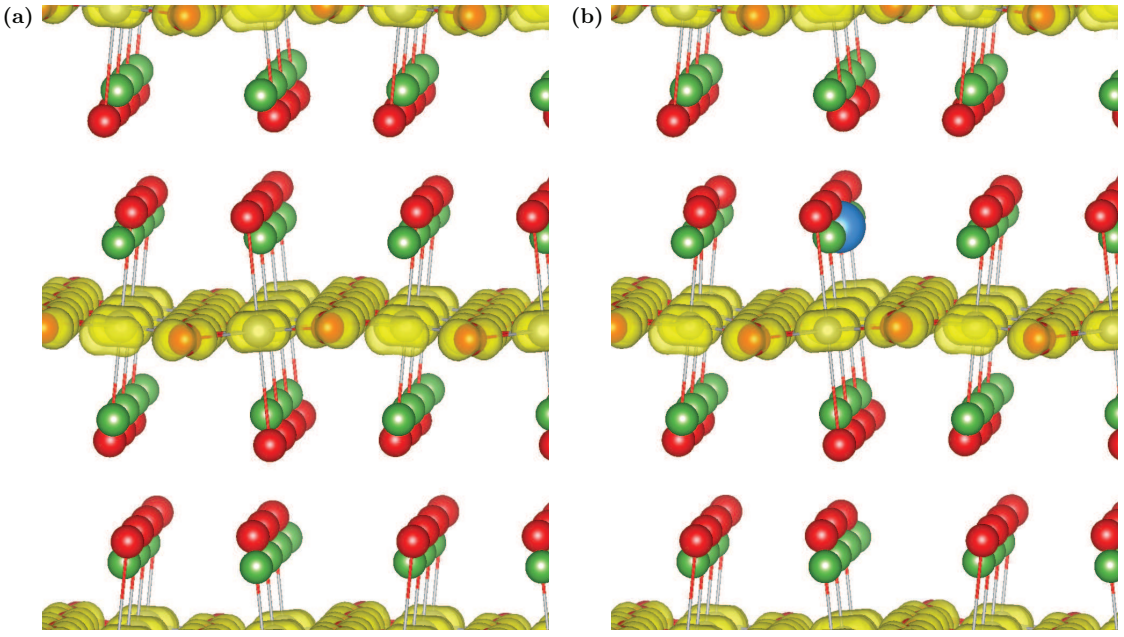

FIGURE 6.16: Partial charge density plot for the hole state in (a) undoped La_2NiO_4, and (b) in Sr-doped La_2NiO_4, at isosurface level of 0.05 eV/Å^3

A significant difference is seen in the stability of the clustered $2Fe^{\bullet}_{Ni} + O_i^{''}$ defect compared to the combined isolated defect, with a binding energy of -1.52 eV. This strong binding energy means that this defect cluster is the second most stable defect under oxygen-rich and SOFC operating conditions. The strong binding of this defect will limit the improvement in ionic conductivity that would arise from the increased oxygen interstitial concentration. As was seen for the isolated defects, $Fe^{\bullet}_{Ni} + Ni^{'}_{Ni}$ is the least stable aliovalent defect, with formation 3.01 eV higher than the most stable defect ($Sr^{'}_{La} + Ni^{\bullet}_{Ni}$) at the O-rich limit. At the extreme O-poor limit however, this becomes the most stable defect, with a formation energy of 1.37 eV, but these conditions correspond to an extremely low oxygen partial pressure which would not be experienced during SOFC operation. A decrease in stability is observed for the $Fe^{\bullet}_{Ni} + Ni^{'}_{Ni}$ cluster compared to the isolated defect. When the system is doped with Fe and the charge compensating defect is an O interstitial, the lowest energy structure is one where both the Fe atoms are in a high spin configuration and hare ferromagnetically coupled. The Fe ions are 3.62 Å and 3.64 Å from the O interstitial, which are nearest neighbour Ni

sites to it, and are 6.71 Å from each other (figure 6.17). Significant structural distortion is seen around the interstitial, with neighbouring oxygen atoms displaced outwards by 0.34–0.53 Å. The formation of oxygen interstitial on introduction of Fe to La_2NiO_4 may affect the ionic conductivity of La_2NiO_4, however, further work to investigate the ionic conductivity in undoped and doped La_2NiO_4 is required, such as the effect of co-doping, or of using different transition metal dopants to increase oxygen interstitial formation. Figure 6.15 (d) shows the partial EDOS of $2Fe_{Ni}^{\bullet} + O_i''$, with two defect peaks, one at 0 eV, in the Ni and Fe $3d$ states and O $2p$ states, and a second at $\sim$2 eV, due to Fe $3d$ states.

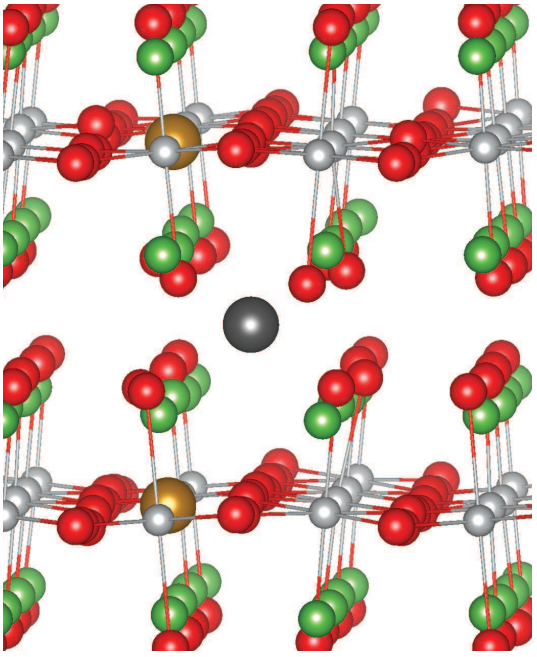

FIGURE 6.17: Structure of the defect cluster for Fe doping compensated by an O interstitial. Fe ions are shown in brown, La ions are shown in green, Ni in light grey, O in red and the oxygen interstitial in dark grey

It is possible that if both Sr and Fe dopants are introduced to the system, the defects could charge compensate. This reaction is given by

$$La_{La}^{X} + Ni_{Ni}^{X} + Sr_{E}^{X} + Fe_{E}^{X} \xrightarrow{La_2NiO_4} La_{E}^{X} + Ni_{E}^{X}Sr_{La}' + Fe_{Ni}^{\bullet} \qquad (6.17)$$

This defect cluster will be considered in future work to determine its likelihood of forming. In addition, alternative dopants to Fe will be considered to reduce the binding

energy of the $2M_{\mathrm{Ni}}^{\bullet} + \mathrm{O}_i^{''}$ defect cluster.

6.8 Conclusions

The structural and electronic properties of bulk orthorhombic La_2NiO_4 have been calculated using PBEsol + U, with $U_{\mathrm{Ni_{3d}}} = 5.3$ eV and $U_{\mathrm{O_{2p}}} = 5.5$ eV, which provides good agreement with the experimental structural and a good description of the valence band structure. The optimised structure of La_2NiO_4 was used to generate slabs for surface studies. The energies of the low index surfaces, in order of increasing energy, were found to be $\{010\} < \{100\} < \{001\} < \{110\} < \{101\} < \{111\} < \{011\}$. Ni-terminated surfaces with higher La and Ni coordination were found to be more stable, and surfaces with high La and low Ni coordination were found to be more stable than those with high Ni and low La coordination. The equilibrium crystal morphology showed that the $\{001\}$ has the largest contribution to the surface area (28%), followed by the $\{010\}$ (21%). The $\{110\}$, $\{100\}$ and $\{111\}$ surfaces also contribute to a large percentage of the surface area (16%, 15% and 13% respectively), while the $\{101\}$ surface contributes 7%. The $\{011\}$ surface is unstable, with a high surface energy of 2.15 eV, and was not present in the equilibrium morphology.

Calculations carried out on oxygen defects in bulk La_2NiO_4 show that oxygen vacancies have a lower formation energy at the O2 site than at the O1 site, and oxygen interstitials are significantly lower in energy than either oxygen vacancy, over the range of oxygen chemical potentials investigated. Oxygen interstitial migration was investigated using CI-NEB calculations, with the lowest barrier to migration occurring for the interstitialcy mechanism in the [010] direction within the LaO layers. The barrier to migration across the perovskite layers was found to be significantly higher, therefore oxygen migration is likely to occur predominantly within the LaO layers. At the low index surface, with the exception of the $\{101\}$ surface, oxygen interstitials are again the lowest energy defects, meaning that they are likely to be the dominant oxygen defect in La_2NiO_4.

The effect of introducing Sr and Fe dopants to La_2NiO_4 was investigated, considering the site selectivity and the charge compensation mechanisms for the dopants. Both of

the defects have significantly higher formation energies when introduced to isovalent sites than when introduced to aliovalent sites. The calculations predict that introduction of Sr dopants will be compensated by hole formation, with very low formation energy (0.07–0.09 eV), and the hole is delocalised over neighbouring Ni and O atoms, which will contribute to the electronic conductivity of the material. The low binding energy of $Sr'_{La} + Ni^{\bullet}_{Ni}$ indicates that the holes are not bound, so doping with Sr will lead to improved electronic conductivity. Introduction of Fe dopants is found to be compensated by the formation of oxygen interstitials under the SOFC operating conditions considered, with a formation energy of 0.81–0.91 eV for the defect cluster, which may improve the ionic conductivity of the material. However, strong binding of this cluster will limit this improvement. Further work is required to examine ionic conductivity of undoped and doped La_2NiO_4, in order to establish whether doping at the Ni site can improve the ionic conductivity for SOFC application.

Chapter 7
$LaCrO_3$ as a novel solid oxide fuel cell cathode

7.1 Introduction

One of the major issues with the use of $LaMnO_3$-based perovskite materials is their reaction with other cell components, such as Cr vapour species which form in the interconnect and can be transported to and deposited in the cathode, inhibiting the oxygen reduction reaction [91, 267–269]. $LaCrO_3$-based materials have been used as interconnects in SOFCs, as they can exhibit good electronic conductivity, good stability in oxidising and reducing atmospheres, and good compatibility with other cell components [130]. However, it has been observed that Cr gas diffuses from the interconnect to the cathode under SOFC operating conditions, which can cause degradation of the electrochemical properties of the cathode. It has been suggested that $LaCrO_3$-based materials, which are stable under oxidising conditions, such $La_{0.75}Sr_{0.25}Cr_{0.5}Mn_{0.5}O_{3-\delta}$, may be effective cathode materials, or as both cathode and anode in symmetrical SOFCs [138]. Although it has reduced electronic conductivity compared to that of Sr-doped $LaMnO_3$, it has increased redox stability, which may reduce the issues associated with Cr poisoning of the cathode. It has been shown that small amounts of Cr substituted on the Mn site of Sr-doped $LaMnO_3$ significantly reduces the conductivity with a minimum in conductivity for 5% Cr content [270], and it has been suggested that materials with a higher content of Cr may be less sensitive to the addition of Cr, and hence to Cr poisoning [138].

$LaCrO_3$ doped with M^{2+} on the La site is a *p*-type semiconductor, with the formation of holes as the charge compensating defect. The electronic conductivity has been seen to increase with increasing concentration of Sr^{2+} or Ca^{2+}, due to increased hole concentration, and with increasing temperature. Ca-doped $LaCrO_3$ is reported to show greater electronic conductivity than Sr-doped $LaCrO_3$, which is suggested to be due to the differences in the lattice distortion of the doped systems, and their stability [130]. The electronic conductivity decreases with decreasing oxygen partial pressure due to a decrease in the hole concentration under reducing conditions. Under reducing conditions, holes and oxygen vacancies are generated. This reaction is given in Kröger-Vink notation by

$$2\mathrm{h}^{\bullet} + \mathrm{O}_{\mathrm{O}}^{\mathrm{X}} \rightarrow V_{\mathrm{O}}^{\bullet\bullet} + \frac{1}{2}\mathrm{O}_2 \tag{7.1}$$

$LaCrO_3$ with Sr dopants on the La site has recently been suggested as a potential *p*-type transparent conducting oxide (TCO). TCOs are a class of materials which exhibit the seemingly exclusive properties of high electrical conductivity and optical transparency [271]. They have a carrier concentration of at least 10^{20} cm^{-3}, conductivity in the region of 10^3–10^4 Scm^{-1} and an optical band gap of greater than 3 eV, allowing them to transmit light in the visible range. TCOs have a wide variety of applications in optoelectronics, including transparent conducting electrodes of flat-panel displays, the transparent top electrode in solar cells, electromagnetic shielding and low–emissivity windows [271–273]. Currently only *n*-type materials, such as Sn-doped In_2O_3 and Al-doped ZnO exhibit high enough conductivity and optical transparency for use in these applications. Improved *p*-type materials would allow production of *p*-*n* heterojunctions, increasing their range of applications.

The development of *p*-type TCOs presents a challenge as in most wide band gap binary oxides, the top of the valence band consists primarily of O 2*p* states [183, 274, 275]. This results in the formation of deep holes localised on oxygen sites when *p*-type defects are introduced, and hence many of these materials exhibit low conductivity. In order to mitigate the problem, research has focused on materials in which the mixing of states

from multiple elements can hinder the formation of these polarons. Copper delafossites ($CuMO_2$; M = Al, Sc, Cr, In, Ga, Y, B) [276–280], d^6 spinels (AB_2O_4; A = Mg, Zn, Cd; B = Co, Rh, Ir) [281, 282] and layered oxychalcogenides ($LaCuOCh$; Ch = S, Se, Te) [283–285] have been examined as potential p-type transparent conductors, but have been found to exhibit poor visible light transparency, low conductivity, or both.

Sr doping is reported to effectively dope holes into the top of the valence band of $LaCrO_3$, resulting in p-type conductivity [286]. Thin films of Sr-doped $LaCrO_3$ were shown to exhibit an increase in conductivity, from 1.2 to 54 S cm^{-1} with an increase in Sr content from 4 to 50%, and hole concentrations of 10^{20} to $10^{21} cm^{-1}$ were observed. The optical transmission of the pure and Sr-doped $LaCrO_3$ films was also investigated, and was found to decrease from 69 to 42% with increasing Sr content. It is proposed that Sr-doped $LaCrO_3$ could be used to fabricate a *pn* heterojunction with La-doped $BaSnO_3$ for all-perovskite oxide transparent electronics.

$LaCrO_3$ is an orthorhombic perovskite, in space group *Pbnm*, with lattice parameters a = 5.513 Å, b = 5.476 Å and c = 7.759 Å [286]. As was seen in $LaMnO_3$, the orthorhombic cell is distorted relative to the ideal cubic perovskite due to a $GdFeO_3$-type distortion, which causes alternating tilting and rotation of the CrO_6 octahedra, and a Jahn-Teller distortion which results in two inequivalent oxygen sites, and three inequivalent Cr-O bond lengths. The unit cell of $LaCrO_3$ used in these calculations is shown in figure 7.1, with the La ions shown in green, Cr ions in blue, O1 ions in red, and O2 ions in orange. The occupied and unoccupied density of states of $LaCrO_3$ have previously been examined using XPS and x-ray absorption spectroscopy (XAS) [286]. The top of the valence band is reported to be made up of mixed O $2p$ and Cr $3d$ states, while the bottom of the conduction band comprises mixed Cr $3d$ and states with at least partial O $2p$ character. The lowest energy excitation in $LaCrO_3$ is reported to be a $t_{2g}^3 \rightarrow e_g^0$ transition at 2.8 eV. Zhang *et al.* also calculated the electronic structure using PBEsol + U (U_{Cr} = 3.0 eV), and determined that the states at the top of the valence band are mixed Cr $3d$ t_{2g}^3 and O $2p$ states, and the unoccupied Cr e_g^0 and t_{2g}^0 states, mixed with O $2p$ states, form the bottom of the conduction band [286].

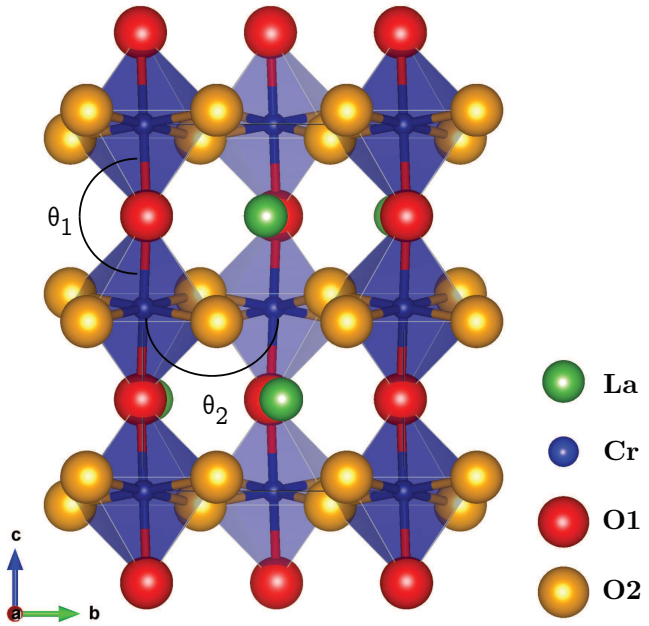

FIGURE 7.1: Unit cell of $LaCrO_3$ used in these calculations. La atoms are shown in green, Cr in blue, O1 in red and O2 in orange

This chapter examines intrinsic and extrinsic carriers in $LaCrO_3$, by performing defect analysis of undoped and $LaCrO_3$ containing Sr defects. A suitable functional for the calculation of defects in $LaCrO_3$ is determined from analysis of the EDOS and comparison to experimental spectra. The origin of charge carriers in undoped and Sr-doped $LaCrO_3$, and defect stabilities have been examined, by calculating formation energies and transition levels for each defect, and the chemical potential dependence of defect formation was investigated. Oxygen ion migration in the undoped $LaCrO_3$ system is investigated using nudged elastic band calculations to investigate whether $LaCrO_3$ would be a suitable mixed ionic and electronic conductor for use as a cathode in IT-SOFCs.

7.2 Methodology

Calculations were carried out with the GGA exchange-correlation functional, testing the PBEsol functional [154], and the hybrid HSE06 functional [162, 163]. When investigating the defect properties of a *p*-type semiconductor, it is important to accurately reproduce the character of the valence band. Standard GGA is incapable of correctly modelling the defect states of doped $LaCrO_3$ due to the approximate nature of the exchange-correlation functionals. Cr(III) ions have a partially filled *d* shell which leads

to a large SIE, a product of the highly localised nature of the $3d$ states. In addition, there is a significant contribution of Cr $3d$ and O $2p$ states to the valence band of $LaCrO_3$ [286], so upon the generation of p-type defects, standard DFT incorrectly predicts hole delocalisation over all of the Cr and O atoms in the simulation cell. In order to reduce the SIE, a $+ U$ correction using the Dudarev approach [155], was applied to Cr $3d$ states, testing values of 3.0, 3.5 and 4.0 eV to determine a suitable U parameter, and the effect of adding a $+U$ correction to the O $2p$ states was examined.

HSE06 has been shown to give an improved description of the electronic structure of many wide band gap oxides, and also significantly improves the modelling of p-type materials, compared to GGA + U [166]. However, this was not observed in our study of $LaMnO_3$, with PBEsol + U giving a better description of its structural and electronic properties, so the HSE06 functional was tested for $LaCrO_3$ to establish whether HSE06 or PBEsol + U gives a better description of the electronic structure for $LaCrO_3$. Previous studies have not included the + U on oxygen p states, which was included our of PBEsol + U calculations for $LaMnO_3$, La_2NiO_4 and $LaCrO_3$.

PAW pseudopotentials were used to describe the valence-core interactions (La: [Kr]; Cr: [Ar]; O: [He]), a plane wave cutoff of 400 eV and 3 × 3 × 2 Monkhorst-Pack [174] k-point mesh were used in bulk calculations. The structure was relaxed using the quasi-Newton RMM-DIIS algorithm [186], with electronic and ionic convergence criteria of 10^{-6} eV and 0.005 eV/Å respectively.

The system used to study the defects comprises a 2 × 2 × 2 supercell of the orthorhombic, 20 atom $LaCrO_3$ unit cell, resulting in a 160 atom supercell. To examine the conductivity of both the intrinsic and extrinsic defects, the thermodynamic transition levels of defective $LaCrO_3$ are calculated and used to plot the transition level diagrams (section 3.3.4).

The chemical potentials are found with reference to the formation energy of the pure system:

$$\Delta\mu_{\mathrm{La}} + \Delta\mu_{\mathrm{Cr}} + 3\Delta\mu_{\mathrm{O}} = \Delta H_f[\mathrm{LaCrO_3}] = -15.25 \text{ eV} \tag{7.2}$$

The limiting conditions on the chemical potentials are determined by the formation of competing phases, La_2O_3, CrO, CrO_2, and Cr_2O_3. The sum of the chemical potentials is set as equal to the formation energy, allowing a set of linear equations to be generated, which can be solved to determine intersection points of a region of stability. Chemical potential limits were calculated using CPLAP [191]. This allows a plot of the defect formation energy as a function of the Fermi energy to be made, and the dominant intrinsic and extrinsic carriers in the material can be determined.

Oxygen vacancy migration in $LaMnO_3$ was investigated using climbing image nudged elastic band calculations, considering O1-O2 and O2-O2 paths. The structures were relaxed using the L-BFGS method, with ionic and electronic convergence criteria of 0.05 ev/Å and 10^{-6} respectively.

7.3 Bulk properties of $LaCrO_3$

7.3.1 Functional testing

In order to determine a suitable functional for the calculation of defects in $LaCrO_3$, the bulk was optimised and the EDOS was calculated to compare to the experimentally reported electronic structure, measured using XPS and XAS [286], shown in red in figure 7.2.

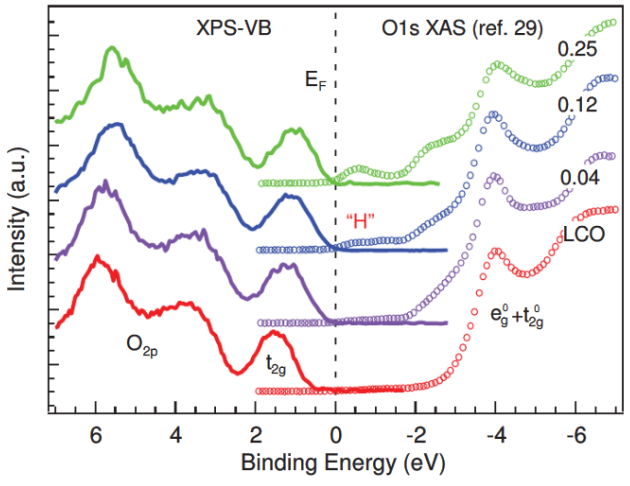

FIGURE 7.2: XPS valence band (solid lines) and O-K-edge XAS (open circles) spectra of $LaCrO_3$ (red), taken from ref. [286]

The EDOS of $LaCrO_3$, calculated using PBEsol + U, with U applied to Cr $3d$ states only, Cr $3d$ and O $2p$ states, and HSE06 are shown in figure 7.3. For the calculation with U applied to Cr only, with $U_{\mathrm{Cr}} = 3.0$ eV, figure 7.3 (a), the character of the valence band is reasonably well described, with mixed Cr $3d$ and O $2p$ states being the main contribution at the top of the valence band (from -0.9–0.0 eV), and oxygen $2p$ states below this (from -5.5–-0.9 eV). In addition, the bottom of the conduction band is predominantly Cr $3d$ states. However the density approaches zero at -0.9 eV, between the main O $2p$ and Cr $3d$ contribution to the valence band. When the value of U_{Cr} is increased, the density of states between the peaks increases. A shift in the ratio of Cr $3d$ to O $2p$ is also observed, with the amount of Cr $3d$ density at the top of the valence band decreasing with increasing U. For $U_{\mathrm{Cr}} = 3.5$ eV, figure 7.3 (b), the Cr $3d$ contribution to the peak at the top of the valence band is greater than the O $2p$, while for $U_{\mathrm{Cr}} = 4.0$ eV, figure 7.3 (c), there is little difference in the Cr $3d$ and O $2p$ contribution to the peak. The calculated band gaps are in reasonably good agreement with experiment, with values of 2.73 eV, 2.92 eV and 3.11 eV for $U_{\mathrm{Cr}} = 3.0$ eV, 3.5 eV and 4.0 eV respectively.

The inclusion of a + U correction on the O $2p$ states is required to correctly model oxygen hole states in a valence band with significant O $2p$ character. A value of 5.0 eV is chosen, which is in line with the values used for the O $2p$ states in Cr_2O_3 (5.0 eV) [184], and similar to that used for $LaMnO_3$ (5.5 eV) [287]. When both U_{Cr} and U_{O} are applied, the character of the EDOS is not changed, but increases in the band gap are observed, with values of 2.81 eV, 2.93 eV and 3.20 eV respectively. The HSE06 calculations provide a good description of the character of the valence band of $LaCrO_3$, with O $2p$ states dominant up to -0.8 eV, and Cr $3d$ states dominant at the top of the valence band. The conduction band is predicted to be predominantly Cr $3d$ states, with some O $2p$ character, also in agreement with experiment. However, the band gap is significantly overestimated, at 4.44 eV.

Based on the EDOS calculations, the PBEsol + U calculations with $U_{\mathrm{Cr}} = 3.5$ eV and $U_{\mathrm{O}} = 5.0$ eV give good agreement with experiment, and inclusion of the $+U$ correction on O $2p$ can correctly model oxygen hole states, so are used in the calculation of the

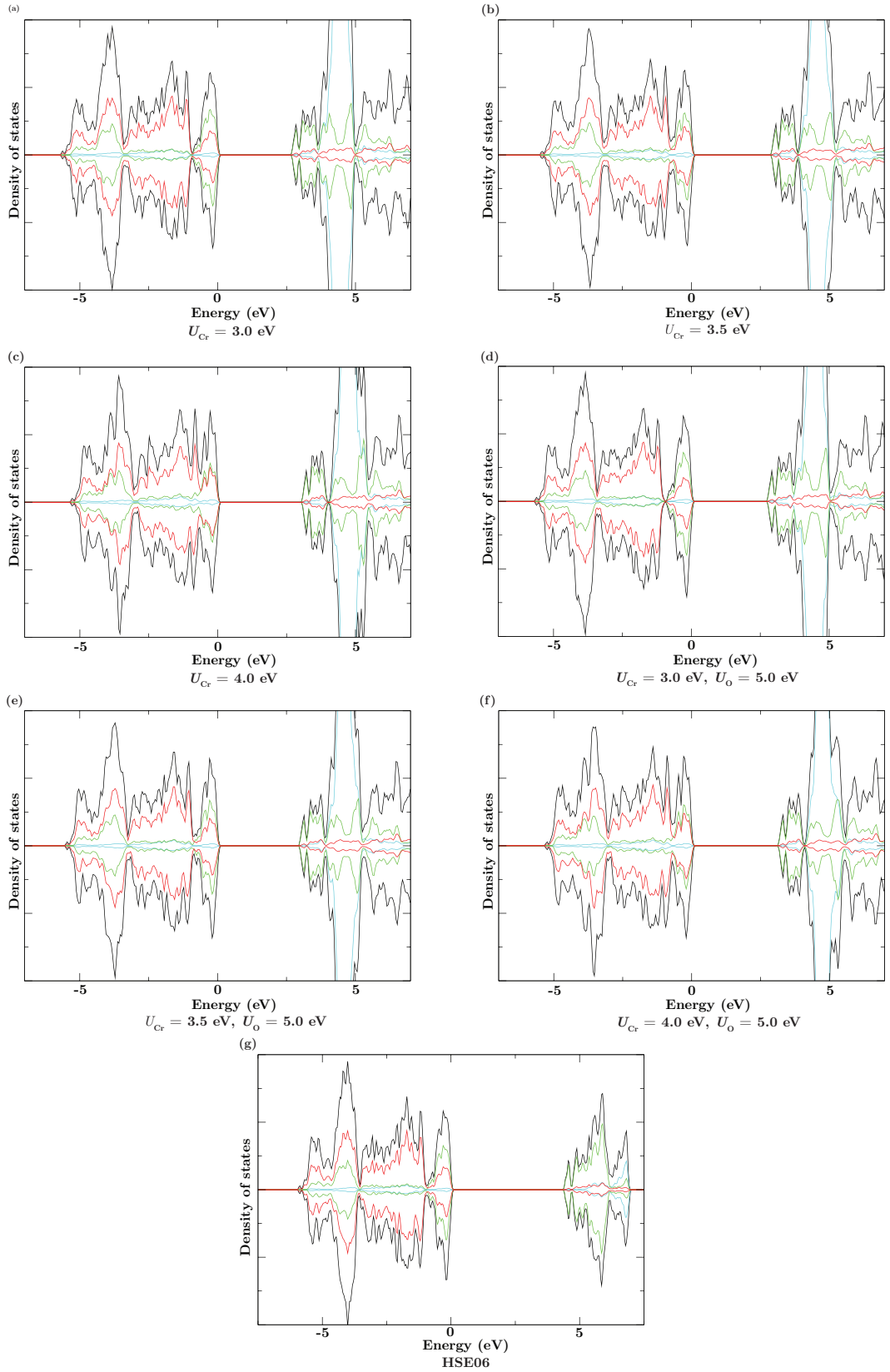

FIGURE 7.3: EDOS for $LaCrO_3$, calculated using PBEsol + U, with (a) U_{Cr} = 3.0e eV, (b) U_{Cr} = 3.5 eV, (c) U_{Cr} = 4.0 eV, (d) U_{Cr} = 3.0 eV, U_O = 5.0 eV, (e) U_{Cr} = 3.5 eV, U_{Cr} = 5.0 eV, (f) U_{Cr} = 4.0 eV, U_{Cr} = 5.0 eV, (g) HSE06. The total DOS shown in black, La f states shown in cyan, Cr d states shown in green and O p states shown in red. The VBM is aligned to 0 eV

defect properties of $LaCrO_3$. These values give a good description of the valence band in comparison to experimental spectra, and are in line with values of 3.0–3.2 eV previously applied to the Cr $3d$ states [287, 288], and the values used for the O $2p$ states in Cr_2O_3 (5.0 eV) [184].

7.3.2 PBEsol + U

The calculated lattice parameters, Cr-O bond distances and band gap for bulk $LaCrO_3$ are presented along with experimental data in table 7.1 The PBEsol+U lattice parameters and bond lengths are in good agreement with the experimental values, though the short Cr-O2 bond is overestimated by 1.8% compared to the experimental value. The calculated electronic structure is shown in figure 7.4 (a), with the total DOS shown in black, La f states shown in blue, Cr d states shown in green and oxygen p states shown in red, and is in good agreement with the electronic structure calculated previously using PBEsol + U [286]. The PBEsol + U calculations predict $LaCrO_3$ to be an indirect band gap semiconductor, with the VBM at S and the CBM at Γ, as shown in figure 7.4 (b). The calculated band gap of 2.73 eV is in good agreement with experiment.The hole effective mass at the VBM is 2.29 m_e and 3.03 m_e in the direction of R and X respectively. The relatively large values of hole effective mass are indicative of non-disperse bands, and poor hole mobility in $LaCrO_3$.

TABLE 7.1: Structural data for $LaCrO_3$, experimental data from ref. [289]. % differences between the experimental and calculated values of the structural parameters are given in parentheses

	Expt.	PBEsol + U
V (Å^3)	234.247	234.859 (0.27)
a (Å)	5.513	5.504 (-0.18)
b (Å)	5.476	5.497 (0.39)
c (Å)	7.759	7.763 (0.06)
Cr-O2$_l$ (Å)	1.997	1.983 (-0.73)
Cr-O1$_m$ (Å)	1.967	1.981 (0.68)
Cr-O2$_s$ (Å)	1.947	1.982 (1.78)

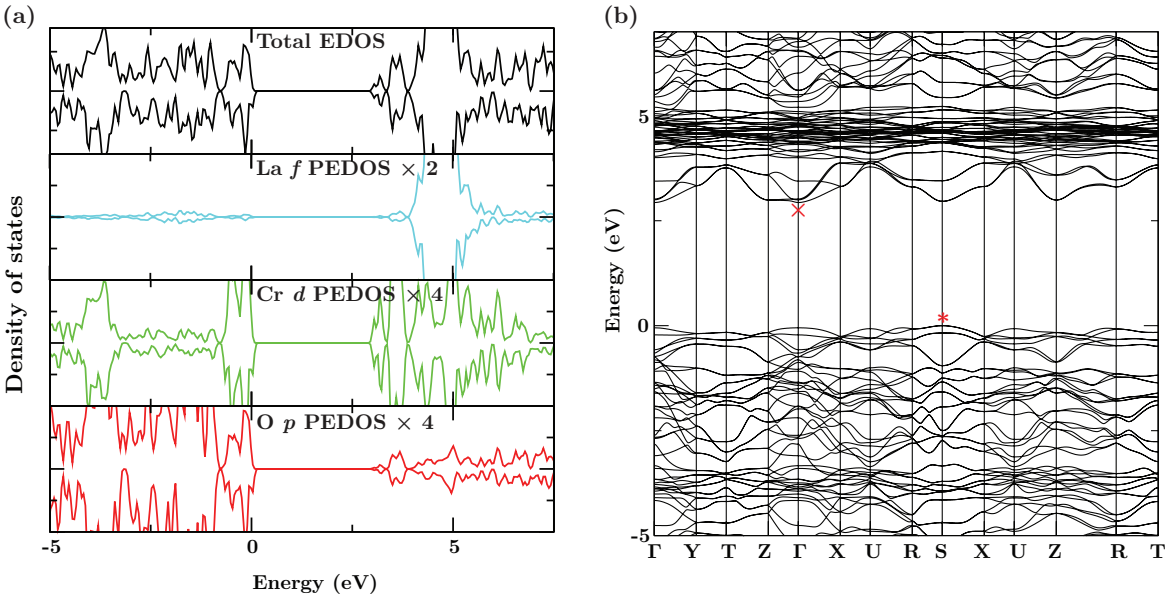

FIGURE 7.4: (a) PEDOS for $LaCrO_3$, calculated using PBEsol + U, total DOS shown in black, La f states shown in blue, Cr d states shown in green and oxygen p states shown in red. (b) Band structure for bulk $LaCrO_3$ calculated using PBEsol + U. The VBM is aligned to 0 eV in (a) and (b). The VBM and CBM are marked by a red * and × respectively

7.4 Defect properties of $LaCrO_3$

7.4.1 Thermodynamic stability of $LaCrO_3$

The chemical potential limits of $LaCrO_3$ were calculated using CPLAP [191], with the formation energies of the competing phases used in the determination of these limits are presented in table 7.2, along with their magnetic orderings. The shaded area of figure 7.5 shows the region of thermodynamic stability spanned by the La chemical potential ($\Delta\mu_{La}$) and the Cr chemical potential ($\Delta\mu_{Cr}$), with the lines showing the limits set by $LaCrO_3$ and its competing phases. The Sr chemical potential at a given O chemical potential is determined from the formation energy of the binary oxide $\Delta\mu_{Sr} + \Delta\mu_O \leq \Delta H_f^{SrO}$. The chemical potentials and the relevant competing phases at each of the limits are presented in table 7.3.

Limits A and C correspond to La-poor, Cr-poor and O-rich conditions, with $\Delta\mu_{Cr}$ higher at point A and $\Delta\mu_{La}$ higher at point C. Limits B and E are the Cr-rich limits,

TABLE 7.2: Formation energies and magnetic ordering of $LaCrO_3$ and its competing phases

Phase	Formation energy (eV)	Magnetic ordering
$LaCrO_3$	-15.25	AFM
La_2O_3	-16.21	
CrO	-4.58	AFM
CrO_2	-6.40	FM
Cr_2O_3	-13.11	AFM

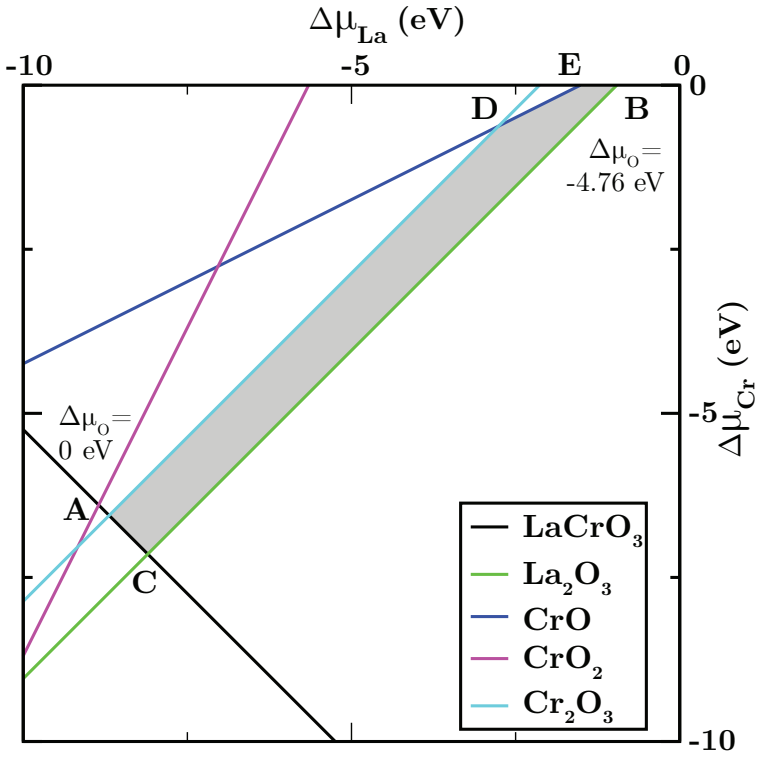

FIGURE 7.5: Thermodynamic stability field of $LaCrO_3$ spanned by $\Delta\mu_{La}$ and $\Delta\mu_{Cr}$. The coloured lines show the limits set by $LaCrO_3$ and its competing phases. Ponts A–E show the intersection points determined by these limits.

B is the La-rich and O-poor limit and E is approaching the O-poor limit and has a relatively high $\Delta\mu_{La}$. Limit D has a low $\Delta\mu_O$, relatively high $\Delta\mu_{Cr}$ and mid-range $\Delta\mu_{La}$. Defect formation energies were calculated at the chemical potentials given by two of the limits of this region of thermodynamic stability. Point A, with chemical potentials $\Delta\mu_{La}$ = -8.69 eV, $\Delta\mu_{Cr}$ = -6.56 eV, $\Delta\mu_O$ = 0.00 eV, describes the La-poor, Cr-poor and O-rich environment. Point B, with chemical potentials $\Delta\mu_{La}$ = -0.96 eV,

$\Delta\mu_{Cr}$ = 0.00 eV, $\Delta\mu_O$ = -4.76 eV, represents La-rich, Cr-rich and O-poor conditions.

TABLE 7.3: Chemical potential limits, in eV, for $LaCrO_3$, with the phases present at each limit

	$\Delta\mu_{La}$	$\Delta\mu_{Cr}$	$\Delta\mu_O$	Phases
A	-8.69	-6.56	0.00	Cr_2O_3, $LaCrO_3$
B	-0.96	0.00	-4.76	La_2O_3
C	-8.10	-7.14	0.00	La_2O_3, $LaCrO_3$
D	-2.76	-0.62	-3.96	CrO, Cr_2O_3
E	-1.51	0.00	-4.58	CrO

7.4.2 Defect formation and transition levels

The perovskite structure can accommodate A and B cation vacancies, anion vacancies, interstitials, and antisite defects. Antisite defects are those where the A cation substitutes on the B or O site, the B cation substitutes on the A or O site, or the O anion substitutes on the A or B site. The A and B cations in $LaCrO_3$ are La^{3+} and Cr^{3+} respectively, so the substitution of one for the other will not change the total charge of the system, therefore the A_B and B_A defects are not examined as they will not contribute to the conductivity. The range of intrinsic defects examined in $LaCrO_3$ is shown in figure 7.6. The *p*-type defects considered are a La vacancy (V_{La}), Cr vacancy (V_{Cr}), O interstitial (O_i), O on a La site (O_{La}), and O on a Cr site (O_{Cr}). The *n*-type defects considered are vacancies on the inequivalent O1 (V_{O1}) and O2 (V_{O2}) sites, Cr on the O1 (Cr_{O1}) and O2 (Cr_{O2}) sites, and La on the O1 (La_{O1}) and O2 (La_{O2}) sites.

The formation energies of the charges states of the defects examined are dependent on the Fermi level, as given by equation 3.5. Each of the defects has between two and six charged states: *p*-type defects have negative slope and *n*-type have positive slope. For V_{La} and V_{Cr}, 0, -1, -2 and -3; for O_i interstitials, 0, -1 and -2; and for O antisite defects, 0, -1, -2, -3, -4, -5 charge states have been calculated (there is a difference of 5 between the charge state of the cation and the O ion). The V_O defects have charge states 0, and the cation antisite defects have charge states 0, +1, +2, +3, +4 and +5. Figure 7.7 shows plots of formation energy of defects in $LaCrO_3$ at the chemical potentials

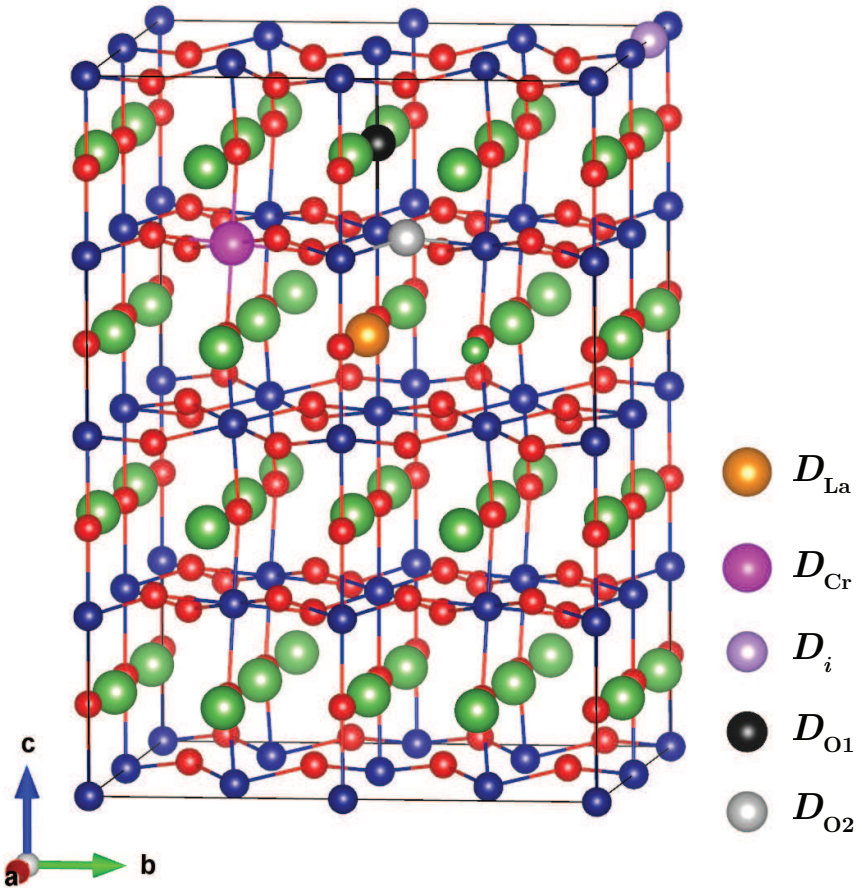

FIGURE 7.6: Sites of the point defects in the $LaCrO_3$ supercell. A defect on a La site is shown in orange, a defect on a Cr site is shown in magenta, an interstitial defect is shown in purple, and defects on the O1 and O2 sites are shown in black and grey, respectively

corresponding to O-rich (point A) and O-poor chemical potential environments, as a function of the Fermi energy between the VBM and CBM.

The formation energies of p-type defects are listed in table 7.4, along with their first ionisation levels, from which it is evident that they have lower formation energies under O-rich/La- and Cr-poor conditions. Under O-rich conditions (figure 7.7 (a)), vacancies at the La and Cr sites are the lowest energy p-type defects, with formation energies of 2.33 and 3.33 eV respectively. Both of these defects have very shallow (0/-1) transition levels, at 0.20 eV above the VBM for V_{La} and 0.06 eV above the VBM for V_{Cr}. Both of the antisite defects have high formation energies, therefore are unlikely to form in $LaCrO_3$. The oxygen interstitial has a higher formation energy than either of the cation vacancies, indicating that the formation of cation vacancies is more favourable under

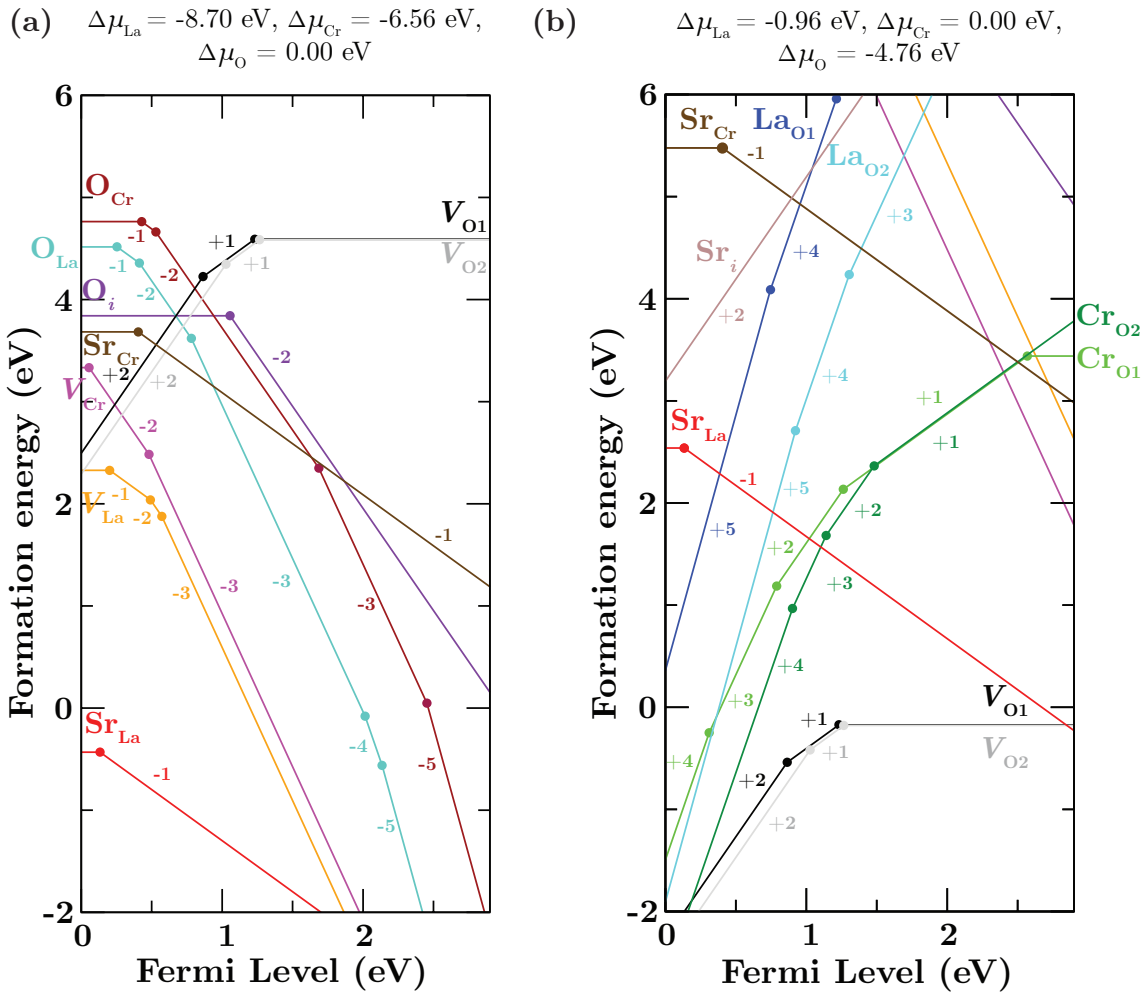

FIGURE 7.7: Transition level diagrams for point defects in $LaCrO_3$, for (a) O-rich and (b) O-poor conditions

oxygen-rich conditions. However, the intersection of the -2 state of V_{Cr} with the +2 state of V_O, will cause pinning of the Fermi level, and the relatively high formation energies of these defects indicate that *p*-type conductivity in undoped $LaCrO_3$ is unlikely. Limit C is also an O-rich environment, and is at the La_2O_3 limit (La-richer), with defects on the La site ≈0.6 eV higher than at limit A (Cr-richer), and defects on the Cr site ≈0.6 eV lower than at limit A. The formation energies of the O interstitial, O vacancies and the Sr interstitial are unchanged as $\Delta\mu_O$ and $\Delta\mu_{Sr}$ are unchanged. Under O-poor conditions, all *p*-type defects have high formation energies.

Table 7.5 lists the formation energies of *n*-type defects in $LaCrO_3$. It can be seen that *n*-type defects have significantly lower formation energies in the O-poor/La- and Cr-rich environment. Under O-rich conditions, all *n*-type defects have higher formation

TABLE 7.4: Calculated neutral defect formation energies (in eV) for p-type intrinsic defects in $LaCrO_3$ at the O-rich/La-, Cr-poor and O-poor/La-, Cr-rich chemical potential limits, and their first ionisation levels

	O-rich/La-, Cr-poor	O-poor/La-, Cr-rich	ε(0/-1)
V_{La}	2.33	10.06	0.20
V_{Cr}	3.33	9.89	0.06
O_i	3.84	8.60	1.06
O_{La}	4.52	17.01	0.25
O_{Cr}	4.76	16.08	0.43

energies than all p-type defects with the exception of the O_{Cr} antisite defect, with only oxygen vacancies having formation energies below 5 eV. Oxygen vacancies are the lowest energy intrinsic defects under oxygen-poor conditions, with formation energies of -0.17 eV and 0.18 eV for O1 and O2 vacancies respectively, followed by Cr_{O1} and Cr_{O2} which are approximately 4 eV higher, at 3.44 eV and 3.80 eV respectively. The oxygen vacancies have deep transition levels, in the middle of the band gap, therefore cannot contribute to conductivity. As all n-type defects have high formation energies, they are unlikely to form under O-rich conditions. At the low oxygen partial pressure given by the oxygen-poor limit, the antisite defects are lower in energy than at the O-rich limit, but are significantly higher in energy than the oxygen vacancies.

TABLE 7.5: Calculated neutral defect formation energies (in eV) for n-type intrinsic defects in $LaCrO_3$ at the O-rich/La-, Cr-poor and O-poor/La-, Cr-rich chemical potential limits, and their first ionisation levels

	O-rich/La-, Cr-poor	O-poor/La-, Cr-rich	ε(0/+1)
V_{O1}	4.59	-0.17	1.23
V_{O2}	4.59	-0.18	1.27
Cr_{O1}	14.76	3.44	2.57
Cr_{O2}	15.12	3.80	2.92
La_{O1}	21.02	8.53	2.67
La_{O2}	21.23	8.74	2.91

Three extrinsic defects were examined, *p*-type Sr on the La site, and Sr on the Cr site, and the *n*-type Sr interstitial, the results of which are presented in table 7.6. The calculations predict that Sr defects will form on the La-site of $LaCrO_3$ and that it will be spontaneous at the La-poor limit. The Sr_{Cr} and Sr_i defects are both significantly higher in energy than Sr_{La}, under both oxygen-rich and oxygen-poor conditions, therefore are unlikely to form in $LaCrO_3$. Sr is more likely to substitute for La than Cr due to the small mismatch between the Sr^{2+} and La^{3+} cations (1.44 Å for Sr and 1.36 Å for La [244]), compared to Cr^{3+} (0.62 Å).

TABLE 7.6: Calculated neutral defect formation energies (in eV) for extrinsic defects in $LaCrO_3$ at the chemical potential limits determined by formation of competing binary oxides, and their first ionisation levels

p-type			
	A (O-rich)	B (O-poor)	ε(0/-1)
Sr_{La}	-0.43	2.54	0.13
Sr_{Cr}	3.68	5.48	0.41
n-type			ε(0/+1)
Sr_i	14.02	9.26	2.89

The substitution of Sr for La is found to be the most favourable defect in $LaCrO_3$ under oxygen-rich conditions, and it is uncompensated for all Fermi energies over the range of the band gap. In addition, Sr_{La} has a shallow (0/-1) transition level, 0.13 eV above the VBM. The low formation energy of the Sr_{La} defect under O-rich conditions, and the shallow acceptor level of the defect indicate that Sr is a suitable *p*-type dopant for $LaCrO_3$. At the oxygen-poor limit, Sr_{La} has a formation energy 2.98 eV higher than at the oxygen-rich limit and is compensated by the Cr_{O2} for Fermi energies less than 1 eV, and thus will not contribute to *p*-type conductivity under these conditions. This indicates that Sr-doped $LaCrO_3$ has potential for *p*-type conductivity under O-rich conditions, and will not be either *p*- or *n*-type under these conditions. A recent computational study by Dabaghmanesh *et al.* [290] examined alkaline earth dopants and a subset of the defects considered here, considering the *p*-type Ca_{La}, Sr_{La} and

Ba_{La}, and n-type V_O and Cr_O. As was seen in this work, they found the alkaline-earth dopants to have low formation energy under oxygen-rich conditions, with shallow acceptor levels. However, under oxygen-poor conditions, they predicted intersection of the +1 charge state of the oxygen vacancy with a -2 charge state of the alkaline earth defects. The -2 defect state of Sr_{La} was not considered here as La is in the +3 charge state in $LaCrO_3$ and Sr is introduced in the +2 charge state, resulting in a -1 defect state, and the -2 defect state does not have a significant impact on the electronic properties. In their work, the authors did not consider the inequivalent oxygen sites in their study, only quoting one defect formation energy each for the V_O and Cr_O defects, therefore a full comparison between the results cannot be made.

7.4.3 Defect formation under SOFC operating conditions

The oxygen chemical potential under SOFC operating conditions, considering an operating temperature of 700 K, is -0.78 eV. At $\Delta\mu_O$ = -0.78 eV, the chemical potentials at the La_2O_3 and Cr_2O_3 limits of the stability field are used to determine the formation energy of the defects in $LaCrO_3$. The chemical potentials of La, Cr, O and Sr under these conditions are presented in table 7.7.

TABLE 7.7: Chemical potentials, in eV, corresponding to a SOFC operating temperature of 700 K textitp$_{O_2}$ = 0.21 atm, and p° = 1 atm

	$\Delta\mu_{La}$	$\Delta\mu_{Cr}$	$\Delta\mu_O$	$\Delta\mu_{Sr}$
La_2O_3	-6.94	-5.98	-0.78	-4.50
Cr_2O_3	-7.53	-5.39	-0.78	-4.50

Under both extremes of chemical potential under SOFC operating conditions, shown in figure 7.8, the lowest energy intrinsic defects (V_{La}, V_{Cr}, $V_{V_{O1}}$ and $V_{V_{O2}}$) have similar formation energies, which are relatively high. It can be seen from figure 7.8 that there is intersection of the charge states of the cation vacancies with those of the oxygen vacancies. At the La_2O_3 limit, for Fermi energies less than 0.76 eV the O2 vacancy acts as a charge compensating defect for the La vacancy, and for Fermi energies less than 0.60 eV it can act as a charge compensating defect for the Cr vacancy. At the Cr_2O_3 limit, the O2 vacancy is a charge compensating defect for the Cr vacancy for

Fermi energies less than 0.72 eV, and for the La vacancy for Fermi energies less than 0.65 eV. The formation energies of the neutral defects are listed in table 7.8.

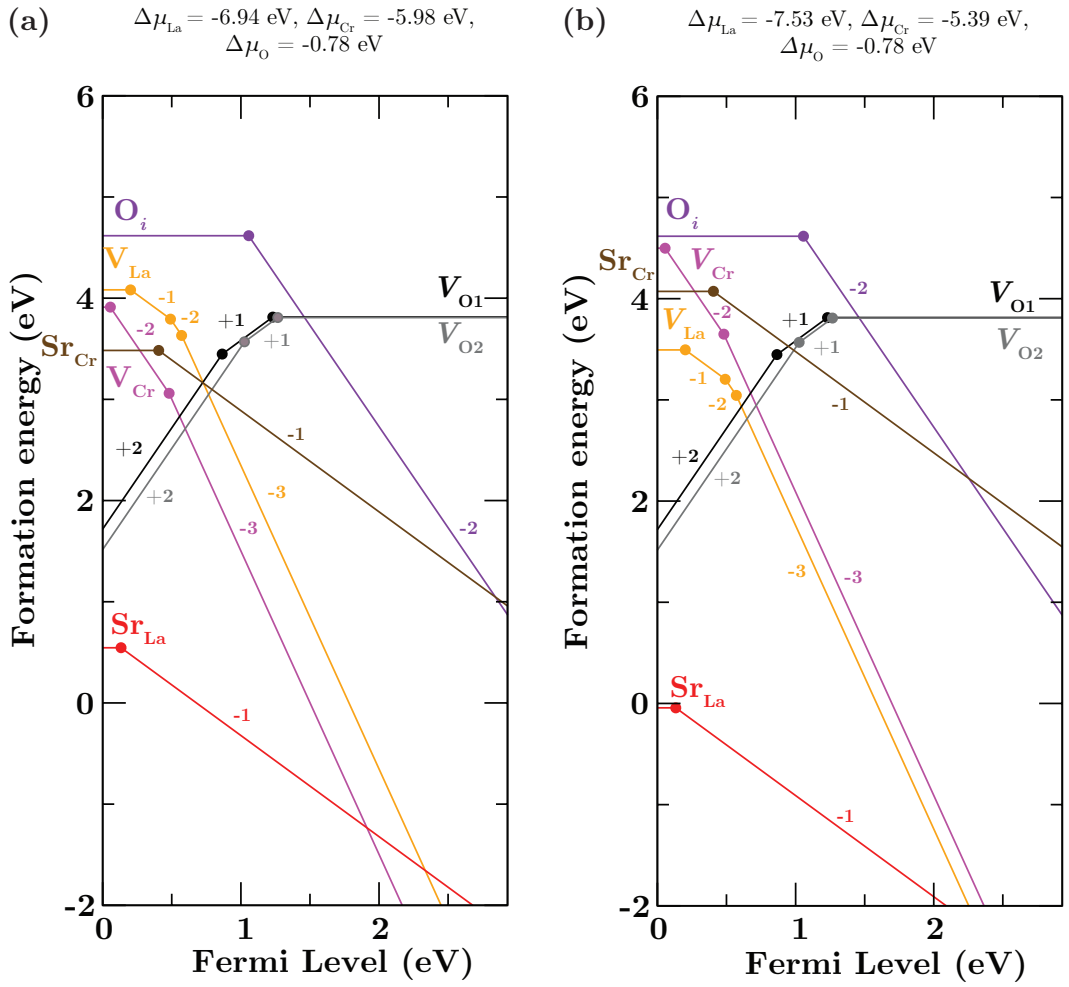

FIGURE 7.8: Transition level diagrams for point defects in $LaCrO_3$, for SOFC operating conditions, with $\Delta\mu_O$ = -0.78 eV, for the (a) La_2O_3 and (b) Cr_2O_3 limits

Under the chosen SOFC operating conditions, Sr_{La} is the lowest energy defect in $LaCrO_3$, with formation energy 0.55 eV at the La_2O_3 limit and -0.04 eV at the Cr_2O_3, and is uncompensated for all Fermi energies. The low formation energies show indicate that it will be the dominant defect under SOFC operating conditions. Due to its low formation energy, and shallow (0/-1) transition level the Sr_{La} will contribute to p-type conductivity in $LaCrO_3$. It may be possible to reduce the oxygen vacancy formation energy in $LaCrO_3$ by introducing dopants to the B-site, which will be investigated in future work.

TABLE 7.8: Calculated neutral defect formation energies (in eV) for defects in $LaCrO_3$ under SOFC operating conditions

p-type			*n*-type		
	La_2O_3 limit	Cr_2O_3 limit		La_2O_3 limit	Cr_2O_3 limt
V_{La}	4.08	3.49	V_{O1}	3.81	3.81
V_{Cr}	3.91	4.50	V_{O2}	3.81	3.81
O_i	4.62	4.62	Cr_{O1}	13.40	12.82
O_{La}	7.05	6.46	Cr_{O2}	13.76	13.17
O_{Cr}	6.12	6.71	La_{O1}	18.49	19.08
Sr_{La}	0.55	-0.04	La_{O2}	18.70	19.29
Sr_{Cr}	3.48	4.07	Sr_i	13.24	13.24

7.5 Oxygen migration in $LaCrO_3$

In $LaCrO_3$, as in $LaMnO_3$, oxygen diffusion occurs along the edges of the CrO_6 octahedra, via oxygen vacancies. Due to the distortion of the CrO_6 inequivalent oxygen sites in $LaCrO_3$, three possible oxygen migration pathways are investigated, as shown in figure 7.9. Two paths are considered from an O1 to an O2 site, one to an O2 coordinated to the central Cr by a short Cr-O bond (Cr-O_l), and the second is to an O2 coordinated to the central Cr by a long Cr-O bond (Cr-O_l). The third path considered is from an O2 site to an adjacent O2 site along the edge of the CrO_6 octahedron. The energy barriers to the migration of an oxygen vacancy in $LaCrO_3$ were calculated using climbing image nudged elastic band calculations. The O1-$O2_s$ pathway has a barrier energy of 2.07 eV in the O1-$O2_s$ direction, and the barrier for the reverse is 2.08 eV. The barrier to migration for the O1-$O2_l$ pathway is 0.07 eV lower, with an energy of 2.00 eV (2.01 eV for the reverse). The barrier energy for the O2-O2 diffusion path is similar to that of the O1-$O2_s$ path, at 2.08 eV. The results of the elastic band calculations indicate that the preferred oxygen migration pathway in $LaCrO_3$ will be $O2_l$-O1-$O2_l$-O1. However the calculated barrier energies are significantly higher than those calculated for $LaMnO_3$ (0.56–0.98 eV, section 5.4). Combined with the relatively high oxygen vacancy formation energies in $LaCrO_3$, and electronic compensation for Sr

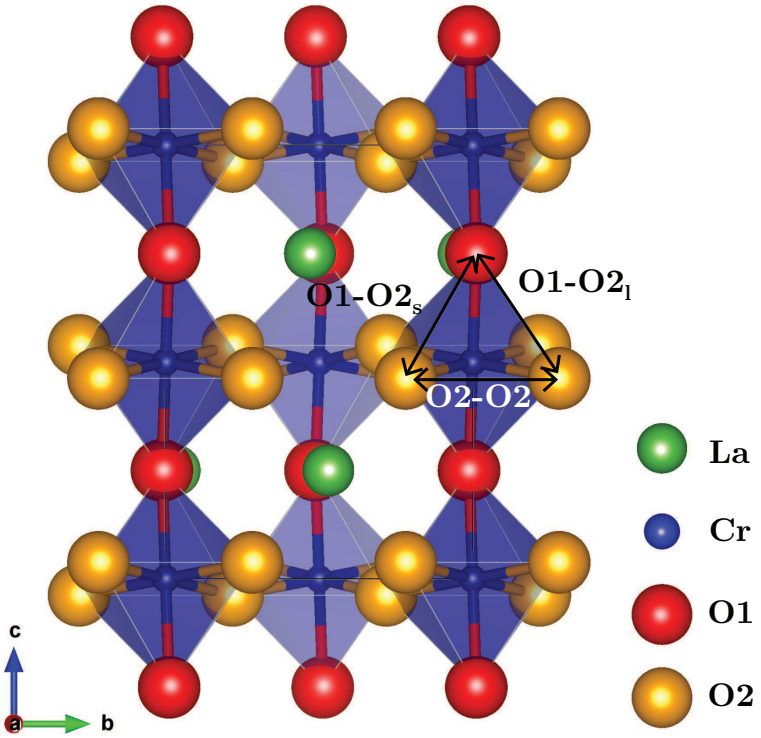

FIGURE 7.9: O1–O2$_s$, O1–O2$_l$ and O2–O2 oxygen migration paths in $LaCrO_3$

dopants under IT-SOFC operating conditions, undoped $LaCrO_3$ or Sr-doped $LaCrO_3$ is unlikely to be a suitable mixed ionic and electronic conductor for use as a cathode.

7.6 Conclusions

PBEsol + U calculations, with U_{Cr} = 3.5 eV and U_O = 5.0 eV have been found to give a good description of the structural and electronic properties of $LaCrO_3$. The formation of defects in $LaCrO_3$ has been investigated in order to determine the potential of $LaCrO_3$ and Sr-doped $LaCrO_3$ as a mixed ionic and electronic conductor for use as a cathode in SOFCs. Under oxygen-rich conditions, p-type defects dominate, with Sr_{La} having a low formation energy and shallow (0/-1) transition level, indicating potential as a p-type semiconductor. Under SOFC operating conditions (T = 700 K, p_{O_2} = 0.21 atm.), the p-type intrinsic defects are charge compensated by oxygen vacancies, but Sr substitution for La is uncompensated for all values Fermi energy in the band gap. However, oxygen vacancy formation in $LaCrO_3$ has a high energy, and the barriers to migration of oxygen vacancies from O1-O2 and O2-O2 sites are significantly higher

than that of other cathode materials, such as $LaMnO_3$. This suggests that $LaCrO_3$ will not be a preferable material for use as a mixed ionic and electronic conductor in SOFCs.

Chapter 8

Conclusions and future work

8.1 Conclusions

In this thesis, three perovskite-based materials have been investigated for use as the cathode in IT-SOFCs. First, the structure and electronic properties of $LaMnO_3$ were examined, testing PBE, PBE + U, PBEsol, PBEsol + U and HSE06 functionals. Accurate modelling of the distorted perovskite structure was found to be volume dependent, with an overestimation of the volume causing an underestimation of the Mn-O-Mn angles. In order to correctly model the electronic structure, correction for the SIE was found to be necessary, PBEsol + U ($U_{\mathrm{Mn}} = 4.5$ eV, $U_{\mathrm{O}} = 5.5$ eV) was found to best describe both the structural properties and electronic structure. Modelling of the low index surfaces found the {111} surface to be dominant, followed by the {010} and {100} surfaces. The investigation into oxygen vacancy formation in bulk $LaMnO_3$ showed that vacancies are more likely to form at the O1 site than the O2 site, while at the surfaces, the lowest energy oxygen vacancy was found to vary. Under the SOFC operating conditions investigated, oxygen vacancy formation energies at the dominant surfaces are high ($\gtrsim 2$ eV). The lowest vacancy formation energies were observed at the {101}, {001} and {011} surfaces, of which only the {001} surface is present in the equilibrium crystal morphology. Experimentally, morphology control could be used to obtain the {101} and {011} surfaces and increase oxygen vacancy concentration. Large differences in vacancy formation energy were observed for a number of the surfaces, which may lead to segregation of vacancies to the surface and hinder oxygen diffusion. Nudged elastic band calculations were used to examine oxygen vacancy migration, with energy barriers of 0.56–0.98 eV, and the migration pathway with the lowest barrier energies

predicted to be $O2_l$–O1–$O2_l$–O1. The introduction of alkaline earth defects (Mg, Ca, Sr, Ba) onto the La and Mn sites of $LaMnO_3$ showed that Mg is more likely to be substituted on the Mn site, while Ca, Sr and Ba are more likely to be substituted on the La site. At low concentration, all alkaline earth defects are compensated by hole formation, with delocalisation of the hole over Mn $3d$ and O $2p$ states. At low dopant concentration, the introduction of alkaline earth defects into $LaMnO_3$ will not increase the oxygen vacancy concentration in $LaMnO_3$, so will not improve its performance as a mixed ionic and electronic conductor.

Secondly, La_2NiO_4 was examined, investigating oxygen defect formation in the bulk and at its low index surfaces, oxygen migration, and the formation of Sr and Fe defects in bulk La_2NiO_4. In bulk La_2NiO_4, under SOFC operating conditions, oxygen vacancies are more likely to form at the O2 site than the O1 site, but oxygen interstitial formation is significantly lower in energy than oxygen vacancy formation, thus oxygen interstitials are likely to be the dominant oxygen defect. Oxygen interstitial migration in bulk La_2NiO_4 was investigated, with the barrier to migration significantly higher across the perovskite layers than within the LaO layers. The lowest energy barrier to migration was significantly lower than in $LaMnO_3$, at 0.15 eV, for an interstitialcy migration mechanism in the [010] direction, and the barrier across the perovskite layer was 1.57 eV, therefore oxygen migration is likely to occur predominantly within the LaO layers.

Modelling of the low index surfaces showed the {001} surface to be dominant. In the low index surfaces, under the SOFC operating conditions investigated, oxygen vacancies have high formation energies, with the exception of the {101} $O1_b$ vacancy, and the vacancies at the {011} surface, however, the {011} surface is unstable and not present in the equilibrium crystal morphology. Oxygen vacancies may act as active sites for oxygen adsorption, which will require further investigation. As in bulk La_2NiO_4, oxygen interstitials have lower formation energies than oxygen vacancies, with the exception of the {101} surface, where the $O1_b$ vacancy has lower formation energy. As the {101} surface contributes a smaller percentage of the total surface area, oxygen interstitials are still likely to be the dominant oxygen defect in La_2NiO_4 cathodes. In the {001} surface, the LaO layers are parallel to the surface termination, so it does not

provide a path for oxygen interstitial migration from the surface to the bulk, the other surfaces present in the crystal morphology can provide a path for interstitial migration. Investigation of doping La_2NiO_4 with Sr and Fe showed that Sr defects are more likely to form on the La site, while Fe defects form on the Ni site. Under oxygen-rich and SOFC operating conditions, doping with Sr is compensated by hole formation, which may contribute to the electronic conductivity of La_2NiO_4. Doping with Fe under these conditions is compensated by oxygen interstitial formation, which may improve the ionic conductivity of La_2NiO_4, however, the high binding energy of the defect cluster will limit this improvement.

Finally, $LaCrO_3$ was investigated as a potential SOFC cathode material. The formation energies and thermodynamic transition levels of intrinsic defects and Sr defects in bulk $LaCrO_3$ were calculated, to examine the origins of conductivity in $LaCrO_3$. Under oxygen-rich and SOFC operating conditions, *p*-type defects dominate, and Sr_{La} has a low formation energy and shallow (0/-1) transition level, and is not compensated by the formation of oxygen vacancies. This suggests that Sr-doped $LaCrO_3$ has potential as a *p*-type semiconductor. Oxygen vacancy formation in $LaCrO_3$ was also investigated, to determine whether $LaCrO_3$ is a potential mixed ionic and electronic conductor, but formation energies in undoped $LaCrO_3$ are high. In addition, the barriers to oxygen vacancies migration in $LaCrO_3$ are significantly higher than in $LaMnO_3$ or La_2NiO_4 (2.00–2.08 eV). This suggests that $LaCrO_3$, or Sr-doped $LaCrO_3$ at low Sr content will not be suitable for SOFC cathode applications.

8.2 Future work

Further work is required to determine whether the ionic conductivity of $LaMnO_3$ can be improved by doping it with lower valence cations. As recent experimental work has reported that $La_{0.7}Sr_{0.3}Mn_{1-x}Mg_xO_3$ ($x = 0.1, 0.2$) exhibits increased oxygen vacancy concentration [79], examining the effect of different dopant concentrations would be a worthwhile exercise. The use of a dipole polarizable ion model, which will be fitted to *ab initio* data (forces, stresses and dipoles), can provide an accurate forcefield which can be used to model oxide ion diffusion in Mg-doped $LaMnO_3$. The effect of dopant

concentration on diffusion will be investigated, in the bulk and at surfaces and grain boundaries.

In La_2NiO_4, as the peroxide is very close in energy to the interstitial at the centre of the tetrahedron of La ions, it will need to be considered as a competing defect, to establish whether it may have a negative impact on oxygen diffusion. Previous work on the interaction of O_2 with La_2NiO_4 surfaces has focused on the (001) surface [110]; the next step in surface studies would be to examine the ORR at all low index surfaces present in the equilibrium morphology. This would allow determination of the active sites for the ORR on La_2NiO_4. In addition, further nudged elastic band calculations are required to determine the height of the barrier to migration from the interstitial site to the peroxide state. The effect of co-doping will be investigated, considering the $Sr'_{La} + Fe^{\bullet}_{Ni}$ cluster, to determine its likelihood of forming and whether it is a competing defect under SOFC operating conditions. Alternative dopants to Fe will be considered to reduce the binding energy of the $2M^{\bullet}_{Ni} + O''_i$ defect cluster, as the high binding energy will limit any improvement to ionic conductivity caused by the increase in oxygen interstitial concentration. When the most suitable dopants for La_2NiO_4 have been established, *ab initio* data can be generated for forcefield fitting, for MD studies, similar to those on $LaMnO_3$.

It may be possible to reduce the oxygen vacancy formation energy in $LaCrO_3$ by introducing dopants to the B-site. However, due to the high activation energy for oxygen vacancy migration, and as $LaCrO_3$ is likely to exhibit better electronic conductivity, it is likely that it would be more suited to applications in electronics. As is has been suggested that introducing Cr to the Mn site of Sr-doped $LaMnO_3$ may reduce the issues associated with Cr poisoning, investigating this would be a worthwhile exercise.

In addition to simulating the oxygen diffusion in the cathode materials using MD, expansion properties can be determined, which will aid in matching cathode and electrolyte materials, so that cathode-electrolyte interfaces can be modelled. This will allow investigation of oxide ion diffusion across the interface, and cation inter-diffusion or segregation at the interface, which may influence the oxygen conductivity. From this, suitable cathode-electrolyte systems for use in IT-SOFCs may be established.

Bibliography

[1] U.S. Energy Information Administration, *Annual Energy Outlook 2017*, 2017.

[2] International Energy Agency, *Key World Energy Statistics*, 2017.

[3] BP, *BP Statistical Review of World Energy*, 2017.

[4] A. B. Stambouli and E Traversa, *Renew. Sustain. Energy Rev.* 2002, **6**, 433–455.

[5] E. D. Wachsman and K. T. Lee, *Science*, 2011, **334**, 935–939.

[6] A. Kraytsberg and Y. Ein-Eli, *Energy Fuels*, 2014, **28**, 7303–7330.

[7] T. Yoshida and K. Kojima, *Interface Mag.* 2015, **24**, 45–49.

[8] H. Liu, C. Song, L. Zhang, J. Zhang, H. Wang, and D. P. Wilkinson, *J. Power Sources*, 2006, **155**, 95–110.

[9] E. Gülzow, *Fuel Cells*, 2004, **4**, 251–255.

[10] G. Mulder, P. Coenen, A. Martens, and J. Spaepen, *Int. J. Hydrogen Energy*, 2008, **33**, 3220–3224.

[11] N. Sammes, R. Bove, and K. Stahl, *Curr. Opin. Solid State Mater. Sci.* 2004, **8**, 372–378.

[12] S. R. Choudhury, in *Recent Trends Fuel Cell Sci. Technol.* Springer New York, New York, NY, pp. 188–216.

[13] M. Bischoff, *J. Power Sources*, 2006, **160**, 842–845.

[14] K. Eguchi, H. Kojo, T. Takeguchi, R. Kikuchi, and K. Sasaki, *Solid State Ionics*, 2002, **152-153**, 411–416.

[15] M. Lo Faro, V. Antonucci, P. L. Antonucci, and A. S. Aricò, *Fuel*, 2012, **102**, 554–559.

[16] S. D. Nobrega, P. Gelin, S. Georges, M. C. Steil, B. L. Augusto, F. B. Noronha, and F. C. Fonseca, *J. Electrochem. Soc.* 2014, **161**, F354–F359.

[17] L. Chick, M. Weimar, G. Whyatt, and M. Powell, *Fuel Cells*, 2015, **15**, 49–60.

[18] J. A. Kilner and M. Burriel, *Annu. Rev. Mater. Res.* 2014, **44**, 365–393.

[19] J. Fleig and J. Maier, *J. Eur. Ceram. Soc.* 2004, **24**, 1343–1347.

[20] M. Johnsson and P. Lemmens, *J. Phys.: Condens. Matter*, 2008, **20**, 264001.

[21] R. J. Cava, B. Batlogg, J. J. Krajewski, R. Farrow, L. W. Rupp, A. E. White, K. Short, W. F. Peck, and T. Kometani, *Nature*, 1988, **332**, 814–816.

[22] Y Tokura and Y Tomioka, *J. Magn. Magn. Mater.* 1999, **200**, 1–23.

[23] T. Kimura, T. Goto, H. Shintani, K. Ishizaka, T. Arima, and Y. Tokura, *Nature*, 2003, **426**, 55–58.

[24] G. H. Haertling, *J. Am. Ceram. Soc.* 1999, **82**, 797–818.

[25] K. Uchino, *Sci. Technol. Adv. Mater.* 2015, **16**, 046001.

[26] H. J. Kim, U. Kim, T. H. Kim, J. Kim, H. M. Kim, B.-G. Jeon, W.-J. Lee, H. S. Mun, K. T. Hong, J. Yu, K. Char, and K. H. Kim, *Phys. Rev. B*, 2012, **86**, 165205.

[27] Q. Liu, J. Dai, X. Zhang, G. Zhu, Z. Liu, and G. Ding, *Thin Solid Films*, 2011, **519**, 6059–6063.

[28] M. Johnsson and P. Lemmens, in *Handb. Magn. Adv. Magn. Mater.* John Wiley & Sons, Ltd, Chichester, UK, 2007.

[29] V. M. Goldschmidt, *Die Naturwissenschaften*, 1926, **14**, 477–485.

[30] P. M. Woodward, *Acta Crystallogr. Sect. B Struct. Sci.* 1997, **53**, 32–43.

[31] H. A. Jahn and E. Teller, *Proc. R. Soc. A Math. Phys. Eng. Sci.* 1937, **161**, 220–235.

[32] A. Orera and P. R. Slater, *Chem. Mater.* 2010, **22**, 675–690.

[33] A. Berenov, H. Wood, and A. Atkinson, *J. Electrochem. Soc.* 2007, **154**, B1362.

[34] E. O. Ahlgren and F. W. Poulsen, *Solid State Ionics*, 1996, **86-88**, 1173–1178.

[35] A. J. Jacobson, *Chem. Mater.* 2010, **22**, 660–674.

[36] S. P. Jiang, *J. Mater. Sci.* 2008, **43**, 6799–6833.

[37] S. T. Aruna, M. Muthuraman, and K. C. Patil, *J. Mater. Chem.* 1997, **7**, 2499–2503.

[38] A. Endo, M. Ihara, H. Komiyama, and K. Yamada, *Solid State Ionics*, 1996, **86-88**, 1191–1195.

[39] I. Yasuda, K. Ogasawara, M. Hishinuma, K. T., and M. Dokiya, *Solid State Ionics*, 1996, **86-88**, 1197–1201.

[40] K. T. Lee and A. Manthiram, *J. Electrochem. Soc.* 2006, **153**, A794.

[41] L.-W. Tai, M. M. Nasrallah, H. U. Anderson, D. M. Sparlin, and S. R. Sehlin, *Solid State Ionics*, 1995, **76**, 273–283.

[42] B. Wei, Z. Lü, X. Huang, J. Miao, X. Sha, X. Xin, and W. Su, *J. Eur. Ceram. Soc.* 2006, **26**, 2827–2832.

[43] E. Boehm, J. Bassat, P. Dordor, F. Mauvy, J. Grenier, and P. Stevens, *Solid State Ionics*, 2005, **176**, 2717–2725.

[44] A. Tarancón, D. Marrero-López, J. Peña-Martinez, J. Ruiz-Morales, and P. Núñez, *Solid State Ionics*, 2008, **179**, 611–618.

[45] M. Burriel, J. Peña-Martínez, R. J. Chater, S. Fearn, A. V. Berenov, S. J. Skinner, and J. A. Kilner, *Chem. Mater.* 2012, **24**, 613–621.

[46] L. Zhao, J. Shen, B. He, F. Chen, and C. Xia, *Int. J. Hydrogen Energy*, 2011, **36**, 3658–3665.

[47] H. Hayashi, M. Watanabe, and H. Inaba, *Thermochim. Acta*, 2000, **359**, 77–85.

[48] S. Gupta, M. K. Mahapatra, and P. Singh, *Mater. Sci. Eng. R Reports*, 2015, **90**, 1–36.

[49] B. C. H. Steele, *Solid State Ionics*, 2000, **129**, 95–110.

[50] S. Y. Gómez and D. Hotza, *Renew. Sustain. Energy Rev.* 2016, **61**, 155–174.

[51] A. Manthiram, J.-H. H. Kim, Y. N. Kim, and K.-T. T. Lee, *J. Electroceram.* 2011, **27**, 93–107.

[52] A Petric, H Peng, and F Tietz, *Solid State Ionics*, 2000, **135**, 719–725.

[53] D. Marinha, J. Hayd, L. Dessemond, E. Ivers-Tiffée, and E. Djurado, *J. Power Sources*, 2011, **196**, 5084–5090.

[54] C. Sun, R. Hui, and J. Roller, *J. Solid State Electrochem.* 2010, **14**, 1125–1144.

[55] A. Aguadero, L. Fawcett, S. Taub, R. Woolley, K.-T. T. Wu, N. Xu, J. A. Kilner, and S. J. Skinner, *J. Mater. Sci.* 2012, **47**, 3925–3948.

[56] D. Rembelski, J. P. Viricelle, L. Combemale, and M. Rieu, *Fuel Cells*, 2012, **12**, 256–264.

[57] S. Švarcová, K. Wiik, J. Tolchard, H. J. M. Bouwmeester, and T. Grande, *Solid State Ionics*, 2008, **178**, 1787–1791.

[58] A. Tarancón, S. J. Skinner, R. J. Chater, F. Hernández-Ramírez, and J. A. Kilner, *J. Mater. Chem.* 2007, **17**, 3175.

[59] J.-H. Kim and A. Manthiram, *J. Mater. Chem. A*, 2015, **3**, 24195–24210.

[60] G. Ehora, S. Daviero-Minaud, M. C. Steil, L. Gengembre, M. Frere, S. Bellayer, and O. Mentre, *Chem. Mater.* 2008, **20**, 7425–7433.

[61] R. Doshi, V. L. Richards, J. D. Carter, X. Wang, and M. Krumpelt, *J. Electrochem. Soc.* 1999, **146**, 1273.

[62] Z. Gao, L. V. Mogni, E. C. Miller, J. G. Railsback, and S. A. Barnett, *Energy Environ. Sci.* 2016, **9**, 1602–1644.

[63] *Proceedings of The Electrochemical Society*, ed. S. C. Singhal and H. Iwahara, 1993, p. 205.

[64] A. Hammouche, E. Siebert, and A. Hammou, *Mater. Res. Bull.* 1989, **24**, 367–380.

[65] V. B. Podobedov, A. Weber, D. B. Romero, J. P. Rice, and H. D. Drew, *Phys. Rev. B*, 1998, **58**, 43–46.

[66] F. Zheng and L. R. Pederson, *J. Electrochem. Soc.* 1999, **146**, 2810.

[67] J. Hemberger, A. Krimmel, T. Kurz, H.-A. Krug von Nidda, V. Y. Ivanov, A. A. Mukhin, A. M. Balbashov, and A. Loidl, *Phys. Rev. B*, 2002, **66**, 094410.

[68] J. M. Ralph, A. C. Schoeler, and M. Krumpelt, *J. Mater. Sci.* 2001, **36**, 1161–1172.

[69] J. H. Kuo, H. U. Anderson, and D. M. Sparlin, *J. Solid State Chem.* 1990, **87**, 55–63.

[70] A. Hammouche, E. J. L Schouler, and M. Henault, *Solid State Ionics*, 1988, **28-30**, 1205–1207.

[71] H. Yokokawa, N. Sakai, T. Kawada, and M. Dokiya, *Solid State Ionics*, 1990, **40-41**, 398–401.

[72] J. Mizusaki, Y. Yonemura, H. Kamata, K. Ohyama, N. Mori, H. Takai, H. Tagawa, M. Dokiya, K. Naraya, T. Sasamoto, H. Inaba, and T. Hashimoto, *Solid State Ionics*, 2000, **132**, 167–180.

[73] H. Kamata, Y. Yonemura, J. Mizusaki, H. Tagawa, K. Naraya, and T.-i. Sasamoto, *J. Phys. Chem. Solids*, 1995, **56**, 943–950.

[74] H. Kozuka, K. Ohbayashi, and K. Koumoto, *Sci. Technol. Adv. Mater.* 2015, **16**, 026001.

[75] S. Carter, A. Selcuk, R. J. Chater, J. Kajda, J. Kilner, and B. C. H. Steele, *Solid State Ionics*, 1992, **53-56**, 597–605.

[76] R. A. De Souza, J. A. Kilner, and J. F. Walker, *Mater. Lett.* 2000, **43**, 43–52.

[77] S. Fearn, J. Rossiny, J. Kilner, and J. Evans, *Solid State Ionics*, 2012, **211**, 51–57.

[78] E. Navickas, T. M. Huber, Y. Chen, W. Hetaba, G. Holzlechner, G. Rupp, M. Stöger-Pollach, G. Friedbacher, H. Hutter, B. Yildiz, and J. Fleig, *Phys. Chem. Chem. Phys.* 2015, **17**, 7659–7669.

[79] L. Gan, Q. Zhong, X. L. Zhao, Y. Song, and Y. F. Bu, *J. Alloy. Compd.* 2016, **655**, 99–105.

[80] Y. Ji, J. Kilner, and M. Carolan, *Solid State Ionics*, 2005, **176**, 937–943.

[81] M. Backhaus-Ricoult, *Solid State Ionics*, 2006, **177**, 2195–2200.

[82] Y. Chen, L. Yang, F. Ren, and K. An, *Sci. Reports*, 2015, **4**, 5179.

[83] A. Mitterdorfer and L. J. Gauckler, *Solid State Ionics*, 1998, **111**, 185–218.

[84] H. Yokokawa, N. Sakai, T. Kawada, and M. Dokiya, *J. Electrochem. Soc.* 1991, **138**, 2719.

[85] H. Yokokawa, T. Horita, N. Sakai, M. Dokiya, and T. Kawada, *Solid State Ionics*, 1996, **86-88**, 1161–1165.

[86] H. Yokokawa, *Annu. Rev. Mater. Res.* 2003, **33**, 581–610.

[87] E. Perry Murray and S. A. Barnett, *Solid State Ionics*, 2001, **143**, 265–273.

[88] K. Huang, M. Feng, J. B. Goodenough, and M. Schmerling, *J. Electrochem. Soc.* 1996, **143**, 3630.

[89] R. Pelosato, I. N. Sora, G. Dotelli, R. Ruffo, and C. Mari, *J. Eur. Ceram. Soc.* 2005, **25**, 2587–2591.

[90] S. C. Paulson and V. I. Birss, *J. Electrochem. Soc.* 2004, **151**, A1961.

[91] S. Badwal, R. Deller, K. Foger, Y. Ramprakash, and J. Zhang, *Solid State Ionics*, 1997, **99**, 297–310.

[92] J. J. Bentzen, J. V. T. Høgh, R. Barfod, and A. Hagen, *Fuel Cells*, 2009, **9**, 823–832.

[93] I. Solovyev, N. Hamada, and K. Terakura, *Phys. Rev. Lett.* 1996, **76**, 4825–4828.

[94] H. Sawada, Y. Morikawa, K. Terakura, and N. Hamada, *Phys. Rev. B*, 1997, **56**, 12154–12160.

[95] D. Fuks, S. Dorfman, J. Felsteiner, L. Bakaleinikov, A. Gordon, and E. A. Kotomin, *Solid State Ionics*, 2004, **173**, 107–111.

[96] T. Hashimoto, S. Ishibashi, and K. Terakura, *Phys. Rev. B*, 2010, **82**, 045124.

[97] E. A. Ahmad, L. Liborio, D. Kramer, G. Mallia, A. R. Kucernak, and N. M. Harrison, *Phys. Rev. B*, 2011, **84**, 085137.

[98] J. He, M.-X. Chen, X.-Q. Chen, and C. Franchini, *Phys. Rev. B*, 2012, **85**, 195135.

[99] D. Muñoz, N. M. Harrison, and F. Illas, *Phys. Rev. B*, 2004, **69**, 085115.

[100] J. He and C. Franchini, *Phys. Rev. B*, 2012, **86**, 235117.

[101] E. A. Kotomin, Y. A. Mastrikov, E. Heifets, and J. Maier, *Phys. Chem. Chem. Phys.* 2008, **10**, 4644.

[102] Y. A. Mastrikov, E. Heifets, E. A. Kotomin, and J. Maier, *Surf. Sci.* 2009, **603**, 326–335.

[103] Y. Choi, D. S. Mebane, M. C. Lin, and M. Liu, *Chem. Mater.* 2007, **19**, 1690–1699.

[104] S. Piskunov, E. Heifets, T. Jacob, E. A. Kotomin, D. E. Ellis, and E. Spohr, *Phys. Rev. B*, 2008, **78**, 121406.

[105] E. A. Ahmad, G. Mallia, D. Kramer, A. R. Kucernak, and N. M. Harrison, *J. Mater. Chem. A*, 2013, **1**, 11152.

[106] J. D. Jorgensen, B. Dabrowski, S. Pei, D. R. Richards, and D. G. Hinks, *Phys. Rev. B*, 1989, **40**, 2187–2199.

[107] L. Minervini, R. W. Grimes, J. A. Kilner, and K. E. Sickafus, *J. Mater. Chem.* 2000, **10**, 2349–2354.

[108] D. M. Halat, R. Dervişoğlu, G. Kim, M. T. Dunstan, F. Blanc, D. S. Middlemiss, and C. P. Grey, *J. Am. Chem. Soc.* 2016, **138**, 11958–11969.

[109] J. Rodriguez-Carvajal, M. T. Fernandez-Diaz, and J. L. Martinez, *J. Phys.: Condens. Matter*, 1991, **3**, 3215–3234.

[110] T. Akbay, A. Staykov, J. Druce, H. Téllez, T. Ishihara, and J. A. Kilner, *J. Mater. Chem. A*, 2016, **4**, 13113–13124.

[111] J. Bassat, P. Odier, A. Villesuzanne, C. Marin, and M. Pouchard, *Solid State Ionics*, 2004, **167**, 341–347.

[112] C. Munnings, S. Skinner, G. Amow, P. Whitfield, and I. Davidson, *Solid State Ionics*, 2005, **176**, 1895–1901.

[113] M. Burriel, G. Garcia, J. Santiso, J. A. Kilner, R. J. Chater, and S. J. Skinner, *J. Mater. Chem.* 2008, **18**, 416–422.

[114] A. Aguadero, M. J. Escudero, M. Pérez, J. A. Alonso, V. Pomjakushin, and L. Daza, *Dalt. Trans.* 2006, 4377–4383.

[115] T. Nakamura, Y. Ling, and K. Amezawa, *J. Mater. Chem. A*, 2015, **3**, 10471–10479.

[116] T. Nakamura, K. Yashiro, K. Sato, and J. Mizusaki, *Solid State Ionics*, 2009, **180**, 368–376.

[117] T. Nakamura, K. Yashiro, K. Sato, and J. Mizusaki, *Solid State Ionics*, 2009, **180**, 1406–1413.

[118] E. Tsipis, E. Naumovich, M. Patrakeev, J. Waerenborgh, Y. Pivak, P. Gaczyński, and V. Kharton, *J. Phys. Chem. Solids*, 2007, **68**, 1443–1455.

[119] A. R. Gilev, E. A. Kiselev, and V. A. Cherepanov, *J. Mater. Chem. A*, 2018, **6**, 5304–5312.

[120] J. Druce, H. Téllez, M. Burriel, M. D. Sharp, L. J. Fawcett, S. N. Cook, D. S. McPhail, T. Ishihara, H. H. Brongersma, and J. A. Kilner, *Energy Environ. Sci.* 2014, **7**, 3593–3599.

[121] M. Burriel, S. Wilkins, J. P. Hill, M. A. Muñoz-Márquez, H. H. Brongersma, J. A. Kilner, M. P. Ryan, and S. J. Skinner, *Energy Environ. Sci.* 2014, **7**, 311–316.

[122] J. Wu, S. S. Pramana, S. J. Skinner, J. A. Kilner, and A. P. Horsfield, *J. Mater. Chem. A*, 2015, **3**, 23760–23767.

[123] R. Sayers, J. Liu, B. Rustumji, and S. J. Skinner, *Fuel Cells*, 2008, **8**, 338–343.

[124] A. Montenegro-Hernández, J. Vega-Castillo, L. Mogni, and A. Caneiro, *Int. J. Hydrogen Energy*, 2011, **36**, 15704–15714.

[125] C. Frayret, A. Villesuzanne, and M. Pouchard, *Chem. Mater.* 2005, **17**, 6538–6544.

[126] W. Xie, Y.-L. Lee, Y. Shao-Horn, and D. Morgan, *J. Phys. Chem. Lett.* 2016, **7**, 1939–1944.

[127] X. Ma, J. S. A. Carneiro, X.-K. Gu, H. Qin, H. Xin, K. Sun, and E. Nikolla, *ACS Catal.* 2015, **5**, 4013–4019.

[128] A. Chroneos, D. Parfitt, J. A. Kilner, and R. W. Grimes, *J. Mater. Chem.* 2010, **20**, 266–270.

[129] M. S. D. Read, M. S. Islam, G. W. Watson, and F. E. Hancock, *J. Mater. Chem.* 2001, **11**, 2597–2602.

[130] T. Horita, in *Perovskite Oxide Solid Oxide Fuel Cells*, 2009, pp. 285–296.

[131] M. Mori, *J. Electrochem. Soc.* 2002, **149**, A797.

[132] J. W. Fergus, *Solid State Ionics*, 2004, **171**, 1–15.

[133] X. Ding, Y. Liu, L. Gao, and L. Guo, *J. Alloys Compd.* 2006, **425**, 318–322.

[134] M. Mori, Y. Hiei, and T. Yamamoto, *J. Am. Ceram. Soc.* 2001, **84**, 781–786.

[135] I. Yasuda and T. Hikita, *J. Electrochem. Soc.* 1993, **140**, 1699.

[136] W. J. Weber, C. W. Griffin, and J. L. Bates, *J. Am. Ceram. Soc.* 1987, **70**, 265–270.

[137] M. Oishi, K. Yashiro, J. Hong, Y. Nigara, T. Kawada, and J. Mizusaki, *Solid State Ionics*, 2007, **178**, 307–312.

[138] D. M. Bastidas, S. Tao, and J. T. S. Irvine, *J. Mater. Chem.* 2006, **16**, 1603.

[139] W. Rativa-Parada, J. A. Gomez-Cuaspud, E. Vera-Lopez, and J. B. Carda, *J. Phys. Conf. Ser.* 2017, **786**, 012029.

[140] S. Wang, K. Huang, B. Zheng, J. Zhang, and S. Feng, *Mater. Lett.* 2013, **101**, 86–89.

[141] P. Luo, B. Zhang, Q. Zhao, D. He, and A. Chang, *J. Mater. Sci.: Mater. Electron.* 2017, **28**, 9265–9271.

[142] P. Duran, J. Tartaj, F. Capel, and C. Moure, *J. Eur. Ceram. Soc.* 2004, **24**, 2619–2629.

[143] R. J. D. Tilley, *Defects in Solids*, John Wiley & Sons, Inc., Hoboken, NJ, USA, 2008, pp. 216–219.

[144] P. Hohenberg and W. Kohn, *Phys. Rev.* 1964, **136**, B864–B871.

[145] W. Kohn and L. J. Sham, *Phys. Rev.* 1965, **140**, A1133–A1138.

[146] P. A. M. Dirac, *Math. Proc. Cambridge Philos. Soc.* 1930, **26**, 376.

[147] D. M. Ceperley and B. J. Alder, *Phys. Rev. Lett.* 1980, **45**, 566–569.

[148] S. H. Vosko, L. Wilk, and M. Nusair, *Can. J. Phys.* 1980, **58**, 1200–1211.

[149] J. P. Perdew, *Phys. Rev. B*, 1986, **33**, 8822–8824.

[150] J. P. Perdew, J. A. Chevary, S. H. Vosko, K. A. Jackson, M. R. Pederson, D. J. Singh, and C. Fiolhais, *Phys. Rev. B*, 1992, **46**, 6671–6687.

[151] A. D. Becke, *Phys. Rev. A*, 1988, **38**, 3098–3100.

[152] C. Lee, W. Yang, and R. G. Parr, *Phys. Rev. B*, 1988, **37**, 785–789.

[153] J. P. Perdew, K. Burke, and M. Ernzerhof, *Phys. Rev. Lett.* 1996, **77**, 3865–3868.

[154] J. P. Perdew, A. Ruzsinszky, G. I. Csonka, O. A. Vydrov, G. E. Scuseria, L. A. Constantin, X. Zhou, and K. Burke, *Phys. Rev. Lett.* 2008, **100**, 136406.

[155] S. L. Dudarev, G. A. Botton, S. Y. Savrasov, C. J. Humphreys, and A. P. Sutton, *Phys. Rev. B*, 1998, **57**, 1505–1509.

[156] M. Cococcioni and S. de Gironcoli, *Phys. Rev. B*, 2005, **71**, 035105.

[157] S. Lany and A. Zunger, *Phys. Rev. B*, 2009, **80**, 085202.

[158] B. J. Morgan and G. Watson, *Phys. Rev. B*, 2009, **80**, 233102.

[159] P. R. L. Keating, D. O. Scanlon, B. J. Morgan, N. M. Galea, and G. W. Watson, *J. Phys. Chem. C*, 2012, **116**, 2443–2452.

[160] P. J. Stephens, F. J. Devlin, C. F. Chabalowski, and M. J. Frisch, *J. Phys. Chem.* 1994, **98**, 11623–11627.

[161] C. Adamo and V. Barone, *J. Chem. Phys.* 1999, **110**, 6158–6170.

[162] J. Heyd, G. E. Scuseria, and M. Ernzerhof, *J. Chem. Phys.* 2003, **118**, 8207–8215.

[163] J. Heyd, G. E. Scuseria, and M. Ernzerhof, *J. Chem. Phys.* 2006, **124**, 219906.

[164] J. Heyd, J. E. Peralta, G. E. Scuseria, and R. L. Martin, *J. Chem. Phys.* 2005, **123**, 174101.

[165] B. G. Janesko, T. M. Henderson, and G. E. Scuseria, *Phys. Chem. Chem. Phys.* 2009, **11**, 443–454.

[166] D. O. Scanlon, B. J. Morgan, and G. W. Watson, *J. Chem. Phys.* 2009, **131**, 124703.

[167] J. P. Allen, D. O. Scanlon, and G. W. Watson, *Phys. Rev. B*, 2010, **81**, 161103.

[168] K. E. Kweon and G. S. Hwang, *Phys. Rev. B*, 2012, **86**, 165209.

[169] S. Baroni, P. Giannozzi, and A. Testa, *Phys. Rev. Lett.* 1987, **58**, 1861–1864.

[170] S. Baroni, P. Giannozzi, and A. Testa, *Phys. Rev. Lett.* 1987, **59**, 2662–2665.

[171] X. Gonze, *Phys. Rev. A*, 1995, **52**, 1086–1095.

[172] X. Gonze, *Phys. Rev. A*, 1995, **52**, 1096–1114.

[173] C. Kittel, *Introduction to Solid State Physics*, Wiley, 7th edn.

[174] H. J. Monkhorst and J. D. Pack, *Phys. Rev. B*, 1976, **13**, 5188–5192.

[175] M. L. Cohen and V. Heine, in *Solid State Phys.* Elsevier Science & Technology, 1970, pp. 37–248.

[176] P. E. Blöchl, *Phys. Rev. B*, 1994, **50**, 17953–17979.

[177] R. P. Feynman, *Phys. Rev.* 1939, **56**, 340–343.

[178] G. Kresse and J. Hafner, *Phys. Rev. B*, 1994, **49**, 14251–14269.

[179] G. Kresse and J. Furthmüller, *Comput. Mater. Sci.* 1996, **6**, 15–50.

[180] G. Kresse and J. Furthmüller, *Phys. Rev. B*, 1996, **54**, 11169–11186.

[181] F. D. Murnaghan, *Proc. Natl. Acad. Sci.* 1944, **30**, 244–247.

[182] J. P. Allen, D. O. Scanlon, S. C. Parker, and G. W. Watson, *J. Phys. Chem. C*, 2011, **115**, 19916–19924.

[183] D. O. Scanlon and G. W. Watson, *J. Mater. Chem.* 2012, **22**, 25236.

[184] A. B. Kehoe, E. Arca, D. O. Scanlon, I. V. Shvets, and G. W. Watson, *J. Phys. Condens. Matter*, 2016, **28**, 125501.

[185] P. R. Keating, D. O. Scanlon, and G. W. Watson, *Chem. Phys. Lett.* 2014, **608**, 239–243.

[186] P. Pulay, *Chem. Phys. Lett.* 1980, **73**, 393–398.

[187] D. Sheppard, R. Terrell, and G. Henkelman, *J. Chem. Phys.* 2008, **128**, 134106.

[188] C. Bradley and A. Cracknell, *The Mathematical Theory of Symmetry in Solids: Representation Theory for Point Groups and Space Groups*, Oxford Classic Texts, 1972.

[189] D. Segev and S.-H. Wei, *Phys. Rev. B*, 2005, **71**, 125129.

[190] C. Freysoldt, J. Neugebauer, and C. G. Van de Walle, *Phys. Rev. Lett.* 2009, **102**, 016402.

[191] J Buckeridge, D. Scanlon, A Walsh, and C. Catlow, *Comput. Phys. Commun.* 2014, **185**, 330–338.

[192] K. Reuter and M. Scheffler, *Phys. Rev. B*, 2001, **65**, 035406.

[193] *NIST-JANAF Thermochemical Tables*, U. S. National Bureau of Standards, Washington DC, 1998.

[194] S. Zhang, N. Han, and X. Tan, *RSC Adv.* 2015, **5**, 760–769.

[195] H. Jónsson, G. Mills, and K. W. Jacobsen, *Class. Quantum Dyn. Condens. Phase Simulations*, World Scientific, 1998, pp. 385–404.

[196] P. W. Tasker, *J. Phys. C: Solid State Phys.* 1979, **12**, 4977–4984.

[197] G. W. Watson, E. T. Kelsey, N. H. de Leeuw, D. J. Harris, and S. C. Parker, *J Chem. Soc., Faraday Trans.* 1996, **92**, 433.

[198] G. Wulff, *Zeitschrift für Krist. - Cryst. Mater.* 1901, **34**, 449–530.

[199] X. Zhu, X. Tu, M. Chen, Y. Yang, C. Zheng, J. Zhou, and X. Gao, *Catal. Commun.* 2017, **92**, 35–39.

[200] Y. Peng, W. Z. Si, J. H. Li, J. Crittenden, and J. M. Hao, *Catal. Sci. Technol.* 2015, **5**, 2478–2485.

[201] C. H. Kim, G. Qi, K. Dahlberg, and W. Li, *Science*, 2010, **327**, 1624–1627.

[202] Z.-J. Sui, L. Vradman, I. Reizner, M. V. Landau, and M. Herskowitz, *Catal. Commun.* 2011, **12**, 1437–1441.

[203] G. Saracco, F. Geobaldo, and G. Baldi, *Appl. Catal. B Environ.* 1999, **20**, 277–288.

[204] Y. Liu, Q. Sun, W. Li, K. R. Adair, J. Li, and X. Sun, *Green Energy Environ.* 2017, **2**, 246–277.

[205] J. T. Mefford, W. G. Hardin, S. Dai, K. P. Johnston, and K. J. Stevenson, *Nat. Mater.* 2014, **13**, 726–732.

[206] Z. A. Elsiddig, H. Xu, D. Wang, W. Zhang, X. Guo, Y. Zhang, Z. Sun, and J. Chen, *Electrochim. Acta*, 2017, **253**, 422–429.

[207] X. Lang, H. Mo, X. Hu, and H. Tian, *Dalt. Trans.* 2017, **46**, 13720–13730.

[208] M. Baldini, T. Muramatsu, M. Sherafati, H.-k. Mao, L. Malavasi, P. Postorino, S. Satpathy, and V. V. Struzhkin, *Proc. Natl. Acad. Sci.* 2015, **112**, 10869–10872.

[209] H. Khanduri, M. Chandra Dimri, S. Vasala, S. Leinberg, R. Lõhmus, T. V. Ashworth, A. Mere, J. Krustok, M. Karppinen, and R Stern, *J. Phys. D: Appl. Phys.* 2013, **46**, 175003.

[210] A. Boukhachem, A. Ziouche, M. en Amor, O. Kamoun, M. Zergoug, H. Maghraoui-Meherzi, A. Yumak, K. Boubaker, and M. Amlouk, *Mater. Res. Bull.* 2016, **74**, 202–211.

[211] Y. Zhou, Z. Lü, B. Wei, X. Zhu, X. Huang, W. Jiang, and W. Su, *J. Power Sources*, 2012, **209**, 158–162.

[212] Y. Choi, M. C. Lin, and M. Liu, *Angew. Chemie Int. Ed.* 2007, **46**, 7214–7219.

[213] Y. Choi, M. E. Lynch, M. C. Lin, and M. Liu, *J. Phys. Chem. C*, 2009, **113**, 7290–7297.

[214] E. A. Kotomin, E. Heifets, J. Maier, and W. A. Goddard III, *Phys. Chem. Chem. Phys.* 2003, **5**, 4180.

[215] R. A. Evarestov, E. A. Kotomin, Y. A. Mastrikov, D. Gryaznov, E. Heifets, and J. Maier, *Phys. Rev. B*, 2005, **72**, 214411.

[216] J. Rodríguez-Carvajal, M. Hennion, F. Moussa, A. H. Moudden, L. Pinsard, and A. Revcolevschi, *Phys. Rev. B*, 1998, **57**, R3189–R3192.

[217] X. Qiu, T. Proffen, J. F. Mitchell, and S. J. L. Billinge, *Phys. Rev. Lett.* 2005, **94**, 177203.

[218] A. M. Glazer, *Acta Crystallogr. Sect. B Struct. Crystallogr. Cryst. Chem.* 1972, **28**, 3384–3392.

[219] A. M. Glazer, *Acta. Cryst. A*, 1975, **31**, 756–762.

[220] R. Kováčik and C. Ederer, *Phys. Rev. B*, 2011, **84**, 075118.

[221] J. B. A. A. Elemans, B. Van Laar, K. R. Van Der Veen, and B. O. Loopstra, *J. Solid State Chem.* 1971, **3**, 238–242.

[222] B. C. Hauback, H. Fjellvåg, and N. Sakai, *J. Solid State Chem.* 1996, **124**, 43–51.

[223] F. Moussa, M. Hennion, J. Rodriguez-Carvajal, H. Moudden, L. Pinsard, and A. Revcolevschi, *Phys. Rev. B*, 1996, **54**, 15149–15155.

[224] J. H. Jung, K. H. Kim, D. J. Eom, T. W. Noh, E. J. Choi, J. Yu, Y. S. Kwon, and Y. Chung, *Phys. Rev. B*, 1997, **55**, 15489–15493.

[225] E. A. Kotomin, R. A. Evarestov, Y. A. Mastrikov, and J. Maier, *Phys. Chem. Chem. Phys.* 2005, **7**, 2346.

[226] C. Franchini, R. Kováčik, M. Marsman, S. Sathyanarayana Murthy, J. He, C. Ederer, and G. Kresse, *J. Phys.: Condens. Matter*, 2012, **24**, 235602.

[227] Z. Yang, Z. Huang, L. Ye, and X. Xie, *Phys. Rev. B*, 1999, **60**, 15674–15682.

[228] E. Symianakis, D. Malko, E. Ahmad, A.-S. Mamede, J.-F. Paul, N. Harrison, and A. Kucernak, *J. Phys. Chem. C*, 2015, **119**, 12209–12217.

[229] I. Solovyev, N. Hamada, and K. Terakura, *Phys. Rev. B*, 1996, **53**, 7158–7170.

[230] G. Trimarchi and N. Binggeli, *Phys. Rev. B*, 2005, **71**, 035101.

[231] B. J. Morgan, D. O. Scanlon, and G. W. Watson, *e-J. Surf. Sci. Nanotechnol.* 2009, **7**, 389–394.

[232] B. J. Morgan and G. W. Watson, *J. Phys. Chem. C*, 2010, **114**, 2321–2328.

[233] R. O. Jones and O. Gunnarsson, *Rev. Mod. Phys.* 1989, **61**, 689–746.

[234] D. C. Patton, D. V. Porezag, and M. R. Pederson, *Phys. Rev. B*, 1997, **55**, 7454–7459.

[235] B. Hammer, L. B. Hansen, and J. K. Norskov, *Phys. Rev. B*, 1999, **59**, 7413–7421.

[236] T. Arima, Y. Tokura, and J. B. Torrance, *Phys. Rev. B*, 1993, **48**, 17006–17009.

[237] T. Saitoh, A. E. Bocquet, T. Mizokawa, H. Namatame, A. Fujimori, M. Abbate, Y. Takeda, and M. Takano, *Phys. Rev. B*, 1995, **51**, 13942–13951.

[238] S. Yamaguchi, Y. Okimoto, K. Ishibashi, and Y. Tokura, *Phys. Rev. B*, 1998, **58**, 6862–6870.

[239] J. Buckeridge, F. H. Taylor, and C. R. A. Catlow, *Phys. Rev. B*, 2016, **93**, 155123.

[240] J. Bielecki, R. Rauer, E. Zanghellini, R. Gunnarsson, K. Dörr, and L. Börjesson, *Phys. Rev. B*, 2010, **81**, 064434.

[241] N. N. Kovaleva, A. M. Oles, A. M. Balbashov, A. Maljuk, D. N. Argyriou, G. Khaliullin, and B. Keimer, *Phys. Rev. B*, 2010, **81**, 235130.

[242] K. Momma and F. Izumi, *J. Appl. Crystallogr.* 2011, **44**, 1272–1276.

[243] N. Mahato, A. Banerjee, A. Gupta, S. Omar, and K. Balani, *Prog. Mater. Sci.* 2015, **72**, 141–337.

[244] R. D. Shannon, *Acta Cryst.* 1976, **A32**, 751–767.

[245] W. Lee, J. W. Han, Y. Chen, Z. Cai, and B. Yildiz, *J. Am. Chem. Soc.* 2013, **135**, 7909–7925.

[246] Y. A. Mastrikov, R. Merkle, E. Heifets, E. A. Kotomin, and J. Maier, *J. Phys. Chem. C*, 2010, **114**, 3017–3027.

[247] S. M. Woodley, J. D. Gale, P. D. Battle, and C. R. A. Catlow, *J. Chem. Phys.* 2003, **119**, 9737–9744.

[248] M. S. Islam, M. Cherry, and C. R. A. Catlow, *J. Solid State Chem.* 1996, **124**, 230–237.

[249] A. Belzner, T. M. Gür, and R. A. Huggins, *Solid State Ionics*, 1992, **57**, 327–337.

[250] M. Pavone, A. B. Muñoz-García, A. M. Ritzmann, and E. A. Carter, *J. Phys. Chem. C*, 2014, **118**, 13346–13356.

[251] M. Medarde and J. Rodríguez-Carvajal, *Zeitschrift für Phys. B Condens. Matter*, 1997, **102**, 307–315.

[252] K. Maiti, P. Mahadevan, and D. D. Sarma, *Phys. Rev. B*, 1999, **59**, 12457–12470.

[253] Y. Chen, Z. Cai, Y. Kuru, H. L. Tuller, and B. Yildiz, *ECS Trans.* 2013, **57**, 1781–1791.

[254] J. M. Bassat, P. Odier, and J. P. Loup, *J. Solid State Chem.* 1994, **110**, 124–135.

[255] H. Eisaki, S. Uchida, T. Mizokawa, H. Namatame, A. Fujimori, J. van Elp, P. Kuiper, G. A. Sawatzky, S. Hosoya, and H. Katayama-Yoshida, *Phys. Rev. B*, 1992, **45**, 12513–12521.

[256] Z. Li and R. Haugsrud, *Solid State Ionics*, 2012, **206**, 67–71.

[257] J. Druce, T. Ishihara, and J. Kilner, *Solid State Ionics*, 2014, **262**, 893–896.

[258] H. Téllez, J. Druce, Y.-W. Ju, J. Kilner, and T. Ishihara, *Int. J. Hydrogen Energy*, 2014, **39**, 20856–20863.

[259] K. G. Godhino, Ph.D. Thesis, Trinity College Dublin, 2011.

[260] H. D. Lee, B. Magyari-Köpe, and Y. Nishi, *Phys. Rev. B*, 2010, **81**, 193202.

[261] S. Park, H.-S. Ahn, C.-K. Lee, H. Kim, H. Jin, H.-S. Lee, S. Seo, J. Yu, and S. Han, *Phys. Rev. B*, 2008, **77**, 134103.

[262] A. M. Ferrari, C. Pisani, F. Cinquini, L. Giordano, and G. Pacchioni, *J. Chem. Phys.* 2007, **127**, 174711.

[263] F. Cinquini, L. Giordano, G. Pacchioni, A. M. Ferrari, C. Pisani, and C. Roetti, *Phys. Rev. B*, 2006, **74**, 165403.

[264] A. Jain, G. Hautier, S. P. Ong, C. J. Moore, C. C. Fischer, K. A. Persson, and G. Ceder, *Phys. Rev. B*, 2011, **84**, 045115.

[265] P. Wanaguru, J. An, and Q. Zhang, *J. Appl. Phys.* 2016, **119**, 084302.

[266] C. Xia, Y. Jia, M. Tao, and Q. Zhang, *Phys. Lett. A*, 2013, **377**, 1943–1947.

[267] R. Wang, M. Würth, U. B. Pal, S. Gopalan, and S. N. Basu, *J. Power Sources*, 2017, **360**, 87–97.

[268] T. Horita, Y. Xiong, H. Kishimoto, K. Yamaji, M. E. Brito, and H. Yokokawa, *J. Electrochem. Soc.* 2010, **157**, B614.

[269] K. Hilpert, D. Das, M. Miller, D. H. Peck, and R. Weiß, *J. Electrochem. Soc.* 1996, **143**, 3642.

[270] R. Raffaelle, H. U. Anderson, D. M. Sparlin, and P. E. Parris, *Phys. Rev. B*, 1991, **43**, 7991–7999.

[271] K. H. L. Zhang, K. Xi, M. G. Blamire, and R. G. Egdell, *J. Phys.: Condens. Matter*, 2016, **28**, 383002.

[272] S. C. Dixon, D. O. Scanlon, C. J. Carmalt, and I. P. Parkin, *J. Mater. Chem. C.* 2016, **4**, 6946–6961.

[273] H. Hosono and K. Ueda, in *Springer Handb. Electron. Photonic Mater.* Springer International Publishing, Cham, 2017, pp. 1–1.

[274] O. F. Schirmer, *J. Phys.: Condens. Matter*, 2006, **18**, R667–R704.

[275] P. R. L. Keating, D. O. Scanlon, and G. W. Watson, *J. Mater. Chem. C*, 2013, **1**, 1093–1098.

[276] N. Duan, A. W. Sleight, M. K. Jayaraj, and J. Tate, *Appl. Phys. Lett.* 2000, **77**, 1325–1326.

[277] R. Nagarajan, A. D. Draeseke, A. W. Sleight, and J. Tate, *J. Appl. Phys.* 2001, **89**, 8022–8025.

[278] S. Sheng, G. Fang, C. Li, S. Xu, and X. Zhao, *Phys. status solidi*, 2006, **203**, 1891–1900.

[279] M. K. Jayaraj, A. D. Draeseke, J. Tate, and A. W. Sleight, *Thin Solid Films*, 2001, **397**, 244–248.

[280] M. Snure and A. Tiwari, *Appl. Phys. Lett.* 2007, **91**, 092123.

[281] H. Kawazoe and K. Ueda, *J. Am. Ceram. Soc.* 1999, **82**, 3330–3336.

[282] M. Dekkers, G. Rijnders, and D. H. A. Blank, *Appl. Phys. Lett.* 2007, **90**, 021903.

[283] K. Ueda, S. Inoue, S. Hirose, H. Kawazoe, and H. Hosono, *Appl. Phys. Lett.* 2000, **77**, 2701–2703.

[284] D. O. Scanlon, J. Buckeridge, C. R. A. Catlow, and G. W. Watson, *J. Mater. Chem. C.* 2014, **2**, 3429.

[285] M. L. Liu, L. B. Wu, F. Q. Huang, L. D. Chen, and J. A. Ibers, *J. Solid State Chem.* 2007, **180**, 62–69.

[286] K. H. L. Zhang, Y. Du, A. Papadogianni, O. Bierwagen, S. Sallis, L. F. J. Piper, M. E. Bowden, V. Shutthanandan, P. V. Sushko, and S. A. Chambers, *Adv. Mater.* 2015, **27**, 5191–5195.

[287] A. L. Gavin and G. W. Watson, *Solid State Ionics*, 2017, **299**, 13–17.

[288] N. J. Mosey, P. Liao, and E. A. Carter, *J. Chem. Phys.* 2008, **129**, 014103.

[289] J. Yang, *Acta Crystallogr. Sect. B Struct. Sci.* 2008, **64**, 281–286.

[290] S. Dabaghmanesh, N. Sarmadian, E. C. Neyts, and B. Partoens, *Phys. Chem. Chem. Phys.* 2017, **19**, 22870–22876.